FACULTY
OF MATHEMATICS
AND PHYSICS
Charles University

DOCTORAL THESIS

Dalibor Preisler

Beta-Ti alloys for medical applications

Department of Physics of Materials

Supervisor of the doctoral thesis: doc. PhDr. RNDr. Josef Stráský, Ph.D.

Study programme: Physics

Specialization: Physics of Condensed Matter and Materials Research

Prague 2023

I declare that I carried out this doctoral thesis independently, and only with the cited sources, literature and other professional sources. It has not been used to obtain another or the same degree.

I understand that my work relates to the rights and obligations under the Act No. 121/2000 Sb., the Copyright Act, as amended, in particular the fact that the Charles University has the right to conclude a license agreement on the use of this work as a school work pursuant to Section 60 paragraph 1 of the Copyright Act.

In…… date…… ……

Author's signature

This thesis is based on my work during my Ph.D. study at the Department of Physics of Materials. I followed up on the previous research done in the so-called Titans group and in this sense, studying the topic of my doctoral thesis was possible because “I stood on the shoulders of Titans”.

I would like to thank my supervisor Josef Stráský for his guidance, inspiration, discussion and ideas during my Ph.D. study. I also thank my consultant Miloš Janeček for his support, mainly regarding the technical issues and his constant push for publications. I am grateful to many other people from the Department of Physics of Materials with whom I could discuss the topics and who also helped me in various ways: Petr Harcuba, Josef Veselý, Jiří Kozlík, Michal Knapek, Jana Šmilauerová and Kristína Bartha as well as other colleagues from the department. I thank Jana Kálalová and Andrea Bendová for help with sample preparation. I would like to further express gratitude to the colleagues from the Department of Condensed Matter Physics, namely Tereza Košutová and Lukáš Horák for their great suggestions regarding the measurements of X-ray diffraction. I thank the colleagues from the Institute of Thermomechanics, namely Hanuš Seiner, Michaela Janovská and Lucie Bodnárová for elasticity measurements and all related discussions. I thank people from the Institute of Plasma Physics and companies COMTES FHT a.s., UJP Praha a.s. and CAMEX, s.r.o. for providing material manufacturing technologies used in this thesis. Financial support by the following funders is acknowledged: Grant Agency of Charles University (projects 1530217 and 146120), Ministry of Education, Youth and Sport of the Czech Republic (project CZ.02.2.69/0.0/0.0/19_073/0016935), Ministry of Industry and Trade of the Czech Republic (project FV20147) and the Czech Science Foundation. Experiments were partly performed in MGML (mgml.eu), which is supported within the program of Czech Research Infrastructures (project no. LM2023065).

Finally, I thank my family and my wife Míša for her support.

Title: Beta-Ti alloys for medical applications

Author: Dalibor Preisler

Department / Institute: Department of Physics of Materials

Supervisor of the doctoral thesis: doc. PhDr. RNDr. Josef Stráský, Ph.D., Department of Physics of Materials

Abstract: Interstitial strengthening by a high amount of oxygen can be used in metastable beta-Ti alloys, for achieving very high strength without compromising ductility. The content of oxygen however influences the phase stability and consequently increases the Young's modulus. Several alloys with various content of beta-stabilizing elements were prepared by common metallurgical route. On top of that, dozens of compositions were prepared by a high-throughput powder metallurgy method and thoroughly studied. Lattice softening due to proximity to a martensitic transformation was utilized to minimize the Young's modulus. Effect of omega phase was thoroughly studied; it was found that the embrittlement by the athermal omega phase is most probably connected with the high oxygen content and its room-temperature diffusion into omega particles. Fundamental difference between elastic behaviour of alloys containing a significant fraction of omega and those with only a limited amount of omega was demonstrated. Regarding the plastic deformation mechanisms, it was found that formation of stress-induced alpha″ martensite is related to differences in lattice parameters of the parent and martensitic phases, which depend on alloy compositions. However, utilizing transformation induced plasticity (TRIP) for ductility enhancement of alloys with high oxygen content was not successful. The thesis describes efficient methodological approach for development of advanced Ti alloys. Finally, alloys with promising properties for biomedical use were selected and characterized.

Keywords: Ti alloys, interstitial strengthening, phase transformations, lattice softening, mechanical properties

Contents

Introduction

The main topic of this thesis was, as the title suggests, development of the metastable β titanium alloys for medical applications, especially for the target application in production of femoral stem of total hip endoprosthesis. This component's requirements of mechanical properties present a challenge for material science as multiple parameters have to be met at once, namely high strength, low Young's modulus, sufficient ductility and biocompatibility of the alloy.

The research followed the pathway of the metastable β alloy Ti-35Nb-7Zr-6Ta-0.7O developed at the Department of Physics of Materials prior beginning of my work and the alloys developed in this thesis are derived from it. The well-known yet complicated physical mechanisms needed to be considered when targeting the required properties of alloys for implant production. The metastable β Ti alloys are known to undergo a wide range of phase transformations, both during heating/cooling as well as during deformation. These phase transformations need to be accounted to achieve the material that can be brought to into industrial use.

In the following, this thesis is divided into several chapters: In the first chapter, the phase transformations and mechanisms affecting the material properties are reviewed together with previous research in the field of metastable β Ti alloys. Second chapter shortly summarizes the aims of the thesis and the third chapter introduces the used experimental techniques as well as the used material preparation methods. In the fourth chapter, novel industrial processing route of the aforementioned alloy is described. The fifth chapter is aimed on the design and characterization of novel alloys prepared by the classical approach while in the sixth chapter, the high-throughput method is used for screening of large number of alloys. The most effort is put into characterization of the phase composition, elastic properties and the deformation mechanisms active during compression testing. In the last chapter, two alloys, selected on the basis of the high-throughput testing, are prepared and thoroughly studied. The thesis is summarized in Conclusions where the work is briefly recapitulated and the most important findings are stated together with future outlook.

1. Literature review – Ti alloys for medical applications

Titanium has not been known to mankind for a long time. Its existence was discovered in an Ilmenite mineral by the end of the 18th century, but it took more than 100 years until this extraordinary element was isolated in its metallic form. Since then, the popularity of titanium is increasing. Its extraordinary properties such as high specific strength (combination of high strength and low density), corrosion resistance as well as its biocompatibility predetermine its use in a wide range of high-added-value fields ranging from aviation and aerospace through petrochemical to the medical industry. It is even used in some people's everyday life (Ti-made jewelry, cookware, luxury sports equipment).

The main drawback of an even wider expansion of titanium is its cost. The expensive production processes include the separation from the ores by the Kroll process (which is also not very friendly to the environment [1]), alloying that has to be done using the vacuum arc remelting (VAR) process to obtain the high temperatures for its melting, high-temperature oxidation during thermomechanical processing and finally, the machining process of the products causing fast wear of even high-quality tools (e.g. carbide inserts for special materials).

Despite the stated drawbacks, in the fields of its use, titanium cannot be currently replaced by any other metal. In the medical industry, it is used e.g. for the production of surgical tools, dental implants and joint implants [2,3]. The last group is of interest in this thesis which focuses mainly on material development for manufacturing femoral stem of a total hip endoprosthesis.

Currently, most Ti-based hip implants are produced from a Ti-6Al-4V (wt%) alloy [4], which was initially developed for the aviation industry where it is still massively used. The strength of the material is the most important for the construction of the implant. Usually, the Ti-6Al-4V alloy serves as a benchmark - it achieves yield stress over 800 MPa even in its weakest and most ductile condition and this value is the required minimum for the hip implant design.

The (Young's) elastic modulus of Ti-6Al-4V as well as of commercially pure Ti is around 100-120 GPa [5,6], which provides a major advantage over previously used steels with an elastic modulus of around 200 GPa as it is closer to the elastic modulus of the bone (10-30 GPa) [7,8]. The misfit in elastic modulus can cause the so-called stress shielding effect [9,10], the stiff implant absorbs much more load than the surrounding bone [11] and the lack of mechanical stimulation causes the bone to atrophy. Bone with developed osteoporosis is very prone to fracture. Therefore, the aims of the research followed this trend and the closer elastic modulus to that of bone was desired [12,13]. In this sense, the class of metastable β titanium alloys is one of the most prospective due to possibility of controlling the target properties (including elastic modulus) via controlling presence and volume fraction of various crystallographic phases.

Another possible advantage of a new alloy over Ti-6Al-4V could be the use of purely biocompatible elements (Ti, Nb, Zr, Ta) that were proven inert in a living body environment [14], which cannot be said about Al and V [15–17].

1.1. Phase transformations in Ti alloys

1.1.1. Stable phases and alloy groups

As mentioned above, phase transformations play a crucial role in the metallurgy of Ti alloys. Depending on the equilibrium phase composition at room temperature (RT), the alloys can be divided into several groups. Pure Ti exists either in a high-temperature β phase with a body-centred cubic (Im-3m) structure or below the so-

called β transus temperature (T_β), in hexagonal close-packed α phase ($P6_3/mmc$). Alloying elements in Ti alloys can either increase the T_β (α stabilizers, typically Al, O and N) or decrease the T_β (β stabilizers, most of the transition metals) [18]. The so-called neutral elements (Zr and Sn) decrease the T_β until they reach concentration corresponding to a congruent point of the β→α phase transformation after which they start to increase T_β again. The β stabilizers can either form intermetallic compounds or be fully soluble in the β phase (isomorphous β-stabilizers). The latter case is the case of the biocompatible β stabilizers (Nb, Ta).

A schematic phase diagram of an isomorphous β stabilizer is shown in Figure 1 showing the locations of α alloys, α+β alloys, metastable β alloys and stable β alloys. The most relevant for this thesis are metastable β alloys. Although lying in the field of stable α+β mixture, the presence of α phase and α′/α″ martensite phases can be avoided by quenching from temperatures above T_β (also referred to as a β solution treatment or just simply ST). This is because the martensite start (M_S) temperature falls below the RT and martensite does not form.

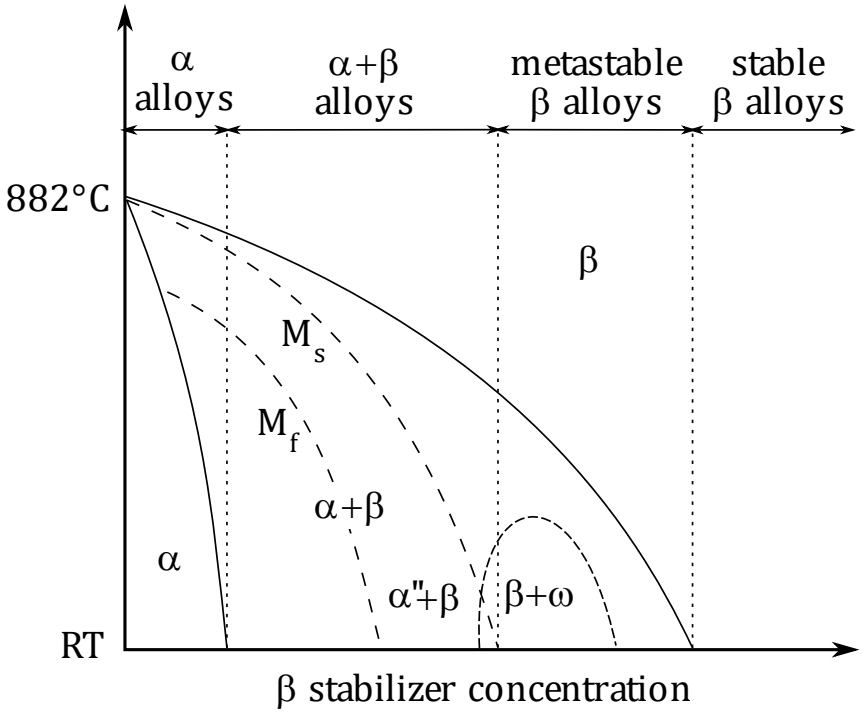

Figure 1: Groups of Ti alloys according to α / β phase presence at RT (adopted from [19]).

1.1.2. Metastable phases: β, α′, α″, ω, O′

Apart from the specified stable phases, a variety of metastable phases can form under various conditions.

The β phase present in the metastable β Ti alloys is obviously metastable as its composition does not correspond to the stable β phase in α+β mixture. Due to its nature, it can easily decompose into secondary phases.

The α′ phase is a martensite phase with the same crystallographic structure as stable α (hcp), but non-equilibrium composition. α′ phase is usually formed in α+β alloys with a lower amount of β-stabilizing elements.

When the amount of β stabilizing elements is higher, yet not high enough to form a metastable β alloy, the martensite formed during quenching is not hcp, but assumes

orthorhombic structure (Cmcm) and is referred to as α″. Both martensite phases have a given lattice correspondence to β phase that is presented in Figure 2. The transformation β→α′/α″ involves two types of atomic movements: $\{11\bar{2}\}\langle 111\rangle_\beta$ shear of the whole crystal lattice and $\{110\}\langle 1\bar{1}0\rangle_\beta$ shuffle of every other $\{110\}_\beta$ plane [20]. In contrast with the stable α phase, the mechanism is purely diffusionless. According to the magnitude of the atomic movement, the result is either the α″ phase (in case of an incomplete shear and shuffle) or α′ phase (in case of complete shear and shuffle). In this sense, the α″ phase can be considered an intermediate phase between the β and α′ (and α). The shear can be visualized in Figure 2 as a change of the interatomic distances marked as a_0, b_0, c_0 in the β phase or as a, b, c in α′/α″ phases (the letters correspond to the lattice parameters of α″).

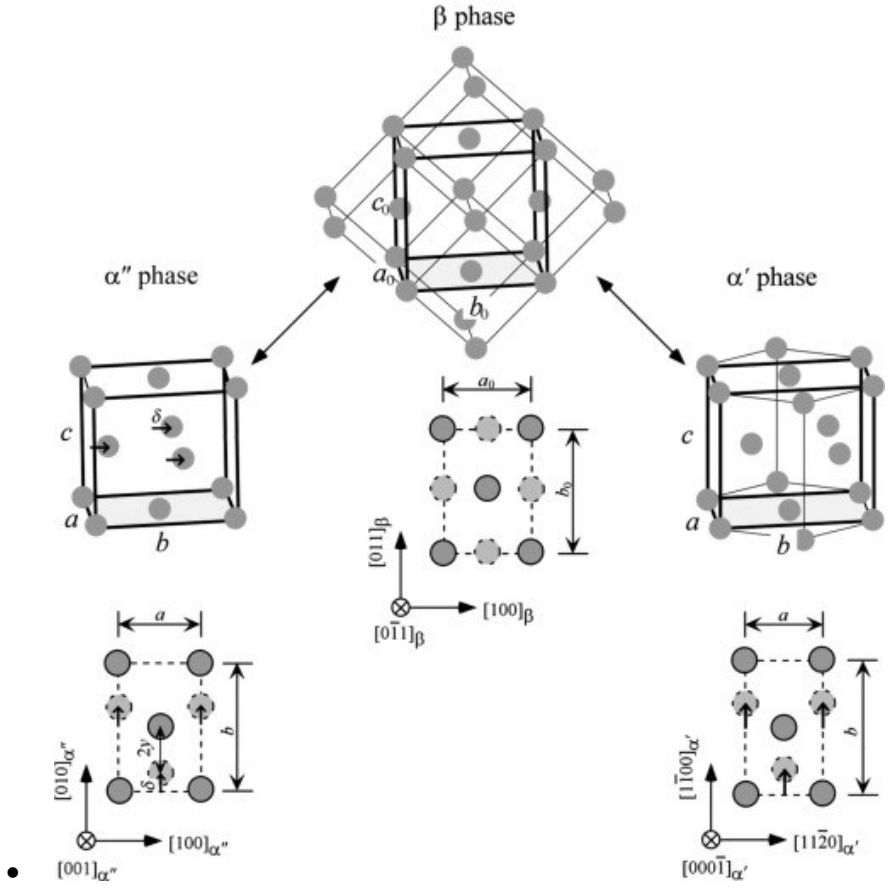

Figure 2: Lattice correspondence between cubic β phase (Im-3m), α″ phase (Cmcm) and α′ phase ($P6_3/mmc$) which is the same as the stable α phase. Adopted from [21].

Following the lattice correspondence between the β and α′, the so-called Burger′s relationships govern their mutual orientations [22,23]:

$$(110)_\beta \,||\, (0002)_\alpha$$

$$[1\bar{1}1]_\beta \,||\, [11\bar{2}0]_\alpha$$

Therefore, the α phase (as well as the α′/α″ martensite) can form in twelve different orientations (variants) with respect to the parent β phase.

Another type of phase that can form in Ti alloys is the ω phase [24]. It can form in alloys with composition already in the group of metastable β alloys, i.e. the M_S line is below the RT. The ω phase is in the form of nano-scale particles and can form either athermally [25] during quenching (then it is called athermal ω or ω_{ath}) or it can chemically stabilize during low-temperature annealing into isothermal ω (ω_{iso}) [26].

The orientation relationship between β and ω phases is shown in Figure 3. In contrast to Burger's relationships, during ω formation, the plane that is parallel to the basal plane of ω is $(111)_\beta$:

$$(111)_\beta || (0001)_\omega$$
$$[011]_\beta || [11\bar{2}0]_\omega$$

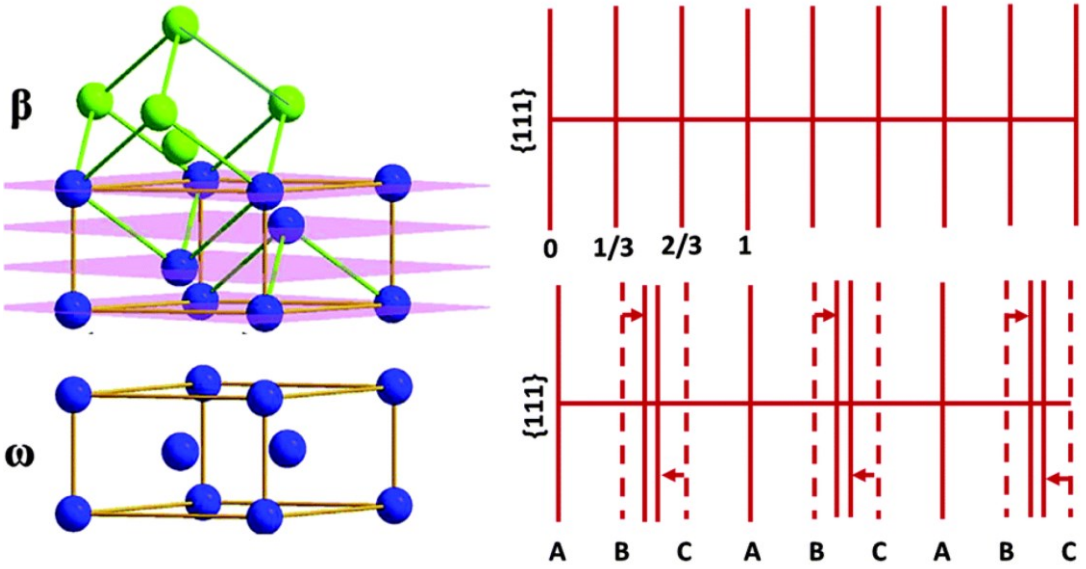

Figure 3: Orientation relationship between β and ω phases. The collapse of atoms in $\{111\}_\beta$ planes (B and C) is visualized on the right. Adopted from [27].

The ω nanoparticles usually do not have a clear boundary with the surrounding β matrix, it is rather a continuous change of the level of collapse of the {111} planes. Their structure is hexagonal (P6/mmc), but not close-packed as in the case of α phase ($P6_3/mmc$).

The last metastable phase in Ti alloys, relevant in this thesis, is only recently discovered O′ phase, which assumes an orthorhombic structure. The formation mechanism is different from α″ because it does not involve $\{11\bar{2}\}\langle 111\rangle_\beta$ shear and only $\{110\}\langle 1\bar{1}0\rangle_\beta$ shuffle is present. The O′ has a form of nanoparticles [28,29] and can be present in metastable alloys that are at an intermediate distance from the M_S line.

1.1.3. Phase transformations during temperature changes

Upon heating to sufficiently high temperatures, metastable phases will start to transform into stable phases, either to a mixture of α+β below T_β or to a β phase above the T_β. This is of course the ultimate condition. At intermediate temperatures, many different transformations may occur:

- Chemical stabilization of α′ martensite
- Chemical stabilization of α″ martensite and change of its crystal structure to hcp.
- Athermal change of the volume fraction of ω_{ath} while changing the temperature around the RT [30].
- Growth and diffusion-assisted change from ω_{ath} to ω_{iso} [31].

- ω-assisted nucleation of fine α phase leading to very fine α+β microstructure [32].
- Dissolution of ω_{iso} into β phase without direct assistance of α nucleation [33].
- O′-assisted nucleation of α phase [34].
- Formation of isothermal α″ from metastable β [35] which can result in very interesting effects such as zero thermal expansion over a temperature range around 300°C [36].

This list is most probably not complete, and it evidences the complexity of the phase transformations during temperature changes. Even more complexity is added when mechanical loading is considered.

1.1.4. Phase transformations during loading

One of the most important phase transformations during loading is the formation of stress-induced martensite (SIM) α″ in the metastable β alloys [37–39]. This transformation is mostly reversible upon unloading and it can result in the so-called super-elasticity (also pseudo-elasticity), where a large portion of the reversible deformation is not due to stretching of interatomic distances, but due to the transformation connected with the deformation [40–42].

If the α″ phase is already present in the material after quenching and the M_S temperature is not very high, another important effect can occur during straining. Due to the applied deformation, the present variants of the α″ phase can reorient into other variants at relatively low stresses. Upon subsequent heating to temperatures above M_S (or more precisely A_F – austenite finish, when the austenite β phase is fully restored), the material shape changes back to the original. Such behaviour is called the Shape memory effect, mostly known from the Ni-Ti (Nitinol) alloy [43], but also observed in Ti-Nb-based alloys [44–46].

The SIM α″ can also serve as an additional plastic deformation mechanism in addition to the dislocation slip. The main condition is that the β→α″ transformation will occur first during the loading, followed by the dislocation slip.

Apart from stress-induced transformations including α″ phase, deformation-induced ω has also been reported [47,48]. Later, it was however found out that the ω phase formation is an accommodation mechanism of twinned α″ martensite transforming back to β during unloading [49] at super-elastic alloys, irrespectively of the twinning mode [50].

Finally, the O′ phase was also found to undergo a stress-induced phase transformation. Due to its nanoparticle nature, the lattice plane in which the shuffle mechanism operates is not coupled with the surrounding nanoparticles. This blocks the formation of the typical martensite lamellae, but the O′ nanoparticles each can transform by the restricted shear into nano-sized α″ as observed in [51].

1.2. Properties of metastable β Ti alloys

Two main, although linked, factors influence the basic properties of metastable β Ti alloys: chemical composition and phase content. Since biocompatibility could be one of the most beneficial aspects of new material in future, the main alloying elements are selected according to previously stated results: Nb, Zr and Ta. On this basis, numerous studies have been published in the last 25 years regarding the development of low-modulus alloys. The developed first alloys with very low elastic moduli are Ti-29Nb-13Ta-4.6Zr [52] (Japan alloy) and Ti-35.3Nb-5.7Ta-7.3Zr [53] (USA alloy). The latter was developed by testing various chemical compositions aiming to minimize the elastic modulus as much as possible [54]. The resulting elastic modulus can be as

low as 50 GPa due to the absence of α, α″ and ω phases in the β solution-treated condition. The main drawback of Ti-35Nb-6Ta-7Zr alloy is its strength reaching only 500 MPa which is insufficient for use in hip implants.

1.2.1. Strengthening mechanisms

Increasing strength in any structural material is based on the known strengthening mechanisms. Usually, their combination is used to achieve the final property.

Substitutional solid solution strengthening

The easiest way to strengthen the material is by alloying with substitutional elements that are soluble (at least to the extent of alloying) in the base metal. Strengthening is then caused by an increased energy barrier to move the dislocation across the site with a foreign atom. Apart from the element concentration, the substitutional strengthening depends strongly on the misfit between the matrix and the solute atom [55]. The values of metallic atomic radii (metallic = based on the experimental lattice parameters) for elements relevant to this thesis are shown in *Table 1*. While Nb nearly doesn't differ from a radius of Ti, Zr and Ta can provide a stronger solution strengthening, although such effects are usually completely obscured by the change in the phase content [56,57]. The Fe is the most efficient from this group (although by far not as biocompatible as other elements in *Table 1*) which was proven even at low concentrations of 2 wt% [58].

Table 1: Atomic radii of Ti [59]*, Nb* [60]*, Zr* [61]*, Ta* [62] *and Fe* [61].

Element	Ti	Nb	Zr	Ta	Fe
Atomic radius (pm)	142	144	156	131	124

Interstitial solid solution strengthening

The most important strengthening mechanism related to this thesis is the interstitial solution strengthening, namely by the oxygen content. In α alloys and α+β alloys, there is a critical O content which causes an abrupt decrease of ductility, this O content is usually roughly 0.3 wt% [63]. This is the reason for the existence of two official Ti grades for Ti-6Al-4V – Ti Grade 5 for regular O content and Grade 23 (Ti-6Al-4V ELI – extra low interstitial) for very low O content which assures better ductility [64]. On the other hand in a recently developed Ti-4.5Zr-0.8O α-Ti alloy, very high strength over 1000 MPa is achieved with elongation of nearly 30% [65] under condition of very low nitrogen content (much lower than in commercial purity Ti grades). This is attributed to oxygen clustering [66] which enables cross-slip leading to work hardening.

One of the most famous low-modulus metastable β Ti alloys strengthened by oxygen is the Ti-35Nb-2Ta-3Zr-0.3O also known as Gum Metal. In this alloy, low elastic modulus was detected and the alloy has high strength in a cold-worked condition [67]. The mechanism for achieving such properties was first believed to be a dislocation-free plastic deformation (ideal shear) as the "giant faults" were observed by TEM [68]. Later, SIM α″ was found to be the main reason for the low elastic modulus [69,70].

Many Ti-Nb-Zr-Ta based alloys were developed since then, containing increased O content, usually up to 0.5% [40,44,71–73] which resulted in improved strength, usually without a detrimental effect on ductility when in β solution-treated condition. On the other hand, nitrogen causes embrittlement in much lower concentrations [40]. Higher concentrations of oxygen (>0.5 wt%) are of the main interest in this thesis. The concentration of 0.7% in Ti-35Nb-7Zr-6Ta alloy causes yield stress increased by more

than 100% compared to O-free alloy [74–76]. Ti-35Nb-7Zr-6Ta-0.7O alloy is set as a starting point for new alloy development in this work. Apart from the high yield stress, such high O content causes also work hardening associated with good ductility. A pronounced yield drop (sharp yield point phenomenon) is a result of unpinning the dislocations from the Cottrell stress fields [77].

Precipitation strengthening

Precipitation of secondary particles is very common for achieving high-strength metastable β Ti alloys. One of the examples is the Ti-5553 alloy that is already being used as an engine holder in Airbus A380 and other aircrafts. This alloy is a metastable β Ti alloy, which is used in the condition after the precipitation of fine α particles.

The ω_{iso} phase precipitation (or growth and stabilization from ω_{ath}) is connected with imminent hardening, but also embrittlement due to restricting the movement of dislocations to the β phase. This leads to a localization of the plastic deformation in the β phase channels and premature cracking. An exception is a very short time ageing at low temperatures (e.g. 200 °C / 60s) leading to a change of ω_{ath} into mildly stabilized ω_{iso} together with an increase in the volume fraction. This results in an increased strength of 700 MPa, without compromising the ductility (35%) [78], however the processing window is very narrow.

1.2.2. Factors influencing elasticity

The phase content is the main factor in achieving low elastic modulus. Any presence of secondary particles (either by formation during quenching or by precipitation in the pure β condition) will increase the stiffness as the β phase has the lowest Young's modulus in comparison to other phases (α, α′, α″, ω) [73,79–81].

Moreover, the lowest elastic modulus is achieved in alloys whose composition lies very close to M_S line at RT [82]. This effect is related to the so-called *premartensitic softening* (also *anomalous* or *c′ softening*) [83]. This effect is known also from other materials that can undergo a martensitic transformation, but the M_S is below their working temperature. In Ti alloys, the M_S and related softening can be controlled by chemical composition. The lattice instability can also result in the formation of the O′ phase [29].

Related to this work, following substitutional alloying elements are well known to be stabilizing the β phase: Nb and Ta are both established isomorphous β-stabilizing elements [84], Fe is the eutectoid β-stabilizer since it is soluble in the β phase up to concentration of 24.7 wt% [85], Zr can be considered as a β stabilizer [86,87] up to very high concentrations (up to the congruent point of β-α phase boundary at 67%).

Oxygen is the classical α stabilizing element as it increases the T_β in pure Ti [88] as well as in metastable β Ti alloys [74,89]. On the other hand, in the competition of the β and α″ phase, oxygen was found to act as a pseudo-β-stabilizing element by shifting the M_S of the α″ formation to lower temperatures [40,67,90–94]. The mechanism was attributed to blocking the shear of adjacent atomic planes which not only supresses α″ formation but also may reduce the effect of the *premartensitic softening*. As a result of oxygen addition into a tailored low-modulus β Ti alloy, the stability of the β phase is increased as well as the elastic modulus [75].

1.2.3. Improving ductility of Ti alloys

Improving the ductility of metastable Ti alloys must take into account the presence of secondary phases. The precipitation of the α phase is an example of a strength-ductility trade-off even at alloys with low oxygen contents (e.g. commercial alloys such as Ti-5553 and Ti-10-2-4) [6]. As an α-stabilizer, the oxygen diffuses into the α phase when the metastable β Ti alloys are aged efficiently promoting α phase formation and consequently reduces the ductility. Nonetheless, metastable β Ti alloys

are expected to be used in the β solution-treated condition to minimize the elastic modulus, therefore embrittlement by α phase formation is not an issue.

While the athermal ω phase usually does not have detrimental effects on ductility due to its coherency, the ω_{iso} generally causes embrittlement with an exception stated earlier. Quenching during the β solution treatment should, however, prevent its formation. Interstitial oxygen may also partly inhibit the ω phase formation [92,95].

The so-called transformation-induced plasticity (TRIP) effect was found in alloys undergoing SIM α″ transformation during loading, often accompanied by the twinning-induced plasticity (TWIP) effect, collectively termed the TRIP/TWIP effect. Alloys showing such effects can reach a remarkable strain hardening and associated extremely high ductility (tensile true strain up to 40%) [96,97]. Since the composition of the alloys undergoing TRIP/TWIP effects has to be finely tuned to obtain both deformation mechanisms at once, the resulting yield stress of only about 600 MPa is obtained [96,98]. Precipitation strengthening was considered for improvement. The yield stress can be increased to a value of about 700 MPa by tailoring a composition in which first the α phase is formed by ageing and the remaining β phase matrix shows the TRIP/TWIP effect due to its favourable composition [99,100].

1.3. Design methods of metastable β-Ti alloys

Several design methods were considered for metastable Ti alloys: molybdenum equivalency, valence electron concentration (e/a ratio) and Bo-Md approach as described further.

1.3.1. Molybdenum equivalency

One of the first methods of quantification of β stabilizing effect of individual elements was based on their relative comparison with the effect of alloying with molybdenum – the so-called molybdenum equivalency ($Mo_{eq.}$). This was determined by experimental establishing of the concentration of each element at which the metastable β phase is retained after quenching without any α″ martensite (i.e. the position of the M_S line crossing the RT). Based on these data, the relative β stabilizing "strength" was evaluated and the $Mo_{eq.}$ value could be calculated for a given alloy from the concentrations of each element [84]. Later an optimized approach was selected to include also the elements that cannot form the metastable β Ti alloys themselves, such as Zr, but some features in the phase diagram (eutectoid points, peritectoid points, congruent points) allow us to compare their relative effect on the T_β temperature. Such an approach was validated to predict the correct phase composition (in the interplay of α″ vs. metastable β) in a wider range of alloy compositions, incl. quaternary alloys [86].

Unfortunately, the $Mo_{eq.}$ cannot be established for oxygen to include its shifting effect on the M_S in metastable β Ti alloys due to its strong α stabilizing effect.

1.3.2. Valence electron concentration, e/a ratio

From the electron theory of solids, it follows that the valence electron concentration plays an important role in the determination of phase stability of various alloys and compounds [101]. It was widely used in many different fields [102–104] and it found its use also in the field of metastable β Ti alloys in the form of e/a ratio, i.e. the number of valence electrons per atom [105,106]. When plotting Young's modulus against the e/a ratio, the following behaviour can be observed as shown in Figure 4. For alloys far from the lattice instability (which is at around e/a = 4.15), Young's modulus rises as the distance from the lattice instability increases to both directions (fully martensitic structure at the low e/a, stabilized β matrix at the high e/a). The theoretical minimum of Young's modulus would be reached at the location of

lattice instability as marked by a dotted curve. However, the formation of the ω has to be taken into account which is the stiffest among the phases in Ti alloys [107]. Due to its formation, a sharp peak appears at the location of the lattice instability. The minimum of Young's modulus is therefore achieved at roughly e/a = 4.24. However, this is rather experimental assertion based on the alloys studied in [105].

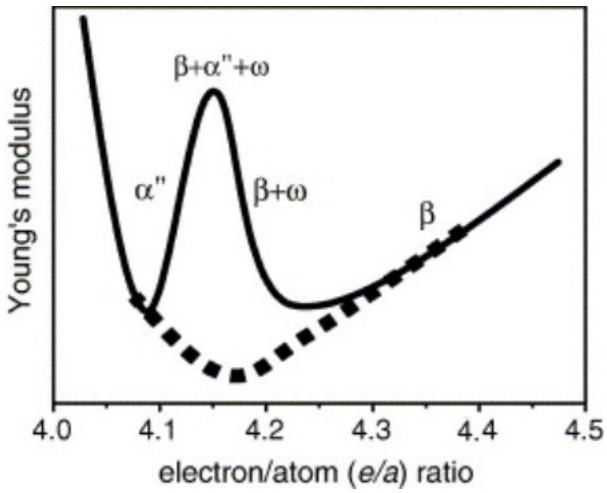

Figure 4: Dependence of the Young's modulus on the e/a ratio (adopted from [105].

In contrast to the $Mo_{eq.}$, oxygen can be incorporated in the e/a concept by attributing some number of electrons to each interstitial to oxygen atom as it surely contributes with electrons into the electron gas of the alloy. Unfortunately, it is not clear, what is the exact value of the contribution. The first issue is that oxygen is not a metal, the nature of its bonding is not clear – number of electrons contributing to electron gas is not known. The second issue relates to its interstitial nature – does it contribute to the number of atoms or not? In the following chapters, the effective contribution of oxygen to e/a ratio will be determined using high-throughput measurements of elastic moduli.

1.3.3. Bo-Md

The last theoretical approach applied to Ti alloys is based on the so-called Bo-Md diagram [52]. An alloy composition can be drawn onto the Bo-Md diagram by calculating the values of bond order (Bo) and energy of the d-electron orbitals (Md) [108]. The Bo-Md diagram together with experimentally determined areas corresponding to activity of various plastic deformation mechanisms (such as SIM [109], TRIP [96] or pronounced lattice softening [67]) provides a useful tool for Ti alloys design. Its use was even extended to Ti-rich high-entropy alloys [110].

Again, the main drawback of using this approach in this thesis is the lack of possibility to correctly incorporate the O content. Regardless of Bo, even the Md – energy of d-electron orbitals is hardly relevant as there are no d-electrons in oxygen.

1.3.4. Experimental examination

For the reasons stated above, experimental evaluation plays a major role in the development of novel biomedical O-rich alloys.

Quite a large number of oxygen-rich and mostly Ti-Nb based alloys was studied throughout last 2 decades. The already mentioned alloy Ti-35Nb-7Zr-6Ta was studied in [76] in 3 versions: O-free alloy (0.06 wt%) and 2 different contents of oxygen (0.46 and 0.68 wt%) after ST and ageing at various temperatures promoting α and/or ω phase precipitation. The conditions after ST were all ductile, with strength varying according

to the O content. When aged, ductility quickly dropped for O-rich alloys. The ageing did not affect the O-free alloy very much (α phase did not form) so in all the conditions the strength remained low, comparable to other O-free biomedical β Ti alloys in ST condition [53,92,111].

Alloy Ti-35Nb was studied in [44] with 5 different contents of O up to 0.55 wt%, each in either heavily cold-rolled (98.5%) or ST condition. The cold-rolled conditions were very brittle while all the ST conditions underwent a double yielding and showed the effects connected with the SIM α″ transformation: shape memory (O-leaner alloys) or superelasticity (O-richer alloys). The strongest alloy was the one with 0.55 wt% O and its 2 yield points were at 500 MPa and 1050 MPa, but the achieved ductility was only about 5%.

In [112], authors studied the effect of various levels of cold-swaging on Ti-35Nb-2Ta-3Zr-0.3O. The ductility deterioration was not too big, elongation of 10% was reached for all cold-worked conditions up to 90% of area reduction, but the increase in the yield strength increase was not very pronounced. The cold-working has resulted in a non-linear elastic behaviour, effectively decreasing the Young's modulus down to 55 GPa. Although the authors have not identified the presence of the α″ phase, the peculiar effects could have been hidden in the (yet undetected) nano-domain O′ phase [51].

Similar cold-worked (90%) alloys Ti-xNb-2Ta-3Zr-yO with x = 30 - 40 wt% and y= 0.3 or 0.5 wt% were studied in [113]. The increased O content was found to shift the minimum of Young's modulus to lower concentrations of Nb. In Ti-32Nb-2Ta-3Zr-0.5O, good combination of properties was found: Young's modulus of 55 GPa (effective value in the non-linear elastic part of tensile curve), ultimate tensile strength of 1370 MPa and ductility of 12%.

Biomedical alloy Ti-29Nb-13Ta-4.6Zr with three O contents (0.12, 0.20, 0.42 wt%) was studied in ST as well as aged condition in [71]. The aged conditions were hard and relatively brittle, but the ST conditions showed the ductility above 15% and Young's modulus between 60 and 80 GPa (higher with increasing O content).

Tane et al. [83] measured properly the dependence of various elastic moduli (c′, B, E, G) of Ti-36Nb-2Ta-3Zr-xO alloys on temperature in single-crystalline form as well as E in cold-swaged rods. It was shown that cold-working induces increases Young's modulus by inducing the α″ phase and ω phase. This increase can however be overcame by the O addition which prevents the secondary phase formation and the only result of the cold-working is then an increase in strength.

The Ti-35Nb-2Ta-3Zr alloy with O content up to 0.5O was studied after solution treatment concluded by air cooling [72]. The strength was increasing with O content, but the same applied for Young's modulus which reached a value of 90 GPa for O content of 0.53 wt%.

Geng et al. [74] studied alloys with O content as high as 0.7 wt%. The yield point phenomenon was observed in this alloy together with an increase in Young's modulus when compared to other alloys with lower amount of oxygen.

In [114] and [115], 0.3 wt% of oxygen was found to suppress the formation of the SIM α″ phase and deformation twinning.

There was also a successful attempt to achieve ultra-low Young's modulus by introducing extremely high deformation (compared with common cold-working) by high-pressure torsion (HPT) [116], high hardness and Young's modulus of 43.3 GPa were obtained. Of course, any practical use of such process is impossible due to tiny sizes of HPT samples.

As already mentioned in previous sections, the O content of 0.7 wt% lead to high yield strength and sufficient ductility also in Ti-35Nb-7Zr-6Ta alloy [75] which serves as a benchmark of low-modulus alloys. In this work, combining of interstitial strengthening with solid solution strengthening by Fe content was also proved.

Combination of Fe and O was considered also in [117], however, the strength improvement comes at a price of drastic decrease of ductility.

1.3.5. Trial and error vs. high-throughput methods

Usually, the experimental approach goes under the not-very-compelling name of Trial and error. However, based on an extensive literature review, the trial part can be directed much more precisely leading to a lower probability of an error.

Even a systematic experimental study usually involves changing of only a limited number of parameters. To explore e.g. a wider range of the multi-component alloying system (say Ti-Nb-Zr-Ta-O), high throughput methods seem very suitable, although the amount of information is always somehow limited. An advantage of the target material is that it will be ultimately used in the β solution-treated condition (to reduce the elastic modulus), therefore the only relevant heat treatment leading to single-phase condition will be quenching from above the T_β temperature. Even the quenching rate can play a significant role in the final microstructure and mechanical behaviour of alloy on the phase stability as shown in [118], where slow quenching by water cooling the sample inside the quartz tube and fast quenching by breaking the tube in water was studied. For this reason, all quenching performed in this thesis should be understood as water quenching by falling the sample from the annealing temperature directly into water.

The need for measurement of both elastic properties and plastic deformation properties (yield stress, UTS, ductility) restricts the possibilities of preparation methods for high-throughput testing. The combinatorial sputtering methods are not suitable for such analyses [119].

On the other hand, blended elemental powder metallurgy [120] can be utilized for the preparation of a large number of alloys that can locally behave as a bulk material. Field-assisted sintering technique (FAST), also known as spark plasma sintering (SPS) is a very suitable method for compaction of a mixture of elemental powders yielding fully dense samples with a precisely known thermal history [121–123]. The temperature needed to achieve homogeneous chemical composition from blended elemental powders has to be much higher than that needed for compaction only [124] especially when using elements with high melting points such as Nb [125].

The variation of ratios between the elemental powders allows to vary the alloy composition even inside a single sample. Namely, step-by-step graded layering is used for high-throughput screening in the studied alloys. This approach is similar to that reported in [126] where conventional sintering was used to prepare a large number of samples in a single sintering step. The parameters of the sintering of the Ti-Nb-Zr-O system were determined in [127,128].

In summary, the design of new Ti-Nb-Zr-Ta-O alloys with high strength and simultaneously with low elastic modulus by simple alloying can be based on following assertions:

- Interstitial oxygen increases strength.
- Oxygen does not compromise the ductility of the β phase.
- The low elastic modulus is caused by reduced stability of the β phase.

- Oxygen stabilizes the β phase with respect to β→α″ martensitic transformation and suppresses the formation of ω_{ath} phase.
- High-throughput method of preparation and testing many compositions might be advantageous for efficient performing of properties optimization.

The research presented in this thesis has followed two interconnected topics:

1) Design of Ti-Nb-Zr-Ta-O alloys with high strength and simultaneously with low elastic modulus by simple alloying.
2) Design of high-strength Ti-Nb-based alloys strengthened by oxygen in which the ductility would be enhanced by activation of SIM α″ transformation, potentially leading to TRIP/TWIP effect.

For the second topic, a high-throughput method of preparation and testing many compositions in a small number of samples was used. This part of the thesis contributed also to the methodology of testing both elastic and mechanical properties by the selected high-throughput approach.

2. Aims of the thesis

The main aim of this doctoral thesis is the development of novel Ti alloys which could be used in medical applications, mainly as a material for load-bearing endoprostheses of large joints. The partial aims can be summarized as:

- Development and optimization of manufacturing process of previously developed biomedical Ti alloy for industrial production of hip implants
- Designing novel Ti alloys to achieve the target properties (high strength and low elastic modulus) by simple alloying and thorough description the physical mechanisms leading to such properties.
- Utilization of lattice softening in the vicinity of martensitic phase transformation for reduction of modulus of elasticity.
- Improvement of material ductility using two strategies: 1) suppression of ω phase and α″ phase, 2) activation of stress-induced martensite / deformation twinning as additional deformation mechanisms.
- Development of high-throughput methods for correlating chemical composition with microstructure and eventually mechanical properties
- Development of dedicated characterization techniques for thorough microstructural characterization of newly developed alloys

3. Experimental methods

3.1. Characterization methods

3.1.1. Inert gas fusion

Generally, the content of interstitial elements, especially the O content, plays a crucial role in any Ti alloy. The need for its measurement is even increased in the case of this thesis, in which I studied metastable β Ti alloys with increased and controlled O content. The most precise method for the measurement of interstitial elements content is the Inert gas fusion (IGF) (also known as CGHE - Carrier gas hot extraction). The destructive measurement of each sample consists of two main parts: 1) heating of the sample to very high temperatures (close to 3000°C) in a graphite crucible under the inert atmosphere of the "carrier" He gas and 2) the suitable filtering and analyses of the products of the reaction (CO, H_2O, N_2, H_2, etc.) by dispersive IR (infra-red) detectors and non-dispersive TC (thermal conductivity) detectors. At first, the measurements had been done at TU Freiberg based on a long-established collaboration. Some of the measurements were done at the laboratory of company ORLEN Unipetrol, a.s. Both laboratories used analyzers by LECO. In November 2021, Bruker Galileo G8 IGF analyzer has been acquired by the Department of Physics of Materials and since then, the measurements were done using this machine. To check the consistency, several samples were measured using multiple analyzers and the scatter was within the statistical error.

3.1.2. Scanning electron microscopy

The general tool for the characterization of microstructure used in this thesis was scanning electron microscopy (SEM). The samples with mirror-polished surface were used for observations.

Most of the SEM images in this thesis were captured by the BSE (back-scattered electrons) detector and accordingly, most of the time, I will just refer to the images as SEM images. Only when the Everhart-Thornley detector (ETD) was used for image capturing, it is specified as the SE (secondary electrons) signal.

The energy dispersive X-ray spectroscopy (EDS) analytical technique was used for the determination of chemical composition along line scans.

Another analytical technique is electron back-scatter diffraction (EBSD). It provides crystallographic orientation information at each measured point and it can be used even for the distinction of different crystallographic structures. In cases when the indexing rate was low i.e. in heavily deformed samples, samples containing phases with a similar crystal structure (i.e. β bcc phase and α″ orthorhombic phase with only small shear component), an advanced post-processing technique was used on the patterns which averages the patterns from neighbouring points. This procedure is called NPAR (Neighbor Pattern Averaging & Reindexing) [129]. From the recorded patterns, the so-called PRIAS (Pattern Region of Interest Analysis System) maps can also be constructed. It is done for each point in the map by taking average from a selected part of the recorded pattern, corresponding to this point [130]. Typical procedure consists of splitting each pattern into 3×3 chess-field and averaging either the bottom 3 fields or the single central field or the top 3 fields.

The sample preparation for SEM incl. the analytical techniques involved first cutting the materials with a precision saw using a water-cooled diamond cutting wheel. The samples were then either attached to a holder with glue or wax or mounted into a conductive resin Struers Polyfast and ground gradually with SiC papers starting from grit #220 up to #2000 (number specifies the amount of abrasive material going through

square inch filter). After grinding, the final polishing was done either by a vibratory polisher on Alumina and Silica suspensions each for several hours or by polishing on fibre cloth with a mixture of 20% solution of hydrogen peroxide in OP-S suspension for 15 min. The former method yielded an extremely well-polished surface, but due to a long preparation (several days), the latter method was mostly used.

For observations, two SEMs were used in this thesis: Zeiss Auriga Compact dual-beam microscope and FEI Quanta 200F. The EDS and EBSD detectors used on both microscopes included several types of detectors from the company EDAX. Typically, the voltage of 15 kV and large currents were used for BSE observations and 15-20 kV was used for EDS and EBSD measurements.

3.1.3. Transmission electron microscopy

Observation of fine secondary phases such as athermal ω or the nanodomains of O′ was not possible by SEM, therefore transmission electron microscopy (TEM) was employed in these cases.

For bulk samples with homogeneous composition, the TEM specimens were prepared by the following procedure, mostly adopted from [131] and [132]. First, the input material in the form of rods was machined to a diameter of 3 mm and then, 0.5 mm thick discs were cut from the rods. The discs were then mechanically ground from both sides to a thickness of about 100-150 μm. These discs were polished by twin-jet electropolishing using the Struers Tenupol 5 with the following solution: 61% CH_3OH + 33% $C_4H_{10}O$ + 6% $HClO_4$. The process was performed at -20 °C and the time (about 1 min) was chosen such that the sample was thinned but the hole was not created yet. Final thinning until the creation of a hole was done by Gatan PiPS ion polisher which uses Ar ions to bombard the surface. The areas just near the hole were thin enough for observations in TEM.

For the preparation of thin foils from layered samples, discs with a diameter of 3 mm could not be made, so another method was used instead. Small lamellae (~ 10 μm wide) were extracted from the material by a focused ion beam (FIB) on the dual-beam Zeiss Auriga Compact. First, the surface of the sample was covered by Pt using a gas injection system (GIS) and then, the lamella was dug by Ga ions and placed on the Cu grid using GIS and a micromanipulator. The final thinning of the lamella was performed on the grid until the desired thickness was reached.

Finally, for observations, JEOL 2200 FS microscope was used using a voltage of 200 kV. The very high dynamic contrast of the CCD camera allowed setting the grayscale levels in postprocessing such that the equivalent diffraction spots for the β phase were set to the same relative intensity. As a result, the intensity of secondary phase reflections can be directly compared between different samples.

3.1.4. X-ray diffraction

For the determination of the phase composition of studied materials, X-ray diffraction (XRD) was used.

One of the most commonly used geometries for XRD pattern acquisition is the so-called Bragg-Brentano geometry. However, it proved not to be suitable for the measurement of coarse-grained alloys. Only a few grains are present in the spot size of the incident beam, compromising quality and comprehensiveness of the powder XRD pattern.

In such cases, it is more convenient to use a different geometry. Thanks to a diffractometer available (Figure 5a), transmission geometry could be used with the detection of diffracted reflection on a curved cylindrical 2D detector. By the following integration, powder-like diffraction patterns were obtained that could be reliably indexed. The detected spots of the stationary sample are shown in Figure 5b. The

central ring (corresponding to (110) reflection of β phase) can already be distinguished. Much larger statistics can be obtained by rocking the sample with the motorized goniometer in axes φ (horizontal rotation) and χ (tilting the sample). The combined movement leads to rings that can be recognized even for large diffraction angles (Figure 5c). Note that Bragg-Brentano geometry would be effectively able to capture reflections only along an arbitrary line crossing through the centre of the 2D pattern without rocking.

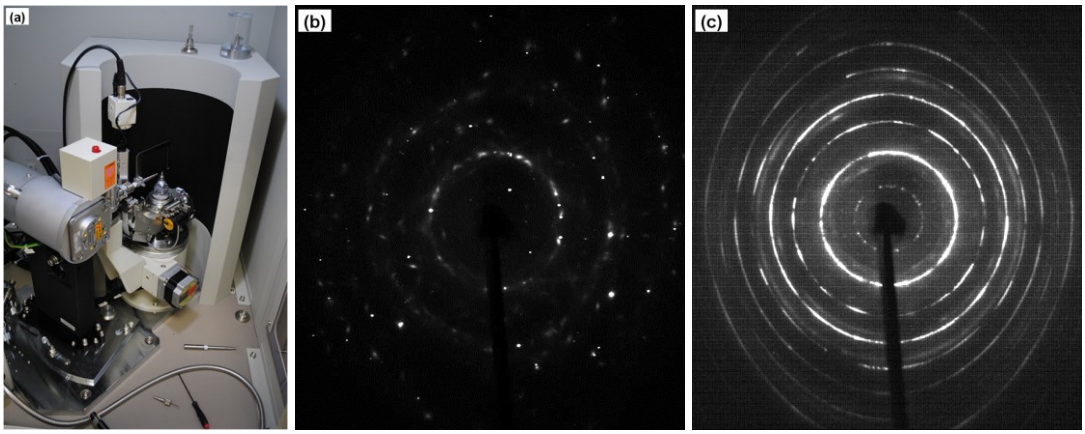

Figure 5: (a) photo of the Rigaku Rapid II diffractometer, (b) diffraction spots of the stationary sample, (c) diffraction rings created by rocking the sample in χ and φ axes.

The X-ray source of Rigaku Rapid II was a sealed Mo tube. A graphite monochromator was used for a primary beam of the Mo Kα wavelength (0.709 Å). Since the voltage of the tube was set to 50 kV, bremsstrahlung corresponding to double the target energy could also pass through the monochromator and resulted in doubling of the most intense peaks at positions equivalent to crystal structures with double lattice parameters (about half of the positions in 2θ axis). This effect was however very weak.

The samples used for the measurement were ground with SiC papers to a thickness of 100 - 300 μm to become transparent for the Mo Kα X-rays. The aperture with a diameter of 300 μm was used for all measurements and a camera inside the chamber allowed a precise selection of measurement spot, which is important in the case of layered samples. The radial integration was performed using 2DP software and Rietveld refinement for determination of lattice parameters and phase analysis was done in software HighScore Plus.

3.1.5. Tensile testing

Tensile testing was done for the determination of yield and ultimate tensile strength as well as the ductility. Two types of samples were initially tested. At first, large samples corresponding to a drawing in Figure 6a were machined from the cast and annealed alloys and tested using Instron 5882 universal testing machine.

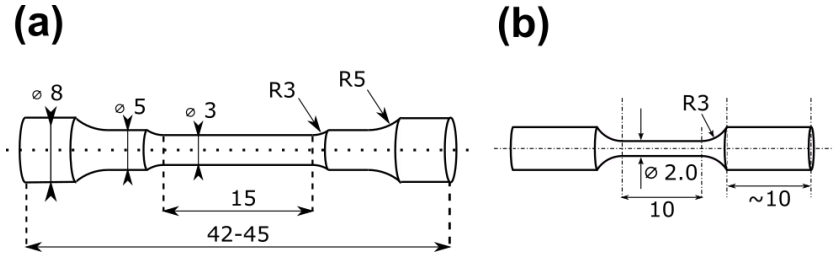

Figure 6: Schemes of tensile specimens' geometries.

The gauge cross-section with a diameter of 3 mm is shown in Figure 7 overlayed on the SEM image of the grain structure after casting and solution treatment only. Such a combination of sample geometry and coarse grain structure together with casting defects (porosity) resulted in poor repeatability of the tests and the achieved ductility was also comparatively low. In materials in which the grains were refined, a smaller sample geometry was used as shown in the drawing in Figure 6b. The outer diameter was not machined, i.e. it was the diameter of the rotary swaged rod. In the active cross-section, a much larger number of grains was present despite the gauge diameter being 2 mm only. This resulted in high repeatability of the tensile tests for all studied alloys. A different machine was used for testing the small samples with refined grains, it was an electro-dynamic Instron Electropuls E10000, in which the samples can be mounted using pneumatic V-jaw grips. The machine is designed for dynamic testing mainly (max. force of ±10 kN), but it can be used also for static testing with a limited force of ±7 kN which was fully sufficient for all tested alloys. The majority of the tests were performed at the strain rate of 10^{-4} s^{-1}. The difference in the used testing machines can be observed mainly from the elastic part of the tensile curves in Figure 7: a much larger deformation of the machine and fixtures is present during testing with Instron 5882. However, even much stiffer pneumatic fixtures of Instron Electropuls still prevent using the tensile test results from determination of Young's modulus due to the inherent elasticity of the load cell. For this reason, much more precise measurements by resonant ultrasound spectroscopy were carried out as described further in 3.1.7.

Selected alloys were tested in tension in-situ in SEM Zeiss Auriga. The deformation stage MTI SEMtester 1000 was used for this purpose and the sample was flat dog-bone shaped with the following gauge dimensions: length of 4 mm, width of 1.5 mm and thickness of 0.6 mm. Each deformation step with the strain rate set to 10^{-3} s^{-1} and was followed by capturing SEM images (BSE and SE) at a constant cross-head position.

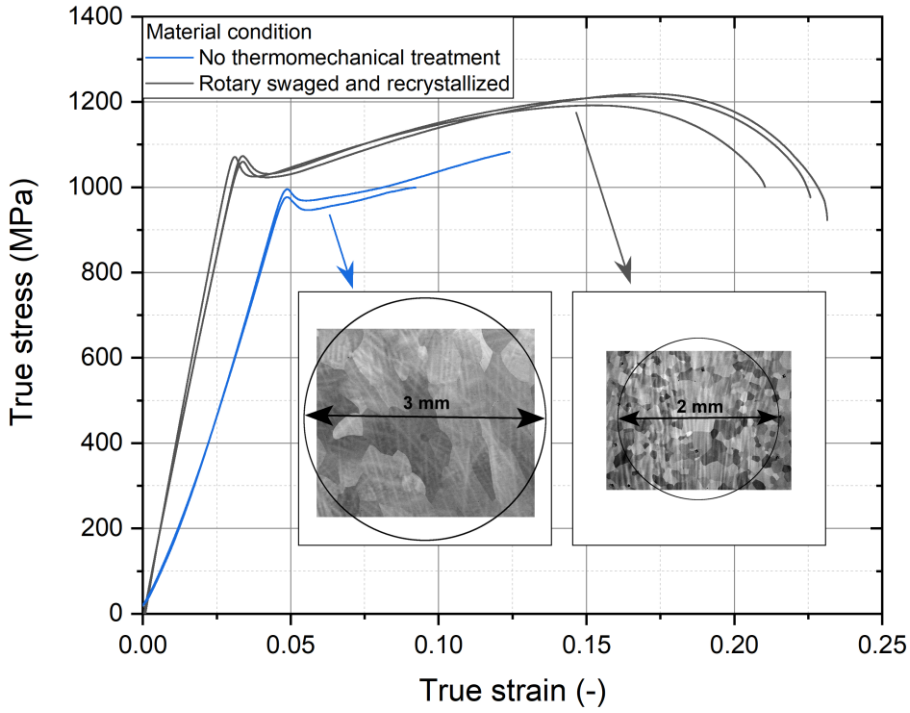

Figure 7: Tensile testing curves for 2 conditions of Ti-35Nb-7Zr-6Ta-0.7O alloy: after casting and solution treatment only and after additional rotary swaging and solution treatment. The insets compare the relative grain size with respect to the diameter of the specimen.

3.1.6. Compression testing, acoustic emission (AE) & digital image correlation (DIC)

Compression testing was performed on the multilayered samples (prepared by FAST, as explained further). Compression samples were prepared from the pellets with the loading direction parallel to the layer normal. The thickness of the pellets and concurrently also the height of the compression samples was about 12 mm and a cross-section of 7×7 mm^2 was used. Some layers in samples with higher O contents were very brittle due to the presence of the α″ phase already after quenching. Since these layers caused very early cracking during compression testing, they were cut off, resulting in smaller samples: for the pellets with 0.5 and 0.7 wt% O, the dimensions were 8×4×3.5 mm^3 and for 0.9 wt% O, the dimensions were 6×3.5×2.5 mm^3.

Compression testing was done using the Instron 5882 machine with a strain rate of 10^{-3} s^{-1} with simultaneous complementary acoustic emission (AE) recording and capturing the surface of the samples for the digital image correlation (DIC) analysis. To prevent imprinting of the hard samples into the compression anvils, corundum discs were placed between the anvils and the sample. The AE acquisition was performed using the Physical Acoustics Corporation (PAC) PCI-2 board with a sampling rate of 2 MHz. The PAC preamplifier 2/4/6 with a gain set to 60 dB and the broadband AE sensor PAC Micro-80S were used. The AE sensor was attached to the corundum plate utilizing a plastic clip; good acoustic contact was facilitated using a vacuum grease (Apiezon M). The AE events were individualized using a standard hit-based processing with the threshold level slightly above the background noise (24 dB_{AE}). Two quantities were determined from the AE measurements. First, the amplitude of each AE event i.e., the "AE intensity". Second, the integrated (cumulative) AE count rate (AE counts per second) i.e., the "AE activity".

Speckle patterns for the DIC analysis were created by first applying white spray paint to prevent surface reflections and then by applying black water-based paints by an Airbrush technique. The images of the samples were captured automatically every 1 s using a Nikon D3100 camera with Nikon 60 mm f/2,8 G ED AF-S Micro lens and external programmable shutter. An example of the experimental arrangement is shown in Figure 8.

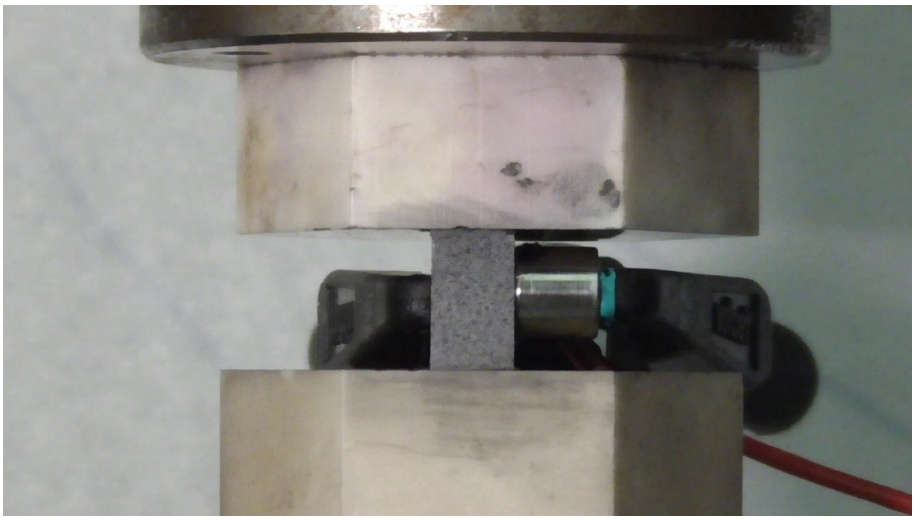

Figure 8: Compression testing arrangement of the layered sample with the speckle pattern and AE sensor attached. This is one of the preliminary tests, in the following, the AE sensor was attached to the bottom corundum plate to improve repeatability.

The DIC analysis was performed in the *ncorr* package [133] implemented in Matlab [134]. As the mean speckle size was about 20 px, subset size with a radius of 30 px and step of 10 px were used to obtain reliable results. High-strain analysis feature of the *ncorr* was used as well to reliably evaluate later stages of the deformation by updating the reference image when correlations worsen. One of the outputs of the DIC analysis was vertical displacement fields u_y parallel to the direction of applied force in the frame reference of the undeformed sample (Lagrangian frame). To evaluate true strains in each layer during deformation, the mean was taken from each horizontal pixel row of the vertical displacement field yielding mean vertical displacement $\overline{u_y}$ for each vertical position and time of the test. For visualization, Figure 9 shows the described procedure for the Ti-xNb-7Zr-0.2O sample. Figure 9a shows the reference image of the undeformed sample with the prepared speckle pattern. In Figure 9b the image of the sample is overlayed with colour-coded vertical displacement field u_y measured by DIC and processed in Matlab. The example shows a vertical displacement field at time t = 150 s (150th image, corresponding to the overall strain of 15 %), but in the reference frame of the undeformed sample. Finally, the mean vertical displacement $\overline{u_y}$ of a pixel row is shown in Figure 9c for every 10th second (highlighted for t = 150 s). Mean vertical displacement $\overline{u_y}$ is represented by a line going from the bottom of the sample to the top, reflecting the compression test geometry – the bottom platen is fixed while the top platen moves downwards. Horizontal lines indicate boundaries between each compositional layer. From the slope of the mean vertical displacement is immediately seen that each layer is strained differently.

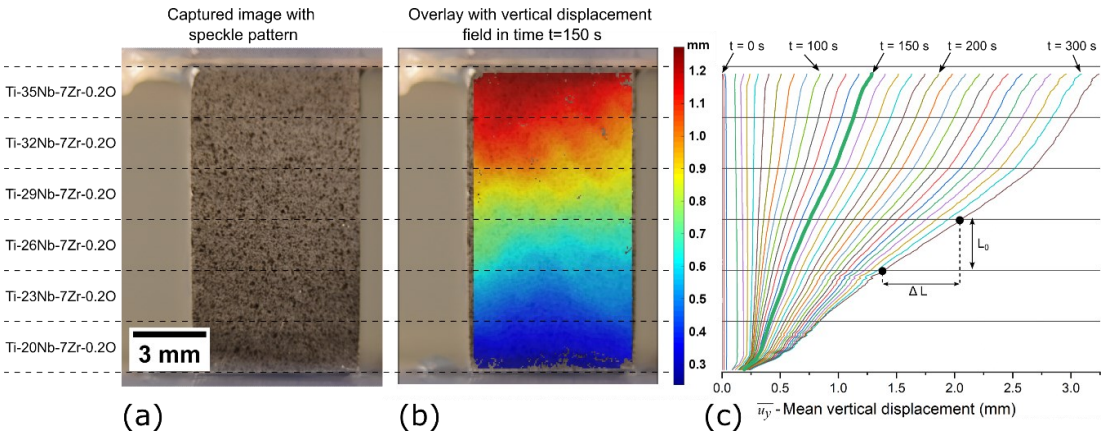

Figure 9: a) image of the undeformed sample (Ti-xNb-7Zr-0.2O) with speckle pattern, b) overlay with vertical displacement field captured by DIC after deformation to 15% (at time t = 150 s), c) mean vertical displacement for every 10th second.

From the $\overline{u_y}$ values, strains were calculated for each layer by the following formula, consistent with the general definition of (engineering) strain:

$$\varepsilon_{i-th\ layer}(t) = \frac{\Delta L}{L_0} = \frac{\overline{u_y}(i\text{-}th\ layer\ start, t) - \overline{u_y}(i\text{-}th\ layer\ end, t)}{h_i}$$

(Equation 1)

where h_i is the initial height of the i-th layer (considered the same for all layers within one sample). It can be easily observed from the slopes of $\overline{u_y}$ for example, that the top two layers and also the bottom two layers have undergone much lower strains compared to the central two layers. The true strain and true stress values were calculated by the usual approaches by using the global stress values and engineering strain for each layer (under the usual assumption of constant volume during deformation). Note that using DIC data, change in the sample cross-section (at least in one direction) could have been established as well and used for true strain / true stress determination. However, using the 2D DIC method only, out-of-plane movements contribution to the measured strain cannot be separated from the real deformation and potential errors would be amplified [135].

After the deformation, the compression samples were analyzed by XRD and SEM.

3.1.7. Ultrasonic methods – RUS & SAM

Resonant spectra of free elastic vibrations of the individual RUS samples, typically with the size of about 2×3×4 mm^3, were measured at 20°C under low nitrogen pressure (approx. 10 mbar) in a chamber enabling a precise temperature control (± 0.1 °C), using a RUS set-up built in the Institute of Thermomechanics and described in detail in [136]. The vibrations were excited on the bottom face of the sample by a focused infrared laser pulse. The upper face of the sample was scanned by a laser vibrometer to identify the individual vibrational modes. Resonant spectra were collected in the frequency range from 100 kHz to 2.5 MHz, which covered more than 100 resonant frequencies for each sample. According to the sample that was measured, different numbers of vibrational modes were selected as the input for the inverse calculation of the elastic constants, which was done by minimizing an objective function:

$$F = \sum_{n=1}^{N} \left(f_n^{exp} - f_n^{calc}(E, G, \rho) \right)^2 \qquad \textit{(Equation 2)}$$

with respect to Young's modulus E and shear modulus G, where N is the number of the selected modes, f_n^{exp} and f_n^{calc} are the experimentally determined and calculated resonant frequencies, respectively, and ρ is the mass density determined for each sample from its weight and dimensions. Only the modes for which their modal shapes were reliably determined from the experiment and their computed counterparts (i.e., outputs of a numerical simulation of the vibrations) were selected for being involved in function in (Equation 2).

For a more robust inverse determination of both E and G, the RUS measurement was complemented by measurements of velocities of longitudinal ultrasonic waves in directions perpendicular to the faces of samples using a pulse-echo technique; the resulting velocity data were then involved in the inverse calculation using the approach described in [136]. An isotropic behaviour of all prepared materials was assumed, with two elastic constants (E and G) being sufficient for describing completely the elastic response. The shear modulus G is typically the elastic constant most accurately determined from RUS [137]. The accuracy of RUS can be estimated according to the number of modes involved in the calculation. Two types of samples in this thesis were measured by RUS:

- fine-grained samples after rotary swaging and recrystallization with grain size between 50 and 200 μm,
- coarse-grained samples made by field-assisted sintering technique (FAST) that had a grain size between 200 – 1000 μm.

This has led to a difference in fulfilling the elastic homogeneity condition that is usually necessary for the proper measurement of elastic constants by RUS. For the fine-grained samples, more than 40 modes were involved in the calculations resulting in the precision of the measurement being particularly good (± 0.5 GPa).

As the grain size of FAST-prepared samples was much higher than that of the fine-grained alloys, the situation was strongly dependent on the present microstructure. For some of the samples containing only or nearly pure β phase, only about 20 resonant modes could have been reliably fitted due to the high anisotropy of the β phase [107]. In cases when there were secondary phases present in the microstructure, the elastic anisotropy was lower and thus also better for resolving the RUS spectra. The accuracy achieved in FAST-prepared samples was approximately ± 1 GPa in G, according to the sensitivity analysis elaborated in detail in [136]. With involving the longitudinal velocity data (from the pulse-echo measurements), a comparable accuracy (± 3 GPa) was estimated also for E, the parameter typically used when evaluating the suitability of metastable β-Ti alloys for biomedical applications. The differences in RUS spectra obtained for different phase compositions present (β, β+ω, α″) were described in detail in joint work with the Institute of Thermomechanics [138]. These discussions are however out of the scope of this thesis.

In addition to the inverse determination of G and E, the internal friction coefficients for all alloys were determined from the RUS spectra. This was done using Lorentzian masks to fit the individual resonant peak of the modes involved in the above-described inverse procedure, and calculating the internal friction parameter for each resonant mode as:

$$Q^{-1}_{n=1,\dots,N} = \frac{FWHM_n}{f_n} \qquad \textit{(Equation 3)}$$

where $FWHM_n$ stands for the full width at the half maximum of the Lorenzian fit. It was observed that for each individual alloy, all analyzed peaks gave approximately the same value of Q^{-1}, which means that this value was representative of the given alloy. None of the alloys exhibited Q^{-1} above 10^{-3} at room temperature (i.e., all alloys exhibited very low internal friction), and the differences between the alloys were small and did not exhibit any systematic dependence on the chemical composition.

For visualization of the elastic heterogeneity in selected layered samples (Section 6.2.3), scanning acoustic microscopy (SAM) available at the Institute of Thermomechanics was used. The principle of the SAM is a spatially resolved pulse-echo method. The time-of-flight of focused longitudinal ultrasonic waves through the thickness of the sample was measured with a spatial resolution of ~ 30 μm over the whole area of each sample, using an UHPulse100 (OLYMPUS, Japan) scanning acoustic microscope (30 MHz spherical lens, C-scan regime).

3.2. Material preparation – classical route

3.2.1. Melting and casting of alloys

The most frequently used method for laboratory preparation of Ti alloys is arc melting with a non-consumable W-based electrode. Due to the high temperature obtained in the arc, alloys containing elements with very high melting points (e.g. W, Ta, Mo, Nb) can be prepared. For the protection of the prepared alloys, water-cooled copper crucibles made from high-purity (high thermal conductivity) oxygen-free copper are used. The amount of material that can be melted by the arc depends on the melting points of the individual elements as well as on the power of the arc source (usually in the form of a welding power supply). The shape, on the other hand, depends mainly on the shape of grooves in the Cu crucible. Two different arc melting furnaces were used for the preparation of materials studied in this thesis:

1) Powerful arc furnace at company ÚJP Praha

Most of the alloys were ordered and prepared in company ÚJP Praha, in the amount of about 200 g per casting. Such ingots were prepared in the crucible shown in Figure 17a by passing the powerful arc with the current of several kA over the mixed elements about ten times during one remelting, which was followed by cooling of the ingot and its flipping and another remelting. The remelting + flipping was repeated 6 times in total to achieve homogeneity of the ingot. The TiO_2 powder was added after the first remelting to control the desired oxygen content. The melting was done in the process chamber which was first evacuated by the Roots pump and then filled with pure He. The resulting ingots had dimensions of about 130 × 35 × 13 mm^3, therefore direct hot or cold working was not applicable. For subsequent rotary swaging, rods were either cut from the cast ingots by an electric discharge wire-cutter (for the first batches) or remelted into the shape of rods using the Monoarc furnace (later batches).

2) Monoarc furnace at the Department of condensed matter physics

The Monoarc furnace available through the MGML infrastructure (cooperation was based on a long-term proposal) was used for two purposes. First, it was used for melting 4 alloys, later denoted as batch #3 directly from pure elements. As the welding power supply of the Monoarc furnace can generate 350 A current arc only, it was not possible to melt the elements into the alloys directly in the grooves for rods. Therefore, several button-shaped pieces with a weight of 5-7 g were melted first from each alloy and they were remelted in the crucible with grooves to prepare a rod (Figure 10b). The

available grooves have either length of 140 mm for rods with a diameter of 10 and 12 mm or a length of 120 mm for rods with a diameter of 7 and 8 mm. The process chamber of the Monoarc can be evacuated to a high vacuum of up to 10^{-6} Pa thanks to a turbomolecular pump and for the melting, it is filled with high-purity Ar.

Figure 10: a) Cu crucible of the ÚJP Praha furnace for 200g ingots, b) Cu crucible of Monoarc for casting rod-shaped ingots suitable for rotary swaging. Rod placed inside for illustration is already after heat treatment and quenching (thus the blue colour).

3.2.2. Homogenization

After the melting, dendritic inhomogeneity was present in the casts. An example of such a dendritic structure is shown in Figure 11. Apart from the dendrites, which are enriched in high-melting and heavy elements (Nb and Ta) and thus appear light in the BSE image, the interdendritic regions depleted of Nb and Ta (appearing darker) contain α phase particles that precipitated during the relatively slow cooling of the melted rods in the crucibles. The interdendritic spacing was about 20-40 μm, which is the main parameter for establishing a successful homogenization treatment.

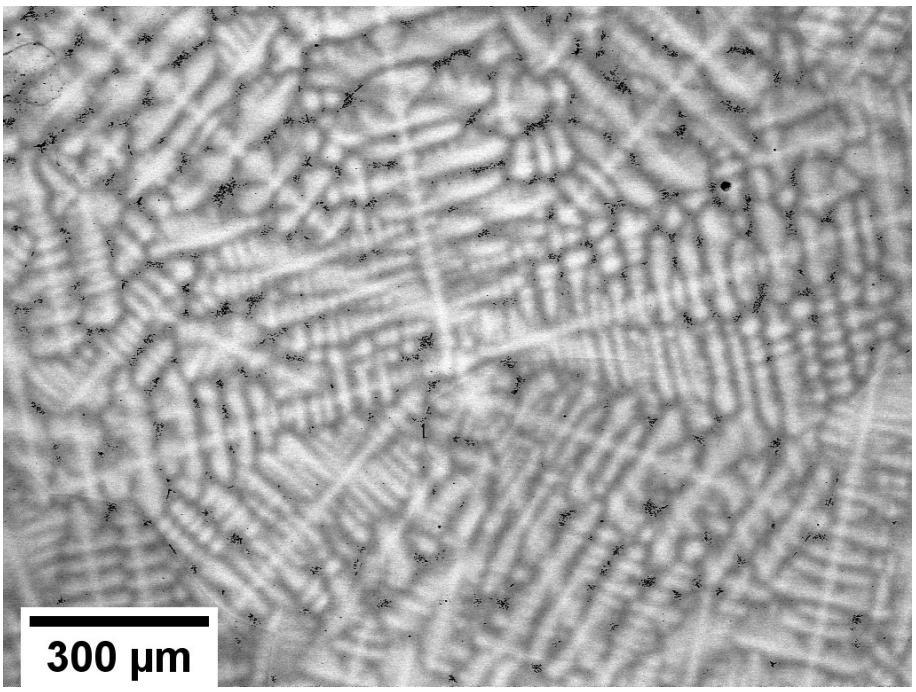

Figure 11: Dendritic structure present in one of the alloys with the lowest content of β stabilizing elements. Black particles in some of the inter-dendritic regions is the α phase.

The homogenization was performed using a vertical tube furnace Nabertherm RHTV that was evacuated by turbomolecular to a high vacuum of about 5×10^{-4} Pa. The samples were wrapped into Zr foil to further limit oxygen intake and hung into the hot zone by Mo wires. Unique vertical setup and home-made sample holders allowed us to immediately water quench the annealed samples, which is quite uncommon for vacuum furnaces. Water quenching by falling directly from the hot zone was allowed by creating a loop on one Mo wire and putting the other wire through the loop. The sample was hung not on the loop, but on the wire that went through it. When water quenching was desired, the vacuum system was disconnected and the chamber was filled with pure Ar, the bottom of the furnace was opened while placing a bucket with water underneath and finally, one of the wires were pulled from the top feedthrough to release the sample(s) into the water.

The homogenization at 1300°C/24h was performed on the prepared arc-melted alloys. The quenching (β solution treatment) was not done directly from the homogenization temperature, but the furnace was left to cool to a lower temperature (that was yet above the β transus), which was usually 1000°C, to prevent furnace damage.

3.2.3. Rotary swaging and recrystallization annealing

To achieve grain refinement of the alloys to allow proper tensile testing, the combination of cold rotary swaging and recrystallization annealing was used. The conditions determined in my diploma thesis [139] were used and further optimized. An area reduction of at least 70% was used during the swaging. Rods for swaging were cut by electric discharge wire-cut, the initial diameter was 8 mm and the final diameter after swaging was 4.3 mm. For the alloys, which were remelted directly into a shape of a rod in the Monoarc furnace, the initial diameter was about 10 mm and the final diameter after swaging was 5 mm.

To achieve a fully recrystallized grain structure, annealing at temperatures 800°C, 900°C, 1000°C and 1100°C / 15 min followed by water quenching (WQ) was applied on the cold swaged alloys and the best processing resulting in recrystallized structure with reasonably refined grains was chosen for each alloy. As the α phase was observed in some of the conditions, this can give us an estimate of the β transus temperature. These estimates are shown in the next chapter in Table 3. Selected α+β microstructures are shown in Figure 12.

Not all recrystallization heat treatments above the β transus have resulted in full recrystallization. As an example, the alloy Ti-35Nb-7Zr-6Ta-0.7O, although having the β transus between 800 and 900°C, was not fully recrystallized after annealing at 1000°C / 15 min + WQ as shown by BSE image and EBSD inverse pole figure (IPF) map in Figure 13 b and d, respectively. The areas marked by green arrows in Figure 13b are not recrystallized but only recovered, i.e. the dislocations introduced during the cold swaging were annihilated by the annealing. This can be seen from the IPF map: the large grains either contain sub-grain boundaries only (left-hand side of the map) or do not contain any sub-grain boundaries nor do they appear deformed anymore. Also, they inherited the texture that was introduced during the cold swaging ($[110]_\beta$ direction parallel with the swaging direction). Therefore, prolonging the annealing would not result in further grain nucleation. In such cases, the use of higher recrystallization temperature was required, which indeed leads to full recrystallization (although with slightly larger grains) as shown in Figure 13c.

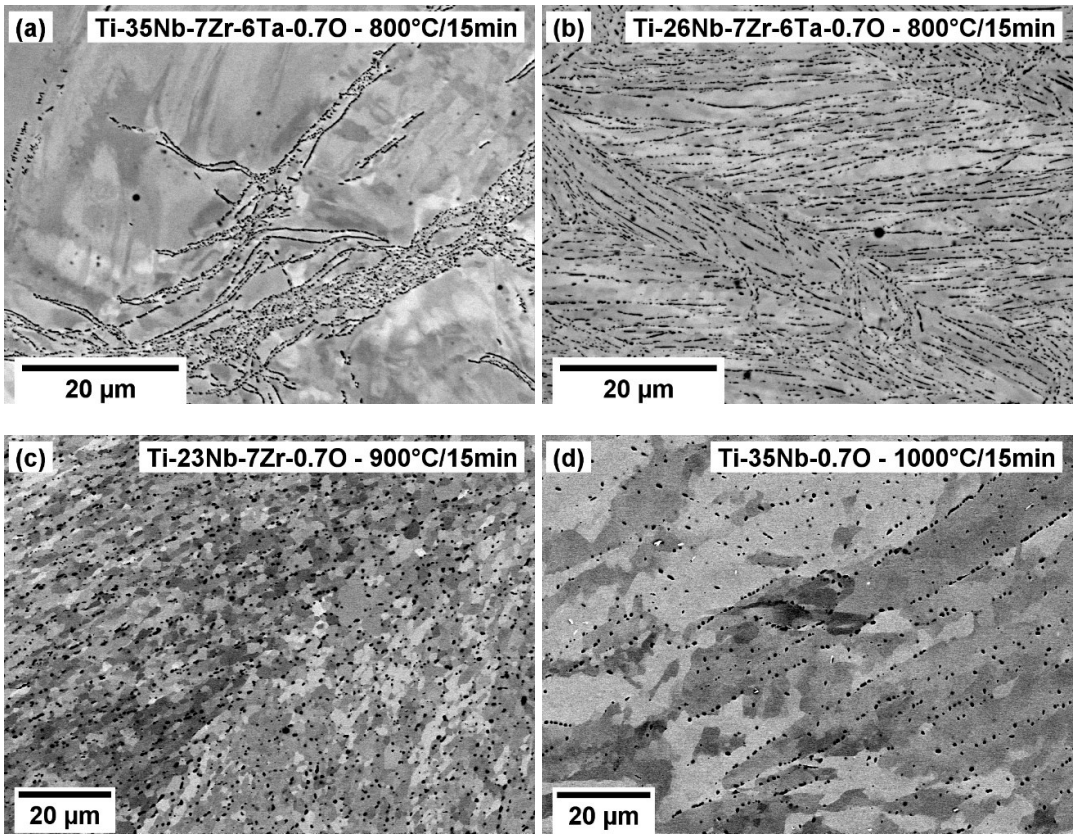

Figure 12: α phase particles grown in the cold-swaged alloys. Examples of the highest temperatures for each shown alloy, when the α phase was formed.

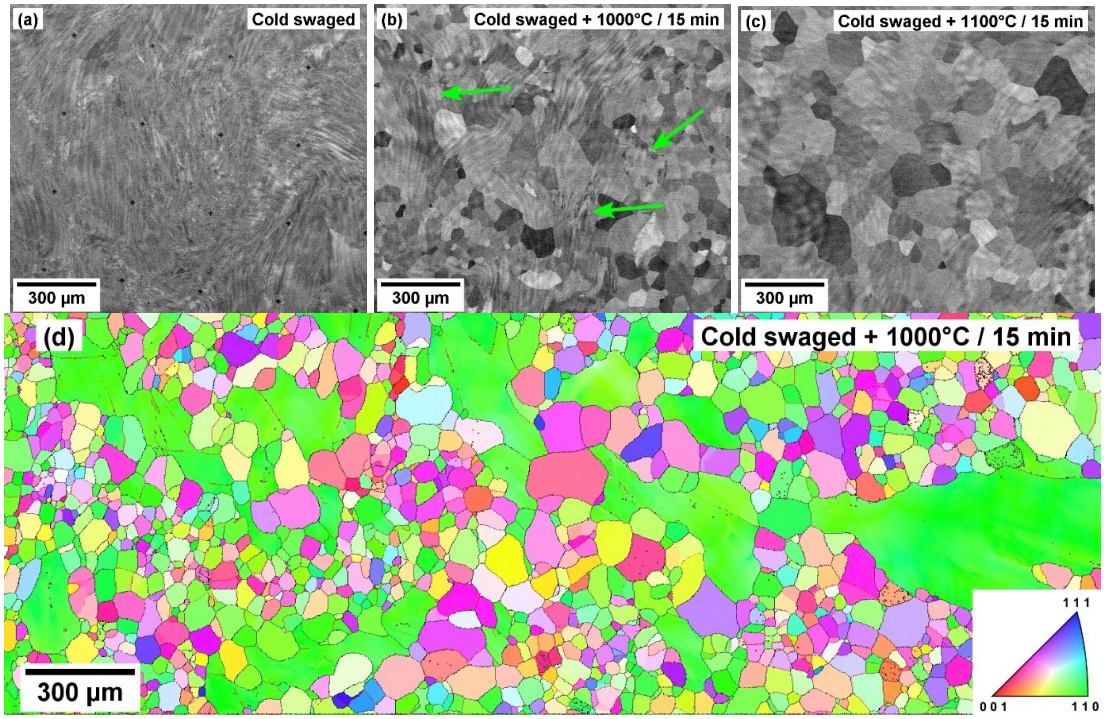

Figure 13: Microstructure after various processing steps of the Ti-35Nb-7Zr-6Ta-0.7O alloy: a) Cold swaging, b) recrystallization at 1000°C / 15 min + WQ (and corresponding EBSD IPF map in d)), c) recrystallization at 1100°C / 15 min + WQ.

3.3. Material preparation for high-throughput testing

The above-described procedure is very demanding in terms of time and resources. High-throughput testing gains more and more popularity and it is suitable also for research in the field of metastable β-Ti alloys containing a higher amount of O content as the established phenomenological descriptions (Bo-Md diagram and Mo equivalency) do not include its effect and therefore, alloy microstructure is uneasy to predict theoretically.

Ti-Nb-based systems were studied with the addition of various amounts of Zr, Fe and O. For each prepared sample by FAST, Zr, Fe and O were held constant while the layered gradient was created in the Nb content. For proper control of the oxygen content, the O concentration in each powder used was evaluated so that the right amount of TiO_2 could be determined. The basic properties of the used powders are summarized in Table 2.

Table 2: Properties of powders used for the preparation of layered samples by FAST. Interstitial contamination of Fe was considered negligible due to its concentrations used. The TiO_2 was in the form of particles smaller than 1 μm which were agglomerated. For this powder, the IGF method is not usable for the determination of O content and the nominal content was used for calculation.

Powder	Supplier	Size	Morphology	O (wt%)	N (wt%)	H (wt%)
Ti	TLS Technik	10 - 80 μm	spherical	0.175(1)	0.0211(5)	0.0013(5)
Nb	Alfa Aesar	< 45 μm	irregular	0.412(1)	0.0734(6)	0.0465(6)
Zr	TLS Technik	< 45 μm	spherical	0.175(1)	0.00856(7)	0.001(1)
Fe	Goodfellow	< 60 μm	irregular	-	-	-
TiO_2	Sigma Aldrich	< 45 μm	agglomerates	-	0.004(2)	0.017(3)

Each powder mixture was first carefully weighted and properly mixed. The first mixed powder was poured into a 30mm graphite die and pressed by a hand press before the next layer was added. This ensured flat interfaces between successive layers. This process was repeated 6 times to prepare 6 alloys/layers in a single sample. The Nb-layering was selected for two reasons: first, Nb is the β-stabilizing element, affecting, thus most directly the phase composition, second, Nb has the lowest diffusivity of the alloying elements [140] which allows maintaining the layered structure after the high-temperature sintering. On the other hand, other elements (Zr, Fe, O) are meanwhile easily homogenized [141]. To prevent the contamination of the sintered material by carbon, a tungsten foil was used to separate the sample from both the graphite die and graphite pistons instead of the C foil that is usually used. The difference between the resulting samples is evident in Figure 14. The contamination and carbide presence is down to a depth of a few millimetres which would effectively restrain us from studying the uppermost and lowermost 1-2 layers. By using the W foil, the carbon contamination is eliminated. On the other hand, tungsten diffusion into the material is observed after the high-temperature sintering, but the penetration depth is only about 200 μm, i.e. much less when compared with C contamination. Note that W is a β-stabilizing element.

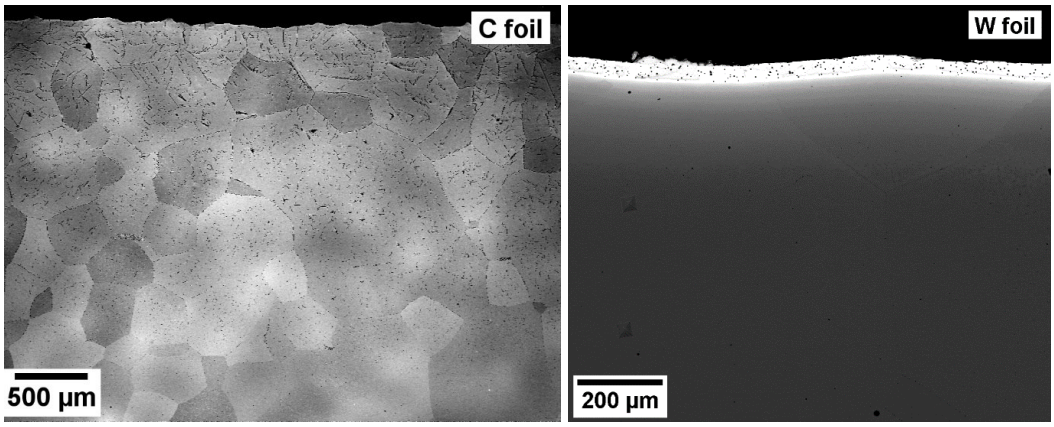

Figure 14: Comparison of the use of C vs. W foil as a separation of the sample from the graphite die and pistons. The contrast of the second image is boosted so the diffused layer of W is apparent.

For the sintering conditions and approaches, I used the results of my colleague Jiří Kozlík who devoted a large portion of his Ph.D. study to develop methods for the preparation of Ti alloys from blended elemental powders by FAST (namely Ti-Nb-Zr-O system and Ti-5553 commercial alloy) [127,128]. The compaction and the homogenization were performed using the sintering furnace (model 10-4) by Thermal Technology LLC, USA, in vacuum created by a dual-stage rotary vane pump. The sintering program that leads to a locally homogeneous composition comprises linear heating at a rate of 200 K/min up to a temperature of 1500°C, 30min holding time, followed by free cooling. The pressure applied during the sintering program was set to 50 MPa and the temperature was regulated by the pyrometer.

An example of the heating program is shown in Figure 15. From the recorded piston position, it is evident, that the compaction was completed almost immediately after reaching the sintering temperature, and thus, only the homogenization took place at the sintering temperature. The subsequent movement of the piston was caused by small leaking of the material between the piston and the die during the holding time and by thermal shrinkage during cooling.

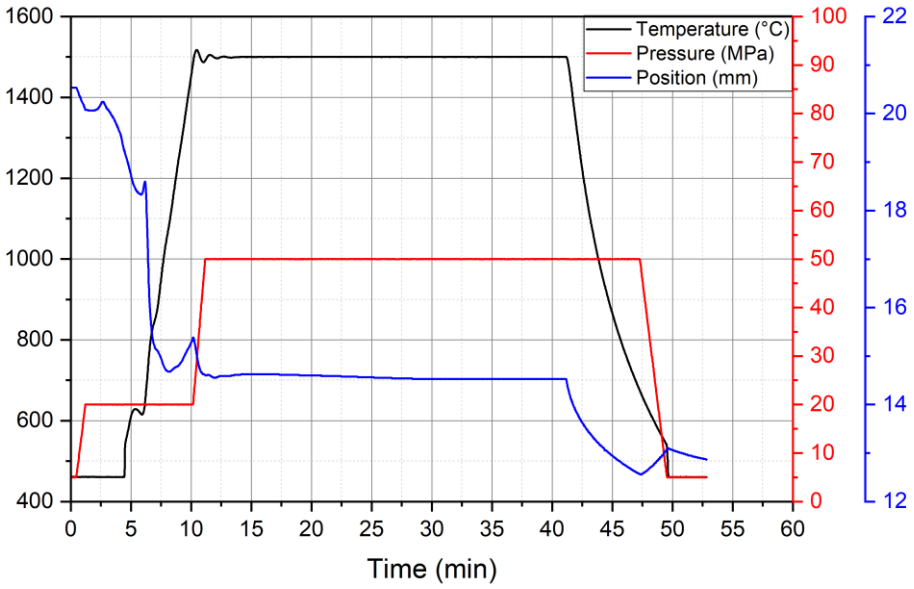

Figure 15: The recorded data of the sintering process used for compaction and homogenization of the prepared samples.

After sintering, the pellets were solution-treated at 1000°C/2h in a vacuum followed by water quenching. Samples for the experimental characterizations were cut from the sintered pellets as indicated in Figure 16. The flat samples with various thicknesses (suitable for each method) were used for scanning electron microscopy (SEM), x-ray diffraction (XRD), microhardness measurements and scanning acoustic microscopy (SAM). For measurements by resonant ultrasound spectroscopy (RUS), cuboidal samples were cut from individual layers using a cutting wheel with a thickness of 0.4 mm. After cutting, the samples were ground using SiC papers to the approximate dimensions of 1.5 × 2.5 × 3.5 mm^3, where the shortest dimension was oriented perpendicularly to the layers (direction x in Figure 16), i.e. each sample covered the central 1.5 mm from the manufactured 2.1 mm thick layer (samples whose elastic properties have been measured had 6 layers). The compression samples were made by simply cutting into dimensions 7 × 7 × 12.5 mm^3 (or smaller, if all the layers were not supposed to be tested due to their brittleness).

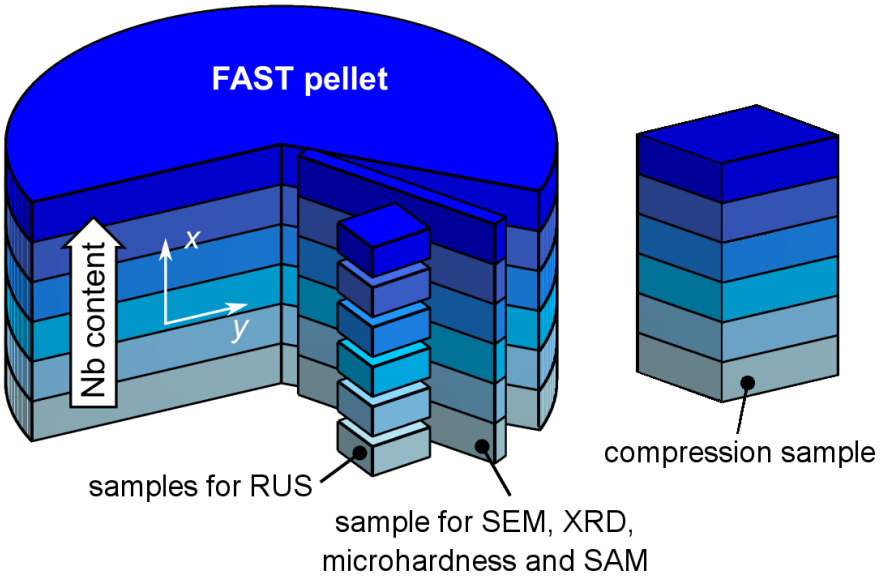

Figure 16: The structure of the graded FAST pellet (diameter 30 mm and height 12.5 mm) and the placement of the samples for experimental characterization.

4. Industrial processing of metastable β-Ti alloy for hip implant manufacturing

One of the parts of my dissertation project was the work on an industrial project "New generation of joint implants manufactured from a beta titanium alloy" led by company Beznoska, s.r.o. with two partners: Charles University and company COMTES FHT, a.s. The main aim of this project was to develop a manufacturing procedure for hip implants stem from the Ti-35Nb-7Zr-6Ta-0.7O alloy which was patented by Beznoska and Charles University previously [142]. A viable industrial technology for manufacturing of hip implant stem is shortly outlined in this chapter. Importantly, such manufacturing technology can be also used for newly developed alloys described in the following chapters.

4.1. Casting and homogenization

The casting of the alloy was performed in company Retech LLC, USA, with which we have previously cooperated on ingot manufacturing [139,143]. The size of the ingot was selected on the basis of further required processing. First the ingot must be thoroughly worked (e.g. forged) with area reduction of at least 70% as shown in my diploma thesis [139]. Second, the worked rod must have a minimum diameter of 35 mm to allow for subsequent die-forging of hip implant stem semi-product. Therefore, large diameter of 100 mm (4 inches, in fact) was selected for the ingot casting.

The input materials were titanium sponge, zirconium sponge, pieces of niobium and tantalum and TiO_2 powder. The large ingot had to be prepared by a dedicated procedure in three steps. In the first step, 2kg compacts with nominal composition were melted by plasma arc in He with a resulting diameter of 100 mm and height of 75 mm. In the second step, 4 ingots with a diameter of 50 mm were prepared by melting of the compacts in a tiltable mould and pouring the melt into an induction-heated (150 kW) crucible with diameter of 50 mm. The crucible can be opened from the bottom and the ingot is pulled a little to enable pouring another 400-500 g of melt. The top part of the material remains liquid until the whole ingot is finished. This procedure is called sequential pour casting. The final ingot with a diameter of 100 mm was prepared by the same procedure using the 4 previous ingots and larger crucible (diameter 100 mm). Note that the material is extremely prone to contamination by oxygen, nitrogen and hydrogen, therefore the whole procedure takes place in a pure He atmosphere. The final ingot is shown in the photo in Figure 17. The surface of the ingot was uneven therefore it had to be machined to a diameter of 90 mm before further processing.

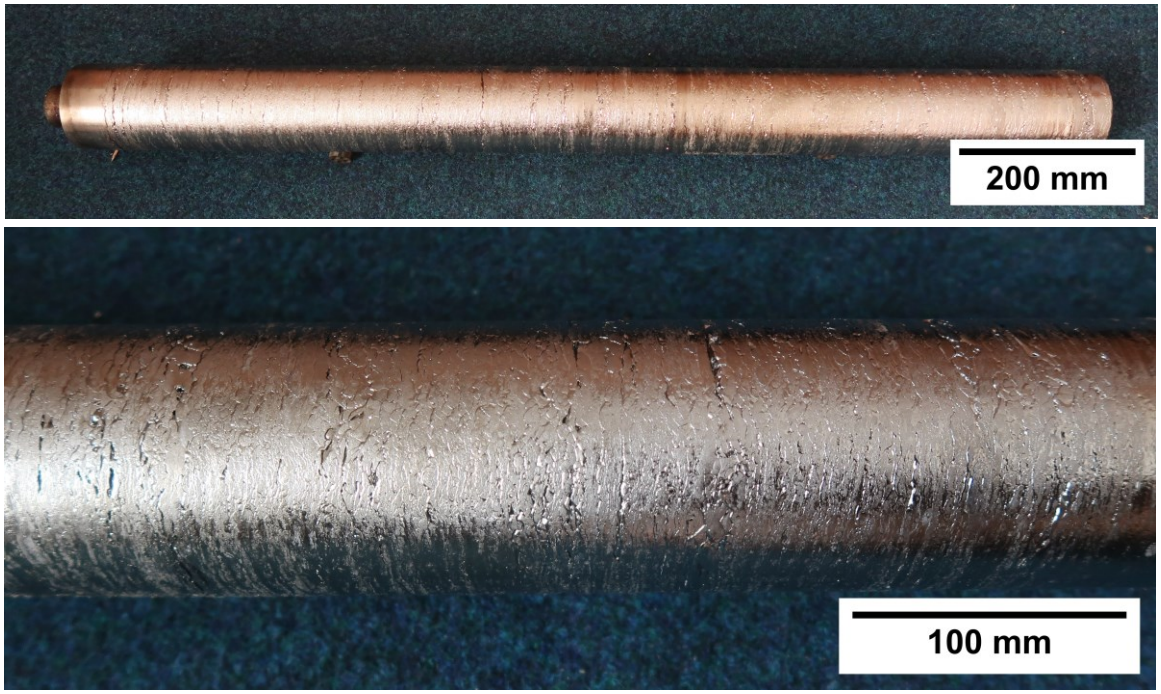

Figure 17: Cast ingot of Ti-35Nb-7Zr-6Ta-0.7O. The detail shows surface irregularities created by fast cooling by the mould during sequential casting.

After casting, the material contains dendritic inhomogeneities caused by preferential solidification of metals with high melting points (Nb, Ta), similarly as in the case of laboratory-scale arc melting. On the other hand, the interdendritic spacing was about 200 µm, which is much more compared to the as-cast microstructure of the laboratory scale arc-melted rods with the interdendritic spacing of about 20 - 40 µm (cf. Figure 11). Consequently, higher temperatures and/or longer annealing times must be used for homogenization of such microstructure. Extensive experimental study was performed to find out that this inhomogeneity can be removed by homogenization annealing at temperatures of 1200 - 1400 °C. The annealing time needed for a full homogenization varies according to the used temperature. While only 4h were sufficient for homogenization at 1400°C, about a day was needed at 1200°C. Since most industrial vacuum furnaces allow a maximum temperature of 1200°C, the ingot was homogenized at 1200°C/24h in a vacuum in the company Pilsen Tools, Czech Republic.

Figure 18 shows SEM images of the as-cast condition and homogenized condition as well as energy-dispersive spectroscopy (EDS) line scans in both conditions. The dendrite spacing in the as-cast condition is in the order of 100-200 µm. In the homogenized condition, the dendrites are fully dissolved and the only remaining heterogeneity is visible on a much larger scale of millimetres with a maximum deviation in the composition of about 1 wt%.

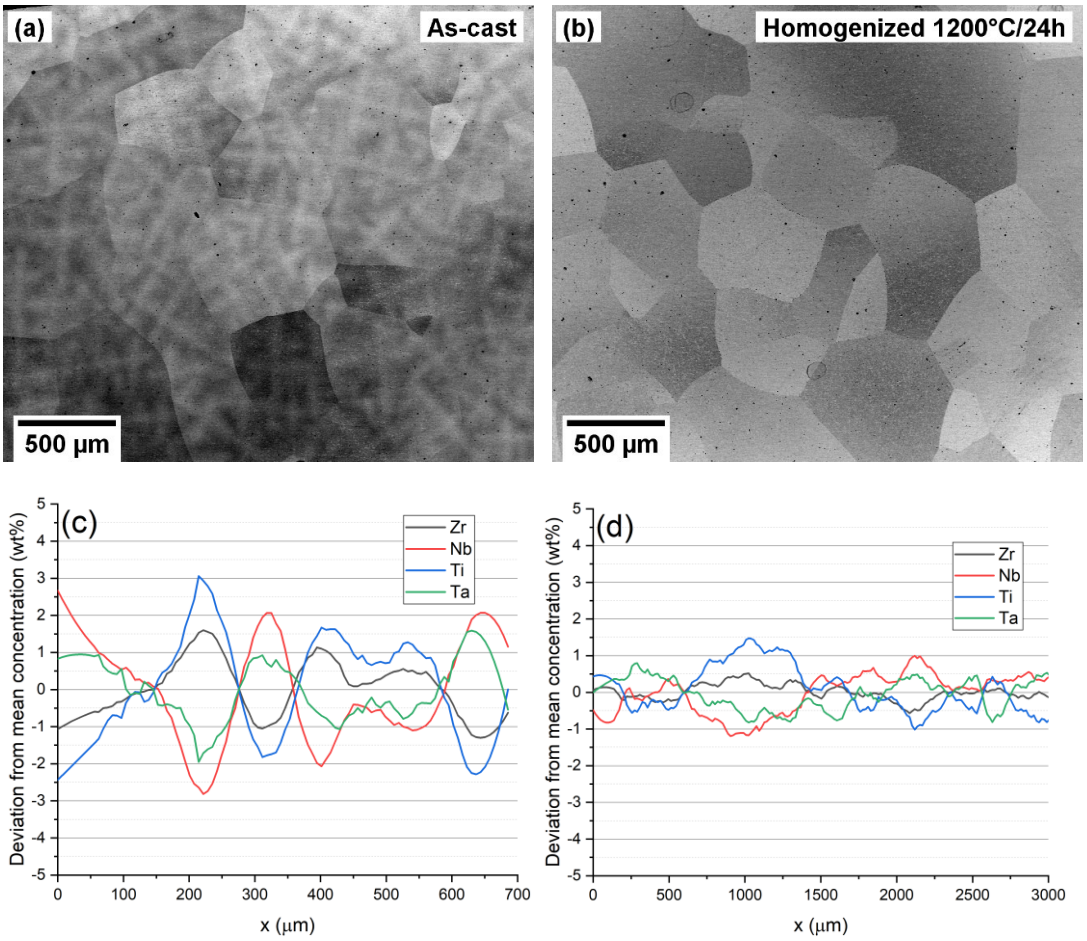

Figure 18: a) SEM image of dendritic inhomogeneity of cast alloy, b) SEM image of microstructure after homogenization 1200°C/24h, c) EDS line scan in as-cast condition, d) EDS line scan after homogenization. Note that the x-axis scale is much wider for the homogenized condition.

4.2. Rotary swaging and solution treatment

First, conventional hot rolling was considered for deformation of the Ti-35Nb-7Zr-6Ta-0.7O alloy. Smaller ingot (diameter 50 mm) prepared previously was used for these experiments not to spoil the large ingot. Common plastometric tests suggested that the material is considerably strong even at increased temperatures above 1000 °C. Indeed, it was found out, that the material remains too strong at even very high temperatures of 1200 – 1300 °C, significantly complicating the rolling process [139,144]. Even more importantly, exposure to high temperatures in aire leads to formation of severely oxidized surface region. Due to these disadvantages of rolling, rotary swaging was selected for material processing and proved to be an effective way for the mechanical working of this alloy.

While the rotary swaging technique is widely spread for working pieces with a diameter of 30 mm or less, bigger machines are much scarcer. In the end, the rotary swaging was performed in company Ingpuls GmbH, Germany, where it was possible to start with a diameter of 80 mm and swage the ingot down to 38.5 mm in 9 steps at the temperature of 900 °C. Machining from a diameter of 90 mm to 80 mm has been performed before the swaging. After each swaging step (10-20% of relative area reduction), the rod was reheated for 15-20 min during which the dies changing

occurred. Finally, the area reduction of 77% has been reached and the rod was left to cool freely.

The microstructure of the rotary swaged rod was analyzed by SEM (Figure 19a,b). Overview image in Figure 19a shows homogeneous deformation at a large scale. In the detailed image (Figure 19b), dark particles were found which were identified as the α phase. It could have precipitated either during the rotary swaging process at 900°C or during the cooling process.

To dissolve the formed α and recrystallize the microstructure, solution treatment (ST) annealing was performed in COMTES FHT, a.s. company. Two-stage heating was performed. First, the rod was preheated to a temperature of 550 °C at the rate of 10 K/min and soaked for 40 min. After preheating, it was inserted into another furnace directly at 1000 °C. The annealing time was 35 min, followed by water quenching. For protection against oxidation, the rod was covered with a surface coating (Tinderex).

The resulting microstructure, shown in Figure 19c,d, is fully recrystallized with a grain size of about 100 µm and free of secondary phase particles. In this condition, tensile and fatigue testing was performed.

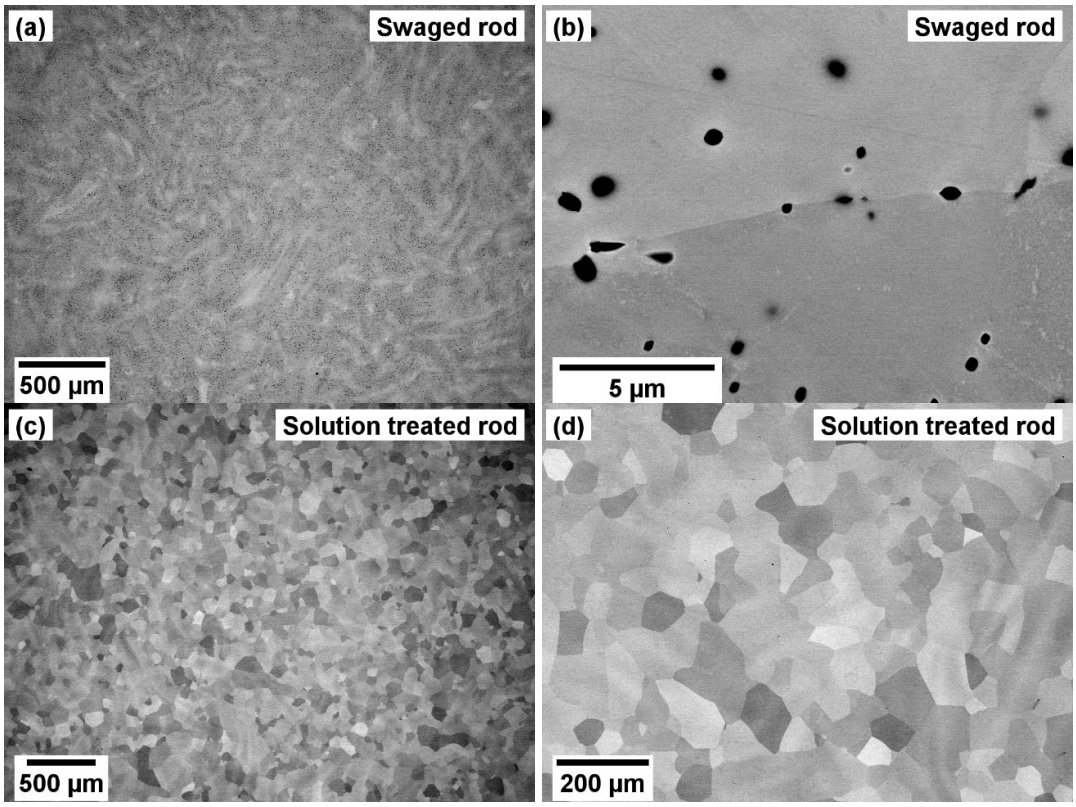

Figure 19: SEM images of the swaged rod a) overview, b) detail with apparent α particles created during slow cooling. SEM images of the swaged and solution-treated rod c) overview, d) detail of refined grain size.

4.3. Finishing procedures and mechanical properties

The last step of thermomechanical processing was the die-forging of the prepared rod into the shape of implant semi-products using a hydraulic spindle press. For this step, the rod was cut into 20 cm long pieces and each piece was processed as follows:

1) induction furnace heating to a temperature of 1150 °C on air (heating time of approx. 10 min),

2) die-forging with a speed of about 0.1 m/s,
3) water quenching of the formed piece within less than 1 min after taking it out of the furnace.

The forged semi-products for the preparation of 8 prototypes are shown in Figure 20a. Final processing included electric discharge machining, electro-polishing and surface treatment by spray-coating with Ti and hydroxyapatite. The final stem prototype is shown in Figure 20b. Six of these prototypes were used for fatigue testing under conditions specified in ISO 7206-4.

Figure 20: a) Implant semi-products formed by die forging from the swaged and solution-treated rod. b) Finished implant stem made from Ti-35Nb-7Zr-6Ta-0.7O alloy.

The mechanical properties evaluated on the solution-treated rod (before die forging) are shown in Figure 21 together with results from the as-cast ingot. From the tensile curves shown in Figure 21a, it follows, that the developed material processing route has substantially improved the yield strength, ultimate tensile strength as well as ductility. Another difference between the two conditions is the much more pronounced sharp yield point after the processing, which is caused by the higher interaction of dislocations with the oxygen atoms.

The results of fatigue testing shown in the S-N plot in Figure 21b indicate that the improvement at higher stress amplitudes is rather negligible, however, below 400 MPa the processed material clearly outperforms the cast condition with the fatigue limit σ_f at 340 MPa. This value is rather surprising when it is compared with static tensile material properties (ultimate tensile strength σ_u of 1300 MPa) yielding a ratio $\sigma_f / \sigma_u = 0.26$ which can be considered very low. This ratio can span however quite wide as depending on many material conditions. In this case the lack of surface compressive stresses [145] seems to play the main role. After solution treatment, the rod does not contain the compressive stresses due to long exposure to high temperature and resulting recovery. Also, the samples were machined from the inside of the solution-treated rod by electric-discharge cutting, which prevented any stresses possibly present at the surface of the rod from affecting the fatigue samples. On the other hand, the forgings of final prototypes were quenched directly after obtaining nearly the desired shape and machining (by electric discharge) the very surface only.

Therefore, the surface compressive stresses are much more likely to be present in the final prototypes.

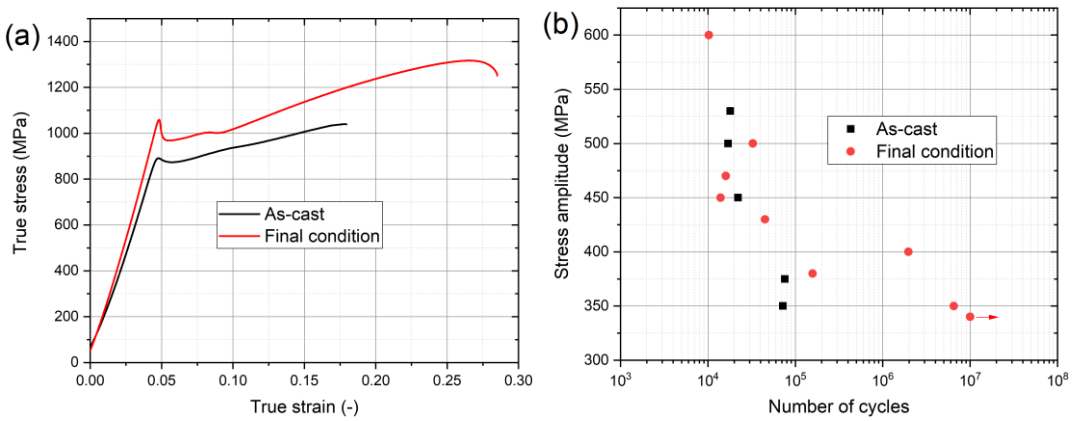

Figure 21: Improvement of the material properties by the applied procedure. a) tensile testing, b) fatigue testing at R = -1.

The fatigue testing of the implant prototypes according to ISO 7206-4 methodology was performed by mounting the prototypes into a low-molecular epoxy resin at a specified angle. A large implant head (i.e. the worst case scenario) from stainless steel was attached to the implant stem and cyclic sine wave load has been applied with the minimum force F_{min} = -250 N and maximum force F_{max} = -2300 N. The regime of fatigue testing was, therefore, compression-compression, however, due to the complex shape of the prototypes and testing geometry used, tensile stresses were present as well. The frequency of the sine wave of 5 Hz was used.

All 6 prototypes have survived 5 000 000 cycles without any apparent cracking in NaCl solution in distilled water (9 g/kg) kept at 37 °C. Moreover, one of the prototypes was tested also with higher force amplitudes. After finishing the testing according to a standard, the F_{max} value was increased by -500 N (i.e. into higher compressive loads) and tested further. This procedure was repeated until F_{max} = -5800 N at which the testing resin has been broken without any apparent damage to the implant stem prototype. Therefore, the implant stems from Ti-35Nb-7Zr-6Ta-0.7O alloy not only fulfils the fatigue requirements of the standard but even exceeds them by a factor of about 2.5 considering the maximum applied force.

In this brief chapter, it has been shown that Ti-Nb-based metastable β alloys with high O content can be manufactured into working products – hip implant stems – fulfilling the required properties. However, the main focus of this thesis is the development of new alloys with the best combination of properties and complete description of the physical processes leading to such properties.

5. Metastable Ti alloys with lower β phase stability

This chapter describes preparation of new alloys with improved properties via the "classical route" described in section 3.2. The prepared alloys are listed in Table 3 that contains their composition (nominal in the case of metallic elements and measured contents of oxygen and nitrogen by IGF) as well as the determined rough β transus temperature intervals.

Table 3: List of studied alloys. The composition given in wt% shows nominal contents for metallic elements and IGF-measured contents for O and N. The β transus ranges determined from testing of recrystallization temperatures are shown.

Batch	Alloy	Nb (%)	Zr (%)	Ta (%)	O (%)	N (%)	β transus temperature
#1	Ti-35Nb-6Ta-7Zr-0.7O	35	7	6	0,669(8)	0,0435(4)	800 – 900 °C
	Ti-32Nb-6Ta-7Zr-0.7O	32	7	6	0,671(3)	0,0353(3)	800 – 900 °C
	Ti-29Nb-6Ta-7Zr-0.7O	29	7	6	0,70(3)	0,034(5)	800 – 900 °C
	Ti-26Nb-6Ta-7Zr-0.7O	26	7	6	0,702(7)	0,0497(13)	800 – 900 °C
	Ti-35Nb-7Zr-0.7O	35	7	-	0,752(8)	0,0293(11)	800 – 900 °C
	Ti-29Nb-7Zr-0.7O	29	7	-	0,699(4)	0,0359(4)	800 – 900 °C
#2	Ti-26Nb-7Zr-0.9O*	26	7	-	0,947(4)	0,080(3)	900 – 1000 °C
	Ti-23Nb-7Zr-0.7O	23	7	-	0,785(3)	0,098(2)	900 – 1000 °C
	Ti-20Nb-7Zr-0.7O	20	7	-	0,756(2)	0,091(1)	900 – 1000 °C
	Ti-35Nb-0.7O	35	-	-	0,767(1)	0,065(9)	1000 – 1100 °C
	Ti-29Nb-0.7O	29	-	-	0,767(4)	0,0497(6)	900 – 1000 °C
#3	Ti-23Nb-6Ta-7Zr-0.7O	23	7	6	0,663(13)	0,0090(6)	< 900°C
	Ti-20Nb-6Ta-7Zr-0.7O	20	7	6	0,676(10)	0,0116(8)	< 900°C
	Ti-17Nb-6Ta-7Zr-0.7O	17	7	6	0,686(9)	0,0088(2)	< 900°C
#4	Ti-32Nb-7Zr-0.5O	32	7	-	0,49(5)	0,054(2)	< 1000°C
	Ti-32Nb-7Zr-0.6O	32	7	-	0,631(9)	0,0329(8)	< 1000°C
	Ti-32Nb-7Zr-0.8O	32	7	-	0,861(12)	0,04(5)	< 1000°C

5.1. Microstructure and phase composition observed by SEM

The microstructure of individual alloys after recrystallization annealing observed by SEM is shown in Figure 22, Figure 23 and Figure 24. Coarse and equiaxed grains were observed in all alloys. The grain size was between 50 and 200 μm, which is a reasonably fine microstructure with respect to the size of other sample dimensions used for characterization (tensile sample with 2 mm diameter, RUS sample with 2 × 3 × 4 mm^3). The grain size is influenced by the recrystallization temperature and the melting temperature of the alloy (i.e., by the homologous temperature of recrystallization). The alloys Ti-35Nb-6Ta-7Zr-0.7O, Ti-32Nb-6Ta-7Zr-0.7O (Figure 22a,b) and Ti-35Nb-0.7O (Figure 24d) were recrystallized at a temperature of 1100 °C and therefore contain comparatively larger grains. All other alloys were recrystallized at a lower temperature of 1000 °C. The grain size of these alloys increases with decreasing the Nb content and with absence of Ta which correlates with decreasing melting temperature of the particular alloy.

Contrast variations (wavy structures) are observed in some alloys with a higher content of high-melting elements (Ta, Nb). These are chemical inhomogeneities present due to incompletely homogenized dendrites formed during casting [146] and partly deformed during cold swaging.

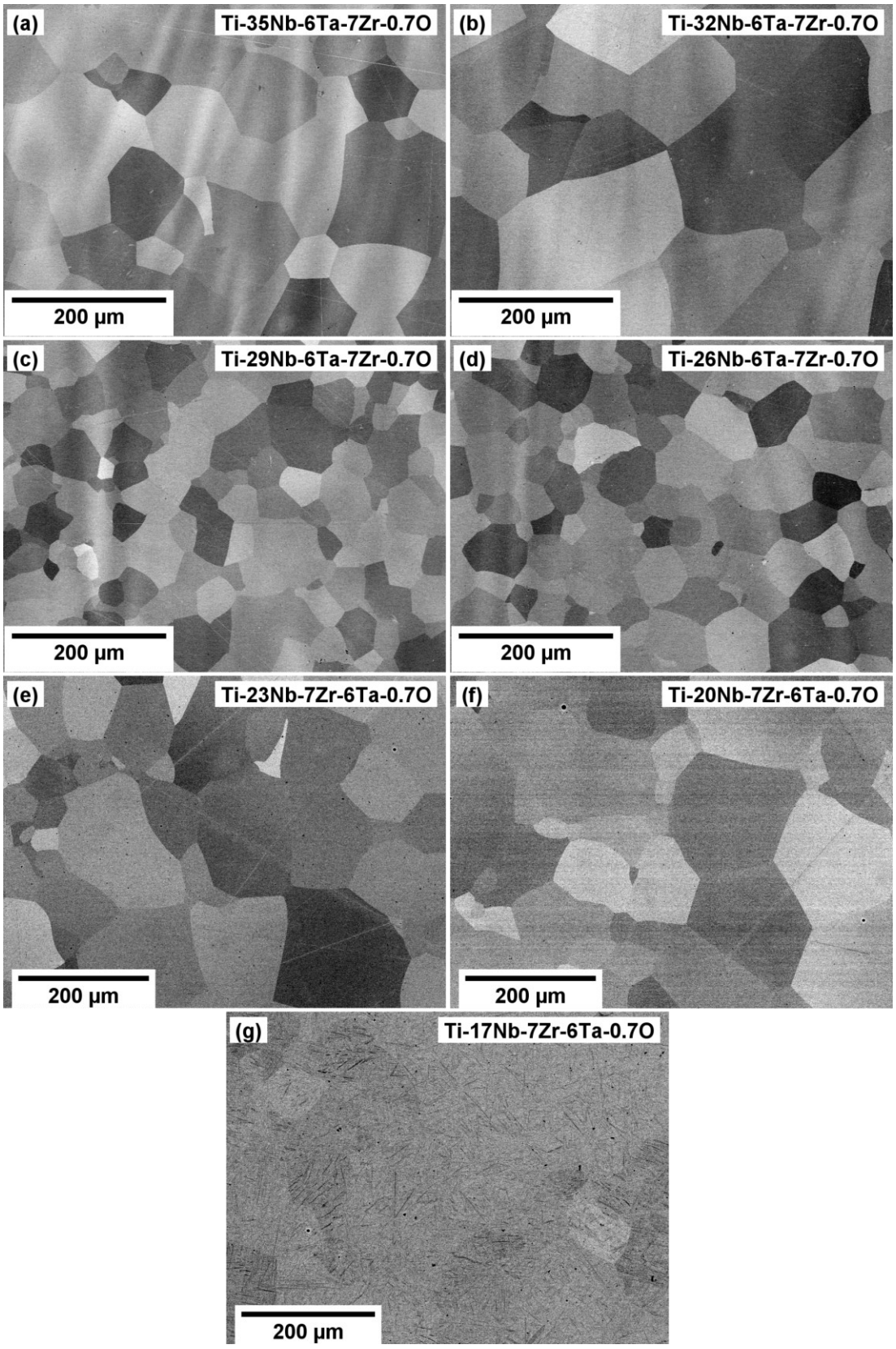

Figure 22: Microstructure of the alloys containing 6% Ta and 7% Zr after swaging and recrystallization annealing. Full recrystallization with no visible secondary phase precipitates is observed in most of the alloys. In contrast, the whole volume of Ti-17Nb-7Zr-6Ta-0.7O alloy has been transformed to α" martensite, yet few prior β grains can still be recognized.

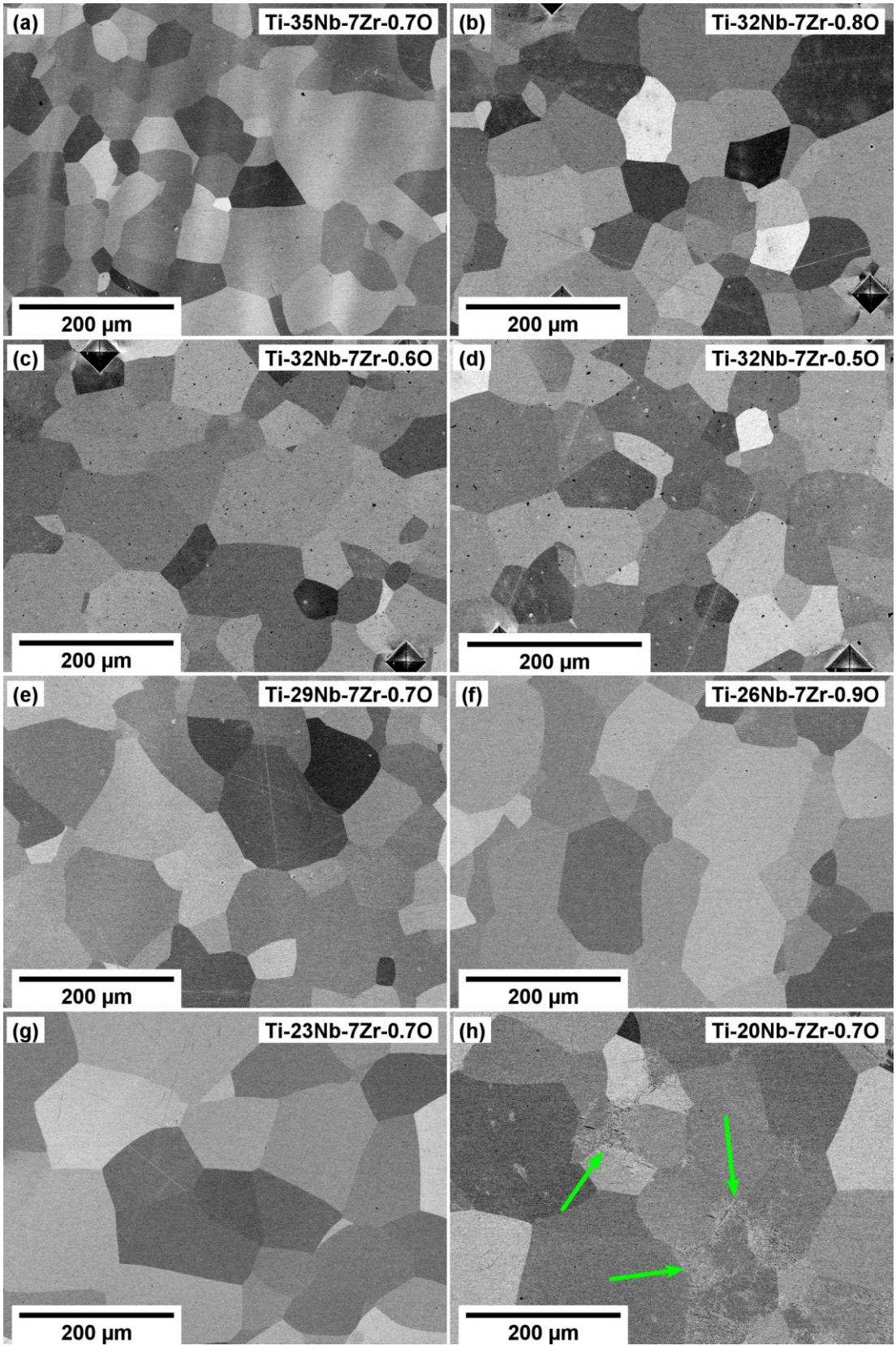

Figure 23: Microstructure of the alloys without Ta and with 7% of Zr after swaging and recrystallization annealing. In h), Ti-20Nb-7Zr-0.7O, secondary α" phase formation is visible in areas denoted by green arrows.

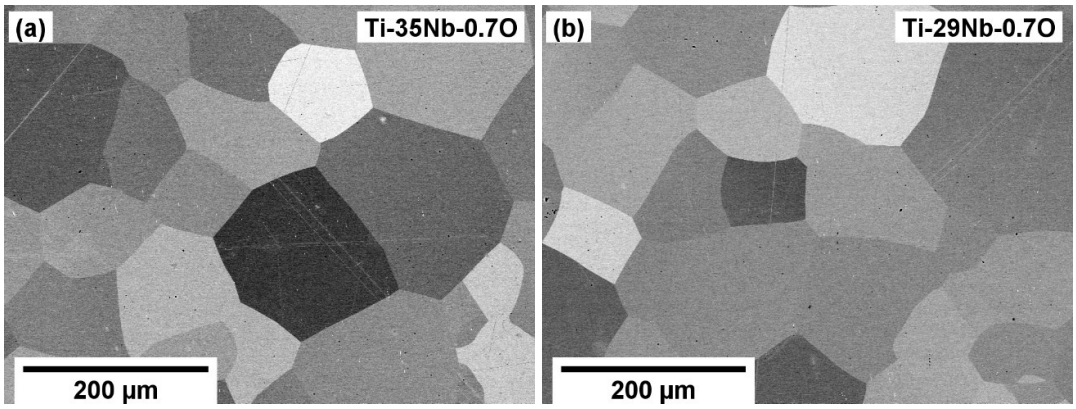

Figure 24: Microstructure of the alloys without Ta and Zr after swaging and recrystallization annealing.

Note that all alloys appear to possess a single-phase microstructure except for Ti-17Nb-7Zr-6Ta-0.7O and Ti-20Nb-7Zr-0.7O. The Ti-17Nb-7Zr-6Ta-0.7O alloy shows full transformation to α″ phase, while in the Ti-20Nb-7Zr-0.7O alloy, there are some regions, marked by arrows in Figure 23c, containing the α″ phase. This phase is shown in detail in Figure 25, where the morphology typical for the α″ martensite can be observed, especially in Figure 25b, with apparent twinning inside a martensite lamella. The reason for the inhomogeneous distribution of the areas with the α″ phase is that this composition is on the very edge of stability of the β phase and even small local fluctuation would lead to a martensitic transformation. It is thus possible, that there are few chemically inhomogeneous areas, similarly as in other alloys with higher Nb/Ta content, and when this area is slightly depleted of Nb, the transformation will occur locally. In contrast, the Ti-17Nb-7Zr-6Ta-0.7O seems to be already behind the edge of stability, its full transformation is further documented by XRD measurements.

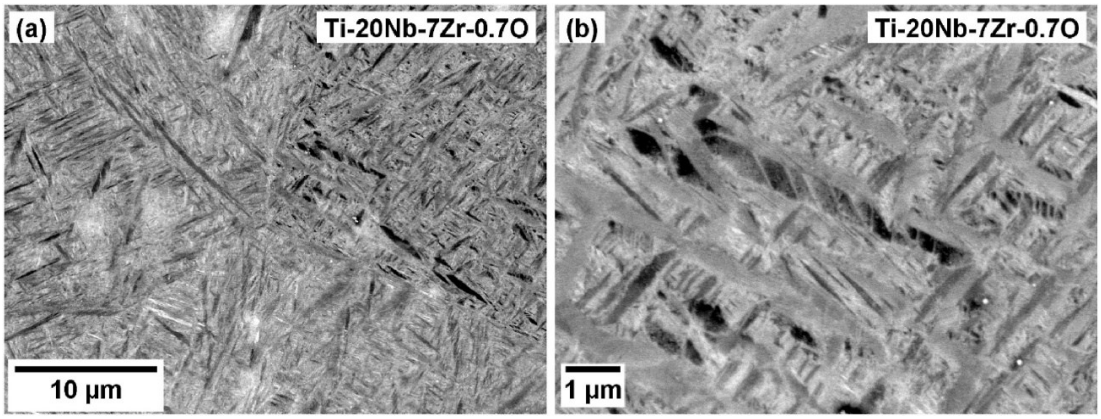

Figure 25: Details of the microstructure of Ti–20Nb–7Zr-0.7O: a) region, containing α'' martensite, b) several lamellae with apparent twinning inside them.

5.2. Phase composition determined by XRD

XRD measurements were used to determine the phase composition of the studied alloys. The diffraction patterns are shown in Figure 26. Alloys containing Ta and Zr are characterized by a single β phase for Nb concentrations of 26% and higher, while for the alloys without Ta and with 7% Zr the single β phase is only down to 29% Nb. The small peaks at 2θ of 15.3° and 20° observed in measured patterns are attributed to

$(211)_\beta$ and $(310)_\beta$ reflections, respectively, arising from the higher harmonic energy of the incident Mo Kα X-ray beam (denoted as λ/2).

On the other hand, ω phase reflections were found in alloys without Ta and with Nb content of 26% and lower (Figure 26b) and for both alloys without Zr and Ta (Figure 26c). The reflections were more intense (higher volume fraction) in alloys with lower Nb content. Note that the ω phase cannot be observed in SEM, as the athermal ω phase particles have a size of a few nm [147].

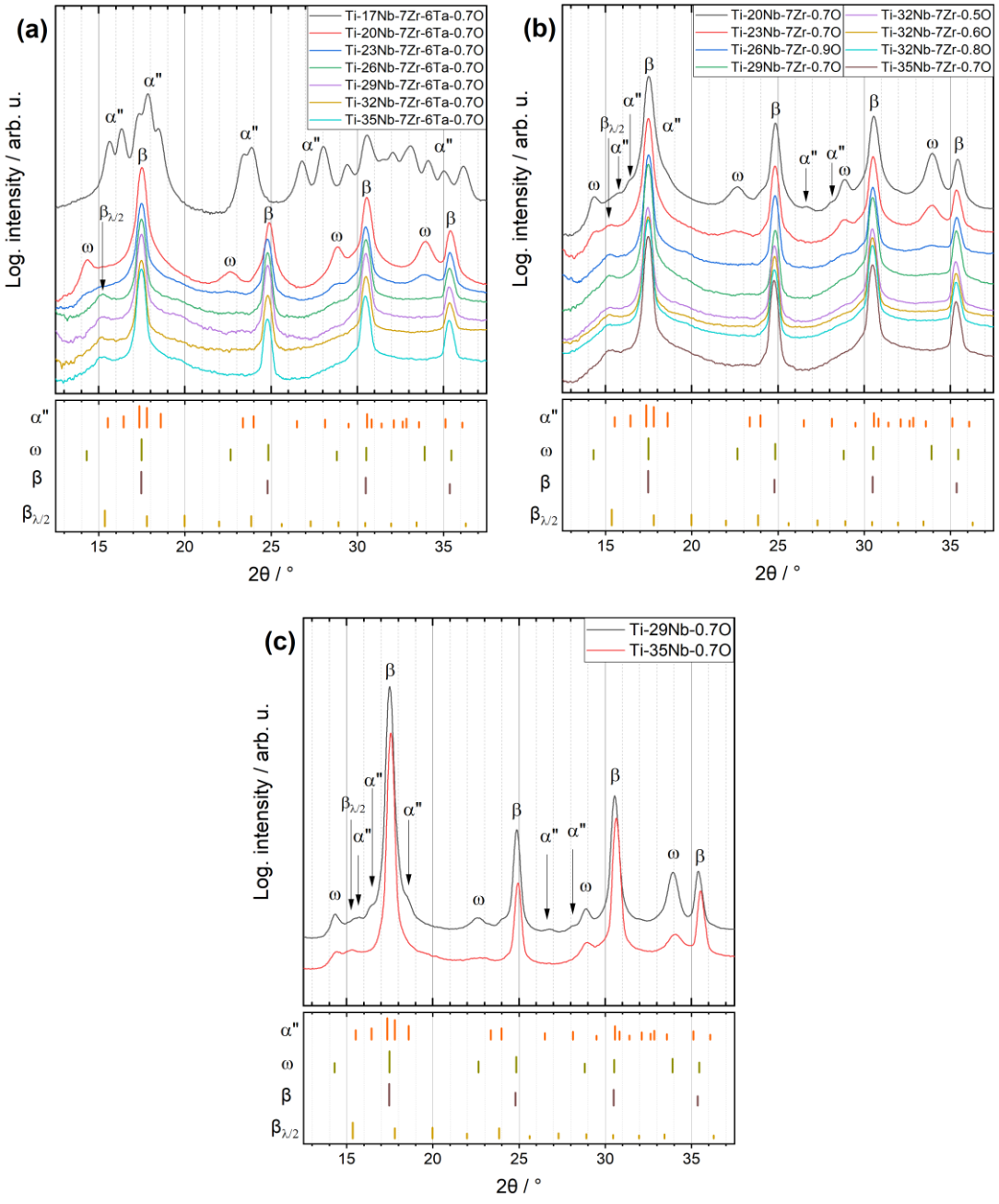

Figure 26: XRD patterns of a) alloys containing 6% of Ta and 7% of Zr, b) alloys without Ta, containing 7% of Zr and c) alloys without Ta and Zr content. The tick marks in the bottom part of each graph indicate the positions of the peaks for each present phase (incl. peaks from the β phase, diffracted at double energy/half wavelength). The lengths of the ticks are proportional to the theoretical relative intensities for each phase present.

In the alloy Ti–20Nb–7Zr-0.7O, the presence of the α″ phase was confirmed, consistently with SEM observations. Its presence is manifested in the asymmetry of the $(110)_{\beta}$ peak and small isolated $(200)_{\alpha''}$ and $(130)_{\alpha''}$ peaks which can be found at 2θ of 26.5° and 28.1°, respectively. However, their intensity is very low due to the low volume fraction of the α″ phase. In the alloy Ti-29Nb-0.7O, the presence of the α″ phase is observed from XRD results, despite the lack of its detection from the BSE-SEM image, which can be caused by its even scarcer presence (i.e. lower volume fraction) and even smaller size of particles compared to Ti-20Nb-7Zr-0.7O. Consistently with the SEM observations, the Ti-17Nb-7Zr-6Ta-0.7O alloy is formed fully by the α″ phase.

5.3. Transmission electron microscopy and detection of nano-sized particles

Detection of the ω phase by XRD is very clear for some of the alloys, while in other cases, it is difficult to determine its presence (or absence). Two alloys with the same amount of Nb but differing in Ta absence/presence were thus selected for observation using TEM: 1) Ti-26Nb-7Zr-0.9O, for which a very small peak, corresponding to ω phase can be still recognized in Figure 26b at 34° and 2) Ti-26Nb-7Zr-6Ta-0.7O in which any fluctuation of intensity at the positions corresponding to ω phase are within the fluctuations of the background intensity. The TEM images are shown in Figure 27. From the electron diffraction patterns, taken at $<110>_{\beta}$ directions, it follows, that no clear ω phase reflections are present in Ti-26Nb-7Zr-6Ta-0.7O alloy, in agreement with the XRD results. In Ti-26Nb-7Zr-0.9O alloy, ω phase reflections are present yet they are not very intense. The dark-field image from the spot in the yellow circle of Figure 27b is shown in Figure 27d. Despite the lack of presence of clear ω reflections in Ti-26Nb-7Zr-6Ta-0.7O, diffuse streaks can be observed at the corresponding locations. This may suggest that there exists an incompletely evolved (collapsed) ω phase which could perhaps be detected only by specialized methods of capturing reflection in reciprocal space. This reflection is forbidden for both the β and ω structures as described in [148]. It has been found in binary Ti-xNb alloys that similar diffuse streaks captured at room temperature can transform into more clear ω phase reflections upon cooling to cryogenic temperatures [149]. Such behaviour is also connected with an increase of electrical resistivity upon cooling due to the formation of the ω particles that are blocking the passing electrons [150].

Apart from the ω phase, there are also other reflections present in both alloys observed by TEM. In the diffraction patterns at $<110>_{\beta}$ direction, they are located at position $½\{112\}_{\beta}$ (in the centre of each four positions of ω phase reflections) and are visible in both alloys (denoted by green circles). These reflections were identified in [29] as nanodomains of the orthorhombic O′ phase. Such nanodomains were first believed to be caused by the presence of oxygen in alloys with high enough O content [151,152], however, the necessity of the oxygen presence was proven redundant after finding such nanodomains in metastable β Ti alloy containing yttrium that has scavenged most of the available oxygen from the matrix [153]. Figure 27c shows the dark-field image of the O′ nanodomains in sample Ti-26Nb-7Zr-6Ta-0.7O alloy. When comparing these particles with the ω particles in Ti-26Nb-7Zr-0.9O alloy, the ω seems to be larger than O′ (note the different scale bar).

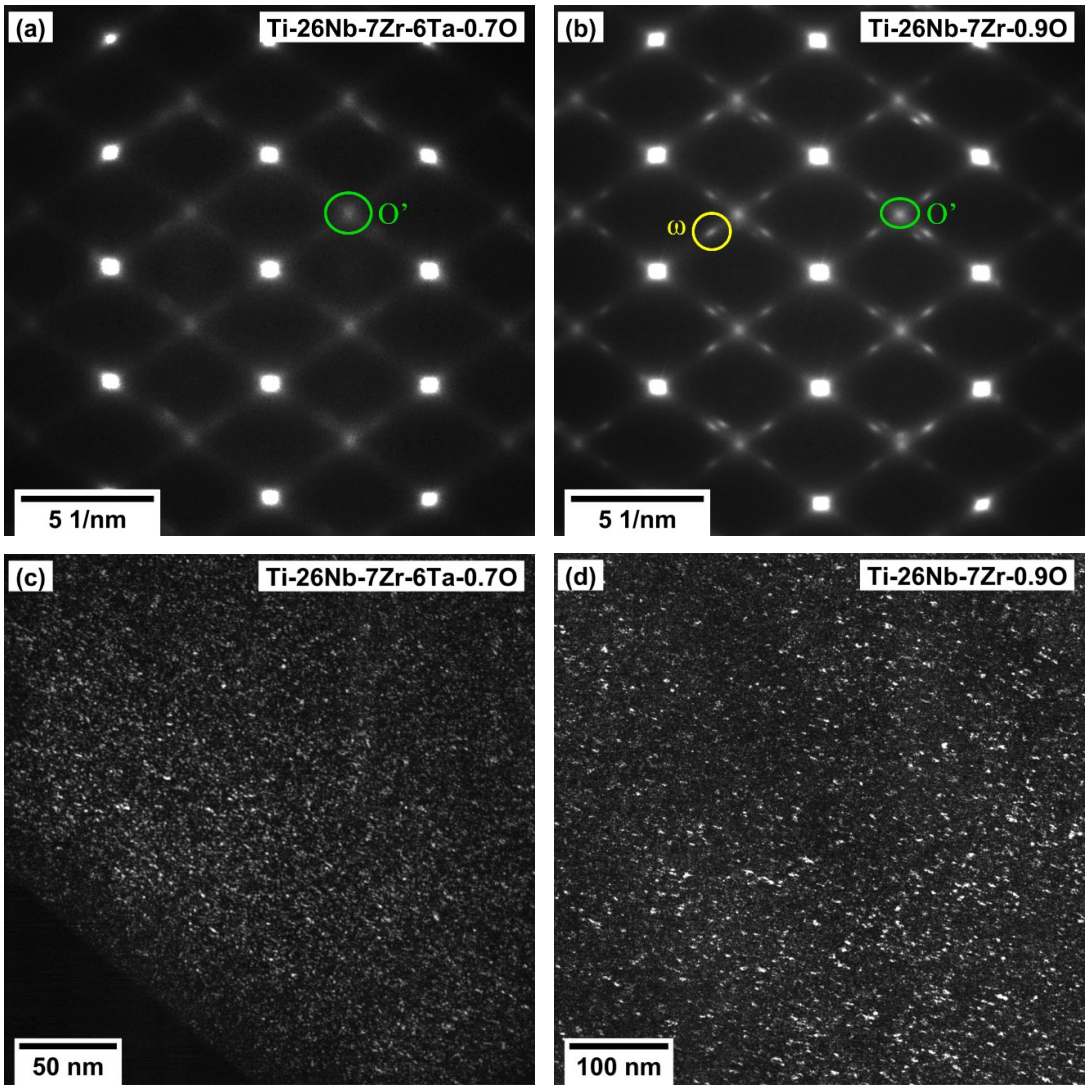

Figure 27: TEM diffraction patterns at <110>$_\beta$ (a-b) and dark-field images (c-d) of: a), c) Ti-26Nb-7Zr-6Ta-0.7O alloy; b), d) Ti-26Nb-7Zr-0.9O alloy. The dark-field images were captured using the diffraction spots of O' phase and ω phase for Ti-26Nb-7Zr-6Ta-0.7O (green circle) and Ti-26Nb-7Zr-0.9O (yellow circle) alloys, respectively.

5.4. Microhardness

The microhardness of the studied alloys is shown in Figure 28 as a function of Nb content for each group of alloys. For the alloys of both types Ti-xNb-7Zr-**6Ta**-0.7O and Ti-xNb-7Zr-0.7O, a minimum is observed at about 29-32% of Nb. Below this Nb content, microhardness rises, which is partly attributed to the increasing content of the ω phase, but the rise begins even before the fully collapsed ω particles are formed. For instance, in Ti-26Nb-7Zr-6Ta-0.7O the microhardness value is already rising although there are only diffuse streaks visible at the diffraction patterns captured by TEM (Figure 27a). It is of course possible, that the difference in microhardness can be caused either by only partially collapsed ω particles or the O′ particles, whose presence was suggested by the TEM diffraction patterns. The rising microhardness for values higher than 29-32 % Nb is caused by higher shear modulus (as shown below) which is directly proportional to the Peierls stress for movement of dislocations. The difference in the amount of the ω phase drives the microhardness of the Ti-29/35Nb-0.7O alloys. In the case of the Ti-32Nb-7Zr-yO with slightly different contents of

oxygen, the strong interstitial hardening effect of O can be compared directly with the effect of ω phase caused by changing several wt% of Nb, Ta or Zr.

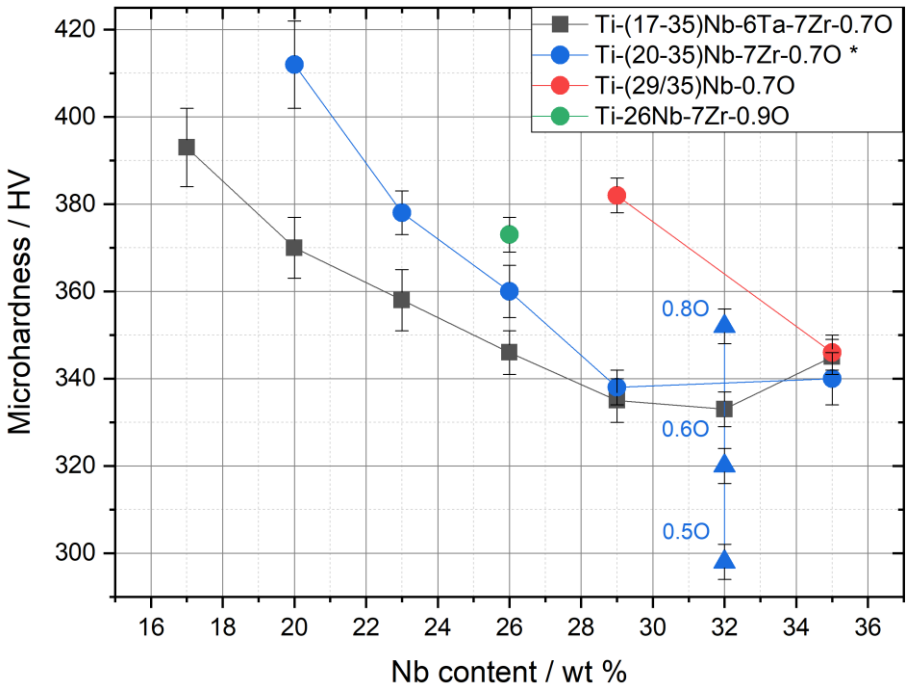

Figure 28: Microhardness of the studied alloys. The blue dots are marked by a star in the legend as three of the shown alloys contain an O content different to 0.7 wt% (which are marked just near the respective points.

5.5. Tensile properties

Tensile curves for all alloys are shown in Figure 29. Due to the high content of interstitial oxygen, most alloys exhibit a sharp yield point, which is attributed to the interaction of oxygen atoms with the dislocations. In these cases, the yield stress was established as the upper yield stress, i.e. peak height of the sharp yield point. For all alloys with 6% of Ta from batch #1, the yield stress exceeded 1000 MPa and the ultimate tensile strength was about 1200 MPa, as shown in Figure 29a. After reaching the ultimate tensile strength, the stress gradually decreases due to plastic instability and formation of the neck. As this part of the tensile curve is very pronounced, it shows us very ductile behaviour even after uniform elongation. Uniform elongation reaches at least 12% while total plastic elongation exceeded 17%.

Similar properties were measured for two of the alloys without Ta: Ti-35Nb-7Zr-0.7O and Ti-29Nb-7Zr-0.7O as shown in Figure 29b. However, a lower content of Nb in the material rapidly decreases its plastic elongation. Both Ti–26Nb–7Zr-0.9O and Ti–23Nb–7Zr-0.7O alloys still showed a pronounced sharp yield point, but elongation was only about 5% and 1%, respectively. The Ti–20Nb–7Zr-0.7O failed already in the elastic region. Decreased ductility of these alloys is caused by the presence of the ω phase particles causing imminent embrittlement [6,127]. The more ω phase was found in the materials (by XRD or TEM), the more brittle the behaviour was observed. Even the Ti-29Nb-7Zr-0.7O alloy was less ductile compared to the more stabilized alloys (in terms of Nb and Ta content) and it can be thus expected that there was some non-zero content of the ω phase also in this alloy.

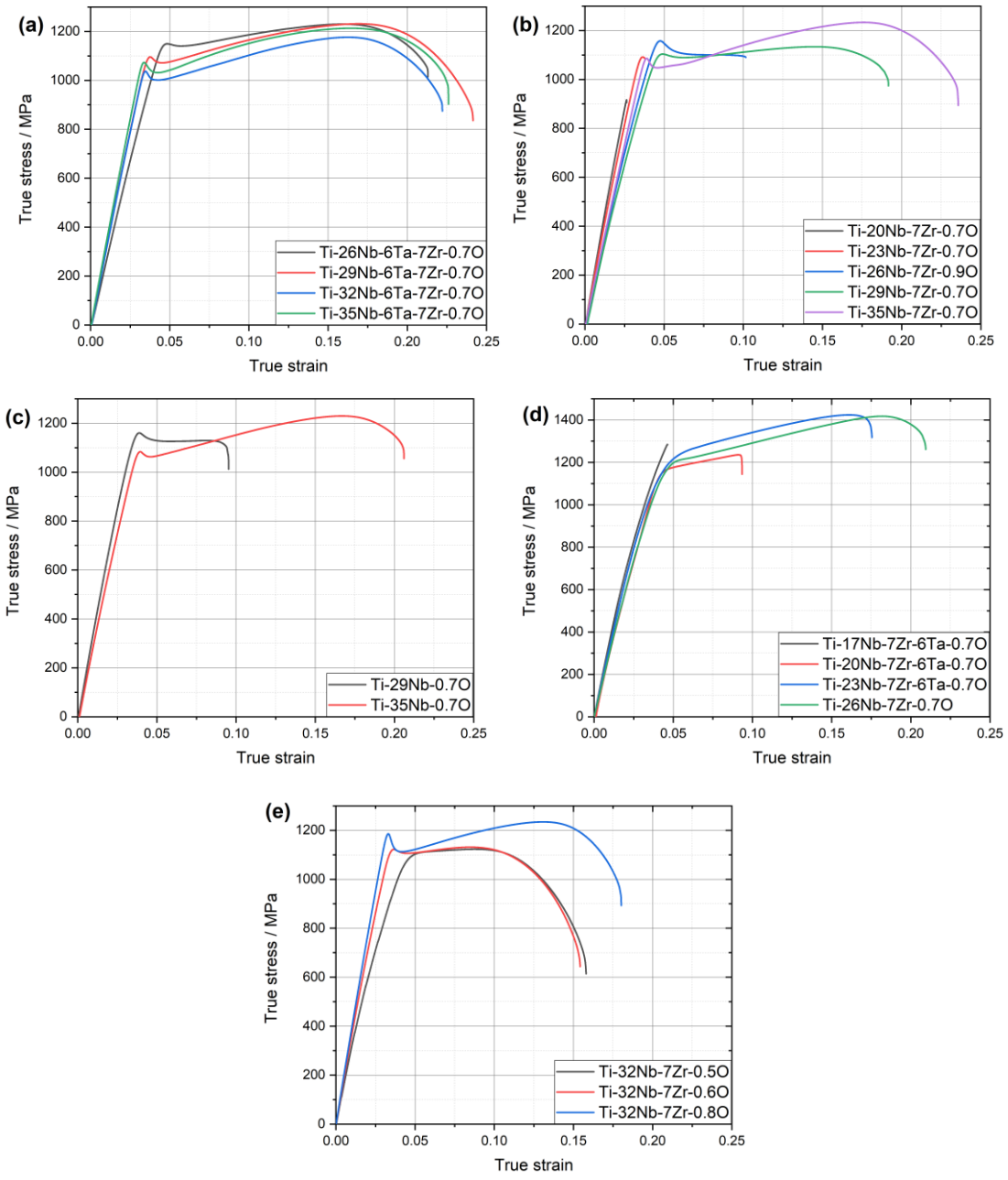

Figure 29: Tensile curves of alloys from batch #1 and #2: a) alloys with 7% of Zr and 6% of Ta; b) alloys without Ta and with 7% of Zr; c) alloys without Zr and Ta. Tensile curves of alloys from batch d) #3 and e) #4.

The two Ti-(29/35)Nb-0.7O alloys from batch #2 have similar tensile behaviour as Ti-26Nb-7Zr-0.9O and Ti-29Nb-7Zr-0.7O, although much higher content of the ω phase was detected in them and even the α″ martensite in Ti-29Nb-0.7O, which was detrimental in terms of ductility of the other alloy, it which the α″ was present (Ti-20Nb-7Zr-0.7O).

Qualitatively different tensile behaviour was observed for the alloys in batch #3. The content of oxygen, which was slightly lower than the nominal 0.7 wt%, was still close to that of the initial alloy Ti-35Nb-7Zr-6Ta-0.7O (about 0.67 wt%). However, the sharp yield point (yield drop) was not observed even for the ductile alloys from this batch and strong strain hardening led to high ultimate tensile strength of more than

1400 MPa for two of them. The yield stress in this batch was between 1100 MPa and 1200 MPa, therefore higher than in the previous batches, but the behaviour of the alloys, consisting of decrease of ductility when approaching the limit of metastability of the β phase, has remained the same: alloy Ti-17Nb-7Zr-6Ta-0.7O has ruptured before undergoing any plastic deformation and another two alloys with 6% of Ta followed by increasing the ductility similarly as in Figure 29b for alloys not containing Ta. The alloy Ti-26Nb-7Zr-0.7O that was prepared in place of the Ti-26Nb-7Zr-0.9O from batch #2 was meant to replace the results with the O content, closer to the nominal and desired 0.7 wt%. Since all alloys from this batch had a behaviour very different from the previous batches, direct comparison of tensile behaviour with other batches is problematic and should be avoided. On the other hand, for other measured properties (phase composition, microhardness, elastic modulus), batch #3 alloys seem to follow the expected trends. The cause of the different behaviour could be hidden in the precise chemical composition: since this batch was melted and cast in-house using very pure input elements (especially Ti with a purity of 99.999%, way more than any commercial Ti grade), the content of N was kept at 0.01 wt% and less, i.e. much lower than for the other studied batches. Small increase in the content of N was observed to cause huge effect on the ductility in β Ti alloys [40] and recently, the extra low N content was found to be a way for strengthening of pure Ti by as much as 0.8 wt% of oxygen while preserving high ductility [65].

Finally, batch #4, comprised three alloys that differed in oxygen content only: Ti-32Nb-7Zr-0.5/0.6/0.8O. The change in tensile behaviour as observed in Figure 29e between the individual O contents was expected based on previous work done in our group [75,154]. While for the O content of 0.5% (actually 0.45%, to be precise), neither strain hardening nor sharp yield point are observed, when increasing the O content to 0.6%, the sharp yield point appears but still no significant hardening. Only the highest O content of 0.8% leads to both mentioned effects, the latter causing an improvement in ductility.

5.6. Elastic moduli

Unlike most previous sections of this chapter, the measurements of Young's moduli by resonant ultrasound spectroscopy are shown as a single graph only in Figure 30. This allows us to follow the trends of different groups of alloys when changing the Nb content. Note that the measurements for alloys in different batches are given in different symbol shapes and measurements for different groups of alloys (e.g. alloys with Ta, without Ta and Zr) are given in different colours.

The two groups, Ti-xNb-7Zr-6Ta-0.7O and Ti-xNb-7Zr-0.7O, that are represented by a high number of alloys (i.e. measurement points) follow a similar trend: when starting at the highest Nb content, Young's modulus gradually decreases with the decreasing Nb concentration, until reaching a minimum of about 65 GPa, that is similar to the original Ti-35Nb-7Zr-6Ta oxygen-free alloy, patented in 1999 [53], having Young's modulus of 63 GPa [75]. These values can be considered very low, especially when compared with the usual β-Ti alloys, having Young's modulus between 78-103 GPa [6]. When removing even more Nb, a steep increase caused by higher ω phase content follows, which brings the value of Young's moduli up to values of 105-115 GPa. The ω phase itself is the stiffest among the phases of Ti alloys [107,155,156]. For the alloy with the lowest content of Nb (Ti-17Nb-7Zr-6Ta-0.7O), Young's modulus started to decrease again. The trend of the Ta-containing group is shifted to lower concentrations of Nb, as expected, by about 3 wt% of Nb. Thus, Nb proved to be a stronger β stabilizing element compared to Ta which is qualitatively in

agreement with their relative values of the Mo equivalences: 0.28 and 0.22 wt% for Nb and Ta, respectively [86].

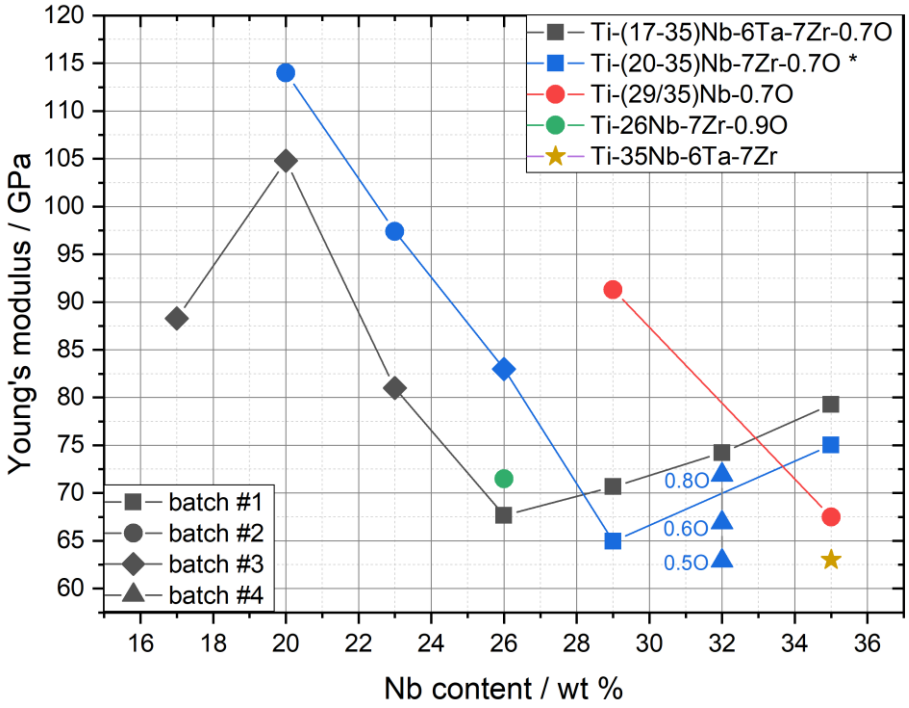

*Figure 30: Young's moduli of the studied alloys. Ti-35Nb-7Zr-6Ta (without oxygen) is shown for comparison [75]. *O content for alloys from batch #4 is specified near the symbols.*

Two alloys Ti-xNb-0.7O fit the behaviour of the previous groups when shifting to the left. The different position on the x-axis (in Nb content) follows from omitting the Zr content. Although Zr is classically considered a neutral element with respect to transformation between α and β phases [84], it was assigned with a non-zero value of Mo equivalent of 0.47 wt% several years ago [86]. Also, Zr was found to hinder the formation of the ω phase in Ti-Nb alloys which supports its β stabilizing role with respect to the proximity of the alloy to lattice instability (causing the formation of the athermal ω phase and/or ultimately of the α″ martensite) [157]. Based on this comparison, we could estimate, that the minimum in Young's modulus would be obtained for Nb content of about 36-38 wt% if the minimum would reach a similar value of about 65 GPa. On the other hand, XRD results suggest, that the α″ phase is present already in Ti-29Nb-0.7O alloy, which could point to a possibility that the minimum in Young's modulus could lie in higher Nb concentrations, close to 40 wt%, as determined for the low-oxygen Ti-Nb alloys [158].

The last point to notice is the behaviour of Ti-26Nb-7Zr-0.9O alloy which has a lower value of Young's modulus, compared to the same composition with lower O content of 0.7%. In other words, in this particular case, the higher O content leads to lower Young's modulus. On the other hand, the three alloys from batch #4 having the same content of Nb and Zr follow the opposite trend and higher O content increases the modulus. The same case is with the original Ti-35Nb-7Zr-6Ta in which O addition increases the modulus [75]. The difference is in the positioning of the alloy relatively to the minimum – as the O content shifts the martensite start (and related region of ω formation) to lower contents of β stabilizers, it lowers the modulus for alloys on the left-hand side but increases for the alloys on the right-hand side from the minimum.

The most promising alloy in terms of its mechanical properties is, therefore, the Ti–29Nb–7Zr-0.7O alloy. This alloy achieved an elastic modulus of 65 GPa, which is nearly as low as in the benchmark Ti–35Nb–6Ta–7Zr alloy [75]. In comparison with this benchmark alloy, the strength of the Ti–29Nb–7Zr-0.7O alloy is more than double, due to the oxygen content. Another benefit follows from the fact that Ta, the most expensive element from the Ti–Nb–Zr–Ta system, is not needed for achieving such a combination of properties, which has a positive effect on the overall price of the final alloy.

5.7. Discussion: achieving high strength and low elastic modulus

The high strength of the studied alloys is easily explained by the interstitial strengthening of the high oxygen content [75,159,160]. In previously developed biomedical Ti alloys with low oxygen content, alloying with Ta provided some solid solution strengthening [13,53,161]. In the presence of oxygen, Ta is not required for strengthening and can be avoided in high-oxygen alloys. This is of particular importance due to both the high price and the high melting point of Ta.

While the effect of oxygen on strength is clearly understood, the effect of composition on ductility and elastic modulus is more peculiar. Since the working temperature of biomedical alloys is body temperature (37°C), the composition of the material should be tuned such that the "ideal" properties (mainly low elastic modulus caused by premartensitic softening) are achieved just at this temperature. This means that the martensite start (M_S) temperature for a given alloy composition should be just sufficiently below the working temperature to prevent formation of α″ phase during quenching after ST, but at the same time, not too low as the effect of the premartensitic softening would be no longer as strong [83]. The presence of the stiff ω phase should be also avoided by composition tuning [162]. Note that while in the individual grains, lattice instability results in premartensitic softening of particular combinations of elastic coefficients, in a polycrystalline material, this softening inside of the grains results in a decrease of the macroscopic Young's modulus [163,164].

In metastable β-Ti alloys, the content of the β stabilizing elements is sufficient to suppress the martensitic transformation β → α″, and the β phase can be retained after quenching. In alloys with high oxygen content such as the Ti–35Nb–7Zr–6Ta-0.7O alloy [75], oxygen significantly affects the phase stability of the β matrix. Oxygen is an α stabilizing element in terms of increasing the β transus temperature in pure Ti [88] and in metastable β-Ti alloys [44,74,89]. This relates to the altering of Gibbs energies of α and β phases by variations in the interstitial content. α stabilization effect is therefore related to thermodynamic equilibrium achieved via diffusional processes. On the other hand, interstitial oxygen acts as a β stabilizing element in the competition between β and α″ and shifts the Ms temperature of α″ formation to lower temperatures [3,40,44,90,109,113,165–167]. Interstitial atoms hinder the possibility of shear of atomic planes, effectively suppressing the martensitic transformation.

These considerations are depicted in Figure 31, which presents a schematic pseudo-binary phase diagram of Ti–Zr–Nb–Ta–O alloys. The diagram is pseudo-binary in the sense that one constituent is not pure Ti, but a Ti–7Zr composition. The horizontal axis represents for simplicity the content of Nb + Ta in wt% (the effect of Ta on phase stability is slightly weaker compared to Nb [86]). This unusual construction allows us to show the position of the quaternary Ti–35Nb–7Zr–6Ta (low-oxygen) alloy in the diagram. Note that the blue lines are relevant for alloys without oxygen.

The effect of oxygen is incorporated into the diagram such that the first constituent in the diagram (on the left-hand side) is not Ti–7Zr but a Ti–7Zr-0.7O

composition. The red lines are relevant for alloys with 0.7% of oxygen. It can be observed that the oxygen increases the stability of the α phase in the equilibrium phase diagram by shifting the solid lines to higher temperatures and higher Nb/Ta concentrations. In this red diagram, the position of Ti–35Nb–7Zr–6Ta-0.7O alloy is depicted, being at the same location as the oxygen-free Ti–35Nb–7Zr–6Ta in the blue diagram.

Apart from solid lines representing the equilibrium diagram, the dashed lines represent M_S temperature - the start of the martensitic transformation β → α″. Low modulus of the Ti–35Nb–7Zr–6Ta (63 GPa) alloy is caused by the partial premartensitic softening - 'proximity to the martensitic transformation' (proximity to the blue M_s line) with no concurrent formation of the ω phase. On the other hand, the elastic modulus of the Ti–35Nb–7Zr–6Ta-0.7O alloy (80 GPa) is much higher, because oxygen is a β stabilizing element with respect to β → α″ martensitic transformation (red M_S line is shifted to the left).

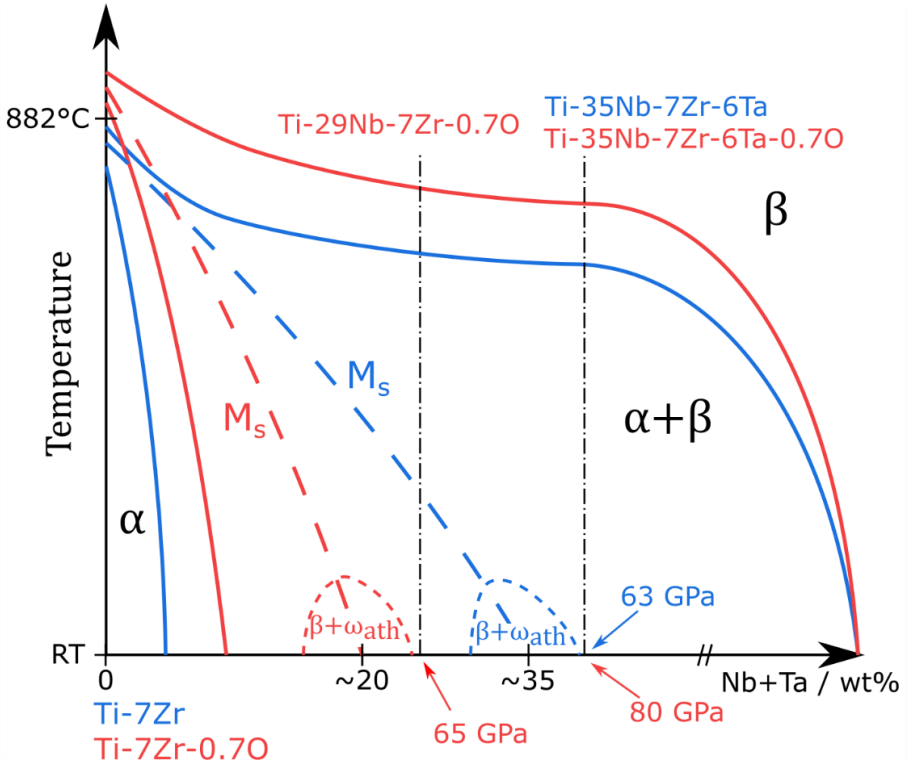

Figure 31: Schematic pseudo-binary phase diagram showing qualitatively different effects of oxygen content on the boundaries between the stable phases (solid lines) and the martensite start temperature (dashed lines). The blue and red lines correspond to the additions of β-stabilizing Nb/Ta into Ti–7Zr and Ti–7Zr-0.7O, respectively.

From the diagram, it is clear, that for the restoration of premartensitic softening causing the low Young's modulus, the alloy with 0.7% of oxygen needs to be shifted to lower contents of Nb/Ta, to a position just near the starting point of the athermal ω phase formation (in red dotted lines). Such an approach yields the favourable composition of the Ti–29Nb–7Zr-0.7O alloy having Young's modulus of 65 GPa. Similarly, the Ti-26Nb-7Zr-6Ta-0.7O also hits this "sweet spot", although it has a slightly higher Young's modulus of 67 GPa. Nonetheless, the use of Ta is not favourable, when there is a viable alternative with only 3% higher Nb content, due to its price and melting point.

The last point relevant to the applicability of the developed alloys is their ductility. It is clear when comparing the tensile curves in Figure 29 and the phase composition following from XRD measurements in Figure 26, that ductility undergoes a serious drop when the ω phase starts to appear. The ω phase is known to reduce ductility and increase hardness of the metastable β titanium alloys [168]. This was firstly evidenced for Ti-15Mo alloy after ageing at 250°C/100h (minor ductility decrease) and 350°C/16h (severe decrease of ductility leading to failure already in elastic part) [169], where the differences were caused not by a different volume fraction of the isothermal ω phase, but due to their different sizes (being larger for higher temperature). In contrast, the athermal ω phase formed during quenching from temperatures above the β-transus usually does not have a devastating influence on the alloy's ductility. This was evidenced for several binary Ti-V alloys for whose even higher content of β-stabilizing V leading to a lower content of athermal ω phase after ST decreased the ductility at the same time [170] and the alloy with the highest content of athermal ω phase was the most ductile, although this was most probably caused by activation of multiple deformation mechanisms (twinning and/or stress-induced martensitic transformation, in addition to dislocation slip). Generally, the influence of the athermal ω phase on the mechanical properties is rarely studied [171] as one cannot easily achieve both conditions with – and without the athermal ω phase – in a single alloy [172].

For alloys, containing higher amounts of oxygen, the presence of the athermal ω phase can be detrimental to ductility. In Ti-xNb-2Ta-3Zr-0.5O alloys, the ductility monotonically decreased when approaching the martensite start (by reduction of Nb content), although the ω phase was not explicitly detected [113]. In the study of oxygen content on the Ti-22.5Nb-0.7Ta-2Zr (at.%), it was found that adding up to 2 at.% of oxygen gradually decreases the ductility to very low values [72]. Unfortunately, the phase composition was not studied. In the case of the present thesis (and the related published paper [173]), it was found out that when the athermal ω phase starts to form in an alloy with high O content of about 0.7 wt%, ductility starts to decrease. For example, the two alloys, that were studied by TEM, Ti-26Nb-7Zr-6Ta-0.7O and Ti-26Nb-7Zr-0.9O, there was not a big difference in their XRD measurements, although, for Ti-26Nb-7Zr-0.9O, a very small and wide ω phase reflections started to appear. In the diffraction pattern by TEM, the diffuse scattering in place of ω reflections suggested the collapse of $(111)_\beta$ planes was not complete, while there were clear ω diffraction spots for the other alloy.

As a result, ω-free alloy had ductility similar to alloys with higher content of Nb while for an alloy with ω phase present, a significant ductility drop occurred, which could have been even amplified by the higher O content of this alloy (0.9 wt%). It was measured by atom-probe tomography (APT) in [174] that the isothermal ω phase is enriched in O content. This enrichment is the strongest at the β/ω boundary [175]. It is thus possible, that for low-oxygen alloys, when the athermal ω phase is formed during quenching, there is not enough of the available oxygen to make any difference in mechanical response, while for high-oxygen alloys, when athermal ω forms, it can consume a lot of O atoms as there is plenty in the matrix. Note that the size of the athermal ω phase is a few nm only [176], so even the limited diffusion length of oxygen during quenching or during subsequent natural ageing at an ambient temperature of the laboratory can have such an effect. In the low-oxygen alloys, during ageing, the ω phase consumes the rest of the oxygen and becomes brittle. In high-oxygen alloys, ageing is not needed, and brittleness is present already in the ST condition.

To put the mechanical properties, achieved in the developed alloys, to a broader context, Figure 32 was constructed with the data for the alloys studied in this thesis (ductility is restricted to a minimum of 10%) and data from various previous studies (papers and patents). The graph shows Young's moduli as a function of yield tensile stress, bigger points mark the alloys from this thesis. Comparison of the achieved elastic moduli from different studies is not straightforward. In some studies, the elastic modulus is determined from tensile tests without the proper use of extensometers, which often leads to its significant underestimation [117]. Note that the extensometer was not used for tensile testing of the alloys studied in this thesis either, however, the Young's modulus was determined independently by a very precise RUS method. Secondly, in super-elastic alloys, the average elastic modulus over the whole (non-linear) elastic deformation is often reported [67,94]. The presented comparison also does not consider the ductility of the material. Some alloys with high strength suffer from limited ductility well below 10% (sometimes only 1-2 %) [44,90]. Finally, the properties of some of the materials are achieved only after intensive cold-rolling (e.g. 90% of area reduction [177]) which limits the final size of the products, e.g. the femoral stem, discriminating their commercial use [178]. The alloys developed in this thesis have particularly high strength in comparison to most developed alloys, while some alloys (namely Ti-29Nb-7Zr-0.7O, Ti-26Nb-7Zr-6Ta-0.7O and Ti-35Nb-0.7O) also exhibit low elastic modulus and sufficient ductility.

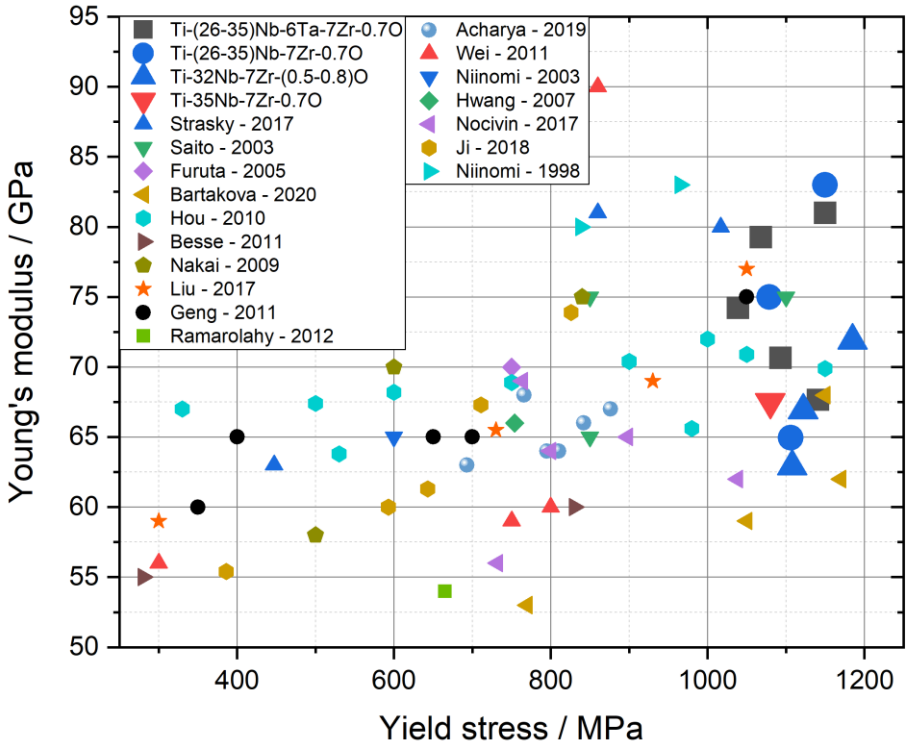

Figure 32: Comparison of achieved Young's modulus and yield stress combinations (only alloys with ductility of at least 10% are shown) with other studies on metastable β-Ti alloys (alloys with any ductility are shown) [13,40,67,71,72,74,75,90,92,93,112,114,117,160,179–181].

These properties were achieved by simple alloying without any subsequent special treatments. Cold-swaging, followed by recrystallization annealing, was used only as a convenient way to refine the casting microstructure [182]. During cold-swaging, no oxygen intake could happen, but the diameter of the final swaged rods

was low (about 4.5 – 5 mm), so the following heat treatment was performed in a protective atmosphere/vacuum to prevent oxidation of inner part of material which could affect the measured properties (mainly tensile and elastic properties). Since a full recrystallization was achieved during the last β solution treatment, any special effects connected with cold working should not affect the final properties. Conventional techniques such as hot-rolling or die-forging lead to similar properties as was shown previously for Ti-35Nb-7Zr-6Ta-0.7O [143]. For the same alloy, the processing route described in Chapter 4 leads also to the fulfilment of the fatigue requirements for a stem – a load-bearing part of the total hip endoprosthesis.

6. High-throughput characterization of layered Ti-Nb based alloys

A total of 17 Ti alloys were studied in the previous chapter, with the composition varying in the content of Nb, Zr, Ta and O. Several candidates with a good combination of high yield strength, high ductility and minimized Young's modulus were identified. However, such a classical approach consumes a lot of time, effort and resources. In this chapter, the so-called high throughput methods were used for studying a wider range of Ti-Nb-based alloys. Alloys were prepared by the layering of powders consolidated by the field-assisted sintering technique (FAST). While the elastic behaviour was also partly in the scope, another aim was to study alloys that can undergo either martensitic transformation upon loading (stress-induced martensite – SIM) or deformation twinning. The perspective of such alloys would be a potential ductility improvement by TRIP and/or TWIP effects.

6.1. Preparation of layered samples

The method of preparation of graded / layered samples was described in section 3.3. The list of prepared samples is shown in Table 4. The selection of alloys followed the studied compositions from the previous chapter. First, a range of samples with various amounts of oxygen was prepared while keeping a content of 7 wt% Zr. Note that Nb content is varied among layers within each of the samples. The sample with the lowest O content (sample 6) was achieved without any addition of TiO_2. The resulting O content was still larger (0.23 wt%) than in commercially used alloys (usually below 0.2 wt%) due to the impurity in powders, mainly in Nb powder (cf. Table 2). Lower values could be achieved by using e.g. spherical Nb powder. The content of Nb was adjusted for samples 1 – 4 to achieve a similar matrix stability (governing the elastic behaviour as well as other properties), for every roughly 0.2 wt% O, the range of prepared Nb concentration was decreased by 3 wt%. However, this has proved to be too pronounced change in Nb content – a large portion of alloys contained α″ martensite already after quenching. Based on these results, for samples 5 and 6 with lower O content (that were designed and prepared later), the Nb concentration range was kept the same as for sample 1 with 0.5 wt% O. In the rest of the samples (samples 7 – 10), the O content was fixed on a value of 0.5 wt% and the content of Zr was varied and/or 2 wt% of Fe was added while shifting the Nb content accordingly.

While most of the alloys were characterized using SEM imaging, other techniques were used only for selected samples. In samples 1-4, the elastic properties and precise phase content were thoroughly studied (this research has been published recently in the Journal of Alloys and Compounds [138]). The compression testing accompanied by DIC measurements and acoustic emission measurements was performed on samples 5 – 10 and partially on samples 1 – 3 (by testing only those layers with β microstructure present after quenching).

Table 4: Samples prepared by FAST: nominal composition, measured O/N content.

	Composition (wt%)	Ti	Nb range (wt%)	Nb step (wt%)	Zr (wt%)	Fe (wt%)	O (wt%)	N (wt%)
Sample 1	Ti-xNb-7Zr-0.5O	bal.	20 – 35	3	7	-	0.49(1)	0.033(2)
Sample 2	Ti-xNb-7Zr-0.7O	bal.	17 – 32	3	7	-	0.68(1)	0.030(1)
Sample 3	Ti-xNb-7Zr-0.85O	bal.	14 – 29	3	7	-	0.84(1)	0.029(2)
Sample 4	Ti-xNb-7Zr-1.01O	bal.	11 – 26	3	7	-	1.01(2)	0.029(2)
Sample 5	Ti-xNb-7Zr-0.3O	bal.	20 – 35	3	7	-	0.30(1)	0.030(1)
Sample 6	Ti-xNb-7Zr-0.2O	bal.	20 – 35	3	7	-	0.23(1)	0.029(3)
Sample 7	Ti-xNb-3Zr-0.5O	bal.	26 – 41	3	3	-	0.55(4)	0.039(3)
Sample 8	Ti-xNb-0.5O	bal.	26 – 41	3	-	-	0.50(1)	0.035(2)
Sample 9	Ti-xNb-7Zr-2Fe-0.5O	bal.	11 – 26	3	7	2	0.49(2)	0.029(2)
Sample 10	Ti-xNb-2Fe-0.5O	bal.	11 – 26	3	-	2	0.47(1)	0.029(1)

As a by-product of the measurement of elastic moduli by RUS, the density of measured alloys was determined by weighting the RUS samples and measuring their dimensions. As shown in Figure 33, all materials exhibited a systematic increase in density with the increasing niobium content; the effect of oxygen ($\lesssim$ 1 wt%) was below the accuracy of the used method for density determination (± 0.05 g.cm^{-3}). Similarly, the measured densities did not differ from the general linear trend (the dashed line in Figure 33) by more than this estimated experimental error, which confirms full compaction of the prepared materials.

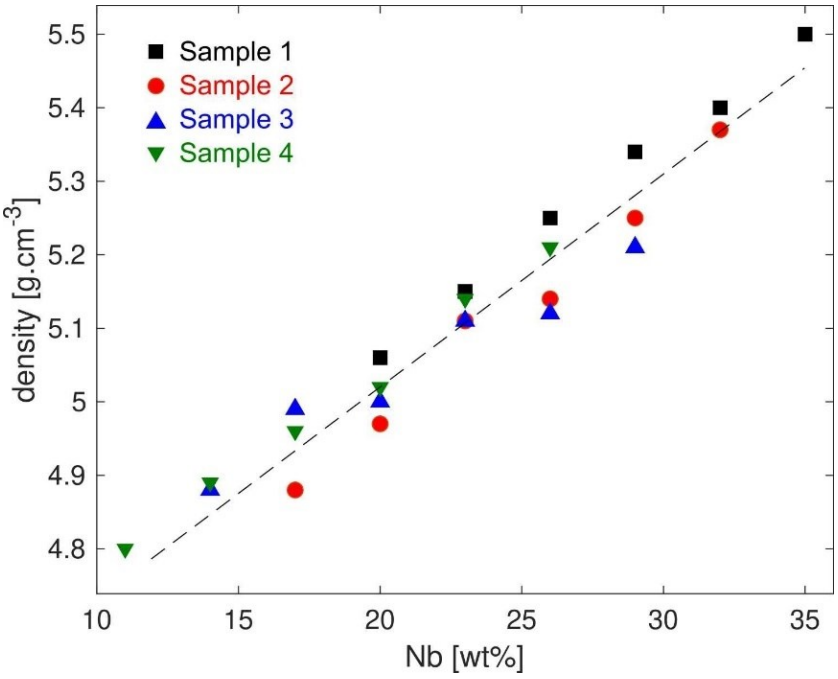

Figure 33: Evolution of the mass density of the examined alloys with the niobium content. The dashed line outlines the general linear trend obtained by linear regression.

6.2. High-throughput characterization of phase composition and elastic moduli

6.2.1. Chemical homogeneity, microstructure, phase composition

In all samples, a good chemical homogeneity within the individual layers was achieved as demonstrated in Figure 34. No undissolved powder particles can be seen. As expected, the material is coarse-grained with a grain size of several hundreds of μm, which is caused by the high sintering temperature, necessary for homogenization. The porosity as it is known from the usual FAST sample preparation from pre-alloyed powders using comparatively lower temperatures [183] was not observed and the material was well compacted as already suggested by density measurements. However, in a few areas, randomly and sparsely distributed in the sample, there are groups of spherical pores as shown in BSE and SE images in Figure 34 b,c. A possible reason for the presence of these pores is that they could be Kirkendall porosity [184] created during the homogenization stage of sintering. Probably, the diffusion of Nb particles into the matrix was faster than the diffusion of the elements that were already in the matrix (Ti, Zr, O) into the Nb particles, leaving small pores in the areas of former Nb particles.

The chemical homogeneity of the individual layers was verified using EDS mapping and line scans. In summary, the local homogenization of material sintered from blended elemental powder was successful as well as maintaining the macroscopic layered structure with varying Nb content. Line scan near the surface is shown in Figure 35a, and other line scans over representative selected layer interfaces are shown in Figure 35b. Zr and Nb contents are simultaneously shown. It was confirmed that, in agreement with the intended design, the Zr content is perfectly homogeneous over the interfaces. Step-like increase in Nb content is not sharp, but gradual within an approximately ± 0.2 mm thin region surrounding the interface. When the samples for RUS were prepared, the ± 0.3 mm regions around the interfaces were removed, which means that the RUS measurements (which are, in principle, insensitive to small gradients of elastic constants [185]) were representative of homogeneous compositions. For high-throughput compression testing, the interface widths were neglected during the DIC analysis as the interface regions represents only about 10% of the total sample height. On the other hand, due to W diffusion into the sample surface, the outer layer boundaries were cropped out for DIC analysis to eliminate errors.

XRD patterns for each layer of sintered samples no. 1 - 6 are shown in Figure 36. Independently of the oxygen content, in all alloys containing 20 wt% Nb and less, martensite phases prevail. In the samples with the least amount of oxygen (Samples 5 and 6 with 0.30 and 0.23 % O, respectively) the prevailing martensite is present up to the Nb content of 23%.

The least β-stabilized alloy (11 wt% Nb) exhibits the hexagonal close-packed structure, implying that the martensite formed in these alloys is of the α′ type. Note that the α′ martensite cannot be easily distinguished from the stable α phase, as both phases have the same hexagonal structure. But, since the material has been produced by rapid quenching, the martensitic α′ formation can be expected.

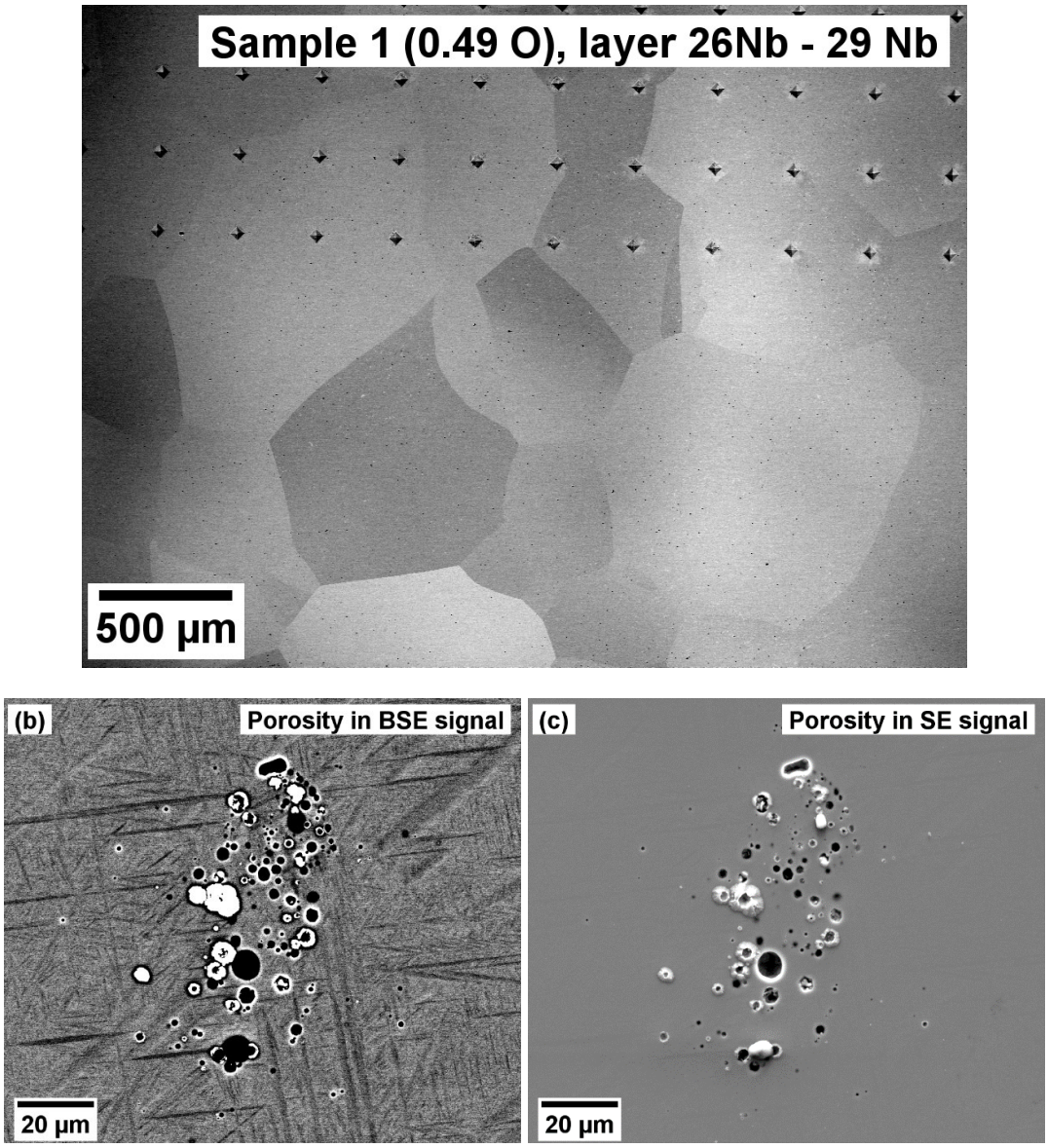

Figure 34: a) BSE image of Sample 1 (0.5% O). Layer with 26 % Nb on the left/centre and layer with 29 % Nb on the right (slightly brighter). In the upper part of the image, microhardness indents are observed. b) Kirkendall porosity in BSE image and c) SE image.

In alloys with 14 wt% Nb and 17 wt% Nb, the dominant phase was identified as orthorhombic α'' martensite. The diffraction 2θ patterns were nearly identical as for the α′ phase, but there were several indications that the hcp symmetry was broken, as illustrated for two alloys with 1.01 wt% O in Figure 37. Most importantly, a (131) peak at approximately 29.3° was found for 14 wt% Nb, which is a forbidden reflection for the structure. Also, the presence of the orthorhombic structure could be deduced from the asymmetrization and shift of the peak at approximately 27.7°. Another effect connected to the intermediate nature of the α'' phase can be seen in Figure 36 from two peaks (200) and (130) that are in Ti-20Nb-7Zr-1.01O located at about 23° and 26°, respectively. These peaks are approaching each other as the orthorhombic structure converges to the hcp structure (the α′ phase) with decreasing Nb content. Not only that these effects make distinguishing between the α′ and α'' structures based on the XRD data difficult and challenging; but they also indicate a strong dependence of the lattice

structure and the lattice parameters on the chemical composition, which might have unexpected effects on the elastic constants.

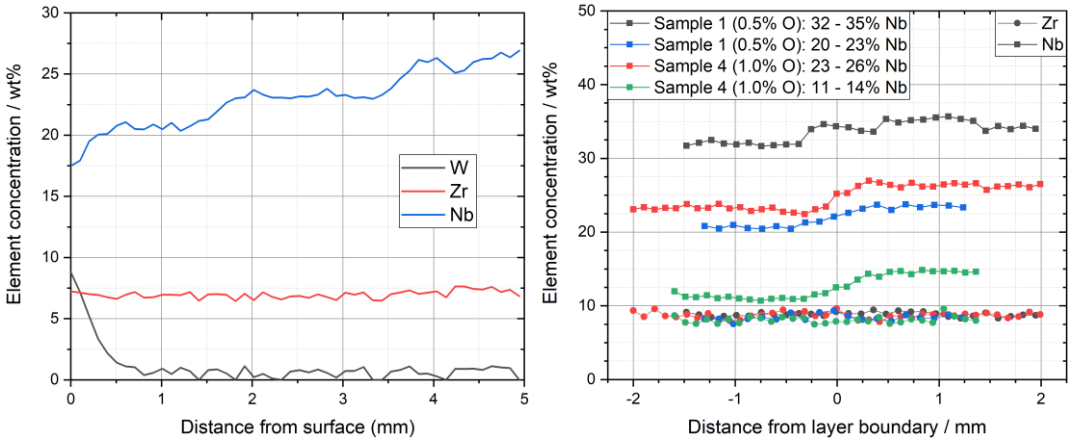

Figure 35: a) EDS line scans near the surface of a sintered sample. The steps in Nb content can be recognized going from 20% through 23% to 26%. Contamination from W foil was measured at the surface down to a depth of about 0.5 mm. b) Representative EDS line scans across the boundaries of selected layers. Notice that the Zr-content lines appear to be approximately 2 wt% higher than the nominal content, which is a quantitative error of standard-less EDS analysis, resulting in this particular case from the overlapping of the Nb and Zr peaks. However, the perfect spatial homogeneity in the Zr content is seen.

In alloys with 23 wt% of Nb and more, the β phase prevails for samples with O content higher than 0.5% while for lower O contents, the β phase starts to prevail at the content of 26% Nb and more. Small peaks corresponding to the α'' martensite in β matrix can be found in alloys Ti-23Nb-7Zr-0.49O and Ti-26Nb-7Zr-0.23O. Furthermore, in alloys with β phase composition that is close to the martensite start composition, the ω phase reflections are observed. The compositional range (in Nb content) of ω phase presence differs with the content of oxygen: e.g. the lowest amounts of oxygen (0.23O) cause the detectable presence of ω phase in three layers (26Nb, 29Nb, 32Nb) while with the highest amount of oxygen (1.01O), ω can be detected in one layer only (26Nb). This is in agreement with the previously discovered property of oxygen as an inhibitor of the ω phase. The nanometer size of the ω phase particles and incomplete collapse make their detection by XRD difficult. Quite often, reliable detection is possible only at very low temperatures [186], or for alloys with composition very close to the stability limit of the β phase, where the $\beta \rightarrow \omega$ lattice collapse is more complete [148]. As can be noticed in Figure 36, the peaks corresponding to the ω phase only are much wider than those of the β phase. As a result, when the volume fraction of the ω phase is too low and/or the size of ω particles is too small, the corresponding peaks become very wide and weak and unrecognizable against the background noise. For this reason, the identification of the presence of the ω particles based solely on XRD diffraction patterns cannot be understood as comprehensive, and therefore it was further completed based on the results of TEM observations.

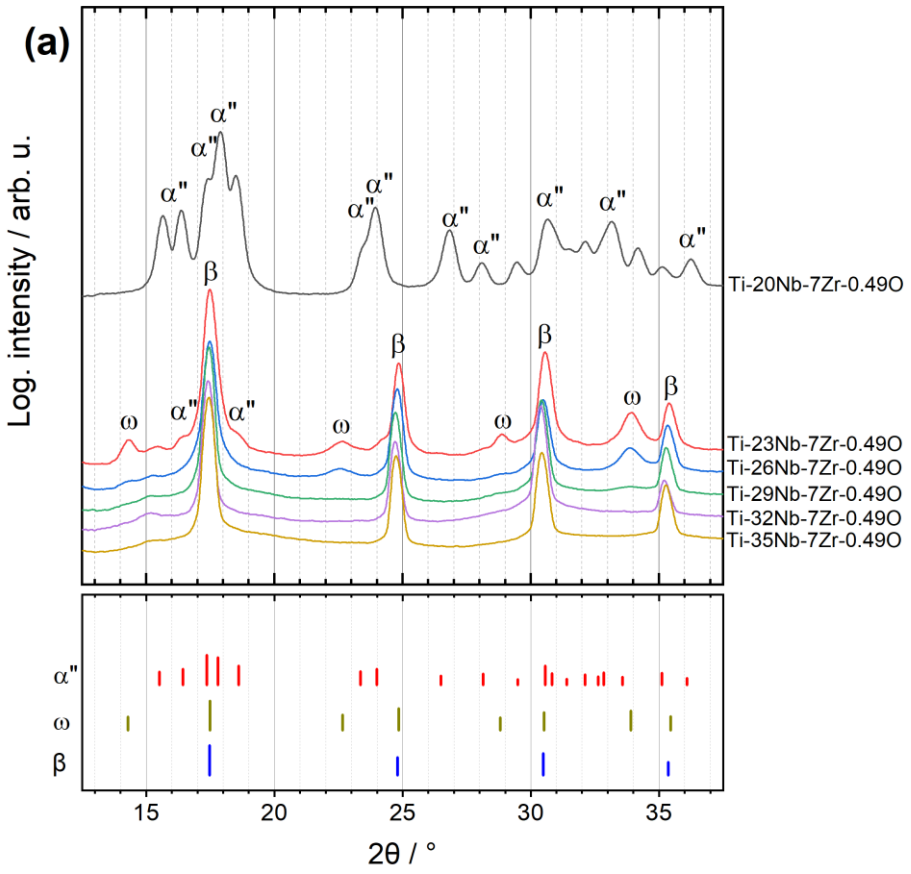
(a)
Log. intensity / arb. u.
α"
β
ω
Ti-20Nb-7Zr-0.49O
Ti-23Nb-7Zr-0.49O
Ti-26Nb-7Zr-0.49O
Ti-29Nb-7Zr-0.49O
Ti-32Nb-7Zr-0.49O
Ti-35Nb-7Zr-0.49O
15
20
25
30
35
2θ / °

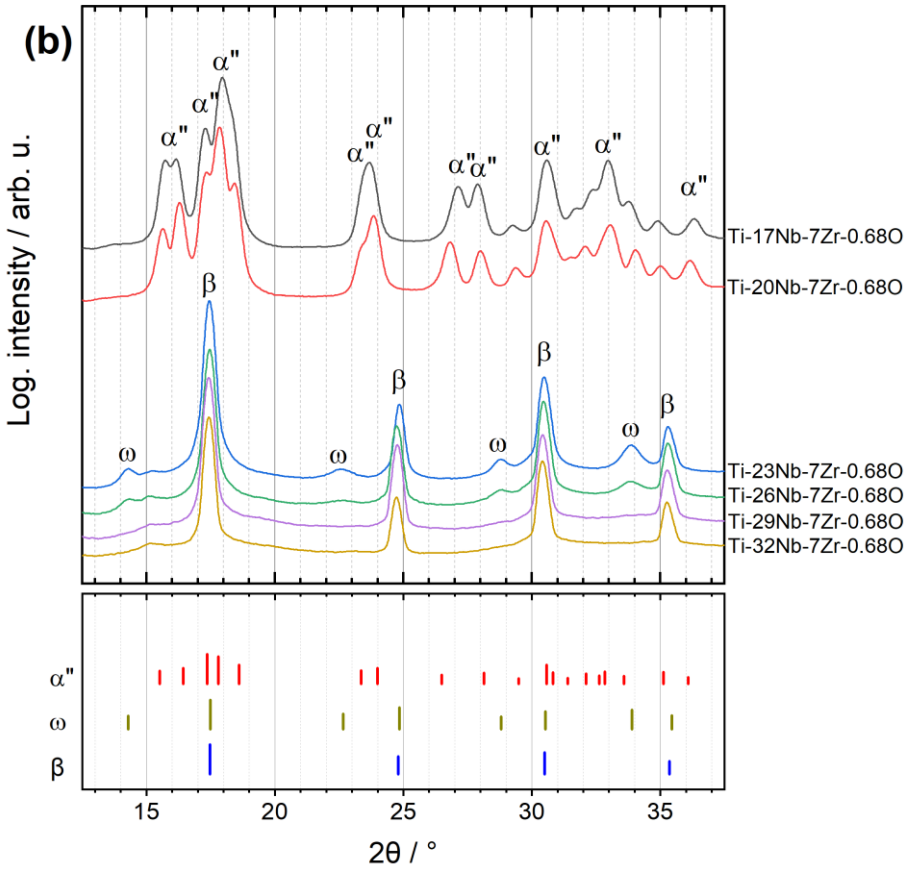
(b)
Log. intensity / arb. u.
α"
β
ω
Ti-17Nb-7Zr-0.68O
Ti-20Nb-7Zr-0.68O
Ti-23Nb-7Zr-0.68O
Ti-26Nb-7Zr-0.68O
Ti-29Nb-7Zr-0.68O
Ti-32Nb-7Zr-0.68O
15
20
25
30
35
2θ / °

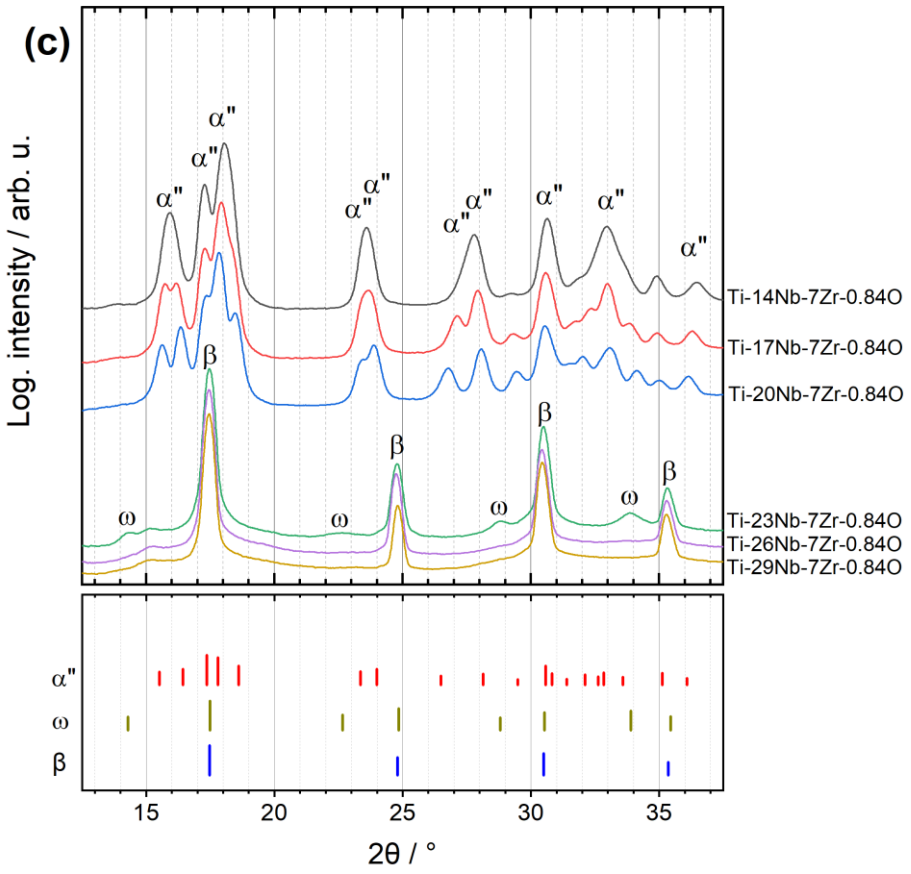
(c)
Log. intensity / arb. u.
α"
β
ω
Ti-14Nb-7Zr-0.84O
Ti-17Nb-7Zr-0.84O
Ti-20Nb-7Zr-0.84O
Ti-23Nb-7Zr-0.84O
Ti-26Nb-7Zr-0.84O
Ti-29Nb-7Zr-0.84O
15
20
25
30
35
2θ / °

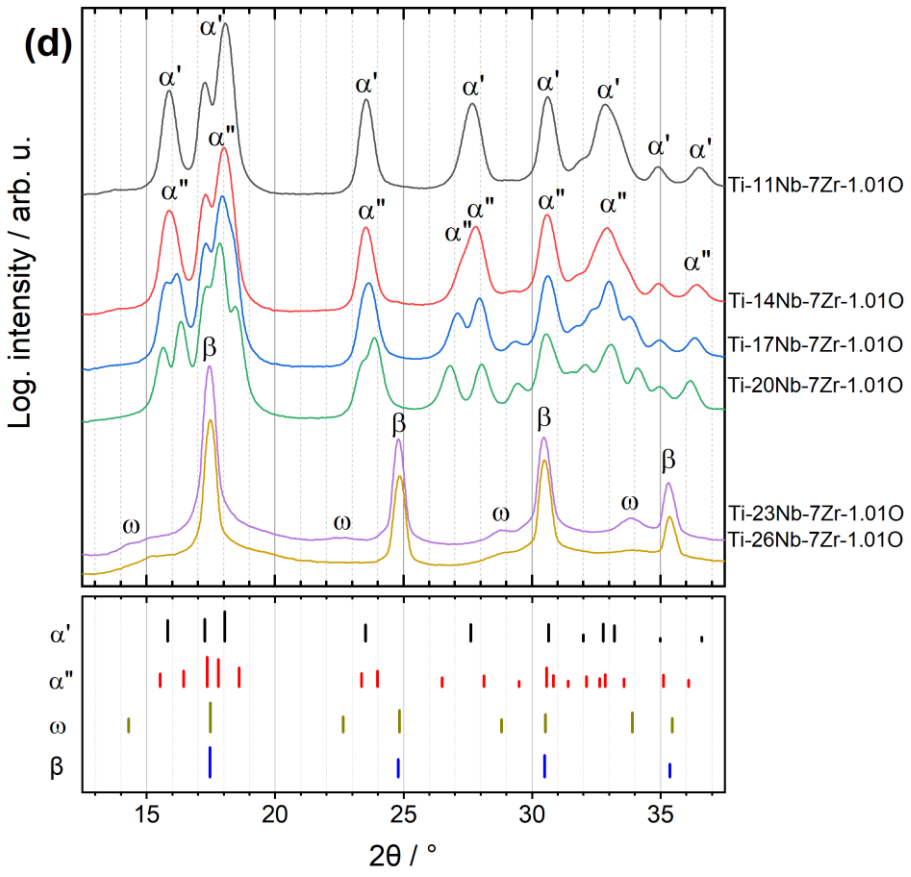
(d)
Log. intensity / arb. u.
α'
α"
β
ω
Ti-11Nb-7Zr-1.01O
Ti-14Nb-7Zr-1.01O
Ti-17Nb-7Zr-1.01O
Ti-20Nb-7Zr-1.01O
Ti-23Nb-7Zr-1.01O
Ti-26Nb-7Zr-1.01O
15
20
25
30
35
2θ / °

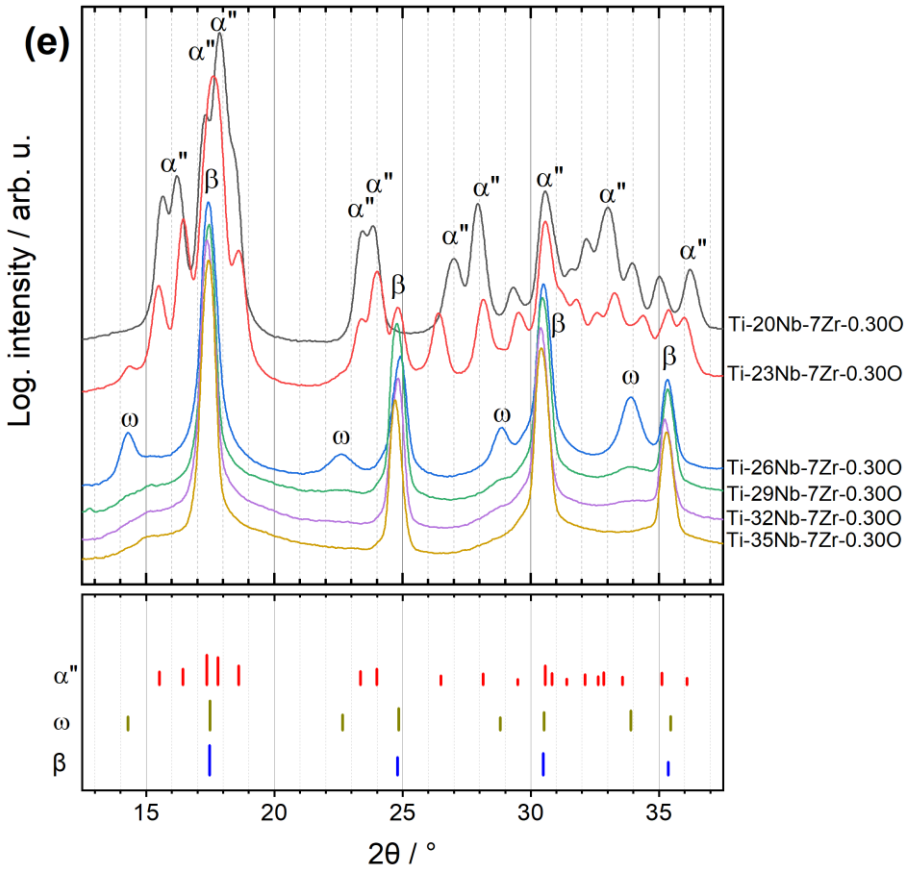
(e)
Log. intensity / arb. u.
α"
β
ω
Ti-20Nb-7Zr-0.30O
Ti-23Nb-7Zr-0.30O
Ti-26Nb-7Zr-0.30O
Ti-29Nb-7Zr-0.30O
Ti-32Nb-7Zr-0.30O
Ti-35Nb-7Zr-0.30O
15
20
25
30
35
2θ / °

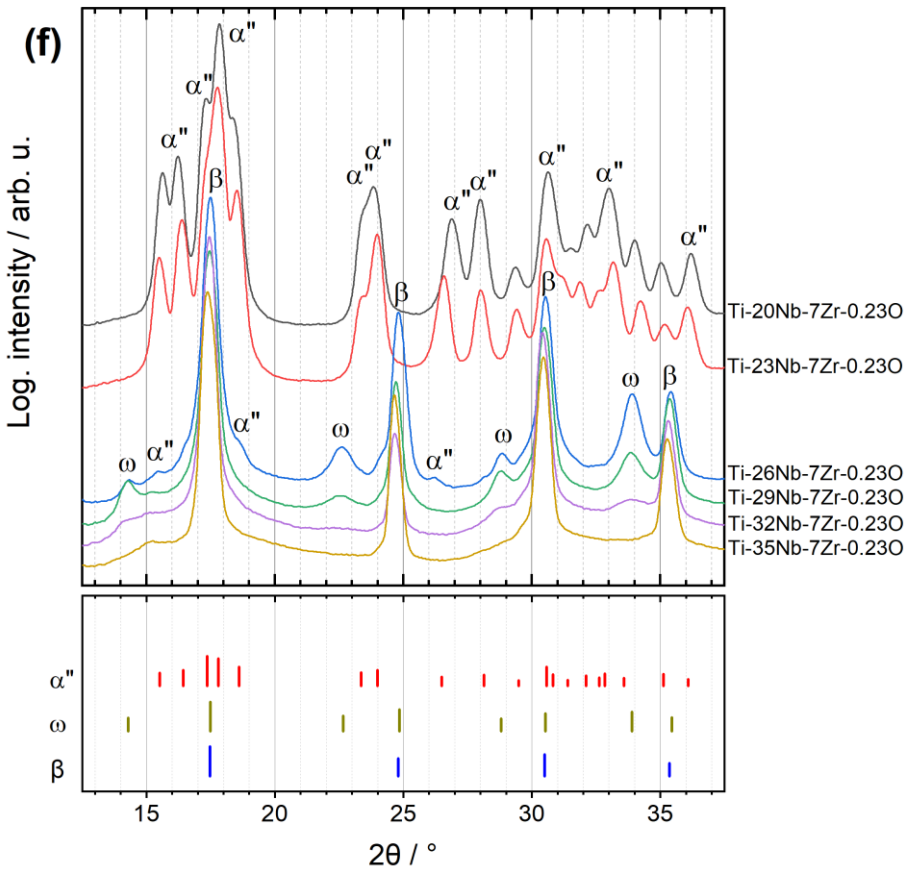
(f)
Log. intensity / arb. u.
α"
β
ω
Ti-20Nb-7Zr-0.23O
Ti-23Nb-7Zr-0.23O
Ti-26Nb-7Zr-0.23O
Ti-29Nb-7Zr-0.23O
Ti-32Nb-7Zr-0.23O
Ti-35Nb-7Zr-0.23O
15
20
25
30
35
2θ / °

Figure 36: XRD measurements on each of the layers in the sintered samples. For each sample, the patterns are shown in groups with respect to the prevailing phase – β, α″ and α′. The theoretical fitted positions are shown as lines in bottom parts of each image and the line lengths reflect the relative intensities. Note that for different alloy compositions, the lattice parameters slightly vary, therefore the positions do not fit exactly every measured pattern; quantitative evaluation of the volume fraction of individual phases is not possible due to peak overlapping [30].

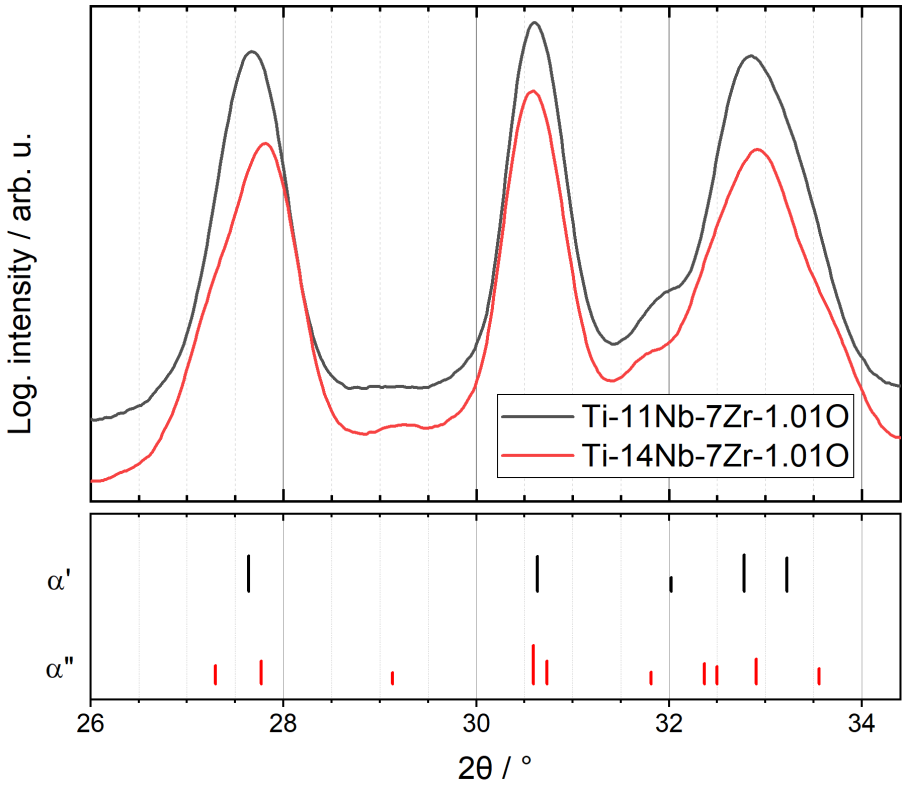

Figure 37: A 26° < 2θ < 34. 5° detail of XRD patterns for selected alloys from Sample 4, showing the deviations of the diffraction peaks for the Ti-14Nb-7Zr-1.01O alloy from the theoretical (hcp) pattern.

Two FIB lamellae were prepared from two layers (compositions) of Sample 1 (0.5O). The first one was from the composition Ti-26Nb-7Zr-0.49O for which XRD has undoubtedly detected the presence of the ω phase. The second one was from the layer of Ti-32Nb-7Zr-0.49O in which there is no evidence of ω phase in XRD patterns. However, the ω phase was found in both prepared lamellae. It was identified from the TEM diffraction pattern as extra spots (yellow circles in Figure 38 a,c) and also using dark-field (DF) imaging (Figure 38 b,d). Nevertheless, there are significant differences between the phase compositions in terms of ω phase reflections, namely Ti-32Nb-7Zr-0.49O shows much weaker intensities of the ω reflections. By comparing the intensities of the ω phase with the reflections of the β phase, it was found that there is about 4 times lower volume fraction of the ω phase in Ti-32Nb-7Zr-0.49O compared with Ti-26Nb-7Zr-0.49O (in the first approximation, the dependence of volume fraction on the diffracted intensity is linear). The differences observed are confirmed also in the dark-field images. Because the used FIB lamellae had approximately the same thickness and the tilt of the sample during TEM observations was also comparable, the DF images in Figure 38 b,d enable a direct visual comparison of volume fractions and particle sizes in both alloys.

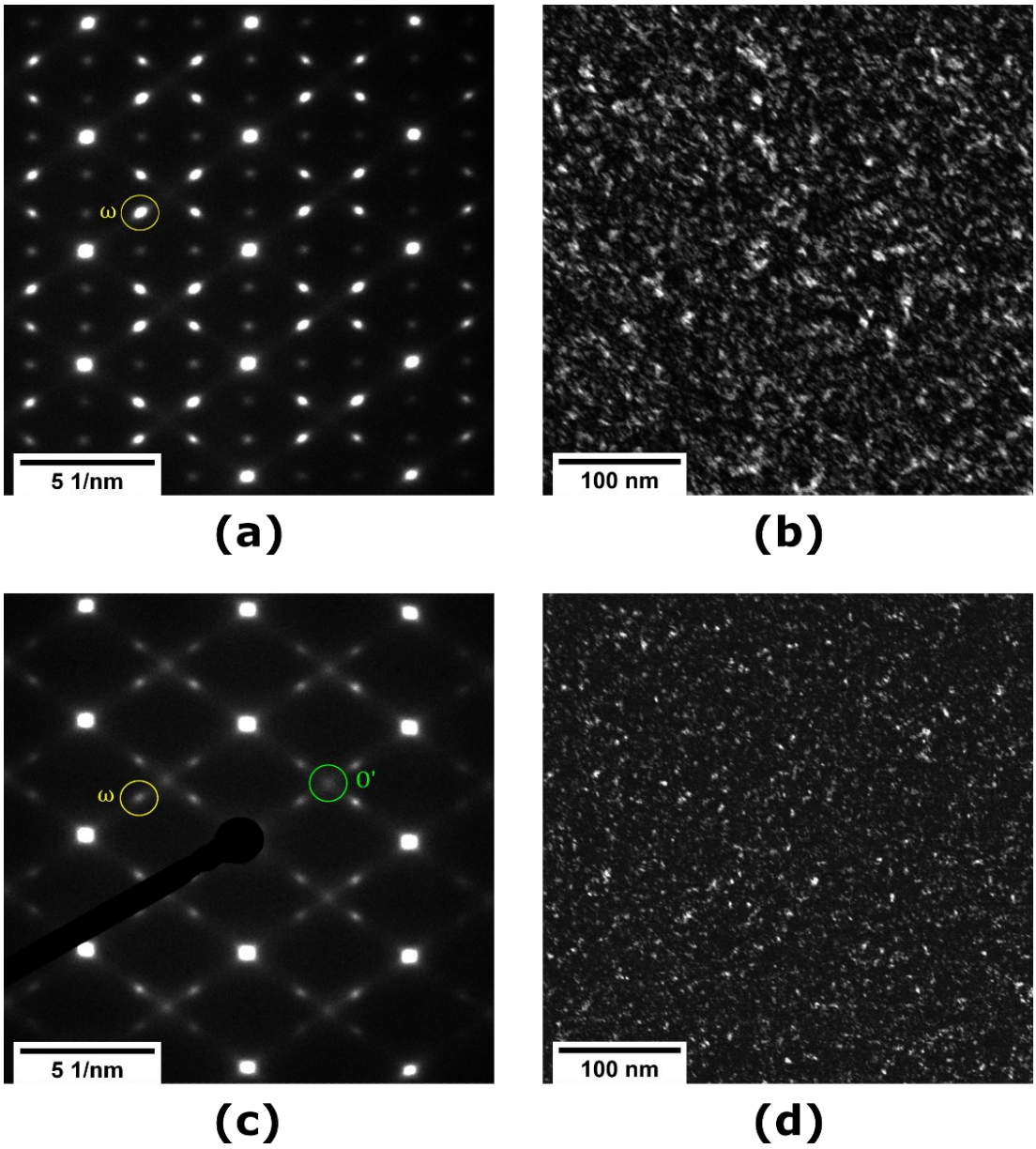

Figure 38: TEM diffraction patterns from two layers from Sample 1 with different Nb compositions, and corresponding dark-field micrographs of the ω phase: (a), (b) Ti-26Nb-7Zr-0.49O, (c), (d) Ti-32Nb-7Zr-0.49O. Yellow circles mark the ω reflections and green circles in Ti-32Nb-7Zr-0.49O correspond to O' nanodomains. Additional weak reflections in Ti-26Nb-7Zr-0.49O correspond to double diffraction of the ω phase due to its large volume fraction.

In Ti-32Nb-7Zr-0.49O, the ω phase could not be detected by XRD measurements. This can be attributed to its lower volume fraction, but more importantly also to the significantly smaller size of the particles. Small ω phase particles may also not be fully collapsed [148], which restricts their detection by a common powder XRD. It is worth mentioning, that the diffraction pattern of Ti-32Nb-7Zr-0.49O alloy (Figure 38c) shows also very weak diffraction spots (the green circle) that can be attributed to the O′ phase [28]. This phase is, in fact, a nano-domain of the martensitic α'' phase, appearing when solute atoms prevent the formation of massive α'' laths [153]. The presence of this phase may bring additional complexity to the

relationships between the chemical composition, phase composition, and macro-scale mechanical behaviour.

The microstructure of all layers in each sample was observed by SEM. Selected SEM images are shown in Figure 39. In the alloys with Nb content of 20 wt% and lower, the lamellae of orthorhombic α'' / hcp α′ martensite can be observed. The alloy with the lowest Nb content of 11 wt% contained also a minor fraction of the α phase, preferentially along grain boundaries, clearly visible in SEM images as dark lenticular regions as shown in Figure 40. These α phase particles were most probably the results of an incomplete $\alpha \rightarrow \beta$ transition during annealing at 1000°C and were not observed for any other alloy. The α and α′ phases could not be distinguished by XRD due to equivalent symmetry, and thus, the presence of the α phase in the Ti-11Nb-7Zr-1.01O alloy was concluded just based on the SEM observations.

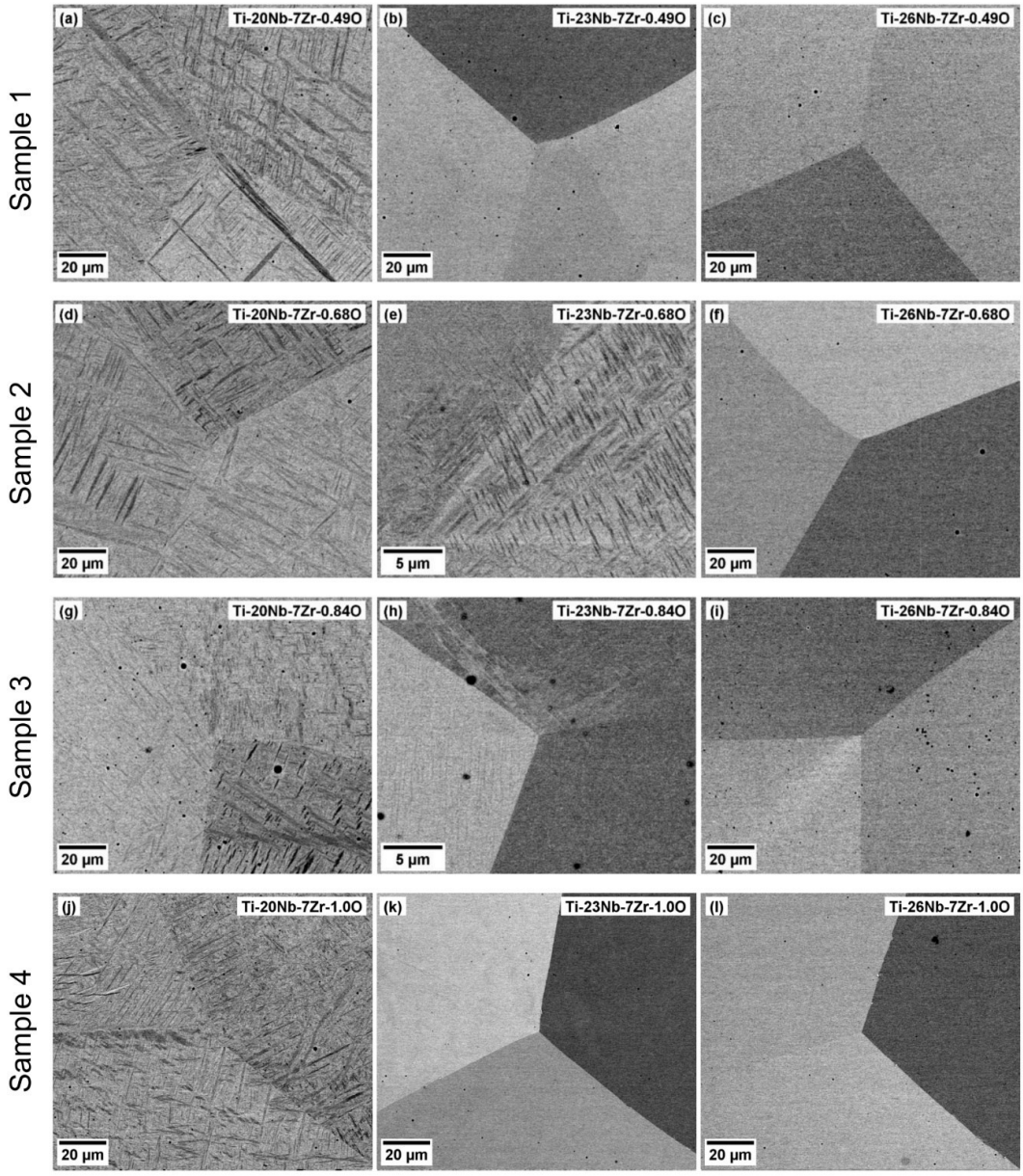

Figure 39: SEM images of selected layers from the prepared graded samples. Occasional black dots are the remnants of polishing suspension.

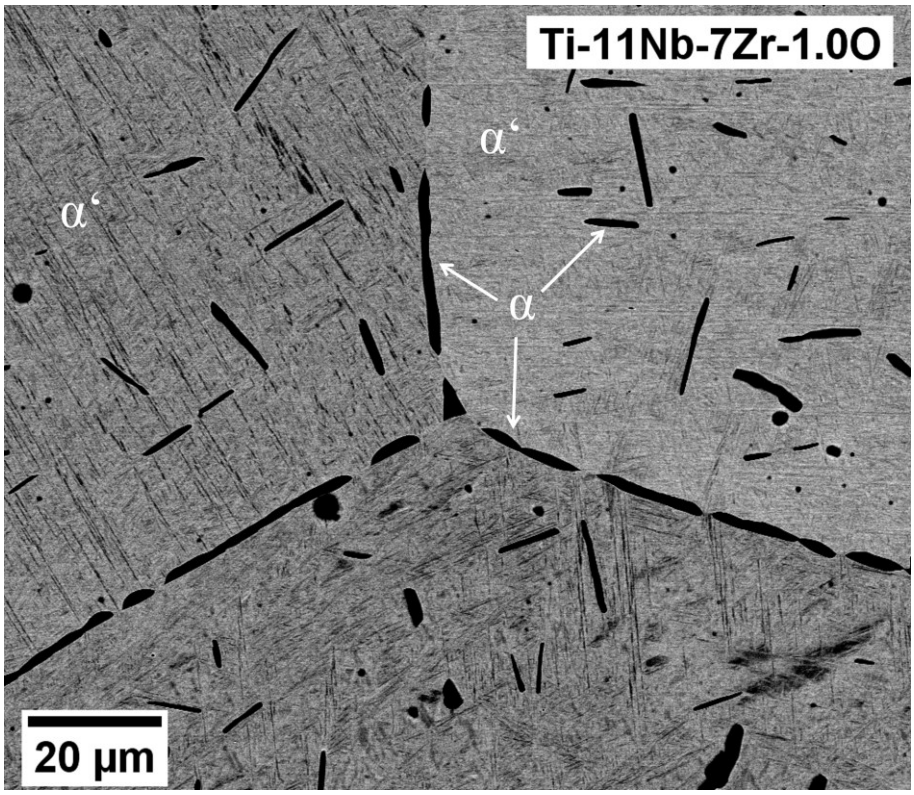

Figure 40: α phase lamellae and α phase on grain boundaries in alloy Ti-11Nb-7Zr-1.0O. The martensitic structure of the α' phase is visible as a matrix.

For the Nb content of 23 %, the β phase prevailed in alloys with an oxygen content of 0.68 % and 0.84 %, but in a few zones, very fine lamellae were visible under high magnification. However, the volume fraction is probably too low for the detection of the martensite phase by XRD. In the Ti-23Nb-7Zr-1.01O alloy and alloys with niobium content of 26 wt% and more, no particles of other phases were observed. Notice, however, that the nanoscale ω particles cannot be resolved by SEM. The SEM images for samples with the lowest content of oxygen are not shown, but their appearance followed the trend set by the XRD results, the martensitic lamellae were visible up to 23% of Nb and after that, the β phase prevailed.

By combining the results of SEM observations and XRD, the phase composition map of the studied alloys was determined and is presented in Table 5. For alloys with 20% of Nb and O content of 0.5% and more, and alloys with 23% Nb and O content of 0.3 and less, it is assumed that there is also some residual β phase between the martensitic lamellae, as the interval of coexistence of β and α'' phases reported in the literature is about 3 at%, i.e. more than 4 wt% [187]. The presence of the ω phase is deduced from the XRD data. The XRD patterns document that the amount of ω phase decreases with the increasing Nb content; e.g., the volume fraction of ω in the Ti-29Nb-7Zr-0.49O alloy is smaller than in the Ti-26Nb-7Zr-0.49O. This is consistent with the assumption that the ω formation is suppressed by the stabilization of the $\beta-$matrix [128,173]. As revealed by the TEM observations for the Ti-32Nb-7Zr-0.49O, small volume fractions of ω phase could be present also in alloys with higher content of Nb but remain undetected by XRD due to its detection limits. For alloys with 20-23 % of Nb, where the β and α'' are assumed to coexist, one can also assume that the residual β may be filled with ω particles, especially because the β phase here is the least stabilized in these alloys [128]. This will be discussed in detail based on the elasticity data in the following sections.

Table 5: Phase composition of the individual studied alloys at room temperature, as estimated by combining the SEM observations and XRD. The phases in the parentheses are those with minor volume fractions. The ω phase is listed in the table only for those compositions for which its presence is clearly indicated by XRD peaks. However, from the TEM diffraction patterns, as well as from the microhardness and elasticity results in the following sections, it is concluded that small amounts of ω particles appear in a broader compositional range, quite probably in all compositions classified here as β.

	11Nb	14Nb	17Nb	20Nb	23Nb	26Nb	29Nb	32Nb	35Nb
Sample 1 (0.49O)	-	-	-	α″ (+β)	β (+α″+ω)	β (+ω) [a)]	β (+ω)	β [b)]	β
Sample 2 (0.68O)	-	-	α″	α″ (+β)	β (+α″+ω)	β (+ω)	β	β	-
Sample 3 (0.84O)	-	α″	α″	α″ (+β)	β (+α″+ω)	β	β	-	-
Sample 4 (1.01O)	α′ (+α)	α″	α″	α″ (+β)	β (+ω)	β	-	-	-
Sample 5 (0.30O)	-	-	-	α″	α″ (+β+ω)	β (+ω)	β (+ω)	β	β
Sample 6 (0.23O)	-	-	-	α″	α″ (+β)	β (+α″+ ω)	β (+ω)	β (+ω)	β

[a)] large volume fraction of ω particles confirmed by TEM, see Figure 38 a,b; [b)] small amounts of ω particles and a possible presence of the O phase revealed by TEM, see Figure 38 c,d.

In summary, based on the XRD, TEM and SEM experiments, it can be concluded that the studied set of alloys contained a complex mixture of various phases, evolving with the contents of both Nb and O. Taking into consideration the assumed compositional dependence of the elastic constants of the individual phases as well, it is clear that one can expect also a quite non-trivial relation between the composition and the macro-scale elastic constants and other mechanical properties for the studied alloys. This further supports the use of a high-throughput approach for the measurement of elastic constants as well as mechanical properties.

6.2.2. Microhardness mapping

To achieve representative statistics of the microhardness of each alloy composition (layer), the indentation was done over a rectangular array of 7×45 indents (300 μm between indents, 7×7 indents within each of the six layers, and extra indents near the sample edges). Each seven microhardness values along the direction parallel to the layers were averaged, resulting in the profiles across the layers as shown in Figure 41 for Samples 1-4 (the horizontal axes for individual samples are shifted such that the regions with the same Nb content coincide). The obtained values of the microhardness are consistent with those reported earlier in this thesis on bulk homogeneous Ti-Nb-Zr-O materials in Figure 28 (Section 5.4), which indicates that the oxygen from the initial TiO_2 powder became fully dissolved in the FAST pellet and resulted in interstitial strengthening. This was an expected result due to the much higher diffusivity of oxygen compared to Zr, Ti, and Nb, the particles of which were also fully dissolved into the target alloys, as illustrated above by the EDS measurements.

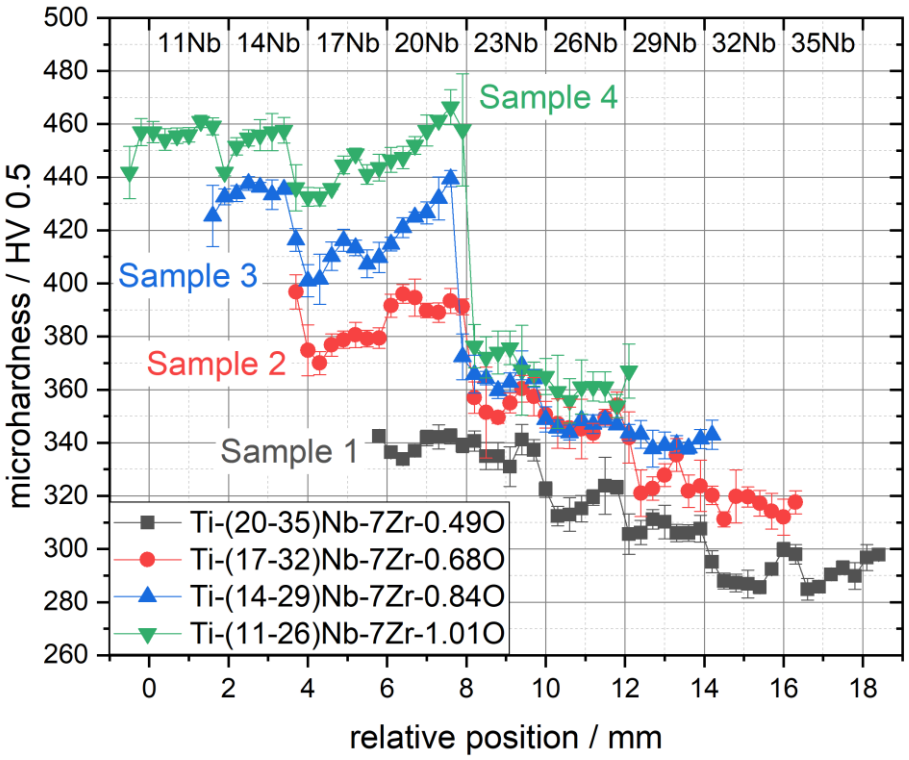

Figure 41: Microhardness profiles in the graded samples. The error bars show experimental scatters along the y − *direction; in the* x − *direction the spatial resolution is seven points per layer.*

In general, microhardness increases with increasing oxygen content for any Nb content. A distinct difference in the microhardness is seen between the alloys (layers) with α'' (or α') particles (Nb content 20 wt% and below) and alloys with dominant $\beta-$phase. The difference increases with the increasing oxygen content. This result suggests that the increasing content of interstitial oxygen atoms in the studied range of concentrations causes a more pronounced interstitial strengthening in α'/α'' than in the bcc β. It can be speculated that the significant interstitial strengthening of the β phase occurs already in range of lower oxygen concentrations due to the anisotropy of lattice distortion of the bcc material [127,128,188]. Increased interstitial strengthening of α'/α'' phases by oxygen corresponds well to the fact reported in the literature [76], that while interstitial oxygen at above 0.2 wt% reduces the ductility of the $\alpha+\beta$ alloys, it does not significantly affect the ductility of meta-stable β alloys [173]. Decreased ductility (embrittlement) is often related to a significant increase in hardness.

Microhardness profiles exhibit a gradual decrease with increasing Nb content at above 23 wt%, which is most probably due to the decreasing volume fraction of the ω phase, the content of which diminishes with increasing stabilization of the β phase. In the alloys (layers) with the lowest oxygen content, the microhardness of α'' is similar to the microhardness of the $\beta+\omega$ mixture, and therefore the otherwise significant step in the microhardness profile is not pronounced for this content of oxygen.

6.2.3. Scanning acoustic microscopy

To confirm that there is a contrast in elastic constants associated with the gradient of the Nb content in the graded samples, thin plates cut from the FAST pellets across the layers were mapped utilizing scanning acoustic microscopy (SAM, see Figure 16 for the orientation of the sample with respect to the graded pellet). Maps of the times-of-flight of focused longitudinal ultrasonic waves (TOFs) related to the

elastic stiffness of the material are shown in Figure 42. It is seen that indeed, the samples were acoustically heterogeneous, i.e., the speed of propagation of longitudinal waves through the sample varied quite significantly with the composition. Nevertheless, the interpretation of the SAM results is much less straightforward than that of the microhardness measurements. In general, the TOFs increase towards the regions with higher Nb content, as expected because the β phase is elastically softer, i.e., the waves are slower in the regions without the α'/α'' martensite phases. In most of the samples, there is a sharp jump separating the soft $\beta-$phase region to the right from the stiffer region to the left. However, the location of the jump in the TOFs does not agree with the locations of the sharp decrease in the microhardness profiles for most of the samples. Moreover, while the microhardness profile shows nearly no jump in Sample 1 with 0.49 wt% oxygen, the jump in the TOFs in this specimen is the most pronounced, and vice-versa, while the steepest jump in microhardness is observed for Sample 4 with 1.01 wt% of oxygen, the TOFs for this sample are those least heterogeneous.

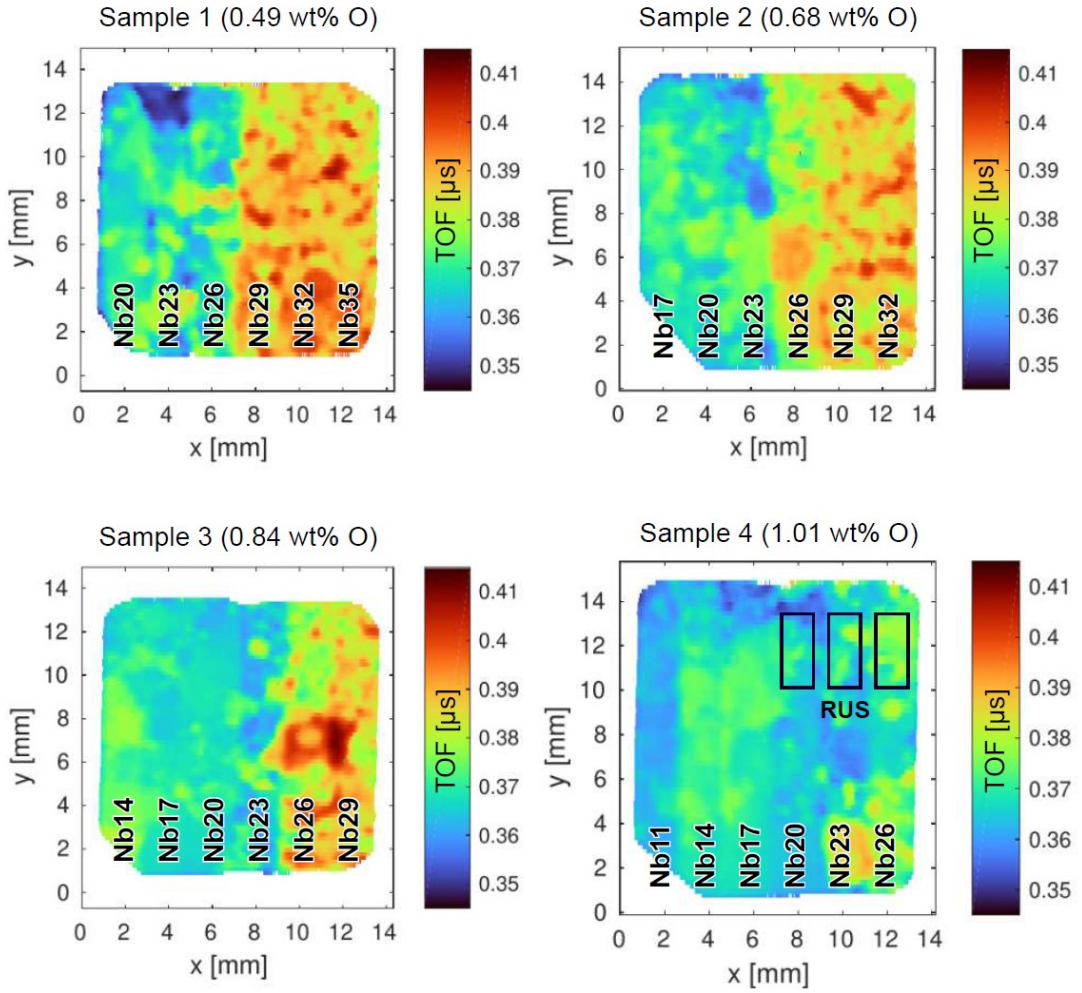

Figure 42: Scanning acoustic microscopy (SAM) maps of times-of-flight of longitudinal acoustic waves through the samples. One corner of each sample was cut out to avoid losing the reference coordinate system. For a visual comparison, the size and shape of the cuboidal samples for RUS are outlined in the map for Sample 4.

In general, SAM mapping is related to the elasticity of the material (resistance to small reversible elastic deformation) while microhardness is related to the strength

of the material (resistance to large irreversible plastic deformation). In particular, the difference is caused by the different effects of ω phase nano-particles on the elasticity and hardness of materials. While the ω phase particles formed after quenching have a limited impact on the microhardness, they significantly increase the elastic constants of the β matrix [80,107]. The region where the elastically soft behaviour of the β phase prevails is therefore shifted to higher Nb contents. The fundamental effect of the ω phase on the elastic constants will be proved in the next section based on the RUS measurements. Here, it is just pointed out that the ω phase also affects quite strongly the SAM maps. For Sample 1, for example, in the layer with the Nb content of 26 wt%, where the complete absence of α'' particles was confirmed both by SEM and from the XRD measurements, the increased speed of ultrasonic waves must be attributed to ω phase. For this sample, a sharp contrast is seen between the 26 wt% and 29 wt% layers. According to the XRD patterns in Figure 36, these two layers have the same phase composition ($\beta + \omega$), see Table 5), but the ω peaks for the 29 wt% layer are hard to distinguish from the background; ω phase particles were also observed in the layer with 32 wt% of Nb by TEM, but with significantly smaller size and lower volume fraction. This indicates that the ω phase volume fraction and/or ω particles size (or possibly the completeness of the ω collapse) is decisive for the measured TOFs, and the layers with 29 wt% Nb and more do not contain a sufficient amount of ω to significantly affect the speed of propagation of longitudinal waves.

Another important piece of information for the high-throughput characterization achieved from the SAM mapping in the context of elasticity is the heterogeneity of the elastic constants inside each layer. As seen from the maps, the variations of TOFs inside the layers are so strong that the boundaries between the layers are often hard to distinguish. The TOF contrast inside the layers originates from differently oriented anisotropic grains. This is clearly demonstrated in Figure 43 showing an EBSD IPF map next to the previously shown SAM map of Sample 1 (0.49 wt% O). By binarizing the SAM maps and analyzing them using the Image Processing Toolbox in Matlab, the average equivalent diameter (number average) of the homogeneous regions was determined as 412 μm, which is slightly lower than the mean grain size (number average) of 480 μm determined from the EBSD map. Direct one-to-one correspondence between the regions of constant TOF and the individual grains is observed only for the larger grains. As the sample was 0.8 mm thick, in some locations the waves travelled through two or more grains across the thickness, and thus, such inconsistency in the grain size might arise. On the other hand, several neighbouring grains, albeit differently oriented, might have appeared for SAM as an elastically homogeneous material, provided that their orientations differed from each other mainly by in-plane rotations preserving the out-of-plane crystallographic orientation.

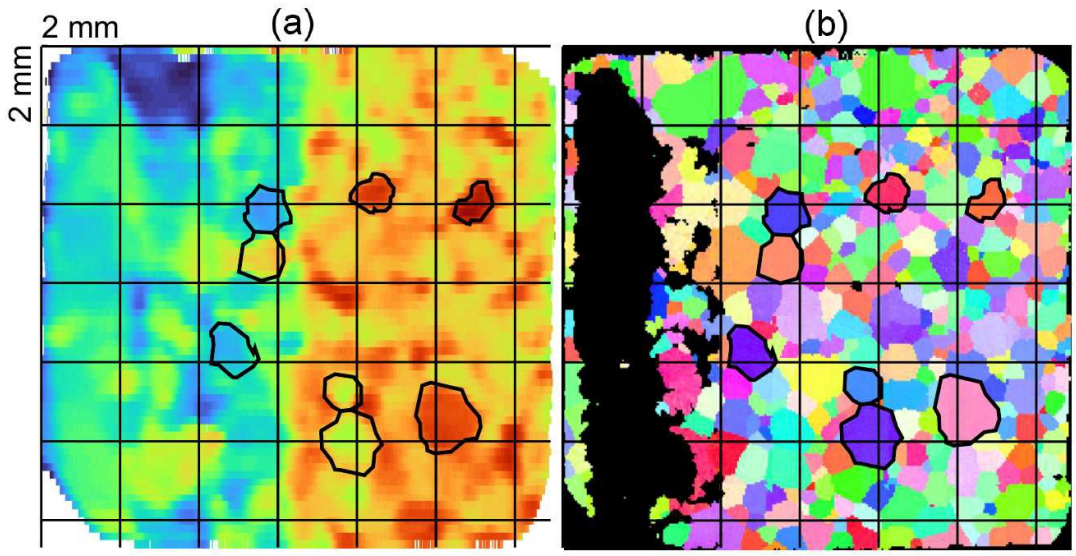

Figure 43: Comparison of (a) scanning acoustic microscopy map with (b) inverse pole figure map acquired by EBSD for Sample 1. In the EBSD measurement, only the β phase was indexed, while the α″ lamellae were too fine compared to the used step size of the EBSD map. For this reason, regions containing the α″ phase in areas with 20 % and 23 % Nb are shown in black. The 2 mm grid is a guide-for-the-eye only, enabling easier comparison of the location of individual grains. Some of the larger grains that exhibit a good one-to-one correspondence between the maps are highlighted.

6.2.4. Resonant ultrasound spectroscopy

In Figure 44, the values of G and E determined by minimization of the objective function (Equation 2) are plotted with respect to the niobium content. It is clearly seen that all materials exhibit a quite similar general trend, regardless of the oxygen content. The highest values of both G and E are achieved for the Nb content being between 20 wt% and 26 wt%. This peak is surrounded by two local minima, the deeper being in the $\beta-$ phase region (minimal values reached for 29–32 wt% Nb).

For the lowest oxygen content (Sample 1), the whole curve is slightly shifted towards higher Nb content, while for the highest oxygen content (Sample 4) an opposite effect is observed, altering significantly neither the shapes of the curves nor the values of the elastic moduli themselves. This is fully consistent with the observation documented in the previous sections that the oxygen has clear effect on the stability of the β phase, additional to the effect of Nb and it can therefore be concluded that Nb and O have qualitatively similar impacts on the elastic constants.

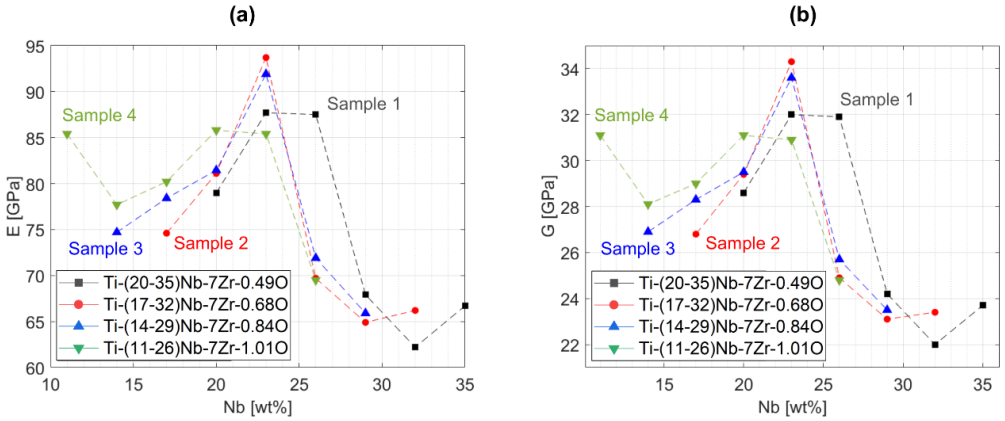

Figure 44: Room-temperature elastic moduli E *and* G *plotted as the function of the niobium content.*

It is also worth noting that the Nb-content dependencies for all materials are nearly identical for G and E, except for the absolute values (E is always approximately 2.7 times higher than G). The Young's modulus E and the shear elastic modulus are related through the bulk modulus K as

$$E = \frac{9KG}{3K+G} \qquad \text{(Equation 4)}$$

Unlike the shear modulus, the bulk modulus is only negligibly affected by the diffusionless martensitic transitions and the related phonon softening [165]. Hence, all variations in E with the chemical composition are dominantly due to variations in G. Moreover, one can assume that $3K \gg G$, and, consequently, $E \approx 3G$.

6.2.5. Discussion: relations between chemical composition, secondary phases content and elastic moduli

The elastic moduli G and E exhibit a systematic dependence on the content of β-stabilizing elements. The following discussion will further focus on the shear modulus G because this modulus is more accurately determined from the RUS measurements and has also a more clear physical relation to the lattice instability and diffusionless martensitic transitions. Also as mentioned above, when the bulk modulus K is not changing, the relation $E \approx 3G$ can be used.

The effect of both Nb and O on the lattice stability with respect to the martensitic transformation is qualitatively similar. For this reason, it can be assumed that the shear modulus G depends on an effective content of these elements,

$$c = c_{Nb} + kc_O, \qquad \text{(Equation 5)}$$

where c_{Nb} and c_O are the contents of niobium and oxygen, respectively, and k is some scalar parameter. The explicit form of the function of shear modulus on the effective content of these elements $G = G(c)$ is not known, but one can heuristically tune the parameter k to achieve the best visual agreement between the experimental data for $c_O = 0.49$ and $c_O = 1.01$ (the lowest and the highest oxygen content). This corresponds to $k \approx 5.6$ when all $G(c)$ data can be matched with accuracy better than ± 1.5 GPa by a single curve, as shown in Figure 45a. The observed behaviour resembles the theoretical dependence of E on the electron/atom ratio for binary Ti-TM alloys (where TM stands for the transition metal), as shown in the first chapter in

Figure 4 and discussed e.g. in [82] (see also the data collected in [189] for an experimental validation). The optimal value of $k \approx 5.6$ allows us to discuss how interstitial oxygen contributes to the total ratio *e/a*, i.e., to the ratio of electrons per atom that is assumed decisive for the stability of the β phase (cf. [190]). Since the ratio between molar weights of niobium and oxygen is $M_{Nb} / M_O = 5.81$, it turns out that the contributions of individual atoms of niobium and interstitial oxygen to the electron gas are equivalent or at least very similar. This would mean that the effective e/a contribution of oxygen is 5 (same as Nb), at least in the studied oxygen concentrations. Approximately the same visual agreement as seen in Figure 45a is obtained when *G* is plotted with respect to the sum of atomic % of niobium and oxygen.

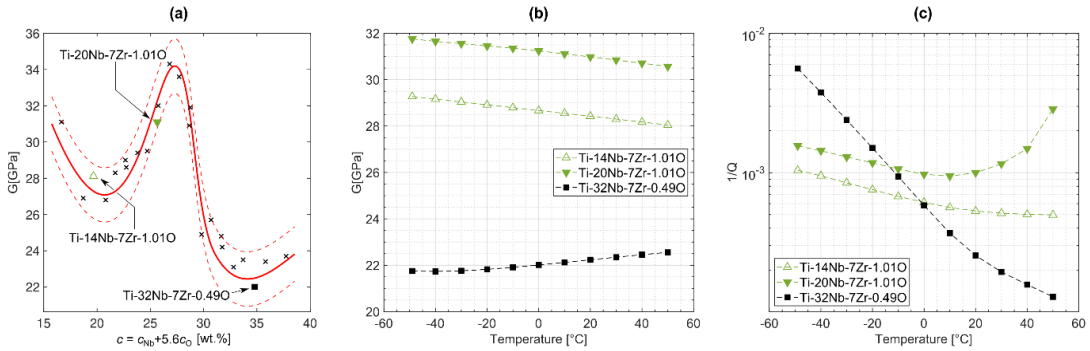

Figure 45: (a) a general behaviour of the shear modulus G *as a function of chemical composition; the thick red line is an optimum fit of the data by a five-point Bezier curve, the dashed lines delimit the ± 1.5 GPa interval; (b,c) temperature dependences of the shear modulus* G *and the internal friction parameter* Q^{-1}*, respectively, for three selected alloys.*

Outside of the plotted interval, one can expect a simple dependence of *G* on *c*: for $c < 15$ %, the quenched material contains α' martensitic phase which is further elastically stabilized (i.e., *G* increases) with decreasing *c*; for $c > 40$ %, the stability of the β phase increases with *c*, and thus, *G* increases. This behaviour is typical for two phases connected by a martensitic transition, both of them elastically softening with composition approaching the critical composition for the martensitic transformation at a given temperature. Inside of the plotted interval, $15\ \% < c < 40\ \%$, a more complex behaviour is observed. For $c \approx 28$ %, a peak in $G(c)$ appears, that cannot be explained by the properties of the α', α'' and β phases. According to the XRD analysis (Figure 36), this maximum of the peak is related to the appearance of the ω phase, which probably formed during cooling from above the β-transus temperature. Decreasing *G* with decreasing *c* ($c < 28$ %) is ascribed to the decreased volume fraction of ω phase and formation of the martensitic α'' phase [82].

Interestingly, for the concentrations between $c \approx 22$ % and $c \approx 27$ %, which mostly cover alloys with 20 wt% of niobium, the shear modulus *G* is higher than that of the pure α'' phase (around $c \approx 21$ %) and much higher than that of the β phase. These are the materials in which the XRD analysis has not confirmed the existence of the β phase, but it is assumed that there can be some residual amount of this phase. The only possible explanation for the high shear modulus is that there are the ω phase particles that make the residual β phase elastically very stiff. In this region, the β phase, if present, is even less stabilized than at the peak of $G(c)$ at $c \approx 28$ % (note that the materials were prepared by β quenching, therefore without any solute redistribution during α'' *formation*). Hence, the same heat treatment as for $c \approx 28$ % must have resulted in a higher volume fraction of the ω phase, and thus, in a more pronounced

increase of the shear modulus. The high volume of the ω particles probably also disturbs the diffraction pattern from the β phase, making it harder to detect by the XRD.

Complementary information on the phase composition in the individual alloys can be obtained by measuring the temperature dependences of the shear moduli and of the internal friction parameters Q^{-1} (see [107] for particular effects of isothermal and athermal ω particles on G and Q^{-1}). This was done for three representative compositions, marked in Figure 45a. In the first alloy (Ti-14Nb-7Zr-1.01 O) the dominant phase is α'' martensitic phase, the second alloy (Ti-20Nb-7Zr-1.01O) falls into the region with increased shear modulus but there is no direct evidence of the β phase or the ω particles from the XRD analysis. The third alloy (Ti-32Nb-7Zr-0.49O) contains mainly the β phase with strong shear instability.

The temperature evolutions of G and Q^{-1} in these three alloys in the range $[-50°C; +50°C]$ are shown in Figure 45b,c. An expected behaviour of $G(T)$ is observed for the single (or nearly single) phases: the martensitic α'' phase stiffens with decreasing temperature, while the metastable β phase softens with decreasing temperature. The internal friction coefficient steeply increases upon cooling for the meta-stable β phase, which indicates that the cooling triggers the local partial collapse of the β matrix into the athermal ω phase. It is worth noting that this behaviour of G and Q^{-1} in ultrasonic measurements, i.e., increased internal friction without increasing the shear modulus is typical for the athermal ω phase, while the fully formed ω phase (such as in the isothermal ω particles) is characterized by a strong increase in G with nearly no effect on Q^{-1} [107]. Indeed, the XRD peaks for the 23 wt% and 26 wt% indicate the presence of fully formed ω particles, and the alloys from this compositional range show stiff shear modulus but small internal friction. This observation supports the conclusions derived in section 5.7, that the oxygen causes the ω phase to behave as the isothermal type (by diffusing into it at room temperature) which is causing embrittlement of the O-rich alloy.

For the α'' phase (the Ti-14Nb-7Zr-1.01O alloy), only a mild increase of Q^{-1} with cooling is observed in Figure 45c, which may originate from the metastability of this phase and its further destabilization upon cooling. In the (Ti-20Nb-7Zr-1.01O) alloy, a combination of these two behaviours is observed. Upon heating, the internal friction steeply increases, which might be due to instability and reversible shrinking of the α'' regions, or because some of the α'' volume fraction undergoes a transition into β and the newly formed β lattice collapses and is spontaneously filled with athermal ω phase particles. The effect can be also explained by the formation of nanodomains of α'' phase described in previous reports [29], the confirmation of which would require extensive high-resolution microscopy examination. However, the shear modulus behaves monotonously in the whole temperature range, and at the highest temperature it stays still much stiffer than in the β phase or in alloys with higher content of α'' or more stabilized α'. This means that this material contains some phase that is stable in the whole temperature range and is elastically stiff and unaffected by the $\beta \leftrightarrow \alpha''$ transition itself or by the vicinity of the transition temperature. From all possible phases in the given system, only the ω phase meets all these requirements. Hence, this confirms that the ω phase is most probably responsible for the whole $G(c)$ peak, in the $22\ \% < c < 27\ \%$ composition region. We can conclude that the precipitation of this phase prevents both the β phase and the α''/α' phases to become particularly soft for compositions close to $c \approx 28\ \%$, although for this composition these stable and meta-stable phases should experience the strongest phonon softening. Instead, the lowest values of the elastic moduli are obtained at some distance from the critical composition

($c \approx 21$ % for α'' and $c \approx 35$ % for β), where the phonon softening is already significant, but the volume fraction of the ω phase particles is small. The peaks in $G(c)$ for samples with different contents of oxygen overlap quite well for correctly chosen c, as seen in Figure 45a.

6.3. High throughput compression testing

The compression testing accompanied by measurements of AE and DIC was conducted on samples 1 – 10 listed in Table 4. The testing method was thoroughly described in Section 3.1.6.

The compression of samples 1 – 4 was done in two rounds. During the first round, it was found that some of the layers cause premature cracking in brittle layers. The compression curves are shown in Figure 46a. The brittle layers coincided with those containing α″ phase after solution treatment, therefore, for the next round, smaller samples without these layers were prepared. The sample 4, containing α″ martensite in 4 out of 6 layers, was excluded from the further measurement completely. The results of DIC for this sample are shown in Figure 46b as a map of ε_{yy} strain in the Lagrangian reference frame for the last image taken before rupture. The top layers are those with the highest content of Nb, i.e. those with the β (β+ω) present after quenching. The bottom layers did not deform plastically at all (displayed in red colour). The crack (dark blue region) has appeared on the boundary between the β (β+ω) phase region and α″ phase region.

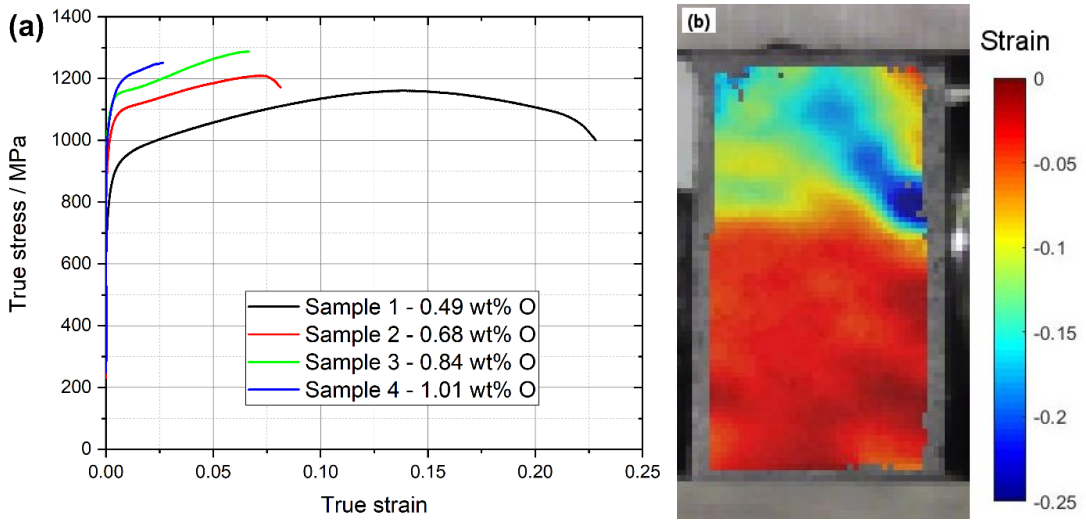

Figure 46: (a) Compression curves of samples 1-4 (1. round – whole samples), (b) ε_{yy} strain map of sample 4 just before rupture.

6.3.1. Compression testing and AE measurement

The macroscopic compression curves of the layered samples are shown in Figure 47 and Figure 48 together with the AE results. Engineering strain is used for the x-axis as it scales linearly with time, so both results of compression and AE can be shown at once. On the left y-axis, true stress is shown, which is calculated from the measured stress-strain curves. As this does not account for different deformation behaviour of each layer, it is marked as an *effective true stress*. Due to large differences in the AE response of individual samples, the amplitude of AE events (blue dots) is drawn in the $\log_{10}$ scale. In contrast, the integrated AE counts are drawn in the linear scale where the differences between the samples with the highest AE activity can be seen.

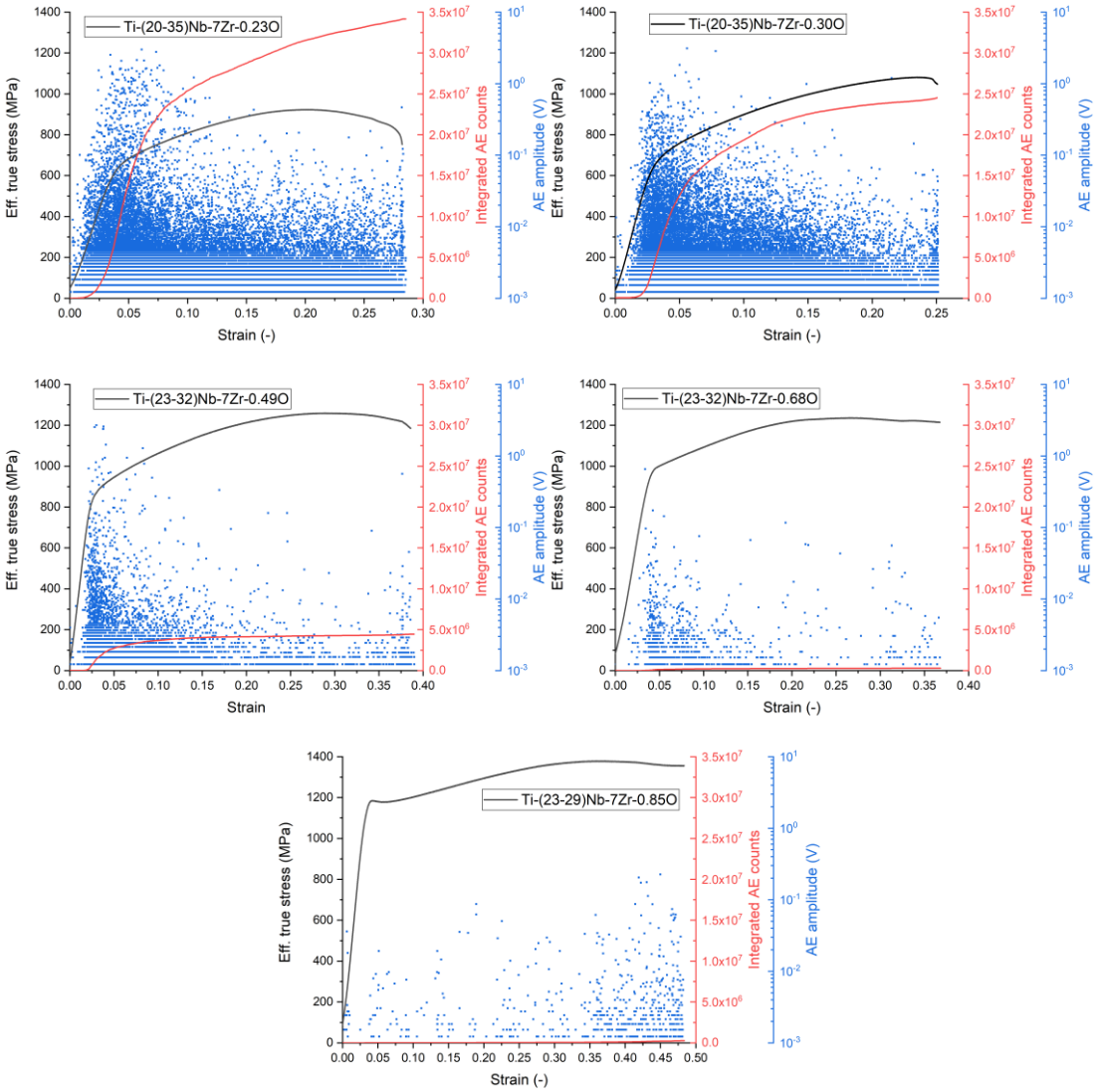

Figure 47: Compression testing of samples 6, 5, 1, 2 and 3 (sorted by increasing O content). Effective true stress-engineering strain compression curves (black lines) plotted together with AE data: AE amplitude (blue dots, log scale) and integrated AE counts (red curve, linear scale).

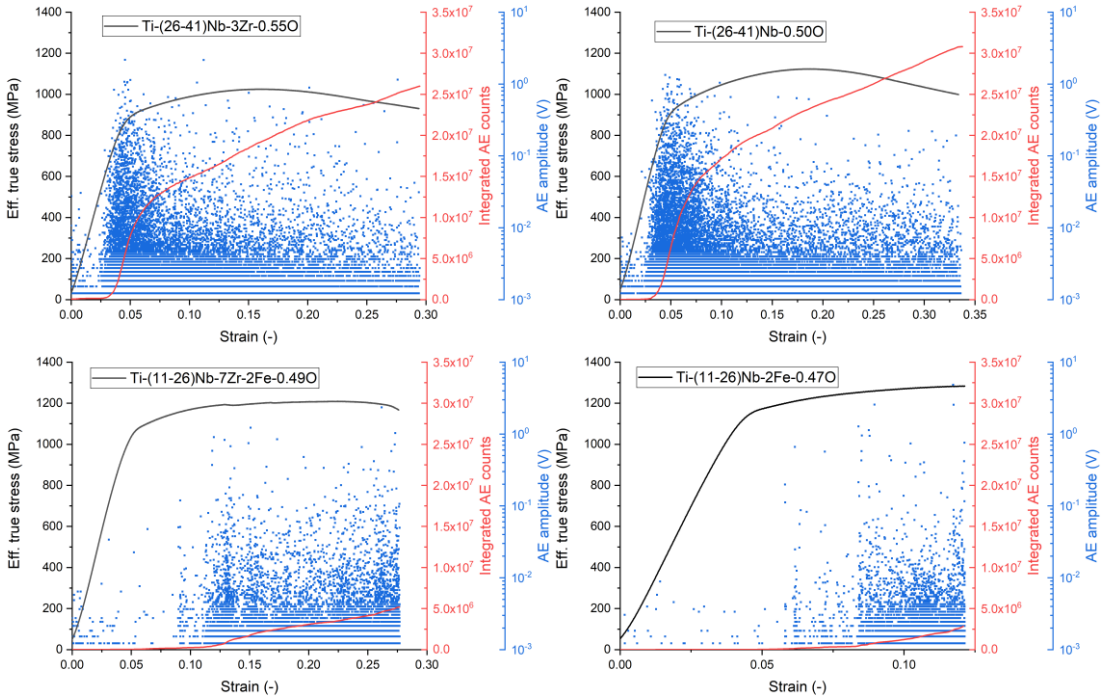

Figure 48: Compression testing of samples 7, 8, 9 and 10. Effective true stress-engineering strain compression curves (black lines) plotted together with AE data: AE amplitude (blue dots, log scale) and integrated AE counts (red curve, linear scale).

It can be directly observed for all samples with 7 wt% Zr (the five samples shown in Figure 47) that the macroscopic effective yield stress monotonically increases with increasing O content. This is an expected behaviour typical in various Ti alloys as well as commercially pure Ti grades [191–193]. While for the samples with the lowest O contents of 0.23 and 0.3 wt%, the yield stress is just above 600 MPa, for the sample with the highest O content of 0.85 wt%, the yield stress of nearly 1200 MPa was observed together with a sharp yield point phenomenon. From the macroscopic flow curves, the trend in total strain at fracture is also clear – increasing O content has led to a dramatic increase in the sample ductility, from fracture strain of 25 % for the Ti-(20-35)Nb-7Zr-0.3O sample to nearly 50% for the Ti-(23-29)Nb-7Zr-0.9O sample.

The results of the AE measurements during the deformation can also be directly compared between the whole samples, although it is clear that AE will differ for each layer. The shown quantities (AE event amplitudes, integrated AE counts) span several orders of magnitude (i.e. are much larger than the potential effects of sample size). In general, AE responds strongly when there is stress-induced twinning or martensitic transformation during deformation. From both analyzed quantities, it is clear that for samples with 7 wt% Zr (Figure 47), acoustic emission is very strong for samples with 0.2 and 0.3 wt% O, while the activity is getting lower for higher O contents until there is nearly no AE activity around the yield point for the 0.85O sample. This is quite a surprising result as one would also expect at least some AE activity during the sharp yield phenomenon that is connected with avalanche unpinning of dislocations from the O atoms. As expected, AE activity always starts to get stronger when the sample rupture is approaching.

The sample with 0.5% of oxygen (Ti-(23-32)Nb-7Zr-0.5O – sample 1) was the only one in which both the macroscopic yield point reached a value above 800 MPa and there was some measurable AE activity as well. Also, this sample was containing the lamellae of α″ martensite observed via SEM (shown further). For these reasons, an

O content of 0.5% was kept constant for the next set of studied layered samples and other alloying elements were varied, namely Zr content (3% and 0% in samples 7 and 8, respectively) and the addition of 2% Fe (together with 7% and 0% of Zr in sample 9 and 10, respectively). The concentration ranges of Nb were set so that the resulting alloys were in β / β+ω condition after quenching (prior testing). As shown in Figure 48, samples 7 and 8 show a similar (macroscopic) yield stress as sample 1 with similar O content. However, the achieved compressive strain is lower due to lower strain hardening, especially in sample 7, Ti-(26-41)Nb-3Zr-0.5O. At the same time, both samples 7 and 8 show an even stronger AE signal compared with the corresponding sample 1, both in the amplitudes of the individual events and in the integrated AE counts.

In contrast, samples 9 and 10, i.e. the ones with 2% Fe show yield stress over 1000 MPa and only limited ductility. The AE signal captured is not present around the yield point but rather in later stages of deformation and can be thus attributed to the formation of cracks. In sample 9, some of the AE signal bursts can even be associated with bumps on the compression curve.

Since the deformation in the individual layers is certainly not uniform, the DIC was used to separate the individual pseudo-compression curves from the measurements as described in Section 3.1.6.

6.3.2. Analysis of DIC data and compression curves

The pseudo-compression curves from the following samples were extracted from samples with varying content of O (numbers 6, 5, 1, 2 and 3 in the order of increasing O content).

It is not a surprise that the yield stresses are roughly similar for alloys in every single sample which is almost definitely due to the significant effect of oxygen. However, the used approach provides insight into the ductility of each composition as well as the ultimate compressive stress (UCS). It is important to note that in the case of samples with an oxygen content of 0.5% and higher, the alloys containing predominantly α″ phase were very brittle and could not be used during high-throughput compression testing. On the other hand, for lower O content, even these layers/alloys which contained predominantly α″ phase, have undergone significant plastic deformation, although they were also the layers in which the cracks / shear bands have originated. When comparing the samples between each other, the total achieved ductility of the most ductile alloy from each sample is increasing with the increasing O content (with one exception of sample 5 with 0.30 O in which the ductility was inferior to sample 6 with 0.23O). Note that an increase in ductility with increasing O content was observed also from tensile testing of Ti-32Nb-7Zr-0.5/0.6/0.8O alloys shown in Figure 29d.

Compression curves of samples 6, 1 and 3, containing 0.23, 0.49 and 0.85 % of oxygen, respectively, are shown in detail together with selected sample images in Figure 50, Figure 51 and Figure 52.

Figure 50 shows the sample with the lowest O content of 0.23% in detail and the selected images of the sample correspond to instants marked on the stress-strain curves. The highest strain (between 0.30 and 0.35) was achieved in layers with 26 and 29% of Nb, i.e. those that were already in the β phase condition after quenching but still very close to the β phase stability. In layers with α″ phase-containing alloys, the achieved strains were significantly lower. The lowest strains together with the highest achieved stresses were captured for alloys with the highest Nb content. This does not have to mean that these alloys are the most brittle, rather the used approach hits its limit. By the end of the compression test, a pronounced shear band has been formed

that originated from the bottom part of the sample (the lowest Nb content) as can be observed in Figure 50d. Due to this fact, the two top layers (32Nb and 35Nb) did not deform further and testing using layers without the α″ phase would probably be more justifiable as in the case of samples 1-4. The samples with 32 and 35% Nb have undergone a significant increase in strain hardening slope after strain of 5%.

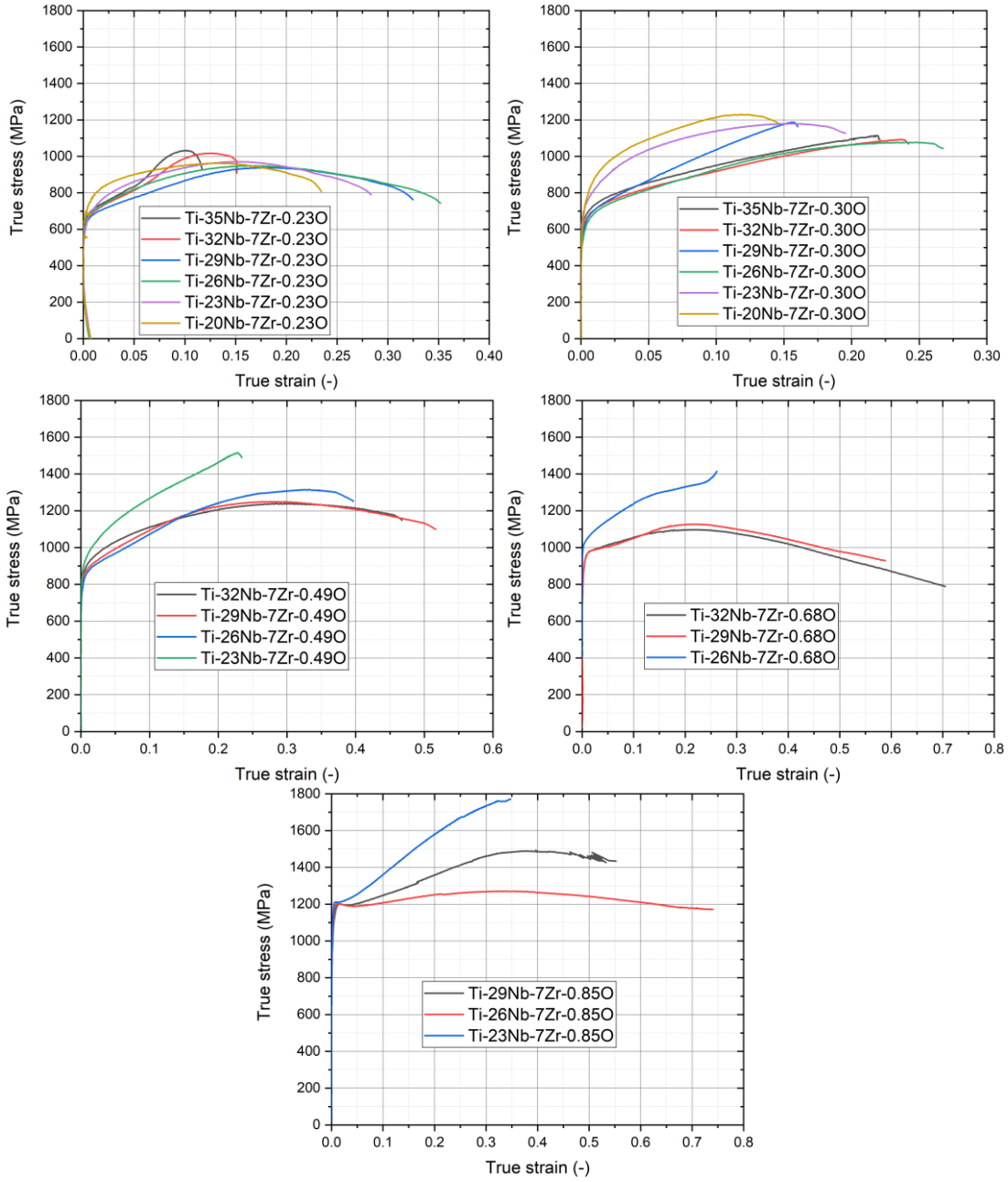

Figure 49: Individual true stress – true strain compression curves extracted from the DIC measurements.

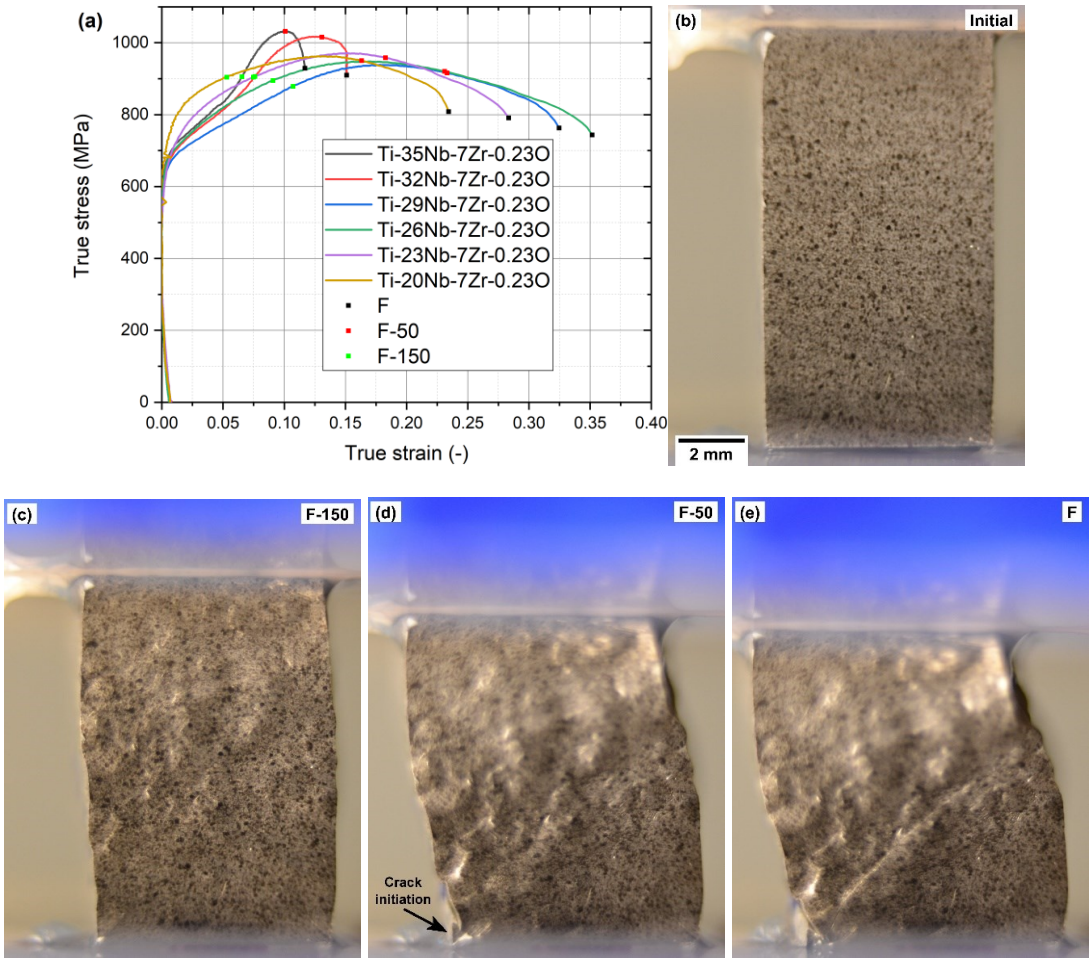

Figure 50: (a) Individual compression curves from Sample 6 (0.23O) with several highlighted test times and selected sample images from (b) the initial part of the test, (c) image at time 150 s before rupture (F-150), (d) image at time 50 s before rupture (F-50) and (e) final image of the ruptured sample (F stands for final) with the shear band and cracking visible in the bottom part.

The 4 alloys deformed in sample 1 (0.49O) show again behaviour which is dependent on the Nb content, i.e. the distance from the martensitic composition as shown in Figure 51. The least stabilized alloy (23Nb) shows the lowest achieved strain and highest strain hardening as well as UCS. Other alloys show similar performance, although the layer with 26Nb is less ductile than the other two layers. Same as in the previous example, the cracking/shear band appears in the bottom sample (lowest Nb content) also in this case. The brittleness is most probably caused by the presence of a large amount of ω phase as was shown by XRD measurements in Figure 36.

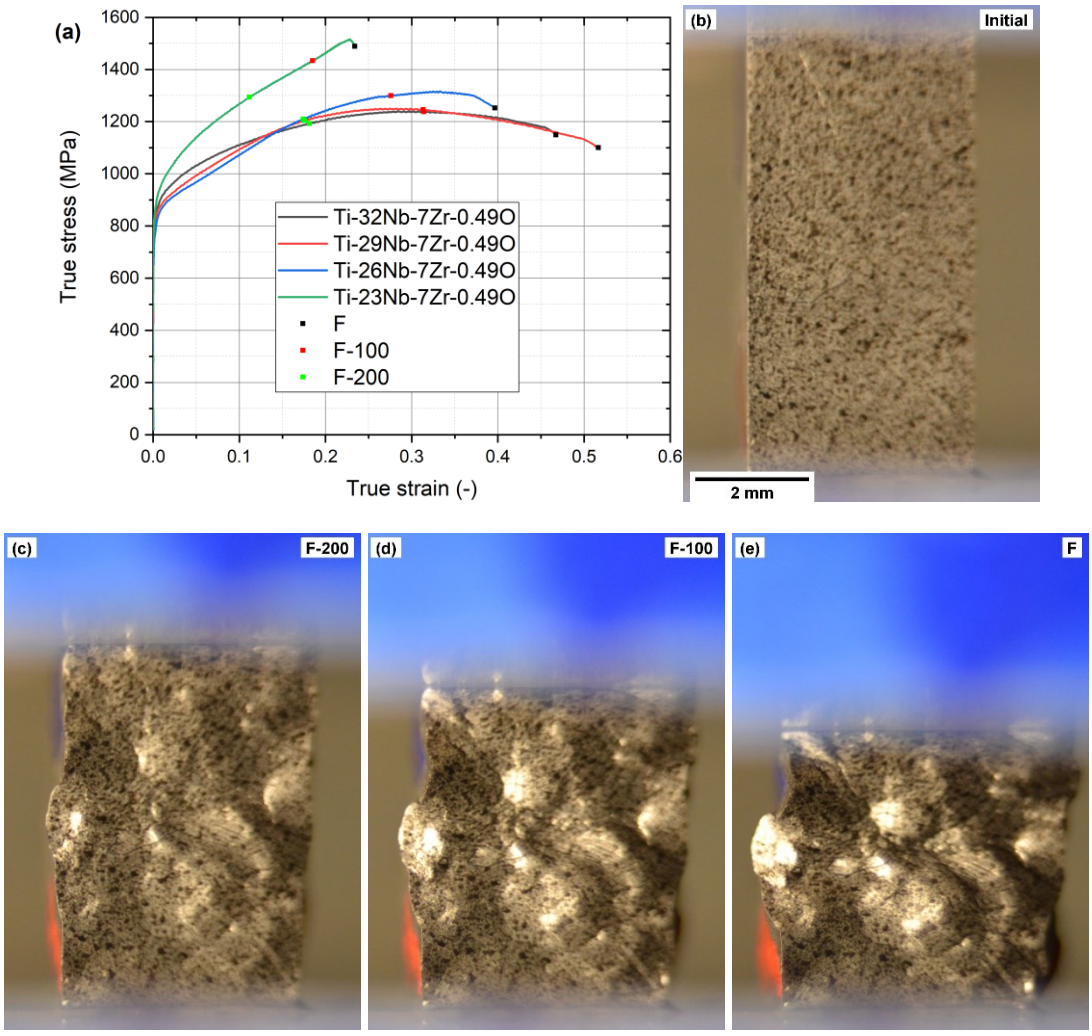

Figure 51: (a) Individual compression curves from Sample 1 (0.49O) with several highlighted test times and selected sample images from (b) the initial part of the test, (c) image at time 200 s before rupture (F-200), (d) image at time 100 s before rupture (F-100) and (e) final image of the ruptured sample (F).

The data from sample no. 3 (0.85% O) are shown in Figure 52. This was the sample in which the biggest true strain of about 0.75 was achieved. As the strain was very high, the DIC analysis failed in the later stages of deformation. This can be observed mainly in the curve corresponding to Ti-29Nb-7Zr-0.85O, where serrations appear near the end. Indeed, when comparing the selected images from different stages of deformation, the speckle pattern from the initial image in Figure 52b is gradually more deformed and less clear in images in Figure 52 c,d until the speckles are very hard to distinguish in Figure 52e. Other problems relate to surface areas that were moving in the out-of-plane direction (towards or away from the camera). First, this causes defocusing of the image. This is not a too big problem due to the used *high strain* algorithms in the *ncorr* package that kept updating the reference image against which the correlations were done. The somewhat bigger issue was the fact that when some parts of the observed surface were rotated, they started reflecting the light used for the illumination of the sample. As a result, these parts could not be correlated anymore (until the test ended) and the corresponding points in DIC post-processing had to be skipped during the calculation of mean vertical displacements $\overline{u_y}$. The last issue with out-of-place movement is that this causes actual distortions of results: object

which moves closer to camera appears larger and the DIC algorithm ascribes this object a positive strain in both *x* and *y* direction. This issue cannot be resolved using a single camera arrangement and at least two cameras have to be used together with much more complicated Stereo DIC algorithms [194] (not available in the *ncorr* package).

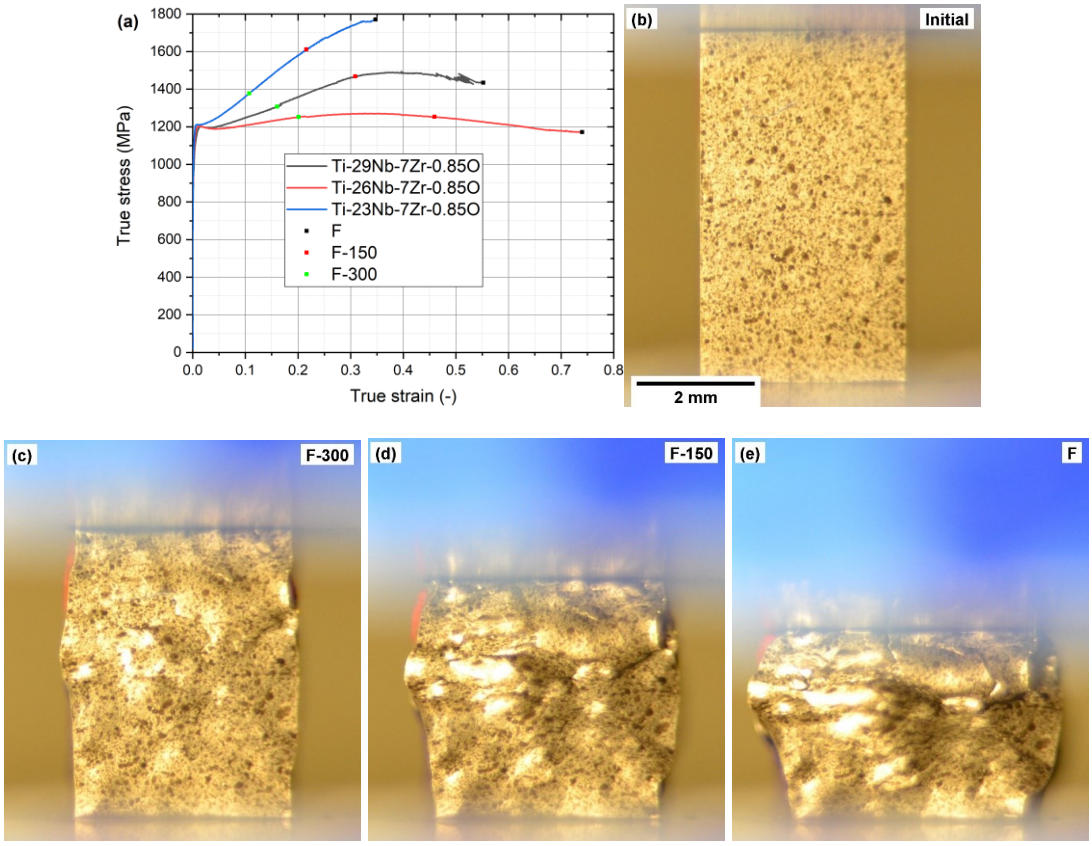

Figure 52: : (a) Individual compression curves from Sample 3 (0.85O) with several highlighted test times and selected sample images from (b) the initial part of the test, (c) image at time 300 s before rupture (F-300), (d) image at time 150 s before rupture (F-150) and (e) final image of the ruptured sample (F).

Despite all the problems described, it is still valid that this sample with 0.85% of oxygen is the one that achieved the highest compressive strain. However, such properties are not achievable in tension due to embrittlement by the presence of the ω phase as was shown in Chapter 5 and the best tensile ductility can be achieved in alloys that do not contain any ω phase.

6.3.3. XRD measurements after compression

Since the motivation for preparation and studying of the layered alloys was the potential of combining the TRIP effect (caused by stress-induced α″ martensite) with the strengthening by oxygen, XRD was performed to find out, if the α″ was really induced in the materials.

The measurements from the individual layers of samples 6, 5, 1, 2 and 3 are shown in Figure 53. Since the α″ phase was present in 2 layers of both samples 6 and 5, it was found there also after compression testing. Other alloys did not show any α″ phase prior deformation or its reflections were very weak meaning the volume fraction was very low. Their phase composition was therefore either pure β phase or β+ω.

Identification of possible α″ formation in these layers is therefore of interest as this clearly demonstrates formation of SIM.

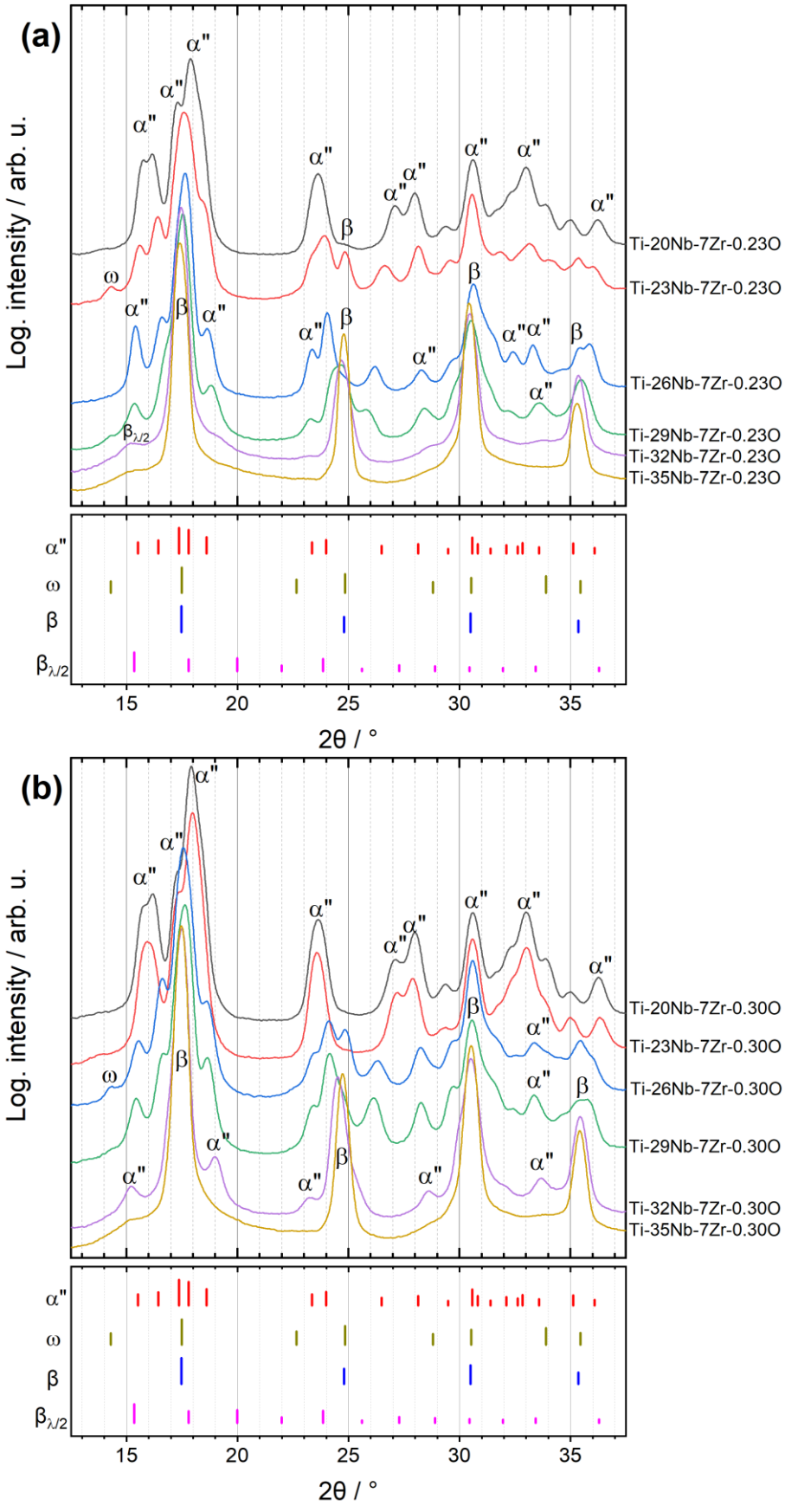

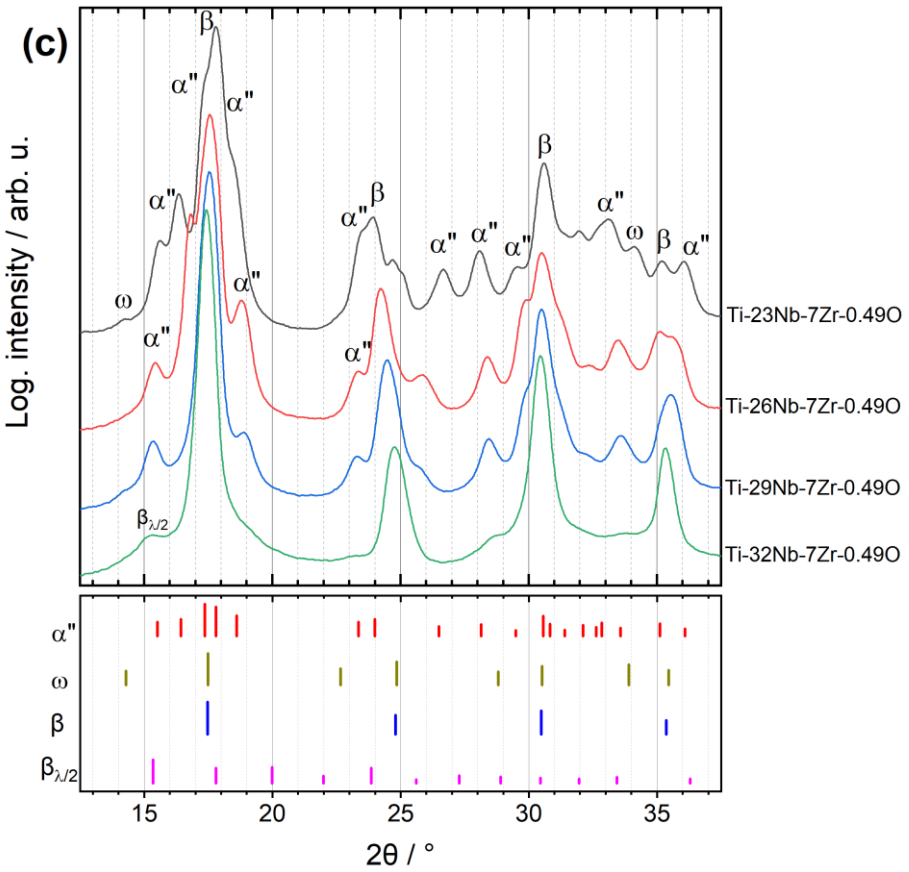
(c)
Log. intensity / arb. u.
Ti-23Nb-7Zr-0.49O
Ti-26Nb-7Zr-0.49O
Ti-29Nb-7Zr-0.49O
Ti-32Nb-7Zr-0.49O
α"
ω
β
β$_{λ/2}$
15
20
25
30
35
2θ / °

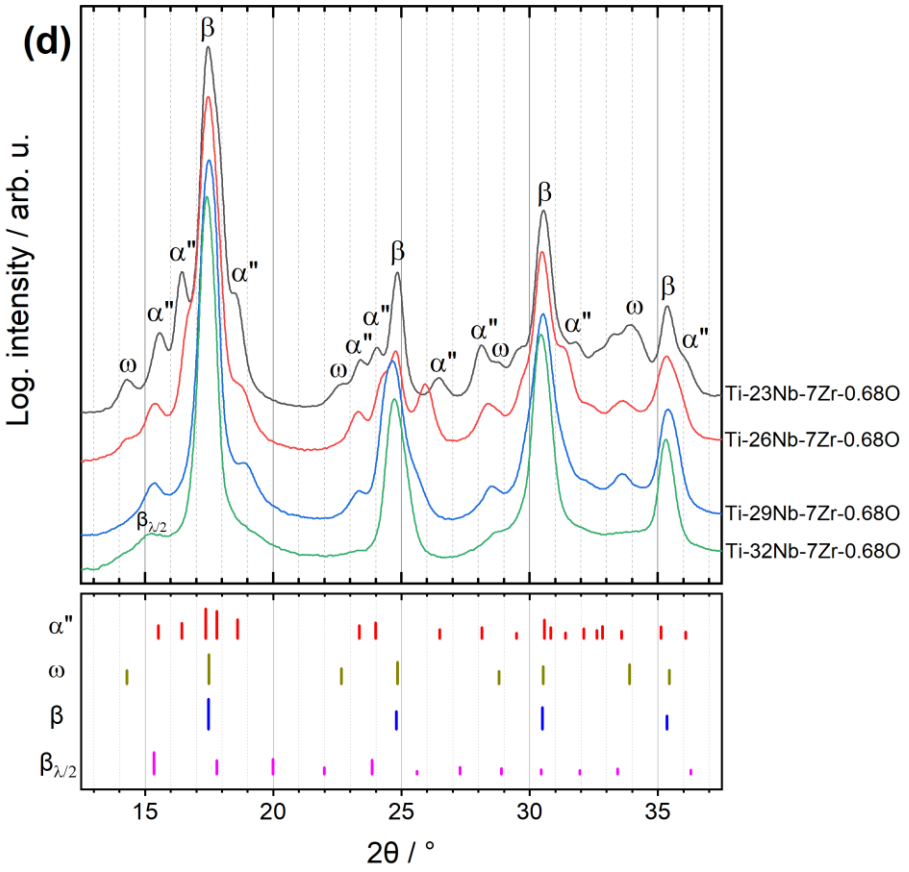
(d)
Log. intensity / arb. u.
Ti-23Nb-7Zr-0.68O
Ti-26Nb-7Zr-0.68O
Ti-29Nb-7Zr-0.68O
Ti-32Nb-7Zr-0.68O
α"
ω
β
β$_{λ/2}$
15
20
25
30
35
2θ / °

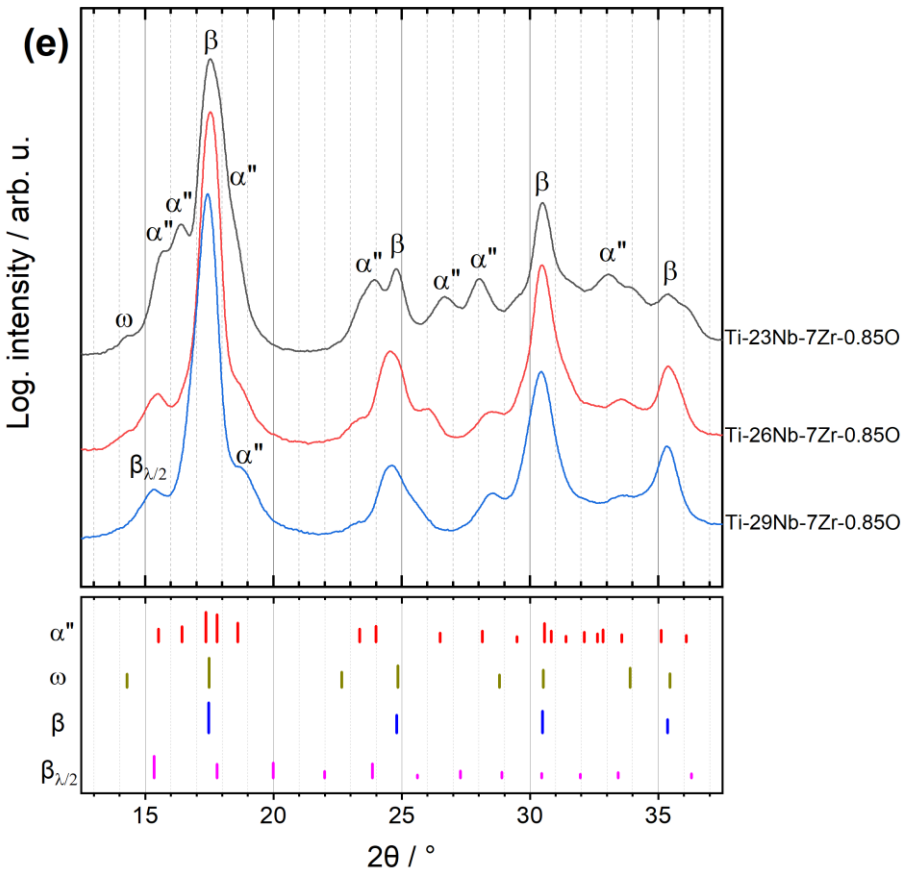

Figure 53: XRD patterns of layered samples after compression. (a) Sample 6 (0.23O), (b) Sample 5 (0.30O), (c) Sample 1 (0.49O), (d) Sample 2 (0.68O), (e) Sample 3 (0.85O).

In all deformed samples, most of the layers exhibit the presence of reflections corresponding to the orthorhombic α″ phase structure. The peak intensity decreases with increasing Nb content and the peak positions (lattice parameters) change as well, therefore the tick marks in the bottom part of the graphs are meant for guiding the eye only. In both samples 6 and 5 (0.23O and 0.30O), the α″ reflections can be confidently recognized up to 32Nb layers. In the last layer (35Nb) the β phase peaks only can be recognized and other phases, if present, have reflections so weak that they are hidden in the background. Also note that the XRD patterns of samples after deformation are much more distorted, compared to those captured in annealed samples, so the weak reflections can get lost in the background even easier. For other samples, 1, 2 and 3, the α″ reflections can be observed in all the deformed layers (neither of them contains a layer with 35% Nb). However, in layers with the highest Nb content, only the strongest and the most isolated reflections can be differentiated, despite using the log scale, which signifies a very low volume fraction of α″ phase in the β matrix.

The ω phase was present in annealed and quenched samples in quite a big fraction, which corresponded to relatively narrow and high XRD peaks in layers that were close to the β phase stability limit but already in the β condition (ω forms in the β phase, not in α″). In contrast, the ω phase reflections found in the deformed samples are very weak and effectively the only reflection that could be reliably ascribed to the ω phase was (0001) reflection located 2θ between 14° and 15°. Also, its intensity was much lower compared to the quenched condition. The reason for this could be that either the distortion by the deformation was so high that the ω phase reflections are

wide and hidden in the background or (more probably), the formation of SIM α″ has relieved the stresses that are partly the driving force for ω phase formation [31].

Upon analysis of lattice parameters acquired by Rietveld refinement of the measured XRD patterns, clear trends can be observed. Samples 6, 1 and 3 were selected to show these trends in Figure 54. Lattice parameters were rescaled according to crystallographic relationships between α″ and β phases as shown in Figure 2. For sample 6, the α″ martensite changes its lattice parameters closer to β phase with increasing Nb content until they coincide at 35Nb where the β phase only could be detected. When taking also the decreasing α″ reflections intensity with increasing Nb content into account, the values near the coincidence can bear a very large error. If the XRD patterns were plotted on a linear scale instead of a log scale, these reflections would be almost undetectable. The same trends are observed also for sample 1 in Figure 54b, although the lattice parameters are more scattered, most probably due to errors caused by peak widening due to larger deformation. This is even more pronounced for sample 3 (Figure 54c), although the linear fits follow the expected directions. Even when the rescaled lattice parameters of the orthorhombic phase precisely fit the lattice parameter of the β phase, it does not have to mean that the material is composed of the β phase only. Specifically, the nanoscale O′ phase is characterized by $\{110\} < 1\bar{1}0 >$ shuffle of every other {110} plane. This breaks the cubic symmetry although the lattice parameters remain unchanged [51]. The parameter governing this shuffle, denoted as δ in Figure 2 could be measured if the intensities of the reflections could be accurately determined, which is however not the case for the current measurements on coarse-grained samples where only the lattice constants can be reliably determined.

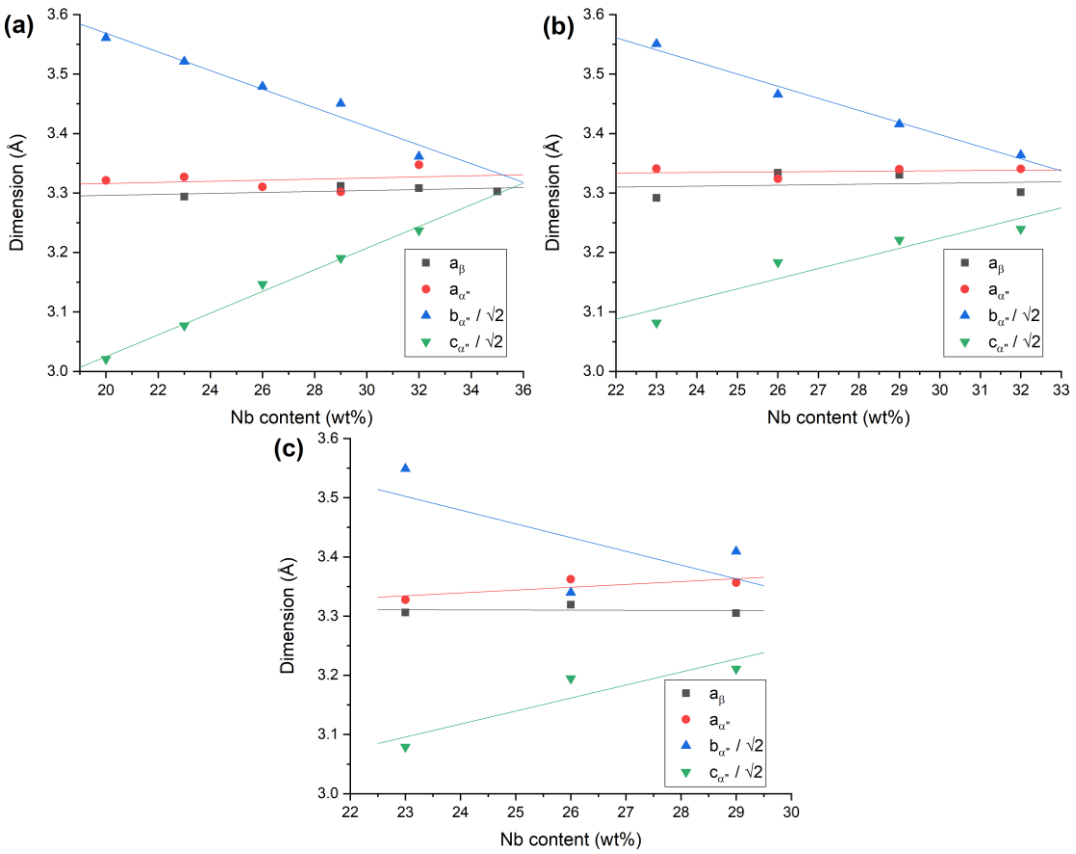

Figure 54: Lattice parameters of deformed layered alloys in a) sample 6, b) sample 1 and c) sample 3.

6.3.4. SEM observations and EBSD measurements after compression

XRD measurements provided insight into the alloy's phase composition, however, the morphology of the SIM α″ in deformed samples was established by SEM observations.

Microstructure images from sample 6 (0.23O) and sample 5 are shown in Figure 55 and Figure 56, respectively. In both alloys, the two layers with the lowest content of Nb show typical quenched-in α″ martensitic microstructure, the same as was in the case of such layers before deformation (cf. Figure 39 and Figure 25). During deformation, they could have undergone the so-called detwinning, which is a common deformation mechanism for shape memory alloys, however, such change in morphology would be hardly observed in SEM using a BSE signal. The two alloys in the middle layers in both samples (26Nb and 29Nb) show lamellae of the stress-induced martensite. These lamellae are much clearer (and larger) in sample 6 with lower O content. In the two Nb-richest alloys in each sample, martensite lamellae are not detected with the exception of Ti-32Nb-7Zr-0.23O alloy. This is consistent with the XRD results where the α″ reflections in these alloys were weak or not present at all.

Figure 57 shows the microstructure of alloys in sample 1. In the first two layers, the α″ lamellae can be clearly observed. In alloy Ti-23Nb-7Zr-0.49O, it is clear that there are multiple levels of the martensite/twinning – the smaller ones were formed in others that were formed previously. In the Nb-richer layers, stress-induced martensite is not observable, again consistently with XRD measurements where there were only very weak α″ reflections. Similar observations can be made also for sample 2 whose microstructures are shown in Figure 58 with the martensite lamellae even less clear.

In the most deformed sample 3 (Figure 59) the previously observed stress-induced martensitic morphology is not visible in any of the studied alloys. The present features look rather like the deformation slip bands.

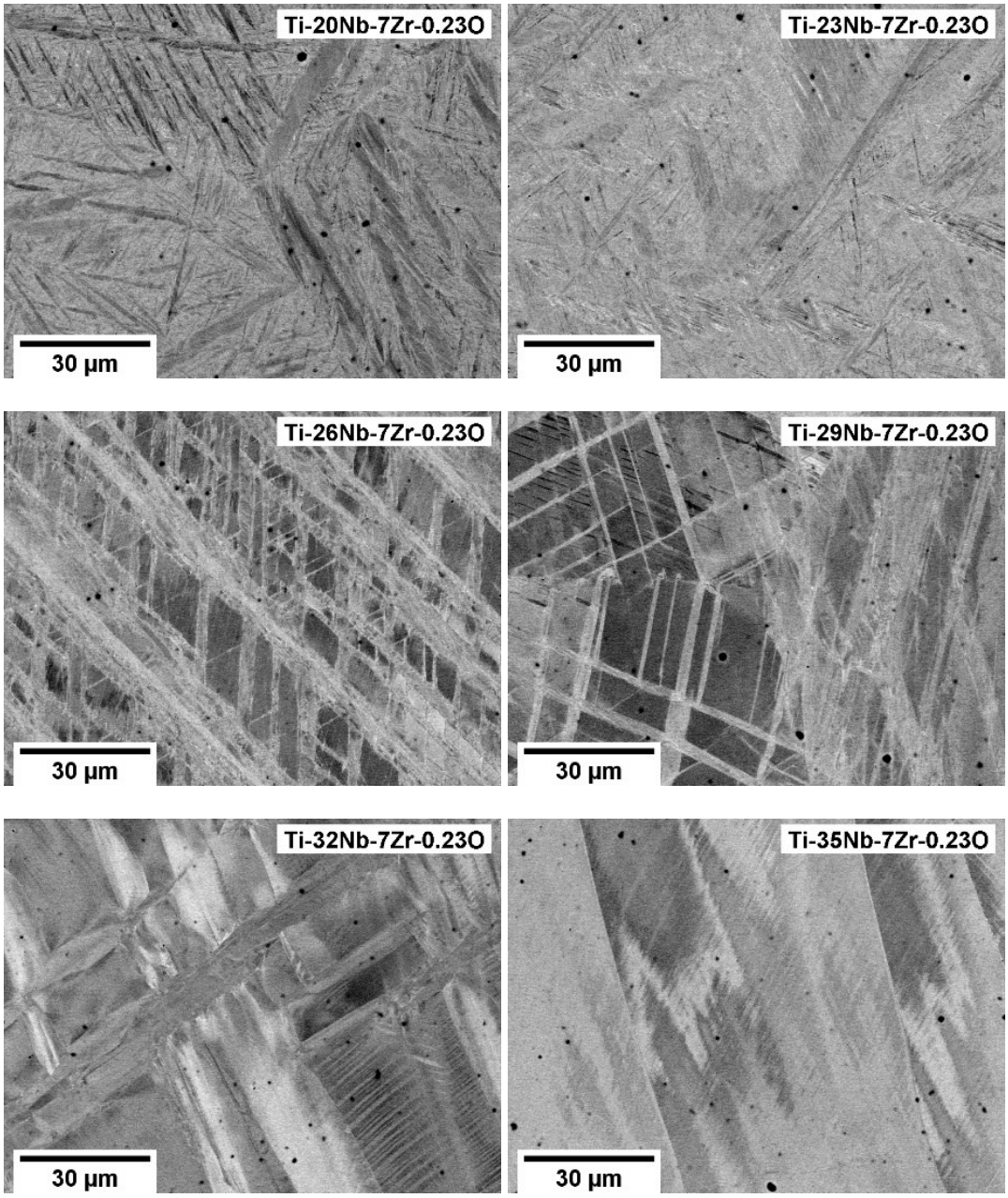

Figure 55: Microstructure of alloys from sample 6 after compression testing.

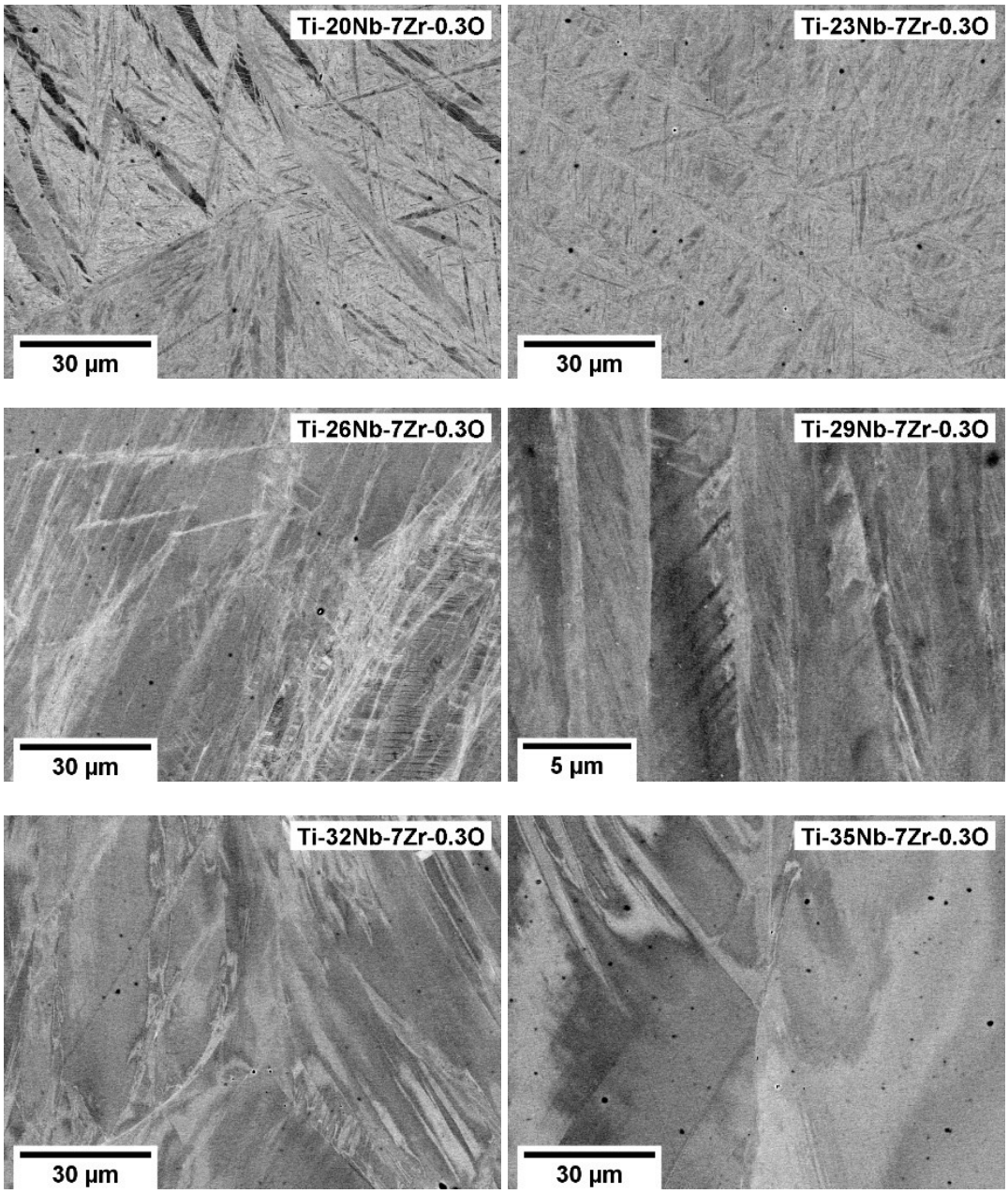

Figure 56: Microstructure of alloys from sample 5 after compression testing.

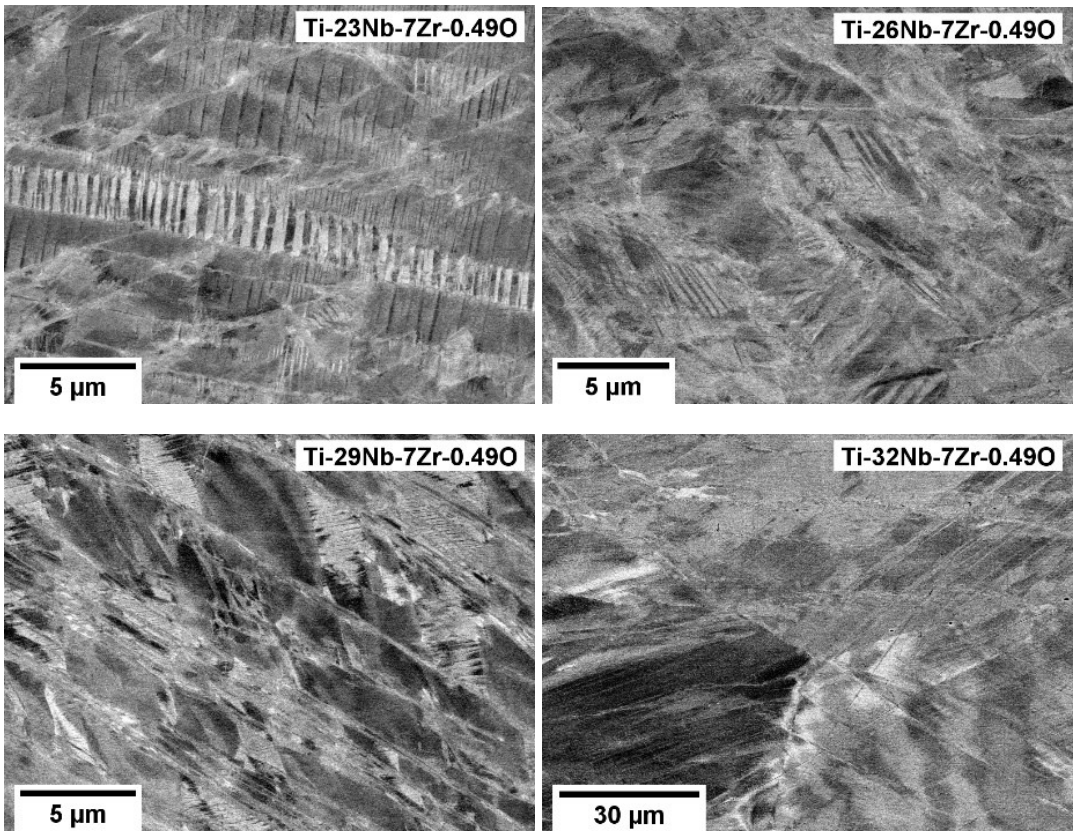

Figure 57: Microstructure of alloys from sample 1 after compression testing.

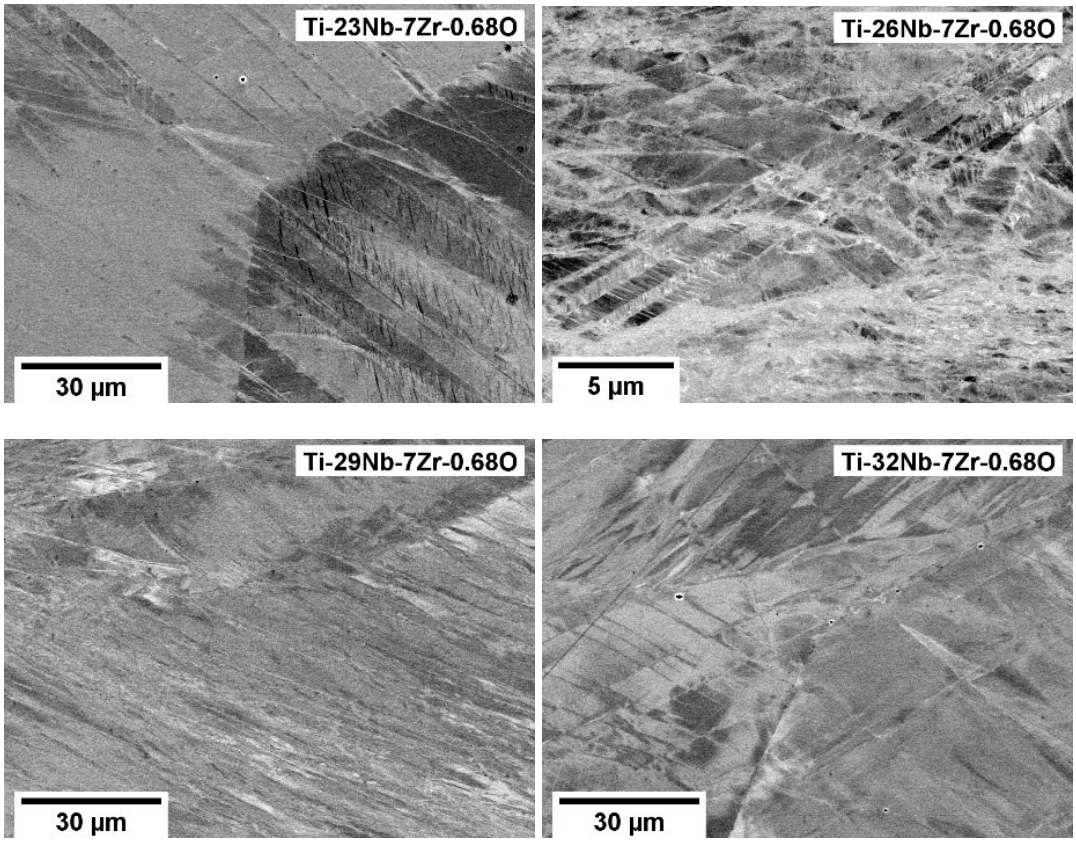

Figure 58: Microstructure of alloys from sample 2 after compression testing.

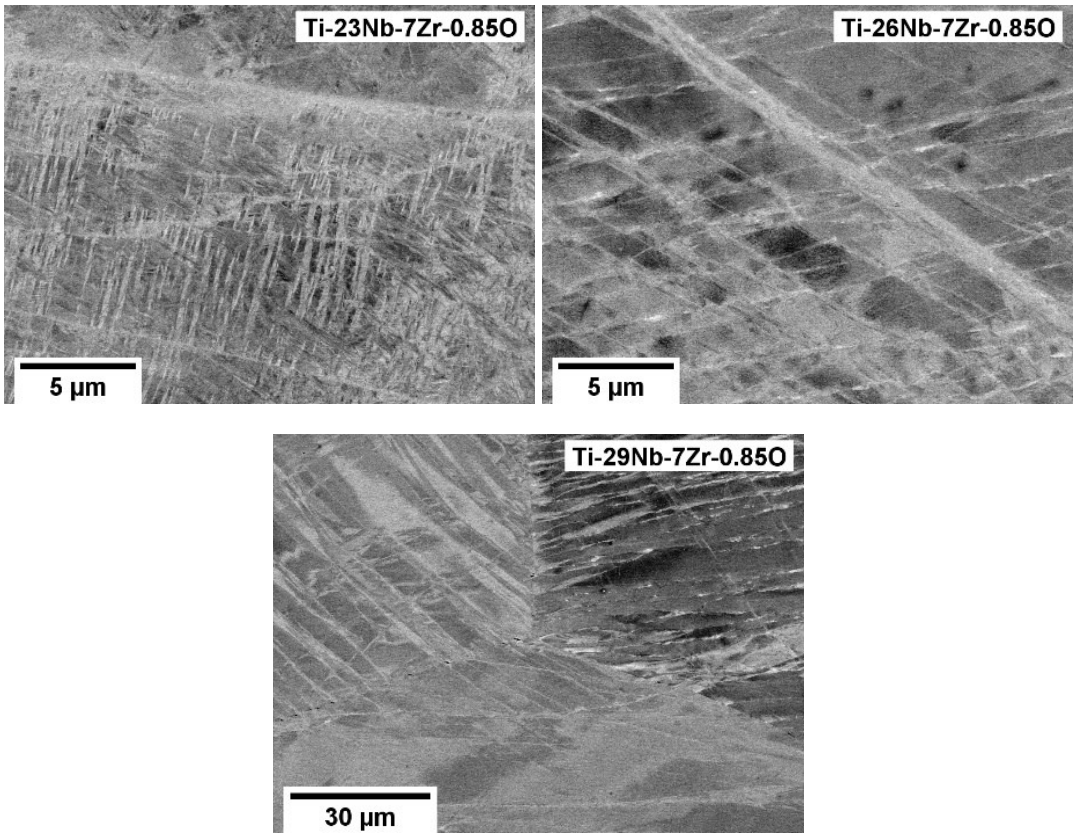

Figure 59: Microstructure of alloys from sample 3 after compression testing.

To acquire more information regarding the microstructure, the EBSD method was used to map selected representatives (with 26% of Nb) of the studied deformed layers: Ti-26Nb-7Zr-0.23O, Ti-26Nb-7Zr-0.49O and Ti-26Nb-7Zr-0.85O. The deformation present in the materials resulted in poor quality of the Kikuchi patterns and to improve this, the NPAR/NLPAR procedure was undertaken point-by-point by taking a mean of the corresponding Kikuchi patterns with the neighbouring points, resulting in reasonable quality of the pattern. Since the Kikuchi patterns depend on lattice parameters ratios (which are constant for BCC phase, as there is only a single lattice parameter, but differ for various orthorhombic lattice parameters), the data from XRD measurements were used for indexing.

Figure 60 a, b and c show the PRIAS bottom signal map, phase map and IPF map of the Ti-26Nb-7Zr-0.23O deformed alloy. The PRIAS bottom signal is comparable to images from the BSE detector (it corresponds to forward-scattered electrons). As shown in the phase map, both β and α″ phases were detected and the crystal orientations can be determined from the IPF map (combined for both phases). To get more precise information, a detailed EBSD scan was performed at the location denoted by a yellow square in PRIAS bottom signal map.

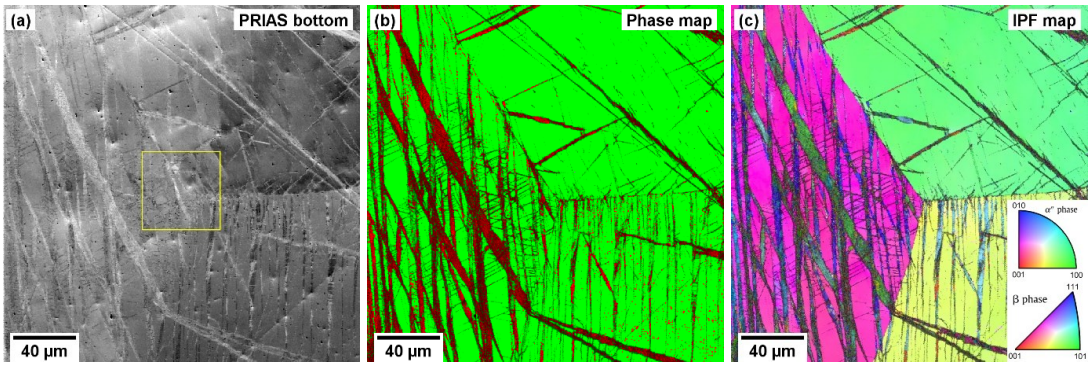

Figure 60: EBSD scan of Ti-26Nb-7Zr-0.23O alloy: a) PRIAS bottom signal map, yellow square denotes the location of the detailed scan (Figure 61), b) phase map shows β phase in green and α'' phase in red, c) IPF map.

The PRIAS signal, phase and IPF map of the detailed EBSD scan are shown in Figure 61. When comparing the phase map with the IPF map, several areas in single grain have a different orientation according to the IPF map but possess the structure of β phase. Two of these areas are marked by black arrows. Upon further analysis, these regions can be identified as the {332}<113> twins of the β phase. Parent-daughter twin recognition feature of OIM software has identified all the corresponding areas that are shown in Figure 61d. Moreover, a misorientation profile was created along the yellow line in the parent-daughter map and shown in Figure 61e. The misorientation of 50.5° is indeed proof of the {332}<113> twinning [49]. It can be concluded that Ti-26Nb-7Zr-0.23O alloy undergoes stress-induced martensitic transformation as well as deformation twinning.

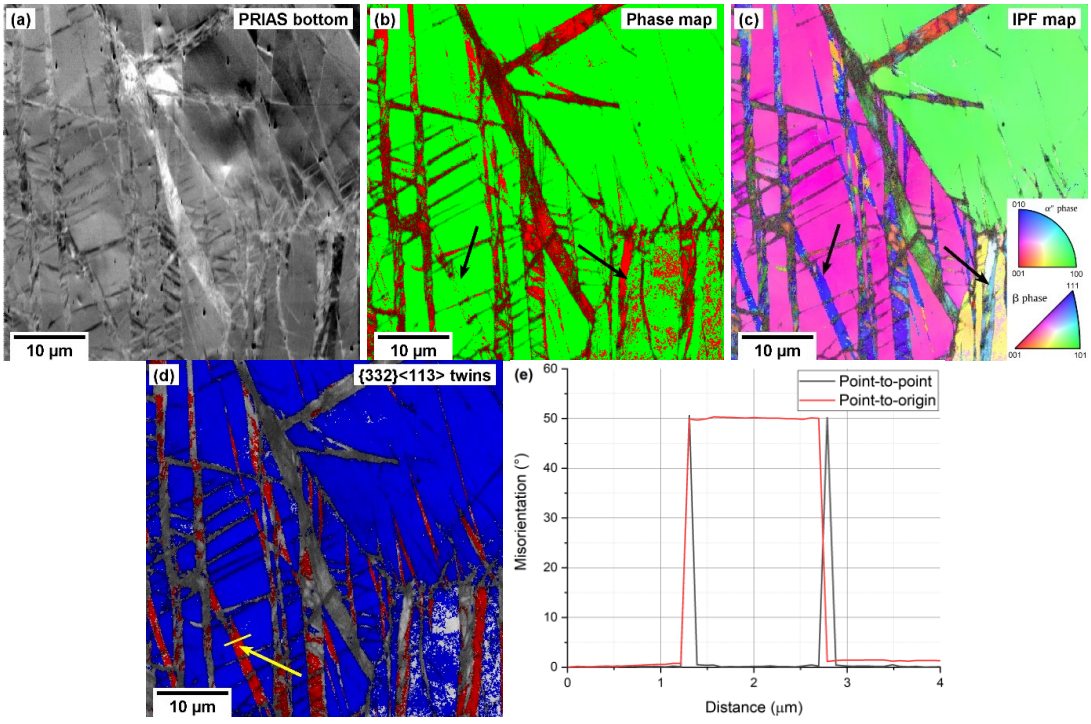

Figure 61: Detailed EBSD scan of Ti-26Nb-7Zr-0.23O alloy: a) PRIAS bottom signal map, b) phase map shows β phase in green and α'' phase in red, c) IPF map, d) parent-daughter map for the {332}<113> twinning in β phase, yellow line marked by arrow denotes the position of the misorientation profile, e) misorientation profile.

Figure 62 shows EBSD results for Ti-26Nb-7Zr-0.49O alloy. There is a lot more deformation present in the structure, as seen in the PRIAS map, which makes it more difficult for indexing. However, the achieved strains in this alloy are comparable with Ti-26Nb-7Zr-0.23O, as shown in Figure 49. It could be a local effect depending on the choice of EBSD scan location, but other factors could have also played a role. Firstly, twinning, which could provide additional deformation mechanism, is almost not present. Also, lattice parameters of the α″ phase are slightly closer to the β phase in Ti-26Nb-7Zr-0.49O alloy (the consequences will be discussed below). Lower image quality (grayscale in phase and IPF maps) is most probably caused by dislocation slip activity.

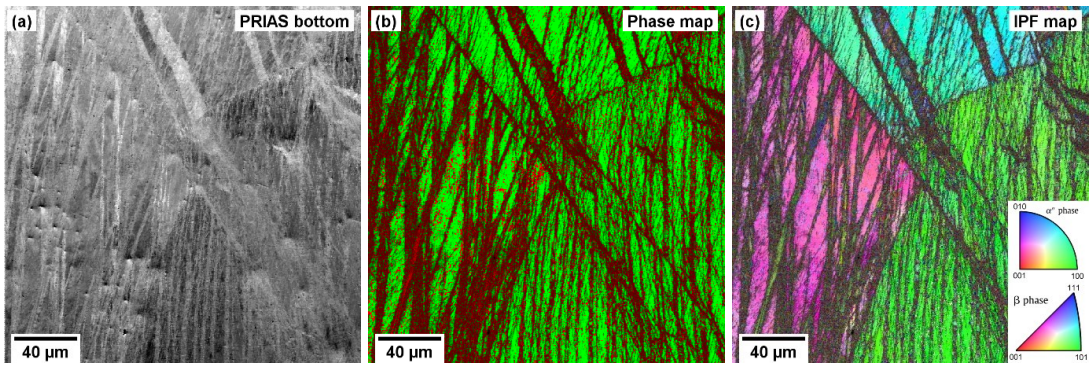

Figure 62: EBSD scan of Ti-26Nb-7Zr-0.49O alloy: a) PRIAS bottom signal map, b) phase map shows β phase in green and α" phase in red, c) IPF map.

Figure 63 shows EBSD data from Ti-26Nb-7Zr-0.85O. The PRIAS bottom signal map shows large deformation present in the alloy, due to the highest achieved true strain (>0.7) when compared with any other studied alloy. The EBSD scan was performed in a triple point of the β grains. Two of the grains show mostly β structure but the third (on the right-hand side of the image) appears to be indexed mostly as α″ phase. This grain is also the most deformed as a lot of deformation bands cause a darker contrast in the IPF map due to lower IQ, serving as an overlay. A more detailed EBSD scan has been made in the area denoted by the yellow square in Figure 63a.

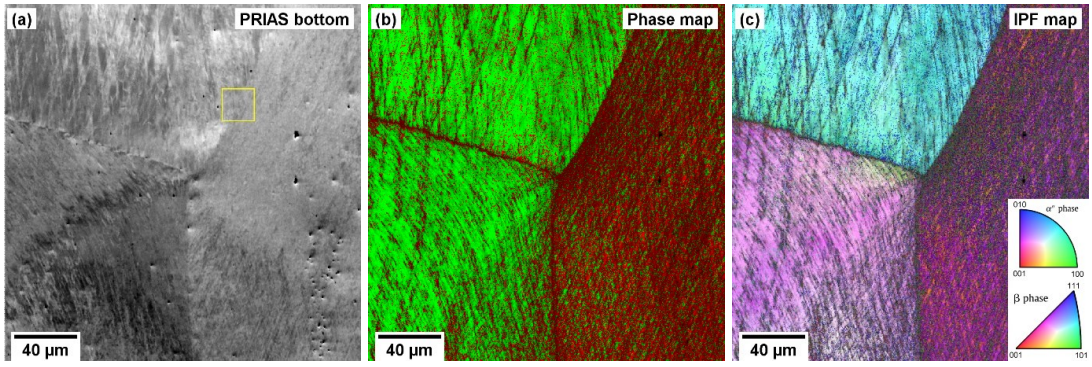

Figure 63: EBSD scan of Ti-26Nb-7Zr-0.85O alloy: a) PRIAS bottom signal map, yellow square denotes the location of the detailed scan (Figure 64), b) phase map shows β phase in green and α" phase in red, c) IPF map.

In the detailed EBSD scan of Ti-26Nb-7Zr-0.85O alloy, shown in Figure 64, individual deformation bands can be recognized as well as areas between them. As follows from the phase map, most of the right grain was indexed as α″ phase (purple

colour in IPF map) and only a few scattered areas seem to retain the β phase (orange colour in IPF map). Examples of Kikuchi patterns for both indexed partitions are shown in Figure 64 d and e for the α″ and β indexed phase marked by arrows in the IPF map, respectively. Both Kikuchi patterns shown are already processed by the NPAR algorithm. When comparing both patterns, no difference can be established even from the image created by subtraction of one of the patterns from another (and appropriate brightness/contrast adjustment) which is shown in Figure 64f. Since the differences between the lattice parameters of the α″ and β phase in Ti-26Nb-7Zr-0.85O alloy are very small (cf. Figure 54c), the resulting Kikuchi patterns are also very similar. The indexing (Hough transform-based) algorithms struggle to accurately assign the appropriate structure. Since the material before deformation did not contain any α″ phase (cf. Figure 36) and the lamellar morphology typical for α″ martensite is not present after deformation, the structure of the right-hand side grain is likely that of the β phase (with the same orientation as the orange-coloured points in Figure 64c).

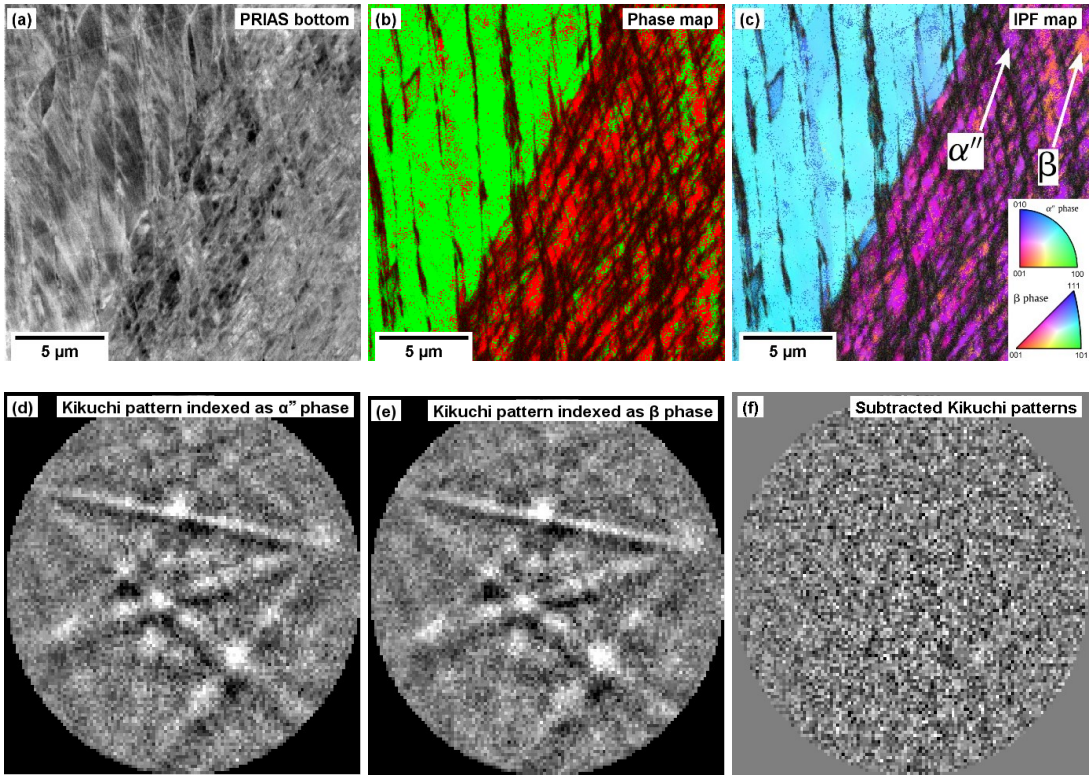

Figure 64: Detailed EBSD scan of Ti-26Nb-7Zr-0.85O alloy: a) PRIAS bottom signal map, b) phase map shows in green and α" phase in red, c) IPF map with areas marked by white arrows that indicate positions of Kikuchi patterns shown in d) and e) indexed as α" and β phase, respectively. f) image resulting from subtraction of images d) and e).

6.3.5. Discussion of deformation mechanisms in layered samples

In the current chapter 6.3, the main aim was to perform mechanical tests and analyse the deformation mechanisms in the prepared layered samples. Finally, based on the achieved results, we aim on selecting the composition of alloy which would be strengthened by O content, but at the same time achieve high ductility by activating the TRIP/TWIP effects.

The first quantity which should point to activation of mechanical twinning and/or martensitic transformation was acoustic emission measured during compression testing of the layered samples. Quite unambiguously, it was found that

the acoustic emission signal is much stronger with lower O contents in Ti-xNb-7Zr-yO alloys. Since the grain size (affecting the AE intensity) was comparable in all FAST-prepared samples, the AE can be compared sample from to sample. While AE signal differs in order of magnitudes, the total sample size changes do not significantly affect the AE measurements [195]. The AE signal was however anticorrelated to the achieved total strain in each sample. The highest strain was achieved in the sample with the highest O content which had the lowest AE activity.

The following sample series (with less or no Zr / with 2% Fe), containing 0.5% O showed also interesting behaviour. The Fe-containing samples were quite brittle and AE was not very active, but in the other 2 samples, Ti-(26-41)Nb-3Zr-0.5O and Ti-(26-41)Nb-0.5O, very strong AE was active and total strain comparable to Ti-(20-35)Nb-7Zr-0.5O sample was achieved. These compositions have not been studied further, yet, although they show a potential for future research.

By the performed DIC-based separation of compression curves layer by layer, it was found that for alloys with lesser O content (0.2 – 0.3%), the layers that were the most ductile had 3-6% of Nb more than the critical concentration needed for α″ phase formation during quenching, i.e. just above the β/α″ phase stability boundary which can be visualized in Bo-Md diagram for low oxygen alloys (Bo/Md values are unknown for oxygen) [97,109,196]. For these alloys, the highest ductility was attributed to α″ SIM and mechanical twinning activation as shown by XRD, SEM and EBSD.

In contrast, for layered samples with higher O (0.5% and more), higher ductility was achieved when the composition was far from the quenched-in α″ composition. Although the reflections that could correspond to α″ phase were detected by XRD in all the corresponding alloys, the typical lamellar microstructure was found only in some of them, namely in alloys with 23Nb and 26 Nb for 0.49O and 0.68O. The lamellar microstructure due to deformation twinning or α″ SIM was completely missing in alloys with 0.85O.

The reason for decreasing α″ phase volume fraction after deformation with increasing β stability of the alloy lies in decreasing differences between the geometry of the corresponding bcc and orthorhombic cells. The principal transformation strains [197] caused by the β → α″ stress-induced transformation can be expressed as:

$$\varepsilon_1 = (a_{\alpha''} - a_\beta)/a_\beta,$$
$$\varepsilon_2 = (b_{\alpha''} - \sqrt{2}a_\beta)/\sqrt{2}a_\beta,$$
$$\varepsilon_1 = (a_{\alpha''} - \sqrt{2}a_\beta)/\sqrt{2}a_\beta.$$

(Equation 6)

From these expressions, it follows that in the case of very similar lattice parameters, such as those in Figure 54 for higher Nb contents, the strains that are accommodated by martensitic transformation are negligible. Therefore, for these compositions, it is not favourable to form the α″ phase as it can accommodate little strain only.

Another consequence of similarity in the bcc and orthorhombic structure is that the classical vote-based pattern indexing using the Hough transform fails to resolve the two structures as shown in Figure 64.

It remains unexplained, why the reflections corresponding to the α″ phase were found in XRD patterns after deformation for alloys that do not show α″ SIM lamellae nor twinning lamellae. Upon closer inspection of the XRD patterns of individual samples, it is apparent that with higher Nb content some of the α″ reflections, close to

the reflections of the β phase, disappear or rather collapse into a single one. This behaviour, corresponding to an increase in crystal symmetry, evokes that it could be caused by the presence of the O′ phase that undergoes shuffle only without any shear. The O′ phase was discovered only recently [198] and it has a nano-scale size which can be observed by TEM only [51]. For visualization of this possibility, XRD reflections were simulated according to lattice correspondence shown in Figure 2 for a) β phase (with an arbitrarily selected lattice parameter a=3.282 Å), b) O′ phase with lattice parameters given by the lattice correspondence with the β phase while setting the nonzero parameter δ governing the $\{011\} < 0\bar{1}1 >_{\beta}$ shuffle and c) α″ phase with the same relative shuffle and with changed lattice constants (due to shear). The simulated positions of reflections for all three phases are shown in Figure 65. The symmetry of the O′ phase is higher due to the lattice correspondence and thus, some of the reflections are shared with the β phase. In the measured XRD patterns, the alloys with the highest Nb content still exhibited reflections that cannot be attributed to the β phase (cf. Figure 53), but when fitted with the α″ phase, the lattice parameters correspond closely to the respective interplane distances in β phase (cf. Figure 54). Thus, it is highly probable that in these alloys, the secondary phase is created by pure shuffle (O′ phase) or nearly pure shuffle (O′-like α″ phase). Note that the parameter δ governing the shuffle does not change the positions of the extra peaks (respectively to β), only their intensity, which is zero for zero shuffle.

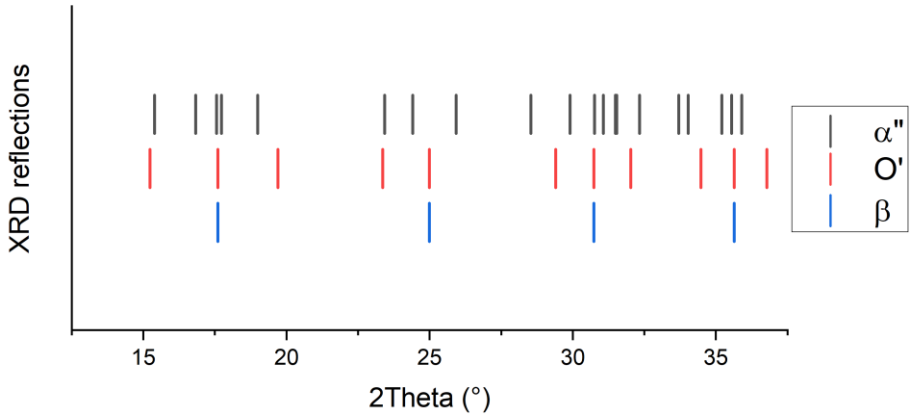

Figure 65: Simulated XRD reflections for β, O' and α" phases. The O' phase shows fewer reflections than the α" phase as some of them are forbidden due to higher symmetry.

It was found in [51], that the O′ phase nanodomains can be manipulated either by decreasing temperature or by mechanical loading into α″ nanodomains (without formation of large martensitic lamellae of α″ phase). From the data, presented earlier in this thesis, it was found that the alloy Ti-32Nb-7Zr-0.49O exhibits O′ reflections in the TEM diffraction pattern (cf. Figure 38c). The nanodomains could have evolved into nanodomains of α″ and detected by XRD.

Alloy with the same composition (Ti-32Nb-7Zr-0.49O) has already been studied in the conventionally prepared form in Chapter 5, including the tensile testing shown in Figure 29e. One fact was not commented in that section which is a nonlinear behaviour before the yield point. From the analysis presented here, it can be concluded that this nonlinear behaviour is most probably caused by the stress-induced change of O′ nanodomains into α″ phase structure.

Based on the results of this chapter, two alloys were selected and prepared in bulk form by the classical route described in section 3.2. These alloys were chosen to potentially have a high yield strength due to the O content and high ductility due to the

proximity to martensitic composition and resulting TRIP / TWIP effects. This has restricted the selection to alloys with at least 0.5% O, lower oxygen content does not lead to the desired yield stress significantly higher than 600 MPa. At the same time, AE activity and detection of the martensitic lamellae in the deformed microstructure are crucial for TRIP / TWIP effect activation. Therefore, the chosen alloys are Ti-26Nb-7Zr-0.5O and Ti-29Nb-7Zr-0.5O and the following chapter is devoted to their examination.

7. Metastable Ti alloys with stress-induced phase transformations

The two selected compositions were prepared first by melting larger 200 g ingots, remelting them into the shape of rods and further homogenizing them at 1300 °C / 24 h which was followed by cold swaging and recrystallization annealing 1000 °C / 15 min concluded by water quenching. The content of oxygen and nitrogen is shown in Table 6. The O content is slightly higher than the target value but it is still closer to 0.5% than the previously studied 0.7%.

Table 6: Interstitial content (O/N) in prepared alloys measured by IGF.

Alloy	O (wt%)	N (wt%)
Ti-26Nb-7Zr-0.56O	0.559 ± 0.003	0.091 ± 0.002
Ti-29Nb-7Zr-0.54O	0.544 ± 0.003	0.055 ± 0.002

7.1. Microstructure and phase composition in ST condition

The prepared alloys showed equiaxed β phase grains with a size of about 100 – 200 μm as can be observed in Figure 66. Note that these images were captured in the longitudinal section of the prepared rods, therefore recrystallization annealing has removed any grain shape anisotropy that could have been present from the cold swaging. In the Ti-26Nb-7Zr-0.56O, the grain size is larger, which could be caused by the lower melting point of this alloy, caused by lower Nb content and thus the recrystallization temperature of 1000 °C leading effectively to faster grain growth. No dendritic segregation can be observed in the shown images; therefore, the homogenization annealing was also successful.

As shown in the previous chapter (Figure 36a), there is also a little of the athermal ω phase in the corresponding alloys in layered samples which was detected by XRD and for Ti-26Nb-7Zr-0.5O also by TEM (Figure 38a).

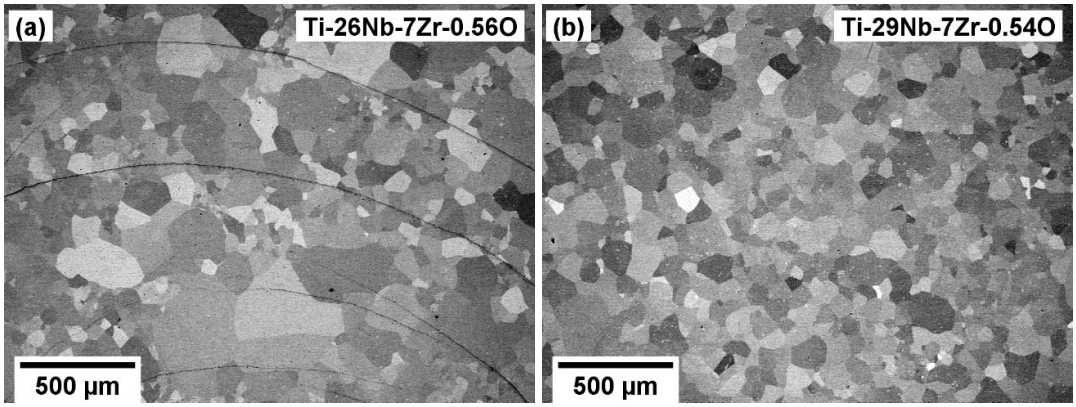

Figure 66: SEM images of the prepared alloys in the longitudinal sections.

7.2. Tensile testing

The tensile curves of the prepared alloys are shown in Figure 67. Contrary to expectations (SIM α″ should be active leading to high ductility due to the TRIP effect), the Ti-26Nb-7Zr-0.56O alloy shows much lower ductility of only about 6%. On the other hand, Ti-29Nb-7Zr-0.54O has reached a ductility of 20% which was reached also in other metastable β Ti alloys in the β solution-treated condition, e.g. those presented in 5. Both alloys have also qualitatively different behaviour: the Ti-26Nb-7Zr-0.56O

alloy reaches yield stress of nearly 1000 MPa and after that, the plastic deformation stage follows without any significant deformation strengthening that is finished by rupture at 6%. On the other hand, Ti-29Nb-7Zr-0.54O alloy first shows a double yielding; the first deviation from the linear elasticity starts at about 500 MPa and a slightly sharp yield point is present at 1100 MPa that is most probably caused by the interaction of dislocations with pinning oxygen atoms [75]. In the following part, very slight deformation strengthening is present until reaching the ultimate tensile strength at 1150 MPa and subsequent formation of a neck.

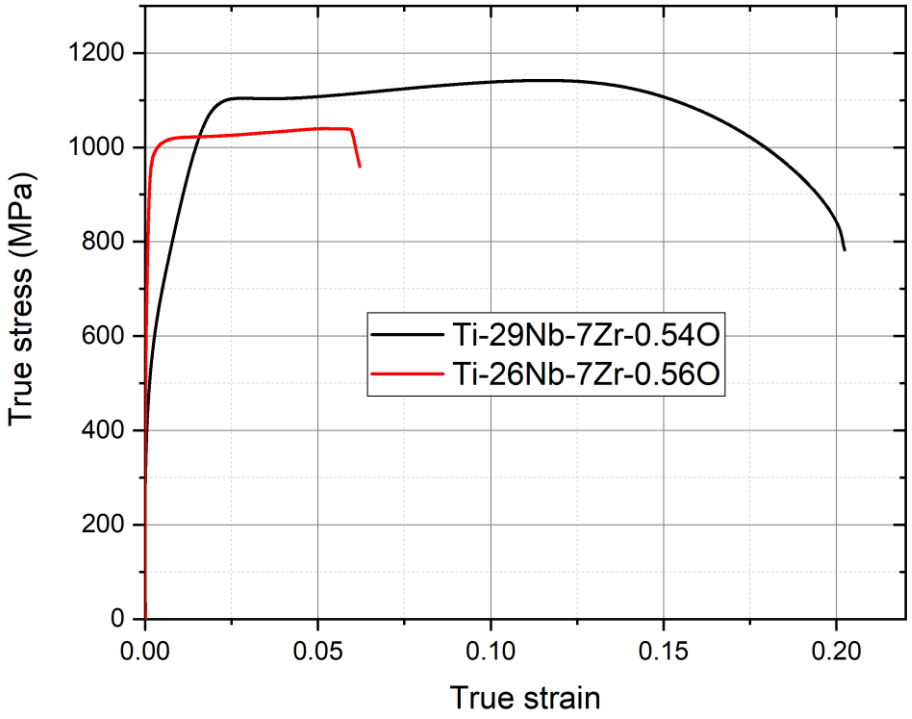

Figure 67: Tensile tests performed on the two alloys.

To be able to explain the differences in the measured tensile properties, the deformed samples were studied by SEM and XRD.

7.3. Microstructure and phase composition after tensile deformation

SEM images of the active parts of tensile samples are shown in Figure 3. As expected from the tensile testing results, Ti-26Nb-7Zr-0.56O alloy shows generally less deformed microstructure than Ti-29Nb-7Zr-0.54O alloy.

While in Figure 68a, the stress-induced martensite lamellae formed by the deformation of Ti-26Nb-7Zr-0.56O alloy are present, similarly to the microstructure after compression (cf. Figure 62), in Figure 68b, only dislocation slip traces are visible. In the respective alloy in layered samples after compression, few martensite-like lamellae were found, this difference could result from slightly higher O content in the alloy prepared in comparison to the sample prepared by FAST.

In Figure 69, XRD patterns measured at the active part of the tensile samples after deformation are shown. In the Ti-26Nb-7Zr-0.56O alloy, both the β and α″ phases are present which indicates that the lamellae shown in Figure 68a are SIM and not (at least not only) a deformation twinning.

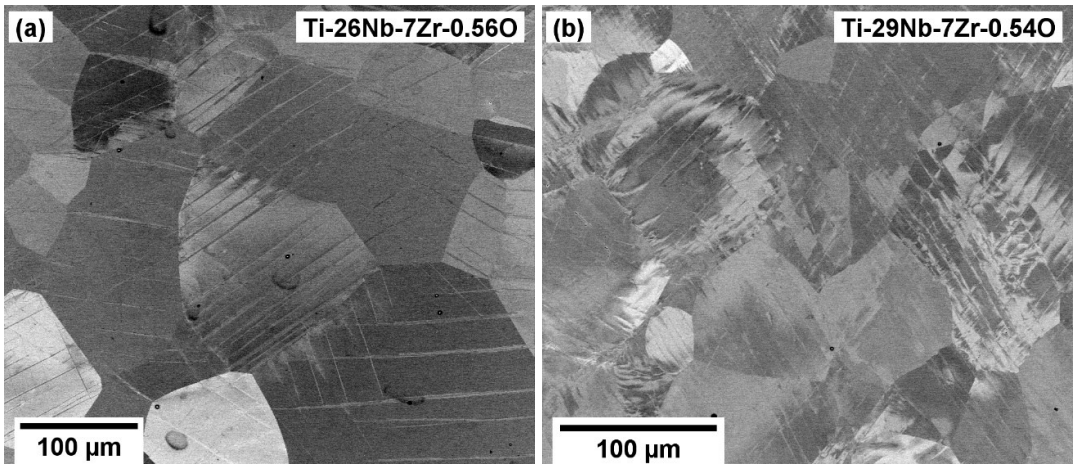

Figure 68: SEM microstructure images of active parts of tensile samples.

In the Ti-29Nb-7Zr-0.54O alloy, peaks of the β phase are the most prominent and very weak reflections from ω are also found (note that the Y-axis is drawn in logarithmic scale). A similar phase composition (β+ω phase) was found in this alloy also before deformation (layered samples, Figure 36a), therefore, classical stress-induced martensitic transformation is not active. Two more peaks cannot be assigned either to the β or ω phase. Peak located just above 15° could be assigned to (211) diffraction of β phase at higher harmonic energy passing through graphite monochromator (as described in section 3.1.4). In contrast, the other peak, positioned at an angle of 19° and marked by a star, cannot be explained as a result of higher harmonics. Nonetheless, is positioned between the (021) peak of the α″ phase and the simulated peak of O′ phase. Note that the α″ phase peak positions are shown for the case of Ti-26Nb-7Zr-0.56O alloy. It can be assumed (accordingly to trends shown in Figure 54) that in Ti-29Nb-7Zr-0.54O alloy, the shear component of α″ phase (the one causing the change of lattice parameters) is very weak and the peak marked by the star could be the (021) peak of the (nano-sized) α″ phase. This phase transformation could be the reason for the double-yielding phenomenon observed in Figure 67. It has been already suggested that the O′ nanodomains (formed by $\{011\} < \bar{1}\bar{1}1 >$ shuffle only) can be transformed into selected variants of α″ phase upon cooling or loading [51] as discussed later. However, for direct observation of the O′ phase or nano-sized α″ phase and their distinction, high-resolution TEM analysis would be necessary.

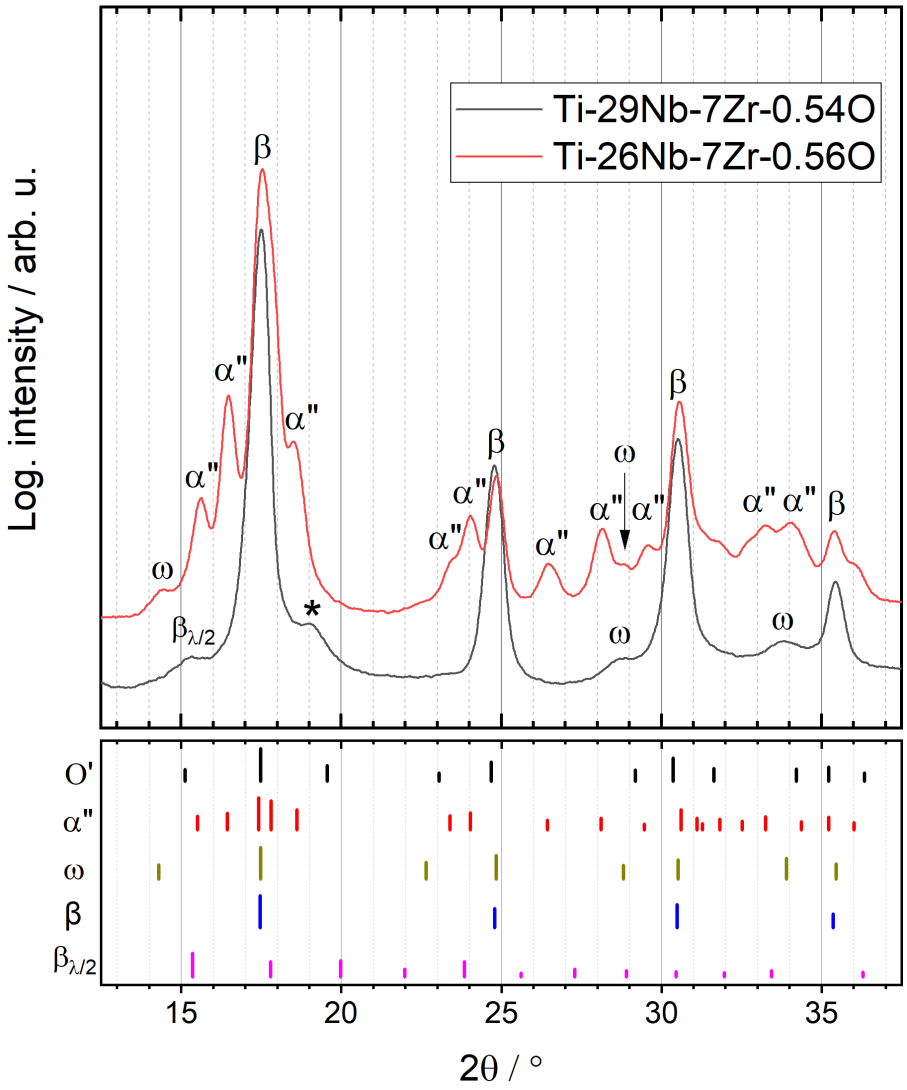

Figure 69: XRD patterns of studied alloys after tensile testing. The peak positions of the α" phase correspond to fitted lattice parameters of Ti-26Nb-7Zr-0.56O, peak positions for O' phase were calculated from the lattice parameter of β phase according to the lattice correspondence relations.

7.4. In-situ tensile testing

To get more insight into the contradiction of Ti-26Nb-7Zr-0.56O alloy undergoing the SIM during deformation while not showing the TRIP effect, but rather having very low ductility, in-situ tensile testing was performed on Ti-26Nb-7Zr-0.56O alloy (and on Ti-29Nb-7Zr-0.54O alloy, but in this case only the dislocation slip activity was observed). The chosen strain rate was the same as in the case of the bulk tensile tests and the step in which the SEM image collection took place was set to be about 0.02 mm of elongation which was equivalent to 0.5% of strain in the plastic region.

Figure 70a shows an SEM image of Ti-26Nb-7Zr-0.56O alloy taken at a stage of deformation equivalent to the strain of 1 %. Two different features can be recognized in the microstructure: 1) lamellae of α″ martensite marked by orange arrows and 2) slip traces marked by white arrows. These features differ mainly in width in the image. While martensite is a 3D region present in the material that appears as the 2D cut of lamella on the polished sample surface, slip traces are only steps that

were created on the sample surface by generation/annihilation of dislocations on the surface. Therefore, slip traces are only 1D features that appear as very thin lines in the SEM image due to the fact that the steps are not exactly parallel with the incident electron column.

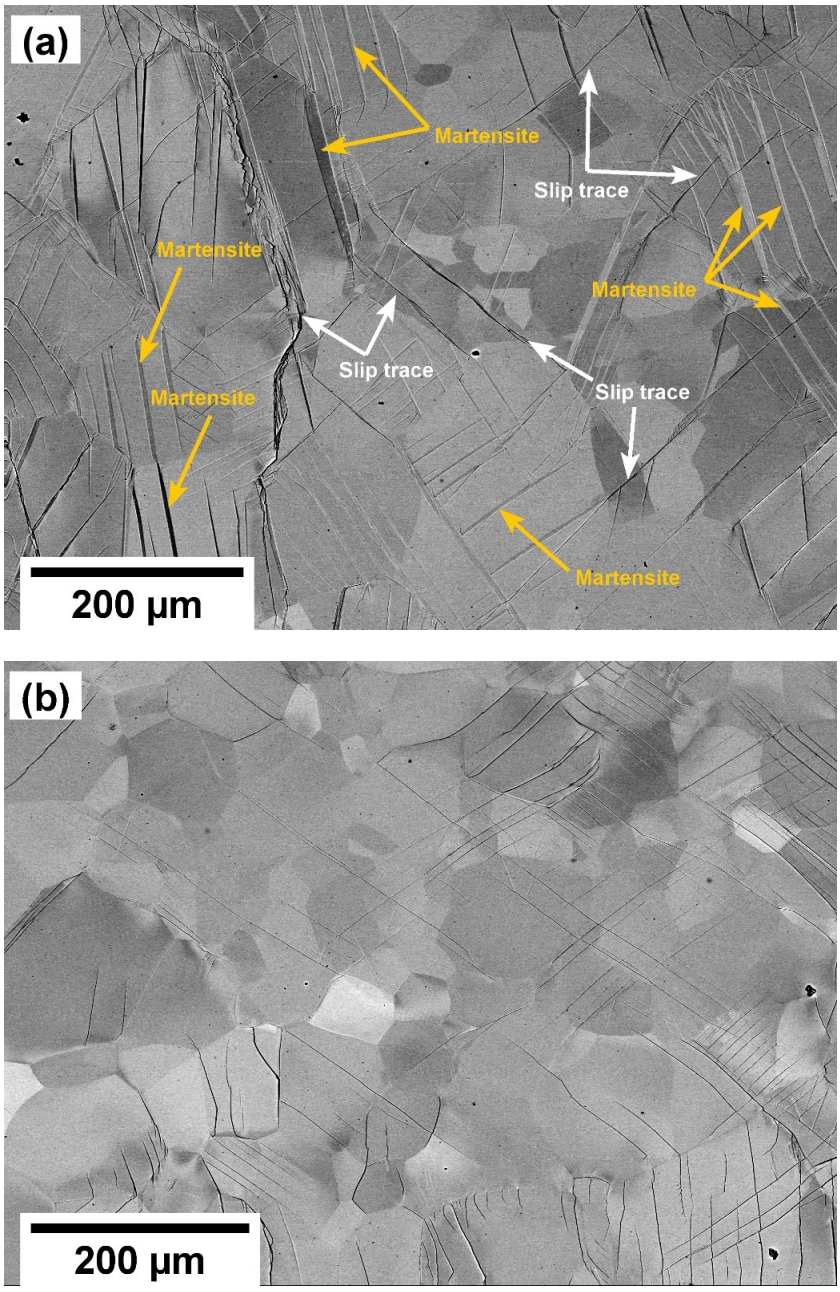

Figure 70: a) In-situ SEM image of Ti-26Nb-7Zr-0.56O alloy during tensile test at a true strain of 1%. Arrows mark the selected locations of both stress-induced martensite and slip traces. b) In-situ SEM image of Ti-29Nb-7Zr-0.54O alloy, showing slip traces only.

Consistently with ex-situ observations, Ti-29Nb-7Zr-0.54O alloy showed the slip traces only during SEM in-situ tensile test as shown in Figure 70b.

The presence of both deformation mechanisms in Ti-26Nb-7Zr-0.56O alloy in such an early stage of deformation is most probably the reason for the low achieved ductility of material with active SIM. Formation of α″ martensite is an essential condition for achieving the TRIP effect (and associated improvement in ductility) and

if formed, secondary SIM lamellae and/or twinning inside the α″ SIM usually follow as well [199,200]. The dislocation slip is then activated as the last deformation mechanism. In Ti-26Nb-7Zr-0.56O alloy, only primary α″ martensite was formed during tension without any usual formation of secondary twins and concurrently, the dislocation slip was also activated. The reason is most probably the high content of interstitial oxygen. Oxygen is believed to block the α″ SIM in general [72,74]. In contrast, an O-rich composition which undergoes SIM during tension has been found, yet, it does not lead to the desired properties (i.e. TRIP effect).

Overview SEM images at various stages of the tensile test are shown in Figure 71. At this low magnification, different deformation mechanisms cannot be resolved, but the crack formation was observed at the bottom edge of the sample active part. The crack started to form at a true strain of about 2.5 % and grew progressively until it was not safe to continue with the tensile test at 5 %.

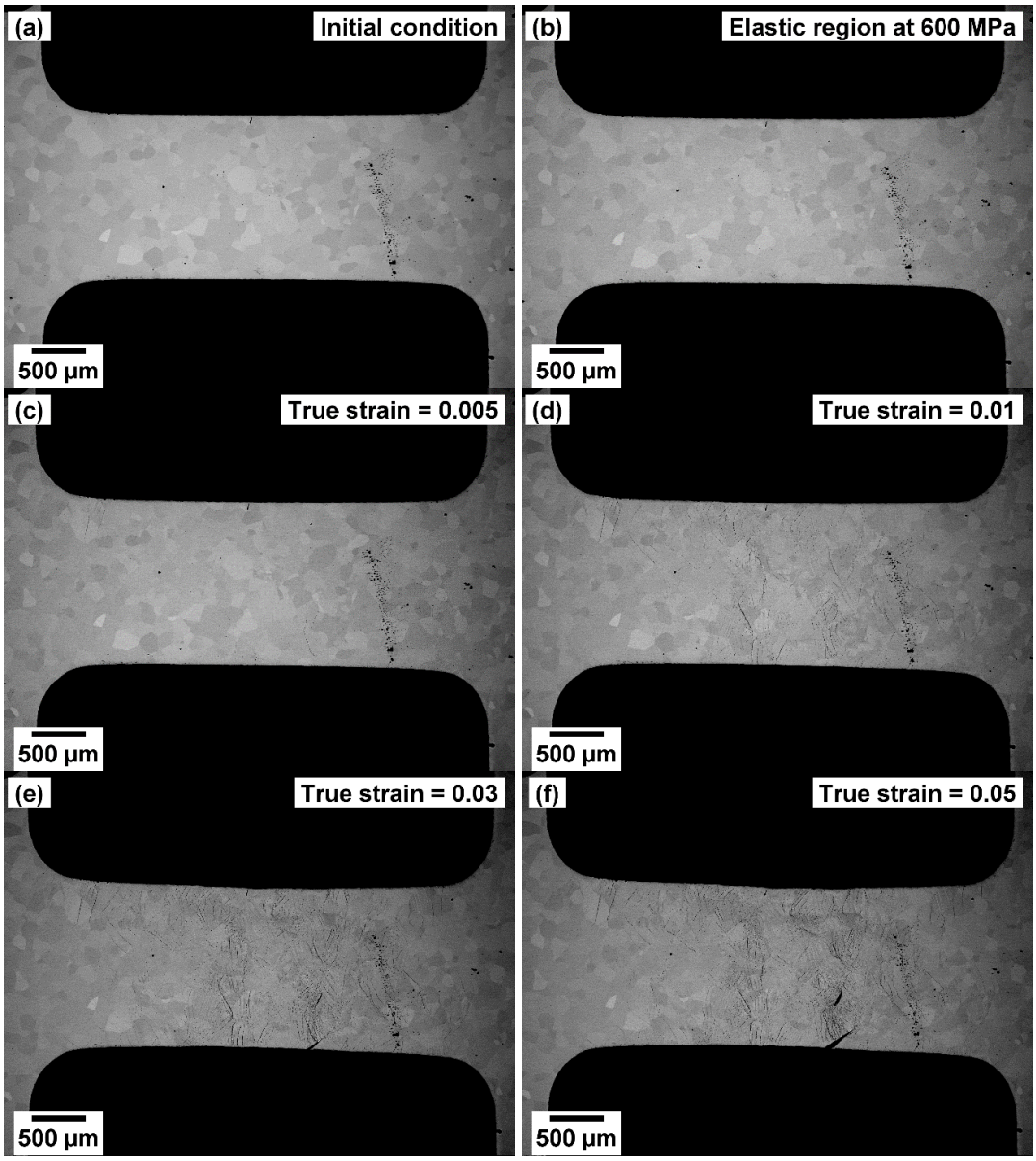

Figure 71: An overview of SEM images captured at various stages of tensile deformation. The crack formation can be noticed at true strains 0.03 and 0.05.

The crack location was captured also before the crack has initiated. Both SE and BSE images are shown in Figure 72 comparing this area without and with the crack. It can be observed that the crack was nucleated at a position where the first slip traces were observed, not the martensite. Based on previous findings of this thesis, shown in Chapter 5, O-rich metastable Ti alloys which contain a high fraction of ω phase tend to be brittle. Therefore, the brittleness of this alloy is most probably caused by the initial β+ω microstructure (together with high O content) and even the activation of α″ SIM cannot overcome this inherent property of O-rich alloy.

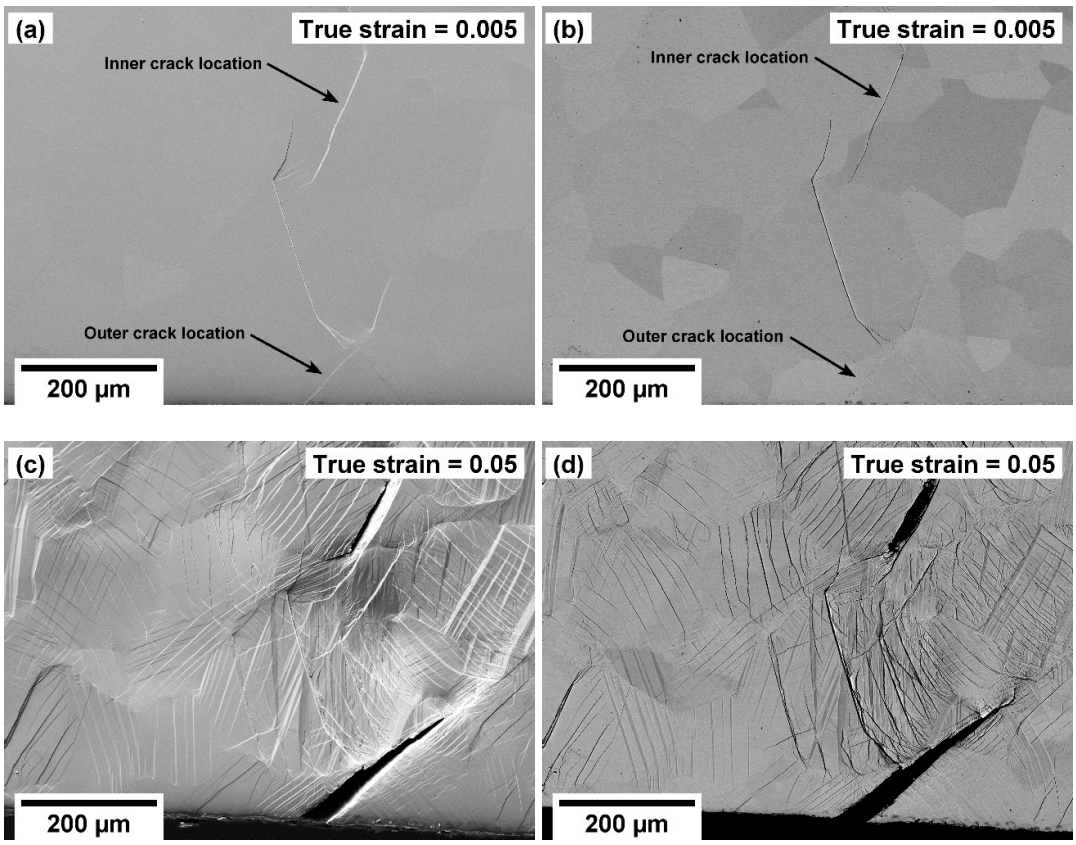

Figure 72: Location of crack formation observed before the crack has initiated (true strain 0.5 %) in a) SE signal, b) BSE signal. Final stage of deformation with large crack observed in c) SE signal and d) BSE signal.

7.5. Discussion of the deformation mechanisms and selection of the best alloy

The two alloys that were prepared and tested show significantly different behaviour. Despite the deformation mechanism by SIM α″ phase formation is present in Ti-26Nb-7Zr-0.56O, it results neither in double yielding nor does it show improved ductility due to the TRIP effect. Rather contrary, the elongation is very low. This behaviour is contrasting with the results of compression tests, where this alloy achieved a true strain of nearly 0.4. The ω phase-caused brittleness expressed itself in tension much sooner, however, this is common behaviour of materials, that are generally more prone to fracture when exposed to tensile stresses rather than compression stresses.

The second alloy does not form α″ SIM not deformation twinning during tension, as shown by both ex-situ and in-situ SEM observations. On the other hand, the double yielding present in the tensile curve is a typical expression of α″ SIM formation [40],

although it was usually found to be suppressed by O content higher than 1 at.% (0.28 wt%) [44,167]. The presented suppression mechanism of oxygen was presented as a formation of modulation of the bcc lattice from the octahedral interstitial positions which resulted in the formation of nanodomains that blocked the large-scale martensitic transformation to α″ (the lamellae) [152]. Such nanodomains that were later called O′ phase [198] were found also in the materials studied in this thesis that contain even higher oxygen content (Figure 27c showing the O′ particles in TEM dark-field and Figure 38c showing the TEM diffraction). While the formation of the O′ itself cannot accommodate any large-scale strain due to the shuffle of atomic planes only, when the α″ phase involving lattice shear is formed, it is connected with strains according to (Equation 6). The formation of α″ structure from O′ precursors has been already confirmed unambiguously with the use of high-resolution TEM during in-situ cooling [51] and after cold-rolling where this was connected with the [332]<113> twin formation as well [201]. It was also found that when the O′ nanodomains serve as precursors for O′ → α″ transformation, they also restrict the possible variants of martensite from 12 in pure bcc structure to only 2 per O′ precursor [51]. This leads to the so-called strain-glass transition, i.e. higher-order phase transformation continuously increasing the shear in the nanodomains as it was observed in [202], where the lattice parameters corresponding to the shear component of β→α″ transformation were changing during the early stages of tensile test, between 2 and 5% of strain (note that the elastic part of the tensile curve was not subtracted as it was in Figure 67).

The above-presented mechanism seems to be viable also for the explanation of the double-yielding phenomenon of the Ti-29Nb-7Zr-0.54O alloy, where no large-scale α″ SIM was formed in the microstructure, but additional peaks were found in the XRD patterns in the deformed material. A similar effect in a tensile curve, although with less pronounced non-linearity was found also for one of the alloys presented in Chapter 5: Ti-32Nb-7Zr-0.5O (Figure 29e), which differs in Nb content only and both alloys could thus share the same mechanism of gradual O′ → α″ transition during loading. It is not surprising that the effect is more pronounced in alloy with less Nb as this composition is also closer to compositions undergoing the large-scale α″ SIM formation.

In summary, the target combination of the desired effects (high oxygen content leading to strengthening and TRIP effect leading to high ductility) was not achieved – the Ti-26Nb-7Zr-0.56O is brittle while Ti-29Nb-7Zr-0.54O alloy shows deviation from linear elasticity already at 500 MPa. The achieved mechanical properties are still better in the selected alloys from Chapter 5.

Since industrial alloy production needs some flexibility in the alloy composition, the target contents must be given as intervals (for the common alloying elements) or as maximum permissible contents (typically for impurities such as N, O and H). This is common practice not only for Ti alloy grades [64] but other materials as well (e.g. steels for surgical applications [203]) and is based on the fact that large-scale manufacturing cannot achieve the precision of laboratory production and the input materials are of the (cheap) commercial purity. For this reason, the following rules are specified for the alloy that was found the most suitable for implant manufacturing in this thesis:

- The main alloying element is Nb and its concentration is between 29 and 32 wt%.
- Another alloying element is Zr with a concentration between 6.5 and 7.5 wt%. Unpurified (Hf-containing) Zr can be used.

- The O content is between 0.7 and 0.85 wt%
- The N content should be kept below 0.05 wt%. Very low N concentrations (below 0.01 wt%) can lead to different tensile behaviour of the material, however, they are not easily achievable on an industrial scale, where the price of input materials is of major importance.
- Other impurities should be kept within the usual limits of commercial alloys: the C content below 0.08 wt%, Fe below 0.3 wt% and residuals below 0.01 wt% each and 0.04 wt% in total.
- Titanium forms the rest of the chemical composition.

While higher β phase stability would cause an increase in Young's modulus "only", lower stability could result in brittleness, therefore the final composition is playing it safe by keeping away from the dangerous compositions embrittled by ω phase.

The alloy specified in the bullet points is similar to the Ti-35Nb-7Zr-6Ta-0.7O alloy, from a metallurgical point of view, therefore the industrial processing developed and described in Chapter 4 is readily usable for implant manufacturing from the specified alloy. Due to omitting the Ta content and lowering the Nb content, the resulting alloy has an even lower melting point which should have a positive impact on the melting feasibility as well as faster homogenization and finally to reduced costs.

Conclusions

The principal aim of this thesis titled *Beta-Ti alloys for medical applications* was to develop a Ti alloy with a target application in joint implant manufacturing. Such a task consisted of two main contributions: 1) to design the most suitable pathways for processing of the alloy and 2) to find the best chemical composition of the alloy. Both tasks were being solved simultaneously, but I will summarize them here apart from each other for clarity.

The processing of the metastable β-Ti alloys was studied on two distinctly different scales: large industrial scale for the products manufacturing and laboratory scale for alloy development. In both cases, similar processing steps were undergone (casting, homogenization, rotary swaging, recrystallization annealing) which ensured that the developed alloys can be readily processed in large scale yielding the same material properties as measured on laboratory scale.

The search for the most suitable chemical composition was also done on two scales: classical and high throughput.

The classical approach involved the preparation of laboratory-scale yet bulk alloys. The set desired properties were high yield strength, high ductility and low Young's modulus. The high yield strength (compared to the reference Ti-6Al-4V alloy) was achieved by high oxygen content in all prepared alloys. The main limiting factor for ductility was found to be the phase composition: when the ω or α″ phase was present in the material with high O content in a significant fraction, it had an embrittling effect. Alloys with β structure only were all sufficiently ductile (the nano-scale O′ phase was found as well but it did not affect the ductility). The Young's modulus was minimized by tailoring the composition to reach the lattice softening due to proximity to martensitic transformation. Avoiding the ω phase formation was the main criterion for the selection of the best alloy.

The high-throughput approach allowed the testing of a high number of different compositions. The characterization of microstructure and phase composition involved methods easily usable for high-throughput testing: SEM, XRD, microhardness measurements, scanning acoustic microscopy and compression testing coupled with AE measurement and DIC evaluation of local strains. Key result is that the oxygen and niobium atoms have a very similar contribution to the stabilization of the β phase with respect to the martensitic transformation to α″.

One of the most important findings of the thesis is the nature of the ω phase in O-rich alloys. In water quenched samples, ω phase should form without any elemental redistribution, which is commonly referred to as athermal ω. The athermal ω has usually only a negligible effect on the mechanical properties of Ti alloys. In contrast, the presence of higher amounts athermal ω phase directly resulted in ductility deterioration in alloys with high oxygen content. Results of measurements of elastic properties suggested that the behaviour of the athermal ω phase after quenching corresponds rather to the isothermal ω phase formed typically after annealing. It was therefore concluded that oxygen can diffuse into the ω phase even at room temperature, which alters its effect on mechanical properties.

XRD analysis showed that higher stabilization of the β phase results in that the lattice parameters of the SIM α″ are closer to those of the β phase. At the same time, lower fraction of α″ is formed. This is due to the fact, that smaller differences in lattice parameters cause smaller accommodated strain by SIM formation and the formation of SIM becomes less favourable. Unique O′ phase nano-domains were resolved by TEM and their transformation into nano-sized particles of α″ phase was also discussed.

Potential of activation of SIM α″ deformation mechanism was studied, however positive effect of TRIP/TWIP on ductility was not achieved. Nevertheless, several compositions of alloys proved unique combination of strength, elastic modulus and ductility, making them ideal candidates for production of load-bearing implants of large joints.

Further opportunities in the field of production of metallic biomedical implants are already open. In particular, additive manufacturing represents a progressive method for manufacturing parts of various sizes and shapes. It is already being considered for production from costly materials such as Ti alloys, where the reduction of waste could save large amounts of resources as well as increase sustainability. The benefits of additive manufacturing directly related to the medical field are the inherent net-shape manufacturing and also the unique possibility of creating graded structures, that will have different properties in different locations (for instance, low Young's modulus near the bone, high strength at the most stressed areas). Such graded material may fulfil contradictory requirements for implant material properties. This research will be of interest in future.

References:

[1] F. Gao, Z. Nie, D. Yang, B. Sun, Y. Liu, X. Gong, Z. Wang, Environmental impacts analysis of titanium sponge production using Kroll process in China, Journal of Cleaner Production. 174 (2018) 771–779. https://doi.org/10.1016/j.jclepro.2017.09.240.

[2] M. Geetha, A.K. Singh, R. Asokamani, A.K. Gogia, Ti based biomaterials, the ultimate choice for orthopaedic implants – A review, Progress in Materials Science. 54 (2009) 397–425. https://doi.org/10.1016/j.pmatsci.2008.06.004.

[3] M. Abdel-Hady Gepreel, M. Niinomi, Biocompatibility of Ti-alloys for long-term implantation, Journal of the Mechanical Behavior of Biomedical Materials. 20 (2013) 407–415. https://doi.org/10.1016/j.jmbbm.2012.11.014.

[4] M. Long, H.J. Rack, Titanium alloys in total joint replacement—a materials science perspective, Biomaterials. 19 (1998) 1621–1639. https://doi.org/10.1016/S0142-9612(97)00146-4.

[5] Y.T. Lee, G. Welsch, Young's modulus and damping of Ti-6Al-4V alloy as a function of heat treatment and oxygen concentration, Materials Science and Engineering: A. 128 (1990) 77–89. https://doi.org/10.1016/0921-5093(90)90097-M.

[6] G. Welsch, R. Boyer, E.W. Collings, Materials Properties Handbook: Titanium Alloys, ASM International, 1993.

[7] J.-Y. Rho, T.Y. Tsui, G.M. Pharr, Elastic properties of human cortical and trabecular lamellar bone measured by nanoindentation, Biomaterials. 18 (1997) 1325–1330. https://doi.org/10.1016/S0142-9612(97)00073-2.

[8] P.K. Zysset, X. Edward Guo, C. Edward Hoffler, K.E. Moore, S.A. Goldstein, Elastic modulus and hardness of cortical and trabecular bone lamellae measured by nanoindentation in the human femur, Journal of Biomechanics. 32 (1999) 1005–1012. https://doi.org/10.1016/S0021-9290(99)00111-6.

[9] M.G. Joshi, S.G. Advani, F. Miller, M.H. Santare, Analysis of a femoral hip prosthesis designed to reduce stress shielding, J Biomech. 33 (2000) 1655–1662.

[10] Y. Watanabe, N. Shiba, S. Matsuo, F. Higuchi, Y. Tagawa, A. Inoue, Biomechanical study of the resurfacing hip arthroplasty: Finite element analysis of the femoral component, The Journal of Arthroplasty. 15 (2000) 505–511. https://doi.org/10.1054/arth.2000.1359.

[11] D.R. Sumner, Long-term implant fixation and stress-shielding in total hip replacement, Journal of Biomechanics. 48 (2015) 797–800. https://doi.org/10.1016/j.jbiomech.2014.12.021.

[12] C. Oldani, A. Dominguez, Titanium as a Biomaterial for Implants, (2012). https://doi.org/10.5772/27413.

[13] M. Niinomi, Mechanical biocompatibilities of titanium alloys for biomedical applications, Journal of the Mechanical Behavior of Biomedical Materials. 1 (2008) 30–42. https://doi.org/10.1016/j.jmbbm.2007.07.001.

[14] E. Eisenbarth, D. Velten, M. Müller, R. Thull, J. Breme, Biocompatibility of β-stabilizing elements of titanium alloys, Biomaterials. 25 (2004) 5705–5713. https://doi.org/10.1016/j.biomaterials.2004.01.021.

[15] J. Taylor, S. Keith, L. Cseh, L. Ingerman, L. Chappell, J. Rhoades, A. Hueber, Toxicological profile for vanadium, Atlanta, US: Agency for Toxic Substances and Disease Registry. (2012) 255.

[16] S. Maya, T. Prakash, K.D. Madhu, D. Goli, Multifaceted effects of aluminium in neurodegenerative diseases: A review, Biomedicine & Pharmacotherapy. 83 (2016) 746–754. https://doi.org/10.1016/j.biopha.2016.07.035.

[17] K. Zaman, A. Zaman, J. Batcabe, Hematological effects of aluminum on living organisms, Comp. Biochem. Physiol. C, Comp. Pharmacol. Toxicol. 106 (1993) 285–293.

[18] C. Leyens, M. Peters, Titanium and titanium alloys, Wiley Online Library, 2003. http://onlinelibrary.wiley.com/doi/10.1002/3527608117.fmatter/summary (accessed November 16, 2016).

[19] K. Šalata, Structure parameters of martensite in Ti alloys modified by presence of oxygen atoms, Diploma thesis, Charles University, 2023.
[20] S. Banerjee, P. Mukhopadhyay, Phase Transformations: Examples from Titanium and Zirconium Alloys, Elsevier, 2010.
[21] H.Y. Kim, S. Miyazaki, Chapter 1 - Martensitic Transformation Characteristics, in: H.Y. Kim, S. Miyazaki (Eds.), Ni-Free Ti-Based Shape Memory Alloys, Butterworth-Heinemann, 2018: pp. 1–52. https://doi.org/10.1016/B978-0-12-809401-3.00001-X.
[22] W.G. Burgers, On the process of transition of the cubic-body-centered modification into the hexagonal-close-packed modification of zirconium, Physica. 1 (1934) 561–586. https://doi.org/10.1016/S0031-8914(34)80244-3.
[23] G. Lütjering, J.C. Williams, Titanium, 2nd ed., Springer-Verlag, Berlin Heidelberg, 2007. https://www.springer.com/gp/book/9783540713975 (accessed October 7, 2019).
[24] P.D. Frost, W.M. Parris, L.L. Hirsch, J.R. Doig, C.M. Schwartz, Isothermal transformation of titanium-chromium alloys, Trans ASM. 1954 (1954) 231–256.
[25] J. Dutta, G. Ananthakrishna, S. Banerjee, On the athermal nature of the β to ω transformation, Acta Materialia. 60 (2012) 556–564. https://doi.org/10.1016/j.actamat.2011.10.005.
[26] T. Li, D. Kent, G. Sha, L.T. Stephenson, A.V. Ceguerra, S.P. Ringer, M.S. Dargusch, J.M. Cairney, New insights into the phase transformations to isothermal ω and ω-assisted α in near β-Ti alloys, Acta Materialia. 106 (2016) 353–366. https://doi.org/10.1016/j.actamat.2015.12.046.
[27] Y.N. Gornostyrev, M.I. Katsnelson, Misfit stabilized embedded nanoparticles in metallic alloys, Phys. Chem. Chem. Phys. 17 (2015) 27249–27257. https://doi.org/10.1039/C5CP04641F.
[28] Y. Zheng, S. Antonov, Q. Feng, R. Banerjee, D. Banerjee, H.L. Fraser, Shuffle-induced modulated structure and heating-induced ordering in the metastable β-titanium alloy, Ti-5Al-5Mo-5V-3Cr, Scripta Materialia. 176 (2020) 7–11. https://doi.org/10.1016/j.scriptamat.2019.09.027.
[29] Y. Zheng, R.E.A. Williams, S. Nag, R. Banerjee, H.L. Fraser, D. Banerjee, The effect of alloy composition on instabilities in the β phase of titanium alloys, Scripta Materialia. 116 (2016) 49–52. https://doi.org/10.1016/j.scriptamat.2016.01.024.
[30] P. Zháňal, P. Harcuba, J. Stráský, J. Šmilauerová, P. Beran, T.C. Hansen, H. Seiner, M. Janeček, Transformation Pathway upon Heating of Metastable β Titanium Alloy Ti-15Mo Investigated by Neutron Diffraction, Materials. 12 (2019) 3570. https://doi.org/10.3390/ma12213570.
[31] A. Devaraj, S. Nag, R. Srinivasan, R.E.A. Williams, S. Banerjee, R. Banerjee, H.L. Fraser, Experimental evidence of concurrent compositional and structural instabilities leading to ω precipitation in titanium–molybdenum alloys, Acta Materialia. 60 (2012) 596–609. https://doi.org/10.1016/j.actamat.2011.10.008.
[32] S. Azimzadeh, H.J. Rack, Phase transformations in Ti-6.8Mo-4.5Fe-1.5Al, Metall Mater Trans A. 29 (1998) 2455–2467. https://doi.org/10.1007/s11661-998-0217-8.
[33] P. Zháňal, P. Harcuba, M. Hájek, J. Stráský, J. Šmilauerová, J. Veselý, L. Horák, M. Janeček, V. Holý, In situ detection of stability limit of ω phase in Ti–15Mo alloy during heating, Journal of Applied Crystallography. 52 (2019) 1061–1071. https://doi.org/10.1107/S1600576719010537.
[34] T. Li, M. Lai, A. Kostka, S. Salomon, S. Zhang, C. Somsen, M.S. Dargusch, D. Kent, Composition of the nanosized orthorhombic O′ phase and its direct transformation to fine α during ageing in metastable β-Ti alloys, Scripta Materialia. 170 (2019) 183–188. https://doi.org/10.1016/j.scriptamat.2019.06.008.
[35] E. Aeby-Gautier, A. Settefrati, F. Bruneseaux, B. Appolaire, B. Denand, M. Dehmas, G. Geandier, P. Boulet, Isothermal α″ formation in β metastable titanium alloys, Journal of Alloys and Compounds. 577 (2013) S439–S443. https://doi.org/10.1016/j.jallcom.2012.02.046.
[36] H. Wang, D.K.Z. Lai, J. Xu, W. Yin, C. Song, Y. Zhao, Y. Yang, M. Bönisch, Z. Sun, Nano-precipitation leading to linear zero thermal expansion over a wide temperature

range in Ti22Nb, Scripta Materialia. 205 (2021) 114222. https://doi.org/10.1016/j.scriptamat.2021.114222.
[37] K.K. Kharia, H.J. Rack, Martensitic phase transformations in IMI 550 (Ti-4Al-4Mo-2Sn-0.5 Si), Metall and Mat Trans A. 32 (2001) 671–679. https://doi.org/10.1007/s11661-001-0083-0.
[38] W. Elmay, F. Prima, T. Gloriant, B. Bolle, Y. Zhong, E. Patoor, P. Laheurte, Effects of thermomechanical process on the microstructure and mechanical properties of a fully martensitic titanium-based biomedical alloy, Journal of the Mechanical Behavior of Biomedical Materials. 18 (2013) 47–56. https://doi.org/10.1016/j.jmbbm.2012.10.018.
[39] R. Davis, H.M. Flower, D.R.F. West, The decomposition of Ti-Mo alloy martensites by nucleation and growth and spinodal mechanisms, Acta Metallurgica. 27 (1979) 1041–1052. https://doi.org/10.1016/0001-6160(79)90192-5.
[40] F.Q. Hou, S.J. Li, Y.L. Hao, R. Yang, Nonlinear elastic deformation behaviour of Ti-30Nb-12Zr alloys, Scripta Materialia. 63 (2010) 54–57. https://doi.org/10.1016/j.scriptamat.2010.03.011.
[41] S.J. Li, M.T. Jia, F. Prima, Y.L. Hao, R. Yang, Improvements in nonlinear elasticity and strength by grain refinement in a titanium alloy with high oxygen content, Scripta Materialia. 64 (2011) 1015–1018. https://doi.org/10.1016/j.scriptamat.2011.02.006.
[42] S.Q. Zhang, S.J. Li, M.T. Jia, F. Prima, L.J. Chen, Y.L. Hao, R. Yang, Low-cycle fatigue properties of a titanium alloy exhibiting nonlinear elastic deformation behavior, Acta Materialia. 59 (2011) 4690–4699. https://doi.org/10.1016/j.actamat.2011.04.015.
[43] W.J. Buehler, J.V. Gilfrich, R.C. Wiley, Effect of Low-Temperature Phase Changes on the Mechanical Properties of Alloys near Composition TiNi, Journal of Applied Physics. 34 (1963) 1475–1477. https://doi.org/10.1063/1.1729603.
[44] J.I. Kim, H.Y. Kim, H. Hosoda, S. Miyazaki, Shape Memory Behavior of Ti–22Nb–(0.5–2.0)O(at%) Biomedical Alloys, Materials Transactions. 46 (2005) 852–857. https://doi.org/10.2320/matertrans.46.852.
[45] N.L. Church, C.E.P. Talbot, N.G. Jones, On the Influence of Thermal History on the Martensitic Transformation in Ti-24Nb-4Zr-8Sn (wt%), Shap. Mem. Superelasticity. (2021). https://doi.org/10.1007/s40830-021-00309-2.
[46] H.Y. Kim, S. Miyazaki, Several Issues in the Development of Ti–Nb-Based Shape Memory Alloys, Shap. Mem. Superelasticity. 2 (2016) 380–390. https://doi.org/10.1007/s40830-016-0087-7.
[47] H. Liu, M. Niinomi, M. Nakai, K. Cho, Athermal and deformation-induced ω-phase transformations in biomedical beta-type alloy Ti–9Cr–0.2O, Acta Materialia. 106 (2016) 162–170. https://doi.org/10.1016/j.actamat.2016.01.008.
[48] H. Liu, M. Niinomi, M. Nakai, J. Hieda, K. Cho, Deformation-induced changeable Young's modulus with high strength in β-type Ti–Cr–O alloys for spinal fixture, Journal of the Mechanical Behavior of Biomedical Materials. 30 (2014) 205–213. https://doi.org/10.1016/j.jmbbm.2013.11.001.
[49] P. Castany, Y. Yang, E. Bertrand, T. Gloriant, Reversion of a Parent { 130 } ⟨ 310 ⟩ α′′ Martensitic Twinning System at the Origin of { 332 } ⟨ 113 ⟩ β Twins Observed in Metastable β Titanium Alloys, Phys. Rev. Lett. 117 (2016) 245501. https://doi.org/10.1103/PhysRevLett.117.245501.
[50] Y. Yang, P. Castany, E. Bertrand, M. Cornen, J.X. Lin, T. Gloriant, Stress release-induced interfacial twin boundary ω phase formation in a β type Ti-based single crystal displaying stress-induced α" martensitic transformation, Acta Materialia. 149 (2018) 97–107. https://doi.org/10.1016/j.actamat.2018.02.036.
[51] Q. Liang, D. Wang, Y. Zheng, S. Zhao, Y. Gao, Y. Hao, R. Yang, D. Banerjee, H.L. Fraser, Y. Wang, Shuffle-nanodomain regulated strain glass transition in Ti-24Nb-4Zr-8Sn alloy, Acta Materialia. 186 (2020) 415–424. https://doi.org/10.1016/j.actamat.2019.12.056.
[52] D. Kuroda, M. Niinomi, M. Morinaga, Y. Kato, T. Yashiro, Design and mechanical properties of new β type titanium alloys for implant materials, Materials Science and

Engineering: A. 243 (1998) 244–249. https://doi.org/10.1016/S0921-5093(97)00808-3.
[53] T. Ahmed, H. Rack, Low modulus biocompatible titanium base alloys for medical devices, US patent no. 5,871,595., 1999.
[54] X. Tang, T. Ahmed, H.J. Rack, Phase Transformations in Ti-Nb-Ta and Ti-Nb-Ta-Zr Alloys, Journal of Materials Science. 35 (2000) 1805–1811.
[55] R. Labusch, A Statistical Theory of Solid Solution Hardening, Physica Status Solidi (b). 41 (1970) 659–669. https://doi.org/10.1002/pssb.19700410221.
[56] J. Málek, F. Hnilica, J. Veselý, B. Smola, K. Kolařík, J. Fojt, M. Vlach, V. Kodetová, The effect of Zr on the microstructure and properties of Ti-35Nb-XZr alloy, Materials Science and Engineering: A. 675 (2016) 1–10. https://doi.org/10.1016/j.msea.2016.07.069.
[57] Y.L. Zhou, M. Niinomi, T. Akahori, Effects of Ta content on Young's modulus and tensile properties of binary Ti–Ta alloys for biomedical applications, Materials Science and Engineering: A. 371 (2004) 283–290. https://doi.org/10.1016/j.msea.2003.12.011.
[58] I. Kopova, J. Stráský, P. Harcuba, M. Landa, M. Janeček, L. Bačákova, Newly developed Ti–Nb–Zr–Ta–Si–Fe biomedical beta titanium alloys with increased strength and enhanced biocompatibility, Materials Science and Engineering: C. 60 (2016) 230–238. https://doi.org/10.1016/j.msec.2015.11.043.
[59] B.W. Levinger, Lattice parameters of beta titanium at room temperature, Journal of Metals. 5 (1953) 195.
[60] C.D. Ling, M. Avdeev, R. Kutteh, V.V. Kharton, A.A. Yaremchenko, S. Fialkova, N. Sharma, R.B. Macquart, M. Hoelzel, M. Gutmann, Structures, Phase Transitions, Hydration, and Ionic Conductivity of Ba4Nb2O9, Chem. Mater. 21 (2009) 3853–3864. https://doi.org/10.1021/cm901644e.
[61] R.W.G. Wyckoff, Crystal Structures - Volume 1, 2nd ed, Interscience Publishers, New York, 1963.
[62] M.H. Mueller, Lattice parameter of tantalum, Scr. Metall.; (United States). 11:8 (1977). https://doi.org/10.1016/0036-9748(77)90141-7.
[63] M. Yan, W. Xu, M.S. Dargusch, H.P. Tang, M. Brandt, M. Qian, Review of effect of oxygen on room temperature ductility of titanium and titanium alloys, Powder Metallurgy. 57 (2014) 251–257. https://doi.org/10.1179/1743290114Y.0000000108.
[64] ASTM B265-20a Standard Specification for Titanium and Titanium Alloy Strip, Sheet, and Plate, ASTM International, n.d. https://www.astm.org/b0265-20a.html (accessed June 6, 2023).
[65] F. Amann, R. Poulain, S. Delannoy, J.P. Couzinié, E. Clouet, I. Guillot, F. Prima, An improved combination of tensile strength and ductility in titanium alloys via oxygen ordering, Materials Science and Engineering: A. 867 (2023) 144720. https://doi.org/10.1016/j.msea.2023.144720.
[66] R. Poulain, S. Delannoy, I. Guillot, F. Amann, R. Guillou, S. Lartigue-Korinek, D. Thiaudière, J.-L. Béchade, E. Clouet, F. Prima, First experimental evidence of oxygen ordering in dilute titanium–oxygen alloys, Materials Research Letters. 10 (2022) 481–487. https://doi.org/10.1080/21663831.2022.2057202.
[67] T. Saito, T. Furuta, J.-H. Hwang, S. Kuramoto, K. Nishino, N. Suzuki, R. Chen, A. Yamada, K. Ito, Y. Seno, T. Nonaka, H. Ikehata, N. Nagasako, C. Iwamoto, Y. Ikuhara, T. Sakuma, Multifunctional Alloys Obtained via a Dislocation-Free Plastic Deformation Mechanism, Science. 300 (2003) 464–467. https://doi.org/10.1126/science.1081957.
[68] S. Kuramoto, T. Furuta, J.H. Hwang, K. Nishino, T. Saito, Plastic Deformation in a Multifunctional Ti-Nb-Ta-Zr-O Alloy, Metallurgical and Materials Transactions: Physical Metallurgy and Materials Science, A; New York. 37A (2006) 657–662.
[69] W. Guo, M.Z. Quadir, M. Ferry, The Mode of Deformation in a Cold-Swaged Multifunctional Ti-Nb-Ta-Zr-O Alloy, Metall and Mat Trans A. 44 (2013) 2307–2318. https://doi.org/10.1007/s11661-012-1598-2.

[70] R.J. Talling, R.J. Dashwood, M. Jackson, D. Dye, On the mechanism of superelasticity in Gum metal, Acta Materialia. 57 (2009) 1188–1198. https://doi.org/10.1016/j.actamat.2008.11.013.
[71] M. Nakai, M. Niinomi, T. Akahori, H. Tsutsumi, M. Ogawa, Effect of Oxygen Content on Microstructure and Mechanical Properties of Biomedical Ti-29Nb-13Ta-4.6Zr Alloy under Solutionized and Aged Conditions, Mater. Trans. 50 (2009) 2716–2720. https://doi.org/10.2320/matertrans.MA200904.
[72] Q. Wei, L. Wang, Y. Fu, J. Qin, W. Lu, D. Zhang, Influence of oxygen content on microstructure and mechanical properties of Ti–Nb–Ta–Zr alloy, Materials & Design. 32 (2011) 2934–2939.
[73] M. Tane, T. Nakano, S. Kuramoto, M. Niinomi, N. Takesue, H. Nakajima, ω Transformation in cold-worked Ti–Nb–Ta–Zr–O alloys with low body-centered cubic phase stability and its correlation with their elastic properties, Acta Materialia. 61 (2013) 139–150. https://doi.org/10.1016/j.actamat.2012.09.041.
[74] F. Geng, M. Niinomi, M. Nakai, Observation of yielding and strain hardening in a titanium alloy having high oxygen content, Materials Science and Engineering: A. 528 (2011) 5435–5445. https://doi.org/10.1016/j.msea.2011.03.064.
[75] J. Stráský, P. Harcuba, K. Václavová, K. Horváth, M. Landa, O. Srba, M. Janeček, Increasing strength of a biomedical Ti-Nb-Ta-Zr alloy by alloying with Fe, Si and O, Journal of the Mechanical Behavior of Biomedical Materials. 71 (2017) 329–336. https://doi.org/10.1016/j.jmbbm.2017.03.026.
[76] J.I. Qazi, H.J. Rack, B. Marquardt, High-strength metastable beta-titanium alloys for biomedical applications, JOM. 56 (2004) 49–51. https://doi.org/10.1007/s11837-004-0253-9.
[77] A.H. Cottrell, B.A. Bilby, Dislocation theory of yielding and strain ageing of iron, Proceedings of the Physical Society. Section A. 62 (1949) 49.
[78] B. Qian, S.A. Mantri, S. Dasari, J. Zhang, L. Lilensten, F. Sun, P. Vermaut, R. Banerjee, F. Prima, Mechanisms underlying enhanced strength-ductility combinations in TRIP/TWIP Ti-12Mo alloy engineered via isothermal omega precipitation, Acta Materialia. 245 (2023) 118619. https://doi.org/10.1016/j.actamat.2022.118619.
[79] M. Tane, S. Akita, T. Nakano, K. Hagihara, Y. Umakoshi, M. Niinomi, H. Nakajima, Peculiar elastic behavior of Ti–Nb–Ta–Zr single crystals, Acta Materialia. 56 (2008) 2856–2863. https://doi.org/10.1016/j.actamat.2008.02.017.
[80] J. Nejezchlebová, M. Janovská, P. Sedlák, J. Šmilauerová, J. Stráský, M. Janeček, H. Seiner, Elastic constants of β-Ti15Mo, Journal of Alloys and Compounds. 792 (2019) 960–967. https://doi.org/10.1016/j.jallcom.2019.03.418.
[81] M.C.M. Rodrigues, T. Garcin, M. Militzer, In-situ measurement of α formation kinetics in a metastable β Ti-5553 alloy using laser ultrasonics, Journal of Alloys and Compounds. 866 (2021) 158954. https://doi.org/10.1016/j.jallcom.2021.158954.
[82] Y.L. Hao, S.J. Li, S.Y. Sun, C.Y. Zheng, R. Yang, Elastic deformation behaviour of Ti–24Nb–4Zr–7.9Sn for biomedical applications, Acta Biomaterialia. 3 (2007) 277–286. https://doi.org/10.1016/j.actbio.2006.11.002.
[83] M. Tane, S. Akita, T. Nakano, K. Hagihara, Y. Umakoshi, M. Niinomi, H. Mori, H. Nakajima, Low Young's modulus of Ti–Nb–Ta–Zr alloys caused by softening in shear moduli c′ and c44 near lower limit of body-centered cubic phase stability, Acta Materialia. 58 (2010) 6790–6798. https://doi.org/10.1016/j.actamat.2010.09.007.
[84] P.J. Bania, Beta titanium alloys and their role in the titanium industry, JOM. 46 (1994) 16–19. https://doi.org/10.1007/BF03220742.
[85] T.B. Massalski, H. Okamoto, P.R. Subramanian, L. Kacprzak, Binary Alloy Phase Diagrams, 2nd Edition, ASM International, 1990. https://www.asminternational.org/binary-alloy-phase-diagrams-2nd-edition/results/-/journal_content/56/57718G/PUBLICATION/ (accessed July 3, 2023).
[86] Q. Wang, C. Dong, P.K. Liaw, Structural Stabilities of β-Ti Alloys Studied Using a New Mo Equivalent Derived from [β/(α + β)] Phase-Boundary Slopes, Metall and Mat Trans A. 46 (2015) 3440–3447. https://doi.org/10.1007/s11661-015-2923-3.

[87] M. Abdel-Hady, H. Fuwa, K. Hinoshita, H. Kimura, Y. Shinzato, M. Morinaga, Phase stability change with Zr content in β-type Ti–Nb alloys, Scripta Materialia. 57 (2007) 1000–1003. https://doi.org/10.1016/j.scriptamat.2007.08.003.
[88] P. Waldner, G. Eriksson, Thermodynamic modelling of the system titanium-oxygen, Calphad. 23 (1999) 189–218. https://doi.org/10.1016/S0364-5916(99)00025-5.
[89] J.I. Qazi, B. Marquardt, L.F. Allard, H.J. Rack, Phase transformations in Ti–35Nb–7Zr–5Ta–(0.06–0.68)O alloys, Materials Science and Engineering: C. 25 (2005) 389–397. https://doi.org/10.1016/j.msec.2005.01.022.
[90] S. Bartáková, J. Málek, P. Prachár, The Effect of Oxygen Addition on Microstructure and Mechanical Properties of Various Beta-Titanium Alloys, JOM. (2019). https://doi.org/10.1007/s11837-019-03879-w.
[91] J. Wang, W. Xiao, L. Ren, Y. Fu, C. Ma, The roles of oxygen content on microstructural transformation, mechanical properties and corrosion resistance of Ti-Nb-based biomedical alloys with different β stabilities, Materials Characterization. 176 (2021) 111122. https://doi.org/10.1016/j.matchar.2021.111122.
[92] M. Niinomi, Fatigue performance and cyto-toxicity of low rigidity titanium alloy, Ti–29Nb–13Ta–4.6Zr, Biomaterials. 24 (2003) 2673–2683. https://doi.org/10.1016/S0142-9612(03)00069-3.
[93] J. Hwang, T. Furuta, K. Nishino, T. Saito, Titanium alloy having high elastic deformation capacity and method for production thereof. US patent no. 7,261,782 B2, US 7,261,782 B2, 2007.
[94] N. Takesue, Y. Shimizu, T. Yano, M. Hara, S. Kuramoto, Single-crystal growth of Ti–Nb–Ta–Zr–O alloys and measurement of elastic properties, Journal of Crystal Growth. 311 (2009) 3319–3324. https://doi.org/10.1016/j.jcrysgro.2009.03.052.
[95] N. Nakanishi, Elastic constants as they relate to lattice properties and martensite formation, Progress in Materials Science. 24 (1980) 143–265. https://doi.org/10.1016/0079-6425(79)90005-7.
[96] M. Marteleur, F. Sun, T. Gloriant, P. Vermaut, P.J. Jacques, F. Prima, On the design of new β-metastable titanium alloys with improved work hardening rate thanks to simultaneous TRIP and TWIP effects, Scripta Materialia. 66 (2012) 749–752. https://doi.org/10.1016/j.scriptamat.2012.01.049.
[97] C. Brozek, F. Sun, P. Vermaut, Y. Millet, A. Lenain, D. Embury, P.J. Jacques, F. Prima, A β-titanium alloy with extra high strain-hardening rate: Design and mechanical properties, Scripta Materialia. 114 (2016) 60–64. https://doi.org/10.1016/j.scriptamat.2015.11.020.
[98] J.Y. Zhang, J.S. Li, Z. Chen, Q.K. Meng, F. Sun, B.L. Shen, Microstructural evolution of a ductile metastable β titanium alloy with combined TRIP/TWIP effects, Journal of Alloys and Compounds. 699 (2017) 775–782. https://doi.org/10.1016/j.jallcom.2016.12.394.
[99] F. Sun, J.Y. Zhang, C. Brozek, M. Marteleur, M. Veron, E. Rauch, T. Gloriant, P. Vermaut, C. Curfs, P.J. Jacques, F. Prima, The Role of Stress Induced Martensite in Ductile Metastable Beta Ti-alloys Showing Combined TRIP/TWIP Effects, Materials Today: Proceedings. 2 (2015) S505–S510. https://doi.org/10.1016/j.matpr.2015.07.336.
[100] S.W. Lee, C.H. Park, J.-K. Hong, J.-T. Yeom, Development of sub-grained α+β Ti alloy with high yield strength showing twinning- and transformation-induced plasticity, Journal of Alloys and Compounds. 813 (2020) 152102. https://doi.org/10.1016/j.jallcom.2019.152102.
[101] N.W. Ashcroft, N.D. Mermin, Solid State Physics, 1st edition, Cengage Learning, New York, 1976.
[102] J. Karthikeyan, V. Kumar, P. Murugan, The Role of Valence Electron Concentration in Tuning the Structure, Stability, and Electronic Properties of Mo6S9–xIx Nanowires, J. Phys. Chem. C. 119 (2015) 13979–13985. https://doi.org/10.1021/acs.jpcc.5b04663.

[103] M. Kamal, A.B. El-Bediwi, T. El-Ashram, M.E. Dorgham, The Role of Valence Electron Concentration on the Structure and Properties of Rapidly Solidified Sn-Ag Binary Alloys, 2012 (2012). https://doi.org/10.4236/msa.2012.33028.
[104] J. Wang, S. Bai, Y. Tang, S. Li, X. Liu, J. Jia, Y. Ye, L. Zhu, Effect of the valence electron concentration on the yield strength of Ti–Zr–Nb–V high-entropy alloys, Journal of Alloys and Compounds. 868 (2021) 159190. https://doi.org/10.1016/j.jallcom.2021.159190.
[105] Y.L. Hao, S.J. Li, F. Prima, R. Yang, Controlling reversible martensitic transformation in titanium alloys with high strength and low elastic modulus, Scripta Materialia. 67 (2012) 487–490. https://doi.org/10.1016/j.scriptamat.2012.06.011.
[106] H.L. Wang, Y.L. Hao, S.Y. He, T. Li, J.M. Cairney, Y.D. Wang, Y. Wang, E.G. Obbard, F. Prima, K. Du, S.J. Li, R. Yang, Elastically confined martensitic transformation at the nano-scale in a multifunctional titanium alloy, Acta Materialia. 135 (2017) 330–339. https://doi.org/10.1016/j.actamat.2017.06.040.
[107] J. Nejezchlebová, M. Janovská, H. Seiner, P. Sedlák, M. Landa, J. Šmilauerová, J. Stráský, P. Harcuba, M. Janeček, The effect of athermal and isothermal ω phase particles on elasticity of β-Ti single crystals, Acta Materialia. 110 (2016) 185–191. https://doi.org/10.1016/j.actamat.2016.03.033.
[108] M. Morinaga, Alloy Design Based on Molecular Orbital Method, Materials Transactions. 57 (2016) 213–226. https://doi.org/10.2320/matertrans.M2015418.
[109] M. Abdel-Hady, K. Hinoshita, M. Morinaga, General approach to phase stability and elastic properties of β-type Ti-alloys using electronic parameters, Scripta Materialia. 55 (2006) 477–480. https://doi.org/10.1016/j.scriptamat.2006.04.022.
[110] L. Lilensten, J.-P. Couzinié, J. Bourgon, L. Perrière, G. Dirras, F. Prima, I. Guillot, Design and tensile properties of a bcc Ti-rich high-entropy alloy with transformation-induced plasticity, Materials Research Letters. 5 (2017) 110–116. https://doi.org/10.1080/21663831.2016.1221861.
[111] K. Wang, The use of titanium for medical applications in the USA, Materials Science and Engineering: A. 213 (1996) 134–137. https://doi.org/10.1016/0921-5093(96)10243-4.
[112] T. Furuta, S. Kuramoto, J. Hwang, K. Nishino, T. Saito, Elastic Deformation Behavior of Multi-Functional Ti–Nb–Ta–Zr–O Alloys, Materials Transactions. 46 (2005) 3001–3007. https://doi.org/10.2320/matertrans.46.3001.
[113] T. Furuta, S. Kuramoto, J. Hwang, K. Nishino, T. Saito, M. Niinomi, Mechanical Properties and Phase Stability of Ti-Nb-Ta-Zr-O Alloys, Materials Transactions. 48 (2007) 1124–1130. https://doi.org/10.2320/matertrans.48.1124.
[114] M. Besse, P. Castany, T. Gloriant, Mechanisms of deformation in gum metal TNTZ-O and TNTZ titanium alloys: A comparative study on the oxygen influence, Acta Materialia. 59 (2011) 5982–5988. https://doi.org/10.1016/j.actamat.2011.06.006.
[115] D.M. Gordin, R. Ion, C. Vasilescu, S.I. Drob, A. Cimpean, T. Gloriant, Potentiality of the “Gum Metal” titanium-based alloy for biomedical applications, Materials Science and Engineering: C. 44 (2014) 362–370. https://doi.org/10.1016/j.msec.2014.08.003.
[116] K.Y. Xie, Y. Wang, Y. Zhao, L. Chang, G. Wang, Z. Chen, Y. Cao, X. Liao, E.J. Lavernia, R.Z. Valiev, B. Sarrafpour, H. Zoellner, S.P. Ringer, Nanocrystalline β-Ti alloy with high hardness, low Young’s modulus and excellent in vitro biocompatibility for biomedical applications, Materials Science and Engineering: C. 33 (2013) 3530–3536. https://doi.org/10.1016/j.msec.2013.04.044.
[117] A. Nocivin, I. Cinca, D. Raducanu, V.D. Cojocaru, I.A. Popovici, Mechanical properties of a Gum-type Ti–Nb–Zr–Fe–O alloy, Int J Miner Metall Mater. 24 (2017) 909–917. https://doi.org/10.1007/s12613-017-1477-3.
[118] E.L. Pang, E.M. Hildyard, L.D. Connor, E.J. Pickering, N.G. Jones, The effect of quench rate on the β-α″ martensitic transformation in Ti–Nb alloys, Materials Science and Engineering: A. 817 (2021) 141240. https://doi.org/10.1016/j.msea.2021.141240.

[119] S. Ding, J. Gregoire, J.J. Vlassak, J. Schroers, Solidification of Au-Cu-Si alloys investigated by a combinatorial approach, Journal of Applied Physics. 111 (2012) 114901. https://doi.org/10.1063/1.4722996.
[120] O.M. Ivasishin, V.M. Anokhin, A.N. Demidik, D.G. Savvakin, Cost-Effective Blended Elemental Powder Metallurgy of Titanium Alloys for Transportation Application, Key Engineering Materials. 188 (2000) 55–62. https://doi.org/10.4028/www.scientific.net/KEM.188.55.
[121] H.Z. Lu, C. Yang, X.X. Li, Q.R. Cheng, H.W. Ma, Z. Wang, X.Q. Li, S.G. Qu, Microstructure evolution and superelasticity of Ti-24Nb-xZr alloys fabricated by spark plasma sintering, Journal of Alloys and Compounds. 823 (2020) 153875. https://doi.org/10.1016/j.jallcom.2020.153875.
[122] J. Chávez, L. Olmos, O. Jimenez, F. Alvarado-Hernández, H. Flores-Zúñiga, J.-P. Camarillo-Garcia, S.J. Guevara-Martínez, Investigation of a Ti–30Zr binary alloy fabricated through spark plasma sintering, Journal of Materials Research and Technology. 9 (2020) 9328–9340. https://doi.org/10.1016/j.jmrt.2020.03.110.
[123] Q. Kong, X. Lai, X. An, W. Feng, C. Lu, J. Wu, C. Wu, L. Wu, Q. Wang, Characterization and corrosion behaviour of Ti-13Nb-13Zr alloy prepared by mechanical alloying and spark plasma sintering, Materials Today Communications. 23 (2020) 101130. https://doi.org/10.1016/j.mtcomm.2020.101130.
[124] Y.F. Yang, S.D. Luo, G.B. Schaffer, M. Qian, Sintering of Ti–10V–2Fe–3Al and mechanical properties, Materials Science and Engineering: A. 528 (2011) 6719–6726. https://doi.org/10.1016/j.msea.2011.05.041.
[125] D.R. Santos, M.S. Pereira, C.A.A. Cairo, M.L.A. Graça, V.A.R. Henriques, Isochronal sintering of the blended elemental Ti–35Nb alloy, Materials Science and Engineering: A. 472 (2008) 193–197. https://doi.org/10.1016/j.msea.2007.03.075.
[126] S. Si, B. Fan, X. Liu, T. Zhou, C. He, D. Song, J. Liu, Study on strengthening effects of Zr-Ti-Nb-O alloys via high throughput powder metallurgy and data-driven machine learning, Materials & Design. 206 (2021) 109777. https://doi.org/10.1016/j.matdes.2021.109777.
[127] J. Kozlík, D. Preisler, J. Stráský, J. Veselý, A. Veverková, T. Chráska, M. Janeček, Phase transformations in a heterogeneous Ti-xNb-7Zr-0.8O alloy prepared by a field-assisted sintering technique, Materials & Design. 198 (2021) 109308. https://doi.org/10.1016/j.matdes.2020.109308.
[128] J. Kozlík, D. Preisler, J. Stráský, T. Košutová, C.A. Corrêa, J. Veselý, L. Bodnárová, F. Lukáč, T. Chráska, M. Janeček, Manufacturing of biomedical Ti alloys with controlled oxygen content by blended elemental powder metallurgy, Journal of Alloys and Compounds. 905 (2022) 164259. https://doi.org/10.1016/j.jallcom.2022.164259.
[129] S.I. Wright, M.M. Nowell, S.P. Lindeman, P.P. Camus, M. De Graef, M.A. Jackson, Introduction and comparison of new EBSD post-processing methodologies, Ultramicroscopy. 159 (2015) 81–94. https://doi.org/10.1016/j.ultramic.2015.08.001.
[130] S.I. Wright, M.M. Nowell, R. de Kloe, P. Camus, T. Rampton, Electron imaging with an EBSD detector, Ultramicroscopy. 148 (2015) 132–145. https://doi.org/10.1016/j.ultramic.2014.10.002.
[131] P. Zháňal, Study of Phase Transformations in Ti Alloys, Doctoral thesis, Charles University, 2016. https://dspace.cuni.cz/handle/20.500.11956/79195 (accessed June 8, 2023).
[132] K. Bartha, Phase transformations in ultra-fine grained titanium alloys, Doctoral thesis, Charles University, 2019. https://dspace.cuni.cz/handle/20.500.11956/107801 (accessed June 8, 2023).
[133] J. Blaber, B. Adair, A. Antoniou, Ncorr: Open-Source 2D Digital Image Correlation Matlab Software, Exp Mech. 55 (2015) 1105–1122. https://doi.org/10.1007/s11340-015-0009-1.
[134] The MathWorks Inc., MATLAB version: 9.13.0 (R2022b), (2022). https://www.mathworks.com.

[135] M.A. Sutton, J.H. Yan, V. Tiwari, H.W. Schreier, J.J. Orteu, The effect of out-of-plane motion on 2D and 3D digital image correlation measurements, Optics and Lasers in Engineering. 46 (2008) 746–757. https://doi.org/10.1016/j.optlaseng.2008.05.005.
[136] P. Sedlák, H. Seiner, J. Zídek, M. Janovská, M. Landa, Determination of All 21 Independent Elastic Coefficients of Generally Anisotropic Solids by Resonant Ultrasound Spectroscopy: Benchmark Examples, Exp Mech. 54 (2014) 1073–1085. https://doi.org/10.1007/s11340-014-9862-6.
[137] J. Nejezchlebová, H. Seiner, M. Ševčík, M. Landa, M. Karlík, Ultrasonic detection of ductile-to-brittle transitions in free-cutting aluminum alloys, NDT & E International. 69 (2015) 40–47. https://doi.org/10.1016/j.ndteint.2014.09.007.
[138] D. Preisler, M. Janovská, H. Seiner, L. Bodnárová, J. Nejezchlebová, M. Koller, P. Sedlák, P. Harcuba, J. Veselý, J. Kozlík, T. Chráska, J. Stráský, M. Janeček, High-throughput characterization of elastic moduli of Ti-Nb-Zr-O biomedical alloys fabricated by field-assisted sintering technique, Journal of Alloys and Compounds. 932 (2023) 167656. https://doi.org/10.1016/j.jallcom.2022.167656.
[139] D. Preisler, Oxygen-strengthened biomedical beta titanium alloys, Diploma thesis, Univerzita Karlova, 2018. https://dspace.cuni.cz/handle/20.500.11956/98671 (accessed March 7, 2023).
[140] G.B. Gibbs, D. Graham, D.H. Tomlin, Diffusion in titanium and titanium—niobium alloys, The Philosophical Magazine: A Journal of Theoretical Experimental and Applied Physics. 8 (1963) 1269–1282. https://doi.org/10.1080/14786436308207292.
[141] H. Araki, Y. Minamino, T. Yamane, T. Nakatsuka, Y. Miyamoto, Pressure dependence of anomalous diffusion of zirconium in β-Titanium, Metall Mater Trans A. 27 (1996) 1807–1814. https://doi.org/10.1007/BF02651930.
[142] J. Fencl, J. Stráský, P. Harcuba, M. Janeček, Biokompatibilní slitina titanu, CZ2017814A3, 2019. https://patents.google.com/patent/CZ2017814A3/cs?inventor=Josef+Str%C3%A1sk%C3%BD (accessed April 27, 2023).
[143] D. Preisler, M. Janeček, P. Harcuba, J. Džugan, K. Halmešová, J. Málek, A. Veverková, J. Stráský, The Effect of Hot Working on the Mechanical Properties of High Strength Biomedical Ti-Nb-Ta-Zr-O Alloy, Materials. 12 (2019) 4233. https://doi.org/10.3390/ma12244233.
[144] D. Preisler, J. Stráský, P. Harcuba, F.G. Warchomicka, M. Janeček, High Temperature Mechanical Properties and Microstructure of Ti-Nb-Zr-Ta-O Biomedical Alloy, Acta Phys. Pol. A. 134 (2018) 636–639. https://doi.org/10.12693/APhysPolA.134.636.
[145] R.I. Stephens, Fatigue Design Criteria, in: K.H.J. Buschow, R.W. Cahn, M.C. Flemings, B. Ilschner, E.J. Kramer, S. Mahajan, P. Veyssière (Eds.), Encyclopedia of Materials: Science and Technology, Elsevier, Oxford, 2001: pp. 2910–2918. https://doi.org/10.1016/B0-08-043152-6/00518-0.
[146] J. Stráský, D. Preisler, K. Bartha, M. Janeček, Manufacturing of Biomedical Ti-Based Alloys with High Oxygen Content and Various Amount of Beta-Stabilizing Elements, Materials Science Forum. 941 (2018) 2471–2476. https://doi.org/10.4028/www.scientific.net/MSF.941.2471.
[147] P. Zháňal, P. Harcuba, M. Hájek, B. Smola, J. Stráský, J. Šmilauerová, J. Veselý, M. Janeček, Evolution of ω phase during heating of metastable β titanium alloy Ti–15Mo, Journal of Materials Science. 53 (2018) 837–845. https://doi.org/10.1007/s10853-017-1519-2.
[148] J. Šmilauerová, P. Harcuba, D. Kriegner, V. Holý, On the completeness of the β→ω transformation in metastable β titanium alloys, J Appl Cryst, J Appl Crystallogr. 50 (2017) 283–287. https://doi.org/10.1107/S1600576716020458.
[149] M. Todai, T. Fukuda, T. Kakeshita, Relation between negative temperature coefficient in electrical resistivity and athermal ω phase in Ti–xNb (26≤x≤29at.%) alloys, Journal of Alloys and Compounds. 577 (2013) S431–S434. https://doi.org/10.1016/j.jallcom.2012.02.026.

[150] P. Wang, M. Todai, T. Nakano, ω-phase transformation and lattice modulation in biomedical β-phase Ti-Nb-Al alloys, Journal of Alloys and Compounds. 766 (2018) 511–516. https://doi.org/10.1016/j.jallcom.2018.06.266.
[151] T. Yano, Y. Murakami, D. Shindo, S. Kuramoto, Study of the nanostructure of Gum Metal using energy-filtered transmission electron microscopy, Acta Materialia. 57 (2009) 628–633. https://doi.org/10.1016/j.actamat.2008.10.002.
[152] M. Tahara, H.Y. Kim, T. Inamura, H. Hosoda, S. Miyazaki, Lattice modulation and superelasticity in oxygen-added β-Ti alloys, Acta Materialia. 59 (2011) 6208–6218. https://doi.org/10.1016/j.actamat.2011.06.015.
[153] Y. Zheng, T. Alam, R. Banerjee, D. Banerjee, H.L. Fraser, The influence of aluminum and oxygen additions on intrinsic structural instabilities in titanium-molybdenum alloys, Scripta Materialia. 152 (2018) 150–153. https://doi.org/10.1016/j.scriptamat.2018.04.030.
[154] J. Stráský, Optimization of properties of Ti based alloys for biomedical and structural applications, Doctoral thesis, Charles University in Prague, 2014.
[155] M. Niinomi, Mechanical properties of biomedical titanium alloys, Materials Science and Engineering: A. 243 (1998) 231–236. https://doi.org/10.1016/S0921-5093(97)00806-X.
[156] M. Tane, Y. Okuda, Y. Todaka, H. Ogi, A. Nagakubo, Elastic properties of single-crystalline ω phase in titanium, Acta Materialia. 61 (2013) 7543–7554. https://doi.org/10.1016/j.actamat.2013.08.036.
[157] E.L. Pang, E.J. Pickering, S.I. Baik, D.N. Seidman, N.G. Jones, The effect of zirconium on the omega phase in Ti-24Nb-[0–8]Zr (at.%) alloys, Acta Materialia. 153 (2018) 62–70. https://doi.org/10.1016/j.actamat.2018.04.016.
[158] S. Hanada, H. Matsumoto, S. Watanabe, Mechanical compatibility of titanium implants in hard tissues, International Congress Series. 1284 (2005) 239–247. https://doi.org/10.1016/j.ics.2005.06.084.
[159] J. Stráský, M. Janeček, P. Harcuba, D. Preisler, M. Landa, Biocompatible beta-Ti alloys with enhanced strength due to increased oxygen content, in: Titanium in Medical and Dental Applications, Elsevier, 2018.
[160] H. Liu, M. Niinomi, M. Nakai, S. Obara, H. Fujii, Improved fatigue properties with maintaining low Young's modulus achieved in biomedical beta-type titanium alloy by oxygen addition, Materials Science and Engineering: A. 704 (2017) 10–17. https://doi.org/10.1016/j.msea.2017.07.078.
[161] J. Málek, F. Hnilica, J. Veselý, B. Smola, S. Bartáková, J. Vaněk, The influence of chemical composition and thermo-mechanical treatment on Ti–Nb–Ta–Zr alloys, Materials & Design. 35 (2012) 731–740. https://doi.org/10.1016/j.matdes.2011.10.030.
[162] S. Hanada, T. Ozaki, E. Takahashi, S. Watanabe, K. Yoshimi, T. Abumiya, Composition Dependence of Young's Modulus in Beta Titanium Binary Alloys, Materials Science Forum. 426–432 (2003) 3103–3108. https://doi.org/10.4028/www.scientific.net/MSF.426-432.3103.
[163] M.F.-X. Wagner, W. Windl, Lattice stability, elastic constants and macroscopic moduli of NiTi martensites from first principles, Acta Materialia. 56 (2008) 6232–6245. https://doi.org/10.1016/j.actamat.2008.08.043.
[164] P. Šittner, P. Sedlák, H. Seiner, P. Sedmák, J. Pilch, R. Delville, L. Heller, L. Kadeřávek, On the coupling between martensitic transformation and plasticity in NiTi: Experiments and continuum based modelling, Progress in Materials Science. 98 (2018) 249–298. https://doi.org/10.1016/j.pmatsci.2018.07.003.
[165] M. Tane, K. Hagihara, M. Ueda, T. Nakano, Y. Okuda, Elastic-modulus enhancement during room-temperature aging and its suppression in metastable Ti–Nb-Based alloys with low body-centered cubic phase stability, Acta Materialia. 102 (2016) 373–384. https://doi.org/10.1016/j.actamat.2015.09.030.
[166] E.G. Obbard, Y.L. Hao, R.J. Talling, S.J. Li, Y.W. Zhang, D. Dye, R. Yang, The effect of oxygen on α″ martensite and superelasticity in Ti–24Nb–4Zr–8Sn, Acta Materialia. 59 (2011) 112–125. https://doi.org/10.1016/j.actamat.2010.09.015.

[167] M. Tahara, T. Inamura, H.Y. Kim, S. Miyazaki, H. Hosoda, Role of oxygen atoms in α″ martensite of Ti-20at.% Nb alloy, Scripta Materialia. 112 (2016) 15–18. https://doi.org/10.1016/j.scriptamat.2015.08.033.
[168] B.S. Hickman, The formation of omega phase in titanium and zirconium alloys: a review, Journal of Materials Science. 4 (1969) 554–563.
[169] A.W. Bowen, Omega phase embrittlement in aged Ti-15%Mo, Scripta Metallurgica. 5 (1971) 709–715. https://doi.org/10.1016/0036-9748(71)90258-4.
[170] X. Zhao, M. Niinomi, M. Nakai, J. Hieda, Effect of Deformation-Induced ω Phase on the Mechanical Properties of Metastable β-Type Ti–V Alloys, Materials Transactions. 53 (2012) 1379–1384. https://doi.org/10.2320/matertrans.M2012116.
[171] J. Ballor, T. Li, F. Prima, C.J. Boehlert, A. Devaraj, A review of the metastable omega phase in beta titanium alloys: the phase transformation mechanisms and its effect on mechanical properties, International Materials Reviews. 0 (2022) 1–20. https://doi.org/10.1080/09506608.2022.2036401.
[172] T.W. Duerig, J. Albrecht, D. Richter, P. Fischer, Formation and reversion of stress induced martensite in Ti-10V-2Fe-3Al, Acta Metallurgica. 30 (1982) 2161–2172. https://doi.org/10.1016/0001-6160(82)90137-7.
[173] J. Stráský, D. Preisler, H. Seiner, L. Bodnárová, M. Janovská, T. Košutová, P. Harcuba, K. Šalata, K. Halmešová, J. Džugan, M. Janeček, Achieving high strength and low elastic modulus in interstitial biomedical Ti–Nb–Zr–O alloys through compositional optimization, Materials Science and Engineering: A. 839 (2022) 142833. https://doi.org/10.1016/j.msea.2022.142833.
[174] K. Chou, E.A. Marquis, Oxygen effects on ω and α phase transformations in a metastable β Ti–Nb alloy, Acta Materialia. 181 (2019) 367–376. https://doi.org/10.1016/j.actamat.2019.09.049.
[175] J. Coakley, A. Radecka, D. Dye, P.A.J. Bagot, H.J. Stone, D.N. Seidman, D. Isheim, Isothermal omega formation and evolution in the Beta-Ti alloy Ti-5Al-5Mo-5V-3Cr, Philosophical Magazine Letters. 96 (2016) 416–424. https://doi.org/10.1080/09500839.2016.1242877.
[176] W. Chen, S. Cao, J. Zhang, Y. Zha, Q. Hu, J. Sun, New insights into ω-embrittlement in high misfit metastable β-titanium alloys: Mechanically-driven ω-mediated amorphization, Materials & Design. 205 (2021) 109724. https://doi.org/10.1016/j.matdes.2021.109724.
[177] S. Guo, Q. Meng, X. Zhao, Q. Wei, H. Xu, Design and fabrication of a metastable β-type titanium alloy with ultralow elastic modulus and high strength, Sci Rep. 5 (2015). https://doi.org/10.1038/srep14688.
[178] L.C. Zhang, E.C.S. Kiat, A. Pramanik, A Briefing on the Manufacture of Hip Joint Prostheses, AMR. 76–78 (2009) 212–216. https://doi.org/10.4028/www.scientific.net/AMR.76-78.212.
[179] S. Acharya, A.G. Panicker, D.V. Laxmi, S. Suwas, K. Chatterjee, Study of the influence of Zr on the mechanical properties and functional response of Ti-Nb-Ta-Zr-O alloy for orthopedic applications, Materials & Design. 164 (2019) 107555. https://doi.org/10.1016/j.matdes.2018.107555.
[180] A. Ramarolahy, P. Castany, F. Prima, P. Laheurte, I. Péron, T. Gloriant, Microstructure and mechanical behavior of superelastic Ti–24Nb–0.5O and Ti–24Nb–0.5N biomedical alloys, Journal of the Mechanical Behavior of Biomedical Materials. 9 (2012) 83–90. https://doi.org/10.1016/j.jmbbm.2012.01.017.
[181] X. Ji, S. Emura, T. Liu, K. Suzuta, X. Min, K. Tsuchiya, Effect of oxygen addition on microstructures and mechanical properties of Ti-7.5Mo alloy, Journal of Alloys and Compounds. 737 (2018) 221–229. https://doi.org/10.1016/j.jallcom.2017.12.072.
[182] D. Preisler, J. Stráský, P. Harcuba, K. Halmešová, M. Janeček, Cold Swaging and Recrystallization Annealing of Ti-Nb-Ta-Zr-O Alloy - Microstructure, Texture and Microhardness Evolution, Materials Science Forum. 941 (2018) 1132–1136. https://doi.org/10.4028/www.scientific.net/MSF.941.1132.

[183] A. Veverková, J. Kozlík, K. Bartha, T. Košutová, C.A. Correa, H. Becker, T. Chráska, M. Janeček, J. Stráský, Preparation of bulk Ti15Mo alloy using cryogenic milling and spark plasma sintering, Materials Characterization. 171 (2021) 110762. https://doi.org/10.1016/j.matchar.2020.110762.
[184] X. Zhao, L. Duan, Y. Wang, Fast interdiffusion and Kirkendall effects of SiC-coated C/SiC composites joined by a Ti-Nb-Ti interlayer via spark plasma sintering, Journal of the European Ceramic Society. 39 (2019) 1757–1765. https://doi.org/10.1016/j.jeurceramsoc.2019.01.020.
[185] H. Seiner, P. Sedlák, L. Bodnárová, A. Kruisová, M. Landa, A. de Pablos, M. Belmonte, Sensitivity of the resonant ultrasound spectroscopy to weak gradients of elastic properties, The Journal of the Acoustical Society of America. 131 (2012) 3775–3785. https://doi.org/10.1121/1.3695393.
[186] S. Dubinskiy, A. Korotitskiy, S. Prokoshkin, V. Brailovski, In situ X-ray diffraction study of athermal and isothermal omega-phase crystal lattice in Ti-Nb-based shape memory alloys, Materials Letters. 168 (2016) 155–157. https://doi.org/10.1016/j.matlet.2016.01.012.
[187] S. Kawano, S. Kobayashi, S. Okano, Effect of Oxygen Addition on the Formation of α″ Martensite and Athermal ω in Ti–Nb Alloys, Materials Transactions. 60 (2019) 1842–1849. https://doi.org/10.2320/matertrans.ME201908.
[188] A.W. Cochardt, G. Schoek, H. Wiedersich, Interaction between dislocations and interstitial atoms in body-centered cubic metals, Acta Metallurgica. 3 (1955) 533–537. https://doi.org/10.1016/0001-6160(55)90111-5.
[189] A.G. Illarionov, S.V. Grib, S.M. Illarionova, A.A. Popov, Relationship between Structure, Phase Composition, and Physicomechanical Properties of Quenched Ti–Nb Alloys, Phys. Metals Metallogr. 120 (2019) 150–156. https://doi.org/10.1134/S0031918X19020054.
[190] R.T. Bryant, The solubility of oxygen in transition metal alloys, Journal of the Less Common Metals. 4 (1962) 62–68. https://doi.org/10.1016/0022-5088(62)90060-7.
[191] X. Shi, X. Wang, B. Chen, J. Umeda, A. Bahador, K. Kondoh, J. Shen, Precision control of oxygen content in CP-Ti for ultra-high strength through titanium oxide decomposition: An in-situ study, Materials & Design. 227 (2023) 111797. https://doi.org/10.1016/j.matdes.2023.111797.
[192] J. Shen, B. Chen, J. Umeda, J. Zhang, Y. Li, K. Kondoh, An in-situ study on deformation and cracking initiation in oxygen-doped commercial purity titanium, Mechanics of Materials. 148 (2020) 103519. https://doi.org/10.1016/j.mechmat.2020.103519.
[193] Y. Zhou, F. Yang, C. Chen, Y. Shao, B. Lu, T. Lu, Y. Sui, Z. Guo, Mechanical property enhancement of high-plasticity powder metallurgy titanium with a high oxygen concentration, Journal of Alloys and Compounds. 885 (2021) 161006. https://doi.org/10.1016/j.jallcom.2021.161006.
[194] J.F. Cardenas-Garcia, H.G. Yao, S. Zheng, 3D reconstruction of objects using stereo imaging, Optics and Lasers in Engineering. 22 (1995) 193–213. https://doi.org/10.1016/0143-8166(94)00046-D.
[195] D.R. James, S.H. Carpenter, The effect of sample size on the acoustic emission generated during tensile deformation of 7075 aluminum alloy, Scripta Metallurgica. 10 (1976) 779–781. https://doi.org/10.1016/0036-9748(76)90362-8.
[196] L. Lilensten, Y. Danard, R. Poulain, R. Guillou, J.M. Joubert, L. Perrière, P. Vermaut, D. Thiaudière, F. Prima, From single phase to dual-phase TRIP-TWIP titanium alloys: Design approach and properties, Materialia. 12 (2020) 100700. https://doi.org/10.1016/j.mtla.2020.100700.
[197] M.J. Lai, C.C. Tasan, D. Raabe, On the mechanism of {332} twinning in metastable β titanium alloys, Acta Materialia. 111 (2016) 173–186. https://doi.org/10.1016/j.actamat.2016.03.040.

[198] Y. Zheng, D. Banerjee, H.L. Fraser, A nano-scale instability in the β phase of dilute Ti–Mo alloys, Scripta Materialia. 116 (2016) 131–134. https://doi.org/10.1016/j.scriptamat.2016.01.044.
[199] Y. Danard, F. Sun, T. Gloriant, I. Freiherr Von Thüngen, M. Piellard, F. Prima, The Influence of Twinning on the Strain–Hardenability in TRIP/TWIP Titanium Alloys: Role of Solute–Solution Strengthening, Frontiers in Materials. 7 (2020). https://www.frontiersin.org/articles/10.3389/fmats.2020.00240 (accessed April 24, 2023).
[200] B. Qian, L. Lilensten, J. Zhang, M. Yang, F. Sun, P. Vermaut, F. Prima, On the transformation pathways in TRIP/TWIP Ti–12Mo alloy, Materials Science and Engineering: A. 822 (2021) 141672. https://doi.org/10.1016/j.msea.2021.141672.
[201] Q. Liang, Z. Kloenne, Y. Zheng, D. Wang, S. Antonov, Y. Gao, Y. Hao, R. Yang, Y. Wang, H.L. Fraser, The role of nano-scaled structural non-uniformities on deformation twinning and stress-induced transformation in a cold rolled multifunctional β-titanium alloy, Scripta Materialia. 177 (2020) 181–185. https://doi.org/10.1016/j.scriptamat.2019.10.029.
[202] Y. Yang, P. Castany, M. Cornen, F. Prima, S.J. Li, Y.L. Hao, T. Gloriant, Characterization of the martensitic transformation in the superelastic Ti–24Nb–4Zr–8Sn alloy by in situ synchrotron X-ray diffraction and dynamic mechanical analysis, Acta Materialia. 88 (2015) 25–33. https://doi.org/10.1016/j.actamat.2015.01.039.
[203] ASTM F899-02 Standard Specification for Stainless Steel for Surgical Instruments, ASTM International, n.d. https://www.astm.org/f0899-02.html (accessed June 6, 2023).

List of Publications

D. Preisler, M. Janovská, H. Seiner, L. Bodnárová, J. Nejezchlebová, M. Koller, P. Sedlák, P. Harcuba, J. Veselý, J. Kozlík, T. Chráska, J. Stráský, M. Janeček, High-throughput characterization of elastic moduli of Ti-Nb-Zr-O biomedical alloys fabricated by field-assisted sintering technique, Journal of Alloys and Compounds. 932 (2023) 167656. https://doi.org/10.1016/j.jallcom.2022.167656

J. Stráský, **D. Preisler**, H. Seiner, L. Bodnárová, M. Janovská, T. Košutová, P. Harcuba, K. Šalata, K. Halmešová, J. Džugan, M. Janeček, Achieving high strength and low elastic modulus in interstitial biomedical Ti–Nb–Zr–O alloys through compositional optimization, Materials Science and Engineering: A. 839 (2022) 142833. https://doi.org/10.1016/j.msea.2022.142833

J. Stráský, M. Janeček, P. Harcuba, **D. Preisler**, M. Landa, 4.2 - Biocompatible beta-Ti alloys with enhanced strength due to increased oxygen content, in: F.H. Froes, M. Qian (Eds.), Titanium in Medical and Dental Applications, Woodhead Publishing, 2018: pp. 371–392. https://doi.org/10.1016/B978-0-12-812456-7.00017-2

D. Preisler, M. Janeček, P. Harcuba, J. Džugan, K. Halmešová, J. Málek, A. Veverková, J. Stráský, The Effect of Hot Working on the Mechanical Properties of High Strength Biomedical Ti-Nb-Ta-Zr-O Alloy, Materials. 12 (2019) 4233. https://doi.org/10.3390/ma12244233

J. Kozlík, **D. Preisler**, M. Haasová, J. Stráský, T. Chráska, M. Janeček, Mechanical Properties of Ti–5Al–5V–5Mo–3Cr Alloy Sintered From Blended Elemental Powders, Metall Mater Trans A. (2023). https://doi.org/10.1007/s11661-023-07048-2

J. Kozlík, **D. Preisler**, J. Stráský, T. Košutová, C.A. Corrêa, J. Veselý, L. Bodnárová, F. Lukáč, T. Chráska, M. Janeček, Manufacturing of biomedical Ti alloys with controlled oxygen content by blended elemental powder metallurgy, Journal of Alloys and Compounds. 905 (2022) 164259. https://doi.org/10.1016/j.jallcom.2022.164259

J. Kozlík, **D. Preisler**, J. Stráský, J. Veselý, A. Veverková, T. Chráska, M. Janeček, Phase transformations in a heterogeneous Ti-xNb-7Zr-0.8O alloy prepared by a field-assisted sintering technique, Materials & Design. 198 (2021) 109308. https://doi.org/10.1016/j.matdes.2020.109308

D. Preisler, T. Krajňák, M. Janeček, J. Kozlík, J. Stráský, M. Brázda, J. Džugan, Directed energy deposition of bulk Nb-Ta-Ti-Zr refractory complex concentrated alloy, Materials Letters. 337 (2023) 133980. https://doi.org/10.1016/j.matlet.2023.133980

T. Krajňák, M. Janeček, **D. Preisler**, J. Stráský, J. Kozlík, T. Škraban, M. Brázda, J. Džugan, Microstructure evolution in compositionally graded Ti(4–12 wt% Mo) prepared by laser directed energy deposition, Journal of Materials Research and Technology. 23 (2023) 4527–4537. https://doi.org/10.1016/j.jmrt.2023.01.215

T. Krajňák, M. Janeček, J. Kozlík, **D. Preisler**, J. Stráský, M. Brázda, J. Kout, K. Halmešová, J. Džugan, Influence of the thermal history on the phase composition of laser directed energy deposited Ti-8.5 wt% Mo alloy, Materials & Design. 222 (2022) 111049. https://doi.org/10.1016/j.matdes.2022.111049

T. Krajňák, M. Janeček, P. Minárik, J. Veselý, P. Cejpek, J. Gubicza, P.T. Hung, **D. Preisler**, F. Nový, A.G. Raab, G.I. Raab, R. Asfandiyarov, Microstructure Evolution and Mechanical Properties of cp-Ti Processed by a Novel Technique of Rotational Constrained Bending, Metallurgical and Materials Transactions A: Physical Metallurgy and Materials Science. 52 (2021) 1665–1678. https://doi.org/10.1007/s11661-021-06157-0

A. Veverková, **D. Preisler**, M. Zimina, T. Košutová, P. Harcuba, M. Janeček, J. Stráský, Novel α+β zr alloys with enhanced strength, Materials. 14 (2021) 1–12. https://doi.org/10.3390/ma14020418

F. Haftlang, A.Z. Hanzaki, H.R. Abedi, **D. Preisler**, K. Bartha, The subsurface frictional hardening: A new approach to improve the high-speed wear performance of Ti-29Nb-14Ta-4.5Zr alloy against Ti-6Al-4V extra-low interstitial, Wear. 422–423 (2019) 137–150. https://doi.org/10.1016/j.wear.2018.12.095

T. Vlasák, J. Čížek, O. Melikhova, F. Lukáč, **D. Preisler**, M. Janeček, P. Harcuba, M. Zimina, O. Srba, Thermal Stability of Microstructure of High-Entropy Alloys Based on Refractory Metals Hf, Nb, Ta, Ti, V, and Zr, Metals. 12 (2022). https://doi.org/10.3390/met12030394

J. Matějíček, M. Vilémová, J. Veverka, J. Kubásek, F. Lukáč, P. Novák, **D. Preisler**, J. Stráský, Z. Weiss, On the Structural and Chemical Homogeneity of Spark Plasma Sintered Tungsten, Metals. 9 (2019) 879. https://doi.org/10.3390/met9080879

Conference papers

D. Medvecká, F. Nový, M. Mičian, O. Bokůvka, **D. Preisler**, Microstructural changes in HAZ of weld joints of S960 MC steel, Materials Today: Proceedings. 62 (2022) 2466–2468. https://doi.org/10.1016/j.matpr.2022.02.595

M. Janeček, T. Krajňák, J. Veselý, P. Minárik, **D. Preisler**, J. Stráský, A.G. Raab, G.I. Raab, R.N. Asfandiyarov, Microstructure evolution in a CuZr alloy and CP Ti processed by a novel technique of free bending in rotating rollers, in: 2019. https://doi.org/10.1088/1757-899X/672/1/012006

D. Preisler, J. Stráský, P. Harcuba, F.G. Warchomicka, M. Janeček, High Temperature Mechanical Properties and Microstructure of Ti-Nb-Zr-Ta-O Biomedical Alloy, Acta Phys. Pol. A. 134 (2018) 636–639. https://doi.org/10.12693/APhysPolA.134.636

D. Preisler, J. Stráský, K. Bartha, J. Džugan, M. Janeček, Beta phase stability of Ti-35Nb-6Ta-7Zr-0.7O beta titanium alloy, IOP Conf. Ser.: Mater. Sci. Eng. 461 (2018) 012068. https://doi.org/10.1088/1757-899X/461/1/012068

J. Stráský, **D. Preisler**, K. Bartha, M. Janeček, Manufacturing of Biomedical Ti-Based Alloys with High Oxygen Content and Various Amount of Beta-Stabilizing Elements, Materials Science Forum. 941 (2018) 2471–2476. https://doi.org/10.4028/www.scientific.net/MSF.941.2471

D. Preisler, J. Stráský, P. Harcuba, K. Halmešová, M. Janeček, Cold Swaging and Recrystallization Annealing of Ti-Nb-Ta-Zr-O Alloy - Microstructure, Texture and Microhardness Evolution, Materials Science Forum. 941 (2018) 1132–1136. https://doi.org/10.4028/www.scientific.net/MSF.941.1132

D. Preisler, J. Stráský, R. Král, M. Janeček, Hot forging of biomedical B-Ti alloy strengthened by high oxygen content, in: METAL 2018 - 27th International Conference on Metallurgy and Materials, Conference Proceedings, 2018: pp. 1310–1314.

D. Preisler, J. Stráský, P. Harcuba, M. Janeček, Effect of hot rolling on microstructure and tensile properties of Ti-Nb-Zr-Ta-O alloy, in: METAL 2017 - 26th International Conference on Metallurgy and Materials, Conference Proceedings, 2017: pp. 1905–1910.

D. Preisler, K. Václavová, J. Stráský, M. Janeček, P. Harcuba, Microstructure and mechanical properties of Ti-Nb-Zr-Ta-O biomedical alloy, in: METAL 2016: 25rd International Conference on Metallurgy and Materials. Ostrava: TANGER, 2016: pp. 1509–1513.